



Universiteit
Leiden
The Netherlands

Host galaxies and environment of active galactic nuclei : a study of the XMM large scale structure survey

Tasse, C.

Citation

Tasse, C. (2008, January 31). *Host galaxies and environment of active galactic nuclei : a study of the XMM large scale structure survey*. Leiden Observatory, Faculty of Science, Leiden University. Retrieved from <https://hdl.handle.net/1887/12586>

Version: Corrected Publisher's Version

License: [Licence agreement concerning inclusion of doctoral thesis in the Institutional Repository of the University of Leiden](#)

Downloaded from: <https://hdl.handle.net/1887/12586>

Note: To cite this publication please use the final published version (if applicable).

Host galaxies and environment of active galactic nuclei

A study of the XMM Large Scale Structure survey

Cover designed by Gilles Tasse.

In the sky: Canada-France Hawaii Telescope Legacy Survey optical data + Very Large Array radio data at 325 MHz (contours). At the center of the front page: the radio galaxy J0226.3-0400.

Host galaxies and environment of active galactic nuclei

A study of the XMM Large Scale Structure survey

Proefschrift

ter verkrijging van
de graad van Doctor aan de Universiteit Leiden,
op gezag van Rector Magnificus prof.mr. P.F. van der Heijden,
volgens besluit van het College voor Promoties
te verdedigen op donderdag 31 januari 2008
klokke 13.45 uur

door

Cyril TASSE

geboren te Saint-Brieuc (Frankrijk) in 1979

Promotiecommissie

Promotor: Prof. dr. G. Miley

Co-promotor: Dr. H. Röttgering

Referent: Prof. dr. R. Windhorst (Arizona State University)

Overige leden: Dr. P. Best (Royal Observatory Edinburgh)
Prof. dr. M. Franx
Dr. P. Katgert
Prof. dr. K. Kuijken

“There is no absolute up or down, as Aristotle thought; no absolute position in space; but the position of a body is relative to that of other bodies. Everywhere there is incessant relative change in position throughout the Universe, and the observer is always at the center of things.”

Giordano Bruno,
Cause, Principle, and Unity (1584)

Contents

1	Introduction	1
1.1	Active galactic nuclei: old and newer paradigm	1
1.2	Triggering processes of the AGN activity	3
1.3	Galaxy formation: brief sketch	4
1.4	AGN and galaxy formation	5
1.5	This Thesis	6
2	Low-frequency observations of the XMM Large Scale Structure field.	11
2.1	Introduction	12
2.2	Observations	13
2.2.1	Observational strategy	14
2.2.2	Data Reduction	14
2.3	Source list	16
2.3.1	Detection	16
2.3.2	Noise dependent errors	16
2.3.3	Calibration errors	18
2.3.4	Completeness:	20
2.3.5	Extended flux density estimation	21
2.4	Results	22
2.4.1	325MHz Results	22
2.4.2	A Radio halo candidate at 325 MHz	25
2.4.3	74MHz Results	25
2.4.4	Source Identification from Literature:	28
2.5	Conclusion and Future Work	29
	Appendices	33
A	Radio images	33
3	GMRT observations of the XMM large scale structure survey field	37
3.1	Introduction	38
3.2	Observations and data reduction	40
3.2.1	Radio Continuum at 610 MHz	40
3.2.2	Radio Continuum at 240 MHz	41
3.3	Source extraction	42

3.4	Determination of source parameters and associated errors	43
3.4.1	Astrometry	43
3.4.2	Flux densities	44
3.5	Results	46
3.6	Radio spectra analysis	49
3.6.1	The multi frequency radio sample	49
3.6.2	Comparison with VLA data	49
3.6.3	Spectral fits	51
3.6.4	Subsample definition	52
3.7	Conclusion and Future Work	54
Appendices		57
A	Radio images	57
4	Radio-loud AGN in the XMM-LSS field: optical identification and sample selection	61
4.1	Introduction	62
4.2	Surveys of the XMM-LSS field	63
4.2.1	VLA Radio data at 74 and 325 MHz	63
4.2.2	GMRT Radio data at 230 and 610 MHz	63
4.2.3	CFHTLS-W1 optical data	64
4.2.4	SWIRE survey data	66
4.2.5	Field selection	66
4.3	Optical and infrared identification of radio sources	66
4.3.1	Visual inspection and classification	67
4.3.2	Optical identification: the likelihood ratio method	68
4.3.3	Contamination correction	70
4.3.4	Completeness and reliability	71
4.3.5	Infrared association	72
4.4	Spectral Energy Distribution fitting	73
4.4.1	Theoretical approach: ZPEG	74
4.4.2	Semi empirical approach	76
4.5	Subsample selection	77
4.5.1	Selection of the basic sample	77
4.5.2	Type-1 AGN contamination	78
4.5.3	Starburst selection	79
4.6	Output parameters accuracies	82
4.6.1	ZPEG standards	82
4.6.2	The influence of emission lines	84
4.7	Radio sources' hosts properties	84
4.7.1	Basic observed properties	85
4.7.2	ZPEG outputs	87
4.8	Conclusion	87

Appendices	91
A Centroid uncertainties for Class 2 sources	91
B Comments on individual sources	92
B1 Class 3 sources	92
B2 Class 4 sources	93
C Tables	94
D overlays	98
5 Radio-loud AGN in the XMM-LSS field: a dichotomy on environment and accretion mode?	105
5.1 Introduction	106
5.2 A sample of radio selected AGN in the XMM-LSS field	107
5.3 Intrinsic properties of the host galaxies of radio sources	110
5.3.1 Stellar mass functions	110
5.3.2 V/V_{max} statistics	111
5.3.3 Infrared properties of radio sources' hosts	113
5.4 The environment of the host galaxies of radio sources	114
5.4.1 The overdensity parameter	117
5.4.2 The environment of radio sources	117
5.4.3 Comparison with X-ray selected galaxy clusters	119
5.5 Discussion and conclusions	121
Appendices	125
A Number density estimator	125
B Overdensity estimator	126
B1 Probability functions	126
B2 Overdensity parameter	126
6 Internal and environmental properties of X-ray selected AGN.	129
6.1 Introduction	130
6.2 Multiwavelength dataset	131
6.2.1 XMM-LSS X-ray survey	131
6.2.2 Optical and infrared surveys	131
6.3 A sample of X-ray selected Type-2 AGN	133
6.3.1 Optical identification	133
6.3.2 Spectral energy distribution fitting and sample selection	134
6.3.3 Extinction correction	135
6.4 Properties of X-ray selected AGN	136
6.4.1 Basic properties of X-ray selected AGN	136
6.4.2 Luminosity function	138
6.4.3 Stellar mass function	139
6.4.4 Infrared properties	139
6.4.5 Environment	141
6.5 Summary and discussion	141

Appendices	145
A Table	145
7 Summary and discussion	151
7.1 Summary	151
7.2 Discussion	152
Nederlandse Samenvatting	155
Résumé en français	161
Curriculum Vitae	167
Acknowledgement	169

CHAPTER 1

Introduction

1.1 ACTIVE GALACTIC NUCLEI: OLD AND NEWER PARADIGM

The study of active galactic nuclei (AGN) have lead to some of the most important discoveries in the last century. Most radio sources detected with the first radio telescopes in the 1950's, were identified at optical wavelength with either point-like sources or faint optical galaxies, located outside the Milky Way. These observations indicated that their radio luminosities were larger than those of normal galaxy by a few orders of magnitude. Some radio sources displayed a significant variability on short time scales, implying that the energy was produced within a small 1 – 10 pc region. Lynden-Bell (1969) proposed that accretion of matter onto super-massive black holes could produce vast amounts of energy on such small scales. However, in the late sixties, the existence of black hole was hypothetical, and the processes responsible for such enormous energy production remained speculative for decades. Nowadays, there is quite substantial evidence that black holes do indeed exist in the Universe: strong relativistic effects are seen in high excitation iron lines (eg. Nandra 1997), while at the center of the Milky Way, stars are seen to be orbiting around a mass of a few million times the mass of the Sun (Genzel et al. 1997).

The zoology of AGN is rich and AGN classification is complicated. Optical quasars are characterised by high $\sim 10^{13} L_{\odot}$ bolometric luminosity associated with a strong UV (the *big blue bump*) and X-ray luminosities. They produce broad ($\sim 5000 - 10000 \text{ km.s}^{-1}$) and narrow ($\lesssim 1000 \text{ km.s}^{-1}$) emission line. Seyfert galaxies can be thought to be the low luminosity ($\sim 1 - 5 \times 10^{12} L_{\odot}$), low redshift counterparts of optical quasars. Seyferts are classified into two Type 1/2 subclasses, with the Type 1 showing broad and narrow emission lines while the Type 2 produce narrow emission lines only. Radio galaxies are radio-loud AGN in general associated with massive, gas-poor elliptical galaxies. Most powerful radio galaxies ($P_{1.4} \gtrsim 10^{26} \text{ W.Hz}^{-1}$) are known to produce emission lines, whose luminosity correlates with the radio power (McCarthy 1993). The radio emission is powered by relativistic jets through synchrotron radiation. Radio galaxies are further classified into two subclasses (Fanaroff & Riley 1974): the FRI's have low radio luminosities and are edge darkened, while FRII's are the more powerful edge brightened ones. The transition between the two regimes sources occur at $P_{1.4\text{GHz}}^{\text{cut}} \sim 10^{25} \text{ W.Hz}^{-1}$.

The properties of many of the observationally defined classes of AGN outlined above can be described in a simple manner by the so called “unified scheme” of AGN. Within that framework, the energy is produced by a hot accretion disk of baryonic matter infalling onto a super-massive

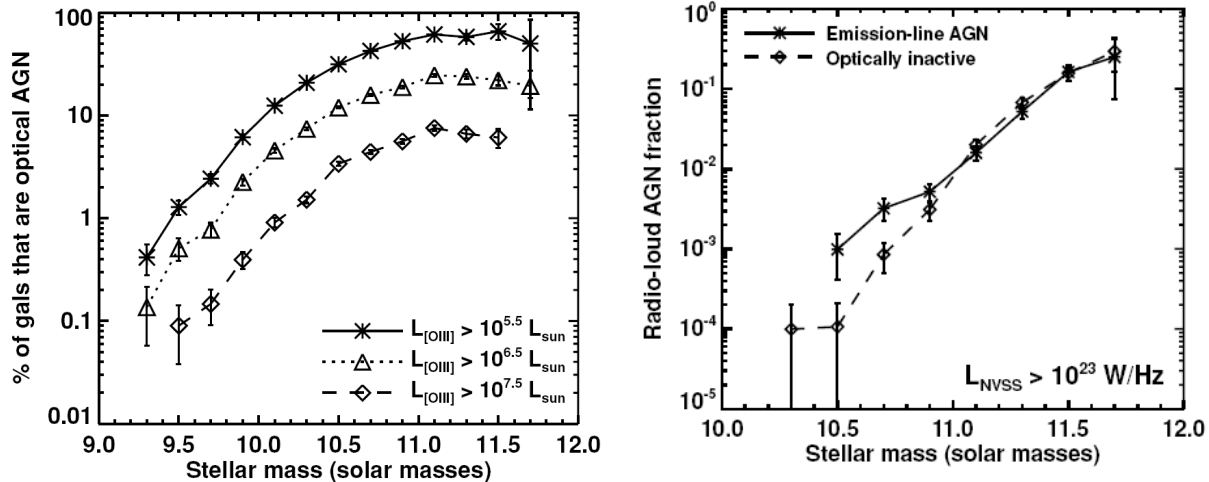


Figure 1.1: Recent results from large surveys indicate that the probability of a given galaxy to be an AGN is strongly dependent on its stellar mass. The left panel shows that relationship for AGN selected based on emission line criteria (Best et al. 2005). The right panel shows the fraction of normal galaxies that are radio-loud AGN with $P > 10^{23} \text{ W.Hz}^{-1}$ and the fraction of emission line AGN that are radio-loud with $P > 10^{23} \text{ W.Hz}^{-1}$ (Best et al. 2005). It appears that the probability that a galaxy is classified as radio-loud does not depend on either it is classified as an emission line AGN, suggesting these phenomenon are statistically independent at these low radio power.

$\sim 10^{6-9} M_{\odot}$ black hole. This accretion produces photo-ionising UV radiation and gives rise to X-ray emission via Compton scattering. An obscuring dusty torus surrounds the accretion disk. The high velocity dispersion of the gas clouds that are situated within the ~ 1 pc of the obscuring torus gives rise to the broad emission lines observed in optical quasars and Seyfert-1 galaxies, while clouds situated outwards at 10 – 100 pc have lower velocity dispersion and produce narrow emission lines. Within this framework, depending on viewing angle, the observer either sees the accretion disk and the broad emission lines, or due to obscuration by the dusty torus, only narrow emission lines are seen. Variability may be another important ingredient in the understanding of AGN properties: radio sources extended on cluster scales have lifetimes of $\gtrsim 10^8$ years, while optically selected AGN may have been active for a few hundred years only.

With the availability of large surveys it has become possible to explore the relationship between galaxies and the various classes of AGN in great detail (see Heckman & Kauffmann 2006, for a review), and test the AGN unified scheme. Recent studies indicate that in the local $z \lesssim 0.3$ Universe, AGN which are selected using optical emission line criteria, are preferentially situated in massive galaxies (Kauffmann et al. 2003), and their structural and environmental properties are similar to those of the massive early type galaxies, except at high emission-line luminosities, where signs of recent star formation are found.

However, the radio-selected AGN of low radio power show great differences compared to the AGN selected using their emission-line luminosity, and it has been suggested by many authors that the unified scheme faces several problems for this class of objects. Hine & Longair (1979) have observed that many radio galaxies do not have the luminous emission lines expected in the framework of the unified scheme (see also Laing et al. 1994; Jackson & Rawlings 1997). These low-excitation radio galaxies (LERGs) are very common at low radio power, and some of the pow-

erful FR II radio galaxies are LERGs as well. In addition, neither the expected infrared emission from a dusty torus is observed (Whysong & Antonucci 2004; Ogle et al. 2006), nor is the accretion related X-ray emission (Hardcastle et al. 2006; Evans et al. 2006). Most strikingly, the optical AGN as probed using emission-line criteria and the low radio luminosity AGN phenomenon are statistically independent (see Fig. 1.1, Best et al. 2005), suggesting these two phenomenon are triggered by different mechanisms. Furthermore, Best et al. (2005) have shown that the emission-line luminosity per black hole mass falls rapidly at the high black hole mass end, while the radio luminosity per black hole mass increases. This dichotomy is hardly explainable in terms of variability, because those two types of AGN, selected using criteria based on emission-line luminosity or radio power, (i) appear to be located in different environments (eg. Best et al. 2005) and (ii) form statistically independent samples.

Many authors have suggested that there are indeed two distinct classes of AGN. In this picture, the first class corresponds to a radiatively efficient accretion mode: these AGN show the features explained by the unified scheme, they have high accretion rates, and they trace a population of growing black-holes. The second class of AGN, for which there is no evidence that the unified scheme applies, corresponds to a radiatively inefficient accretion mode, and traces the dormant population of the most massive black holes (see Heckman et al. 2004; Best et al. 2005; Heckman & Kauffmann 2006; Hardcastle et al. 2007, for a discussion). It has been suggested that these two accretion modes are driven by the temperature of the gas reaching the super massive black hole. Within that framework, the accretion of cold gas produces a radiatively efficient accretion disk, while the hot gas accretion drives a rather advective accretion, having low radiative efficiency. In the following, we refer to these two modes as the “Quasar”, or “Cold” mode, and to the “Radio” or “Hot” mode, respectively. It has been proposed that the type of triggering process might determine the temperature of the gas reaching the black hole, and drive the accretion type (see Hardcastle et al. 2007, for a detailed discussion). In this thesis, we test this scheme, in which accretion modes and triggering processes are closely connected.

1.2 TRIGGERING PROCESSES OF THE AGN ACTIVITY

The question of the physical phenomenon that triggers the AGN activity remain poorly understood. The two necessary ingredient for making an AGN is a super-massive black hole and a significant supply of gas to fuel it. To achieve these conditions, a broad range of triggering processes have been proposed, including major (Petrosyan 1982; Bergvall & Johansson 1995) and minor (eg. Taniguchi 1999) galaxy mergers, large scale and nuclear bars instability (eg. Wada & Habe 1995), and inter galactic medium hot gas cooling.

For the low luminosity AGN, the situation is quite ambiguous (Veilleux 2003). The most recent studies of Seyfert galaxies samples suggest that bar driven gas inflow is not a dominant mechanism (Ho et al. 1997; Mulchaey & Regan 1997), while Seyfert 2 galaxies tend to have more companion that the normal galaxies at a 95% significance (De Robertis et al. 1998). In addition, only $\sim 10\%$ of Seyfert galaxies have companion galaxies (Rafanelli et al. 1995).

For the more luminous AGN, there is quite strong evidence that the galaxy mergers and interactions play an important role. The star forming ultra luminous infrared galaxies (ULIRGS) are in general seen to be associated with galaxy mergers, while optical and infrared selected quasars tend to lay in morphologically disturbed hosts (eg. Baker & Clements 1997). Furthermore, ULIRGs

have high bolometric luminosity comparable to the ones of quasars (Sanders et al. 1988a), and signs of buried quasars have often been observed in these objects (Sanders et al. 1988b). Recently, numerical simulations (Springel et al. 2005a,b) have shown that galaxy mergers can trigger both starburst and AGN activity.

Alternatively, it has been suggested that the inter galactic medium (IGM) gas cooling could also trigger the AGN activity by feeding the black hole. Best et al. (2005) using a sample of ~ 2000 low redshift $z \lesssim 0.3$ NVSS radio sources (Condon et al. 1998) in the SDSS, showed that the fraction f_{RL} of galaxies that are radio-loud is strongly dependent on the stellar mass M of the host galaxy. This relation scales as $f_{RL} \propto M^{2.5}$, with fractions of radio-loud galaxies as high as 20–30% for galaxies of $\sim 5 \times 10^{11} M_{\odot}$ and radio power $P_{1.4} > 10^{23} \text{ W.Hz}^{-1}$. Best et al. (2005) have suggested that the large quantities of gas that are seen to be cooling in the atmosphere of massive elliptical galaxies (see Mathews & Brighenti 2003, and references therein) provides a natural way of triggering the black hole activity, as this hot gas cooling rate \dot{M} has the same dependence on stellar mass ($\dot{M} \propto M^{2.5}$).

Whatever the detailed physics of AGN is, the enormous amount of energy they liberate during their short lifetime have great influence on their environment. In the last decade, AGN have regained attention as they are thought to play a major role in the galaxy formation scenarios.

1.3 GALAXY FORMATION: BRIEF SKETCH

The distribution of mass in the local Universe is highly inhomogeneous. The observed Universe indeed seems to harbour a complex, scale dependent structure: the spacial distribution of stars is structured on $\sim 10 - 100$ kpc scales, and these structures are called galaxies, while the distribution of galaxies themselves shows a $\sim 1 - 100$ Mpc scale called the “large scale structure”. The goal of galaxy formation theories is to describe and understand the state and evolution of the Universe’s structure.

The most widely spread and successful cosmological model is the Lambda Cold Dark Matter (Λ CDM) cosmology. Λ CDM potentially describes theoretically the manner in which the homogeneous early Universe has evolved into the highly inhomogeneous local Universe. With a minimum of parameters, Λ CDM gives a simple well understood framework for studying galaxy formation, the contributions to the energy density being a cosmological constant Λ (or dark energy), cold dark matter, and baryonic matter at levels of $\sim 74\%$, $\sim 22\%$ and $\sim 4\%$ respectively. In this theory the Universe’s structure grows hierarchically. It evolves through the gravitational instability in an expanding space: halos of cold dark matter collapse and merge together to form more massive structures. Λ CDM is successful in accurately describing a great variety of observations such as the cosmic microwave background (CMB, Spergel et al. 2003), large scale structure Kilbinger (LSS, 2003) and type Ia supernovae surveys (Amendola et al. 2006).

The baryonic matter that represents a lower fraction of the mass density, *slides* onto the gravitational potential shaped by the dark matter halos. In order to describe galaxy formation at the smaller scales, physical mechanisms other than gravitational interaction have to be taken into account. The gas is heated by shocks in the deep gravitational potential wells that will later evolve in galaxy clusters and groups of various masses. The heated gas cools, and the stars are being formed. Galaxies are thought to be evolving from gas rich late type systems into massive gas poor elliptical through galaxy mergers and interactions.

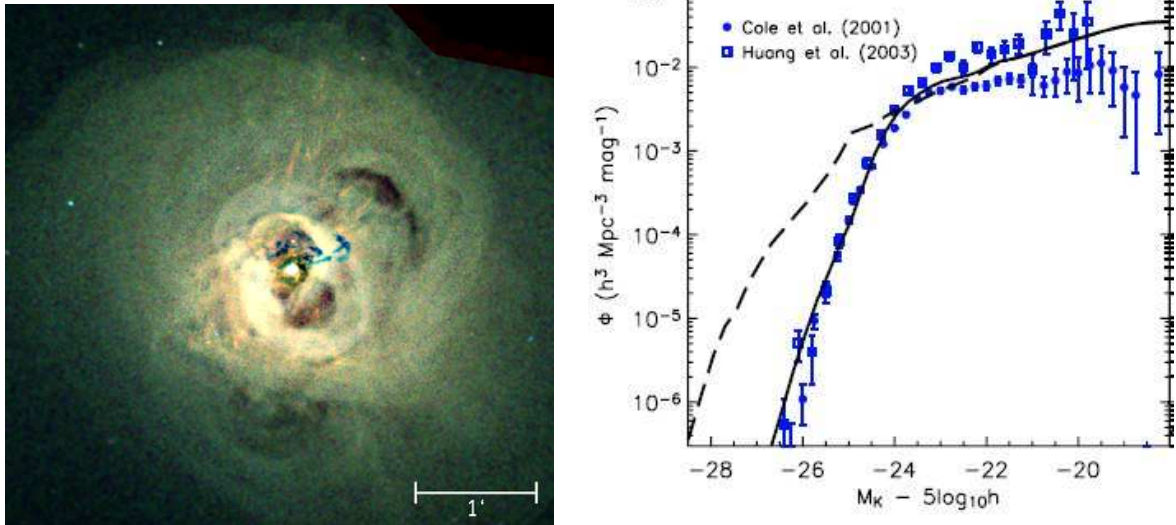


Figure 1.2: This X-ray image (Fabian et al. 2003) of the inner regions of the Perseus-A galaxy cluster reveals the dynamics of the intra cluster medium is greatly disturbed by the radio-loud AGN activity at the center of the picture. The $1'$ scale corresponds to ~ 22 kpc. The energy input by radio-loud AGN in the intergalactic medium may play an important role in theories of galaxy formation. Left panel shows the observed (*squares* and *circles*) galaxy luminosity function as well as results from numerical simulations (Croton et al. 2006). In the absence of AGN feedback (*dashed line*) mechanism, the model overestimate the number of luminous galaxies by order of magnitude. Including the energy input from radio-loud AGN produces a satisfying fit to the data (*full line*).

1.4 AGN AND GALAXY FORMATION

Evidence is mounting that AGN activity plays a key role in the framework of galaxy formation: during their short 10^{6-8} years lifetime AGN produce an enormous amount of energy that is injected into their surrounding environment through ionising radiation and relativistic jets. The comoving density evolution of AGN is remarkably similar to the evolution of the total star formation rate density and to the evolution of the space density of starbursting galaxies. All three rise by ~ 2 orders of magnitude between $z = 0$ and $z = 2 - 3$ (Sanders & Mirabel 1996; Dickinson 1998; Boyle & Terlevich 1998), suggesting that AGN activity and galaxy formation processes are tightly connected.

Furthermore, the striking discovery that essentially all nearby galaxies possess a super-massive black hole at their center, and that the black hole mass is correlated with the bulge mass and velocity dispersion (Ferrarese & Merritt 2000; Gebhardt et al. 2000) also suggest a strong link between galaxy formation and black hole growth (ie AGN activity). An interpretation is that the black hole and the bulge grow together until the AGN is luminous enough so that the radiative pressure drives winds that expels the cold gas in the intergalactic medium thereby stopping the star formation (eg. Springel et al. 2005a,b). This AGN feedback in the form of radiative pressure, is referred in the literature as the “Quasar mode”.

Attempts to model galaxy formation (Kauffmann et al. 1999; Cole et al. 2000) have used semi-analytical models taking into account important physical processes such as galaxy mergers, star

formation, gas cooling, metal enrichment, and supernovae feedback. These models could reproduce the observed shape of the galaxy stellar mass function, except for high stellar masses ($M \gtrsim 10^{11} M_{\odot}$), where it was needed to artificially switch-off the gas cooling inside the most massive dark matter halos, which suggests the existence of a source of heating that balances the intergalactic medium (IGM) gas cooling. The energy input by relativistic jets of radio-loud AGN may be a good candidate for solving that issue (see Fig. 1.2 Croton et al. 2005). The energy injection by radio-loud AGN into the IGM (referred as the ‘‘Radio mode’’ in the literature) has recently been witnessed in the form of jet driven bubbles, shocks and sound waves in the X-ray emitting intracluster medium (ICM) of closeby galaxy clusters (Fig. 1.2, Fabian et al. 2003; Blanton et al. 2004; Fabian et al. 2005). Furthermore, the radio jets and X-ray emitting ICM morphologies have been observed to be strongly coupled (Croston et al. 2005).

1.5 THIS THESIS

Where are the different classes of AGN located with respect to the distribution of mass in the Universe? What are the respective influence of internal and environmental properties on the AGN activity? What are the mechanisms that trigger the AGN activity? Are there connections between triggering process and the AGN properties such as the accretion mode (‘‘Quasar mode’’ versus ‘‘Radio mode’’)? How do those relations evolve with redshift? A good way to address these issues is to study the statistical properties of large samples of AGN.

In this thesis, we select two samples of AGN in the XMM-Large Scale Structure survey (XMM-LSS, see Pierre et al. 2004) based on (i) their radio luminosity (Chapter 2, 3, 4, 5) and (ii) their X-ray luminosity (Chapter 6), our idea being that these samples may be dominated by Radio mode and Quasar mode AGN respectively. A series of internal and environmental estimators have been attached to each AGN in these sets including: stellar mass, redshift, and star formation rates of the host galaxy, infrared excess and overdensity parameter. By studying the bias introduced by the radio or X-ray selection on the observed internal and environmental properties, we might be able to address some of the questions outlined above. Bellow is a more detailed description of the chapter contents.

In **Chapter 2** we present a low frequency radio survey of the XMM-LSS field using the Very Large Array (VLA) at 74 and 325 MHz over 132 and 15.3 degree². Given the perturbing nature of the ionosphere and the width of the field to be surveyed, we paid particular attention to a careful reduction of the data. At 74 MHz, the resolution is 30'', and the obtained median 5σ sensitivity is ~ 162 mJy/beam. At 325 MHz, we have a resolution of 6.7'', a sensitivity of 4 mJy/beam (5σ). We detect ~ 1500 radio sources in total.

To enlarge the radio sources sample size, and retrieve information on the radio spectra, in **Chapter 3** we make use of the large collecting area of the Giant Meterwave Radio Telescope (GMRT) to map out the XMM-LSS field at 240 and 610 MHz. Covered areas are 18.0 and 12.7 degree² with resolutions of 14.7'' and 6.5'' and sensitivity of ~ 12.5 and ~ 1.5 mJy/beam (5σ) at 230 and 610 MHz respectively. We have combined these data with the available source lists at 74, 325 (Chapter 1) and 1400 MHz (NVSS, Condon et al. (1998)), to build a multifrequency catalog containing ~ 1500 radio sources. By fitting a simple synchrotron radiation model to the brightest radio sources, we found that $\sim 26\%$ of sources in our sample show signatures of spectral ageing,

while $\sim 6\%$ show self absorption.

In **Chapter 4** we identify the radio sources detected at 74, 240, 325 and 610 MHz with their optical counterparts using high quality optical catalog and images. For doing this, we used a modified version of the likelihood ratio method that takes into account *a priori* knowledge on the radio sources host galaxy properties. It gives for each radio source a set of optical candidates with a probability of association. We estimate that $\sim 75\%$ of the radio sources have a detected optical counterpart, and derive the photometric redshift for the 3×10^6 galaxies in the surveyed field, including the radio sources hosts. We develop a method for rejecting the radio sources that are likely to have corrupted photometric redshifts. This method uses two different photometric redshift method, combined with an optical color-color criteria.

In **Chapter 5** we study the properties of the sample of radio-loud AGN defined in Chapter 4, by investigating their internal and environmental properties. For studying the environment of radio sources, we build a scale dependent overdensity parameter based on the photometric redshift probability function. The scaling relation between the fraction of galaxies that are radio-loud and their stellar mass inferred from low redshift studies (Best et al. 2005) is seen to flatten in the redshift range $0.5 \lesssim z \lesssim 1.2$ redshift. This suggests that the low masses radio-loud AGN were more numerous in the past. We report an environmental dichotomy: compared to the normal galaxies of the same mass, the radio-loud AGN are located in large 450 kpc scale overdensities. In contrast, the lower mass systems prefer large 450 kpc scale underdensities. In addition they show an infrared excess in the mid infrared, while the higher stellar mass systems do not have an infrared excess. We argue that the analysis of the dataset presented in that chapter support the picture in which the radiatively efficient accretion is triggered by galaxy mergers, while the radio mode accretion is triggered by the gas cooling in the atmosphere of massive ellipticals.

In **Chapter 6** we present a sample of AGN selected in the hard [2-10] keV X-ray band, and carry out a similar analysis done for the sample of radio selected AGN (Chapter 4&5). We first identify their optical and infrared counterpart, and select a subsample of Type-2 AGN. Based on the ratio of hard band to the soft band flux ([0.5-2] keV), for each object we estimated the hydrogen column density in the line of sight, and derive intrinsic, absorption corrected X-ray luminosities. The X-ray luminosity function of these sources are in good agreement with previous studies conducted in the past. Interestingly, the mass dependency of the fraction of galaxies that are X-ray AGN is in good agreement with the same relation for the emission line selected AGN. However, there is a significant normalisation difference between these relations. This is explained in terms of emission line AGN, which accretion related X-ray emission is strongly absorbed by high column density. In addition AGN in our sample show a strong infrared excess, at wavelength as short as $3.5 \mu\text{m}$ and in the whole stellar mass range, while they are preferentially found in underdense environment. Globally, the environment of X-ray selected AGN resembles the environment of the low stellar mass radio-loud AGN that are in their radiatively efficient mode. We argue in this chapter that the X-ray selected sample probes a population of AGN that is similar to the population selected based on their emission lines.

In **Chapter 7** we outline the most important results of the thesis. We argue that our data is consistent with the idea that there is a connection between triggering process and accretion mode.

REFERENCES

- Amendola, L., Gasperini, M., & Piazza, F. 2006, *Phys. Rev. D*, 74, 127302
- Baker, A. C. & Clements, D. L. 1997, in *Extragalactic Astronomy in the Infrared*, ed. G. A. Mamon, T. X. Thuan, & J. Tran Thanh van, 295–+
- Bergvall, N. & Johansson, L. 1995, *A&AS*, 113, 499
- Best, P. N., Kauffmann, G., Heckman, T. M., et al. 2005, *MNRAS*, 362, 25
- Blanton, E. L., Sarazin, C. L., McNamara, B. R., & Clarke, T. E. 2004, *ApJ*, 612, 817
- Boyle, B. J. & Terlevich, R. J. 1998, *MNRAS*, 293, L49
- Cole, S., Lacey, C. G., Baugh, C. M., & Frenk, C. S. 2000, *MNRAS*, 319, 168
- Condon, J. J., Cotton, W. D., Greisen, E. W., et al. 1998, *AJ*, 115, 1693
- Croston, J. H., Hardcastle, M. J., Birkinshaw, M., & Worrall, D. M. 2005, in *X-Ray and Radio Connections* (eds. L.O. Sjouwerman and K.K Dyer) Published electronically by NRAO, <http://www.aoc.nrao.edu/events/xraydio> Held 3-6 February 2004 in Santa Fe, New Mexico, USA, (E7.06) 7 pages
- Croton, D. J., Farrar, G. R., Norberg, P., et al. 2005, *MNRAS*, 356, 1155
- Croton, D. J., Springel, V., White, S. D. M., et al. 2006, *MNRAS*, 365, 11
- De Robertis, M. M., Yee, H. K. C., & Hayhoe, K. 1998, *ApJ*, 496, 93
- Dickinson, M. 1998, in *The Hubble Deep Field*, ed. M. Livio, S. M. Fall, & P. Madau, 219–+
- Evans, D. A., Worrall, D. M., Hardcastle, M. J., Kraft, R. P., & Birkinshaw, M. 2006, *ApJ*, 642, 96
- Fabian, A. C., Sanders, J. S., Allen, S. W., et al. 2003, *MNRAS*, 344, L43
- Fabian, A. C., Sanders, J. S., Taylor, G. B., & Allen, S. W. 2005, *MNRAS*, 360, L20
- Fanaroff, B. L. & Riley, J. M. 1974, *MNRAS*, 167, 31P
- Ferrarese, L. & Merritt, D. 2000, *ApJ*, 539, L9
- Gebhardt, K., Bender, R., Bower, G., et al. 2000, *ApJ*, 539, L13
- Genzel, R., Eckart, A., Ott, T., & Eisenhauer, F. 1997, *MNRAS*, 291, 219
- Hardcastle, M. J., Evans, D. A., & Croston, J. H. 2006, *MNRAS*, 370, 1893
- Hardcastle, M. J., Evans, D. A., & Croston, J. H. 2007, *MNRAS*, 376, 1849
- Heckman, T. M. & Kauffmann, G. 2006, *New Astronomy Review*, 50, 677
- Heckman, T. M., Kauffmann, G., Brinchmann, J., et al. 2004, *ApJ*, 613, 109
- Hine, R. G. & Longair, M. S. 1979, *MNRAS*, 188, 111
- Ho, L. C., Filippenko, A. V., & Sargent, W. L. W. 1997, *ApJ*, 487, 591
- Jackson, N. & Rawlings, S. 1997, *MNRAS*, 286, 241
- Kauffmann, G., Colberg, J. M., Diaferio, A., & White, S. D. M. 1999, *MNRAS*, 307, 529
- Kauffmann, G., Heckman, T. M., Tremonti, C., et al. 2003, *MNRAS*, 346, 1055
- Kilbinger, M. 2003, *ArXiv Astrophysics e-prints*
- Laing, R. A., Jenkins, C. R., Wall, J. V., & Unger, S. W. 1994, in *Astronomical Society of the Pacific Conference Series*, Vol. 54, *The Physics of Active Galaxies*, ed. G. V. Bicknell, M. A. Dopita, & P. J. Quinn, 201–+

- Lynden-Bell, D. 1969, *Nature*, 223, 690
- Mathews, W. G. & Brighenti, F. 2003, *ARA&A*, 41, 191
- McCarthy, P. J. 1993, *ARA&A*, 31, 639
- Mulchaey, J. S. & Regan, M. W. 1997, *ApJ*, 482, L135+
- Nandra, K. 1997, in *Astronomical Society of the Pacific Conference Series*, Vol. 113, IAU Colloq. 159: Emission Lines in Active Galaxies: New Methods and Techniques, ed. B. M. Peterson, F.-Z. Cheng, & A. S. Wilson, 36–+
- Ogle, P., Whyson, D., & Antonucci, R. 2006, *ApJ*, 647, 161
- Petrosyan, A. R. 1982, *Astrophysics*, 18, 312
- Pierre, M., Valtchanov, I., Altieri, B., et al. 2004, *Journal of Cosmology and Astro-Particle Physics*, 9, 11
- Rafanelli, P., Violato, M., & Baruffolo, A. 1995, *AJ*, 109, 1546
- Sanders, D. B. & Mirabel, I. F. 1996, *ARA&A*, 34, 749
- Sanders, D. B., Soifer, B. T., Elias, J. H., et al. 1988a, *ApJ*, 325, 74
- Sanders, D. B., Soifer, B. T., Elias, J. H., Neugebauer, G., & Matthews, K. 1988b, *ApJ*, 328, L35
- Spergel, D. N., Verde, L., Peiris, H. V., et al. 2003, *ApJS*, 148, 175
- Springel, V., Di Matteo, T., & Hernquist, L. 2005a, *ApJ*, 620, L79
- Springel, V., Di Matteo, T., & Hernquist, L. 2005b, *MNRAS*, 361, 776
- Taniguchi, Y. 1999, *ApJ*, 524, 65
- Veilleux, S. 2003, in *Astronomical Society of the Pacific Conference Series*, Vol. 290, Active Galactic Nuclei: From Central Engine to Host Galaxy, ed. S. Collin, F. Combes, & I. Shlosman, 11–+
- Wada, K. & Habe, A. 1995, *MNRAS*, 277, 433
- Whyson, D. & Antonucci, R. 2004, *ApJ*, 602, 116

CHAPTER 2

Low-frequency observations of the XMM Large Scale Structure field.

C. Tasse, A. S. Cohen, H. J. A. Röttgering, M. Pierre, N.E. Kassim, R. Perley, P. Best, M. Birkinshaw, M. Bremer, H. Liang

Astronomy & Astrophysics 456, 791, 2006

The XMM Large Scale Structure survey (XMM-LSS) is an X-ray survey aimed at studying the large scale structure of the Universe. The XMM-LSS field is currently being followed up using observations across a wide range of wavelengths, and in this paper we present the observational results of a low frequency radio survey of the XMM-LSS field using the Very Large Array at 74 and 325 MHz. This survey will map out the locations of the extragalactic radio sources relative to the large scale structure as traced by the X-ray emission. This is of particular interest because radio galaxies and radio loud AGN show strong and complex interactions with their small and larger scale environment, and different classes of radio galaxies are suggested to lie at different places with respect to the large scale structure.

For the phase calibration of the radio data, we used standard self-calibration at 325 MHz and field-base calibration at 74 MHz. Polyhedron-based imaging as well as mosaicing methods were used at both frequencies. At 74 MHz we have a resolution of 30'', a median 5σ sensitivity of ~ 162 mJy/beam and we detect 666 sources over an area of 132 square degrees. At 325 MHz, we have a resolution of 6.7'', a median 5σ sensitivity of 4 mJy/beam, and we detect 847 sources over an area of 15.3 square degrees. At 325 MHz we have detected a region of diffuse radio emission which is a cluster halo or relic candidate.

2.1 INTRODUCTION

Extragalactic radio sources such as radio loud quasars and radio galaxies, have been extensively studied to understand the physical processes relating active galactic nuclei (AGN), host galaxies, and environments. For powerful radio sources emission line and radio luminosities seem to be well correlated (McCarthy 1993), while at lower radio luminosities ($L_{1.4GHz} \lesssim 10^{25} \text{ W.Hz}^{-1}$) radio loudness becomes decoupled from the AGN activity as probed by emission line luminosity (Zirbel & Baum 1995; Best et al. 2005). It has been suggested that environment plays a major role in making a galaxy radio loud or radio quiet. In the local universe, FRI-type (Fanaroff & Riley 1974) radio galaxies inhabit moderately rich cluster environments, while FR II-type radio sources tend to lie in either small groups or isolated fields (Yates et al. 1989; Hill & Lilly 1991; Ledlow & Owen 1996). Furthermore a number of recent X-ray observations have shown a strong, FRI/FR II morphology-dependent coupling between steep spectrum radio emission and their surrounding intergalactic medium (IGM) Fabian et al. (2003); Blanton et al. (2004); Fabian et al. (2005); Croston et al. (2005). The question therefore arises as to what extent both AGN activity and environment properties are coupled with radio activity.

One way to statistically study the connections between various radio source populations and their environment is to compare X-rays emitted by the hot IGM plasma tracing Large Scale Structures (LSS), to low-frequency radio observations ($\nu < 1\text{GHz}$). The XMM-Large Scale Structure Survey (XMM-LSS) is an X-ray survey designed to investigate the nature, properties and content of the LSS in the Universe up to redshift $z \sim 1$ (Pierre et al. 2004). The XMM-LSS field is being observed by the XMM-Newton satellite and will cover 10 degree^2 . It is predicted to detect 1,500 X-ray quasars, and 100 – 200 galaxy clusters up to $z = 1$, and ~ 50 within $1 < z < 2$ (Refregier et al. 2002). At present, $\sim 5 \text{ degree}^2$ of the XMM-LSS field has been observed.

The XMM-LSS field will be mapped in five bands using the 1 deg^2 CCD camera MEGACAM as part of the Canada France Hawai Telescope Legacy Survey (CFHTLS¹). The XMM-LSS field is also observed as part of the SWIRE (Lonsdale et al. 2003) survey in 9 bands between 3.6 and $24\mu\text{m}$. Spectroscopic follow-up (NTT, Magellan, VLT) of the ~ 70 galaxy cluster candidates found in the first 5 degree^2 of the survey is completed (Pierre et al 2006, Pacaud et al 2006, in preparation). Standard spectroscopic follow-up of the SWIRE and XMM sources is underway at the 2-degree field spectrograph (2dF). Combining these data will provide an unprecedented view of the LSS of the universe (see Pierre et al. 2004, for a general lay-out of the associated surveys).

Using the Very Large Array (VLA) radio telescope, we have begun a low frequency radio survey at 325 and 74 MHz of the XMM-LSS field in order to address the following questions: (1) Where are different classes of radio sources located with respect to the distribution of mass on cosmological scales as traced by the X-ray emission? (2) Can the radio loud/quiet aspect of optical and X-ray quasars be understood in terms of environmental effects? (3) How does the hot IGM influence the physical properties of the radio sources such as linear size and radio power?

In this paper we describe the observations we have conducted using the VLA in July 2003 in the A-configuration (most extended) and in June 2002 in the B-configuration. This combination provides resolutions of $6.7''$ and $30''$ at 325 and 74 MHz, respectively. Following the observational strategy described in Cohen et al. (2003), but using a mosaic of four pointings, at 325 MHz we cover a $\sim 15 \text{ degree}^2$ area with a resolution of $6.7''$ and a mean flux density limit per beam (5σ)

¹for more information on the CFHT Legacy Survey, see <http://www.cfht.hawaii.edu/Science/CFHLS/>

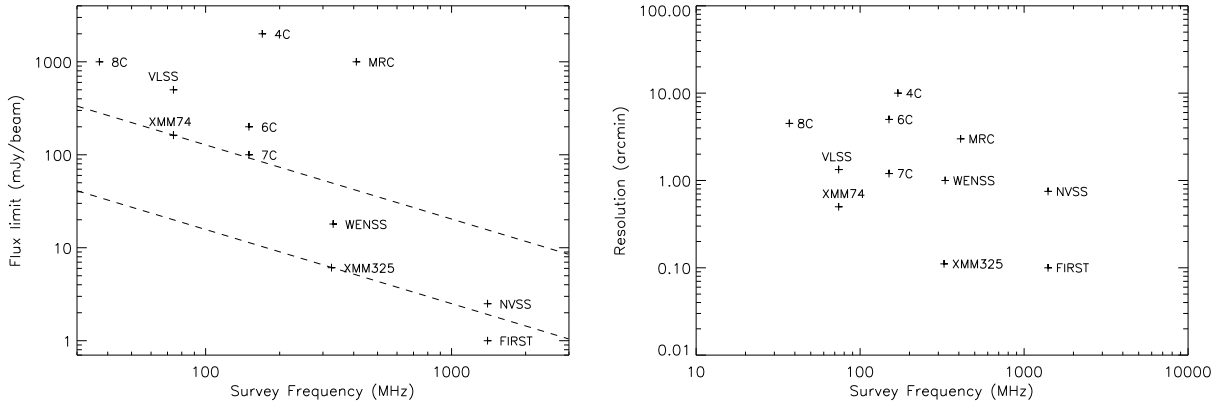


Figure 2.1: Sensitivity and resolution of our XMM-LSS radio surveys, in comparison with that of other surveys. The dashed lines represent fiducial sources with a spectral index $\alpha = -0.8$.

of ~ 4 mJy/Beam. At 74 MHz, we cover a 132 degree² area with a resolution of $30''$ and a flux density limit per beam of ~ 160 mJy/Beam. A summary of these results appear in Table 2.1.

Fig. 2.1 shows the sensitivity and resolution of the XMM-LSS low-frequency counterpart, at 74 and 325 MHz, compared with others radio surveys. At 325 MHz, the low-frequency survey of the XMM-LSS field is deeper than the WENSS survey (Rengelink et al. 1997) by a factor of ~ 3 , and in resolution by a factor of ~ 10 . At 74 MHz, we exceed the VLSS (Cohen et al. 2006) by a factor of ~ 3 in both sensitivity and resolution. The NVSS survey (Condon et al. 1998) covers the whole XMM-LSS field, and most of our 74 MHz sources will have a counterpart at 1.4 GHz, whereas our 325 MHz data is deep enough so that many sources will not have detected counterparts in the NVSS. Compared with the VLA-VIRMOS deep field at 1.4 GHz (Bondi et al. 2003), reaching a brightness temperature limit at 5σ of ~ 90 μ Jy/Beam, probing nearby starbursts over ~ 1 degree² area, we are probing powerful AGN over a larger area.

This paper is organized as follows. In Section 2.2 we describe the observations, and the data reduction. In Section 2.3 we describe the sources extraction and we study the reliability/completeness aspects of the source lists. Section 2.4 presents the final results and we conclude in section 2.5 by discussing the survey, and future plans.

2.2 OBSERVATIONS

The XMM-LSS field ² is centered at $\alpha(\text{J2000})= 2^{\text{h}}24^{\text{m}}00.27^{\text{s}}$, $\delta(\text{J2000})= -4^{\circ}09'47.6''$ (Pierre et al. 2004). This location was chosen because of its high Galactic latitude and low extinction. The declination near the equator also gives the advantage of being visible from many astronomical observatories.

²for more information on the present status of the XMM-LSS survey see http://vela.astro.ulg.ac.be/themes/spatial/xmm/LSS/index_e.html.

Table 2.1: Observational parameters for the VLA radio survey of the XMM-LSS field.

Array configuration	A	B
Obs. dates	31 Jul. 03, 5 Aug. 03, 3 Sept. 03	15, 16, 17, 20 Jun. 02, 16 Jul. 02
Number of pointings	4	4
Int. time per pointing	~ 6 hrs	~ 8 hrs
Observing frequency	73.8/325 MHz	73.8/325 MHz

Frequency	73.8 MHz	325 MHz
Band Width	1.56 MHz	6.25 MHz
$N_{channel}$	128	2×16
Channel Width	12.20 kHz	195.31 kHz
Band Pass Calibrator	3C405	3C48
Flux Calibrator	3C405	3C48
Resolution	30''	6.7''
Area (degree ²)	132	15.3
Sensitivity (at 5σ)	162 mJy/Beam	4.0 mJy/Beam

2.2.1 Observational strategy

The first radio observations at 74 and 325 MHz of the XMM-LSS field were carried out with the VLA (Cohen et al. 2003) in an 8 hour run. It covered 5.6 degree² at 325 MHz with a resolution of 6.3'', and reached a flux density limit per beam of 4 mJy beam⁻¹ (5σ), leading to the detection of 256 sources. At 74 MHz the primary beam covered a 110 degree² area with a resolution of 30'', and a flux density limit per beam of 275 mJy.beam⁻¹ (5σ), leading to the detection of 211 sources.

We carried out a 24 hour observation of the XMM-LSS field simultaneously at 74 and 325 MHz in the A-configuration. This observation was spread over July, August and September 2003. At 325 MHz, we have added data from a ~ 35 hour observing run in the B-configuration, observed in June and July 2002. The observational parameters are listed in Table 2.1. The A-configuration gives us the needed high resolution to determine morphologies of the radio sources, and the B configuration is used for the determination of reliable flux densities and provides sensitivity to large angular scale emission needed, for example, to detect giant radio halos. At 74 MHz the primary beam is large enough to cover the whole XMM-LSS field in a single pointing, and at 325 MHz the pointing grid has been set so that we cover ~ 90% of the XMM-LSS field with four pointings.

2.2.2 Data Reduction

For the data reduction, we used the *Astronomical Image Processing System* (AIPS).

The 325 MHz data

After a first round of flagging data affected by Radio Frequency Interference (RFI), we calibrated the relative response within each channel (i.e. *bandpass*), and performed gain and amplitude calibration. On the calibrated data, RFI was removed manually using the AIPS's routines TVFLG and SPFLG. In each of the four pointings $\sim 15\%$ of the data have been flagged. We combined the A and B configuration data in the u-v plane using the AIPS routine DBCON.

The phase calibrator we used (3C48) being far from the field, the initial phase calibration is very poor. Assuming a median spectral index $\alpha_{325}^{1400} = -0.8$, we generate a model of the sky at 325 MHz from the NVSS database at 1.4 GHz (Condon et al. 1998). This model consists of a list of clean components located at the position of the sources from the NVSS survey. Fourier transforming the modeled image allows for a phase-only calibration of each antenna using a solution interval of one minute, providing better results than the traditional calibrator-based phase calibration.

Because of the very large primary beam and the non-coplanar geometry of the VLA array, imaging would normally require the use of a 3D Fourier transform. However, this is currently too computationally expensive to be practical. The commonly used solution is to compute a pseudo-three-dimensional Fourier transform (Perley 1999), in which the field of view is divided into much smaller fields (facets). The 3D Fourier transform can then be approximated by using a two dimensional one. For the 325 MHz data, we used 286 facets, each 512×512 pixels, sampled at $1.5'' \cdot \text{pixel}^{-1}$, with an overlap of two pixels between the facets. After the u-v data have been imaged into individual facet and deconvolved, the facets are combined into a single image. After a few iterations of phase-only self-calibration, we combined the four pointings (each 2.5 degree in diameter) as described by Condon et al. (1998) in a 15.3 deg^2 single map.

The resulting noise is quite inhomogeneous across the field, ranging between ~ 0.5 and ~ 2.5 mJy beam $^{-1}$. The noise is higher close to the bright sources, where sensitivity is dynamic-range limited. In each of the four pointings, the size of the synthesized beam was $\sim 6.7'' \times 6.3''$ and we have set the restoring beam to be a circular Gaussian with a $6.7''$ FWHM.

The 74MHz data

For the 74 MHz data, we used Cygnus-A (3C405) as bandpass and flux density calibrator. Due to its large angular size, the calibrator is resolved by our observation. To calibrate the data, we used a standard model available from previous observations.

The problems of RFI and the non-coplanar geometry are solved in a similar way as with the 325 MHz data. However, at 74 MHz the ionosphere poses an additional challenge. Electrons in the ionosphere produce distortion of the wavefront and the resulting phase shifts $\Delta\phi$ increases linearly with the wavelength (Kassim et al. 1993). Moreover at higher frequencies the primary beam is relatively smaller in size so that angle-variant phase shifts across the field-of-view can be ignored and standard self-calibration can be utilized to derive one time variable phase correction per antenna. Below 150 MHz positional-dependent phase variations become significant, and simple angle-invariant self-calibration breaks down. Therefore at 74 MHz we have used the technique of "field-based calibration" first developed for the VLSS survey in which the phase calibration is position-dependent across the field-of-view (Cotton et al. 2004). This technique was also used and discussed into much details in Cohen et al. (2003).

Combining the A and B-configuration data in the UV-plane didn't lead to much improvement, probably because of complications of the ionospheric calibration routine. We therefore only considered the higher resolution A-configuration data. For each pointing, after the uv plane has been imaged in the 184 facets, we used a circular Gaussian restoring beam of 30'' FWHM. The four pointings have then been combined into a single map. As with the 325 MHz data, the noise is inhomogeneous across the field and as low as ~ 20 mJy/Beam and as high as ~ 55 mJy/Beam near bright sources.

2.3 SOURCE LIST

2.3.1 Detection

As a first step in our source finding algorithm, we have normalized the image by a noise map, produced using AIPS's task RMSD. The noise is calculated within windows, fitting a Gaussian to the histogram of the pixel values. The data above and below the 3σ domain are rejected, and after 30 iterations, a reliable estimation of the noise is obtained. The size of the window is critical since if it is too small, the noise evaluation will be overestimated by the presence of a strong signal, while if it is too big, it will not take into account the smaller scale variation in the noise pattern. We set the window to be 80×80 pixels, corresponding to $10' \times 10'$ and $2' \times 2'$, at 74 and 325 MHz, respectively, and in order to save computing time, the rms is evaluated every 3×3 pixel, which is of the order of the correlation length. This introduces pixel-to-pixel uncorrelated noise, and in order to avoid for discontinuous variation in the noise level, we convolve this noise map with a circular Gaussian with diameters of 100'' and 20'' at 74 and 325 MHz respectively which slightly smooths the noise image. Fig. 2.2 shows the area mapped as a function of sensitivity for each frequency.

Dividing the original map by the noise map we get an image containing uniform noise, where we can apply the AIPS's source extraction algorithm 'Search And Destroy' (SAD). SAD is given an input cut of 5 in the noise-normalized map ($\leftrightarrow 5\sigma$ in the original map) applied on both peak and integrated flux density, above which each pixel group is considered as a potential source (island). SAD fits one or more Gaussian components to these islands, thereby producing an initial source list. Assuming the noise distribution to be Gaussian, the input cut of 5σ leads to a total number of false detection over the surveyed areas of $\lesssim 5 \cdot 10^{-2}$ at 325 and 74 MHz. A visual inspection of the residual map does reveal some false detections, due to the non-Gaussian, correlated nature of the noise in the proximity of bright sources. We have deleted these false detections from the list while comparing the source list positions with NVSS as described below.

2.3.2 Noise dependent errors

Finally, the absolute flux densities are obtained by multiplying the measured noise-normalized flux density by the local noise. Following Condon (1997) we calculate the true uncertainties, from the signal-to-noise ratio of the Gaussian fit ρ , as expressed by:

$$\rho^2 = \frac{\theta_M \theta_m}{4\theta_N^2} \left[1 + \left(\frac{\theta_N}{\theta_M} \right)^2 \right]^{\alpha_M} \left[1 + \left(\frac{\theta_N}{\theta_m} \right)^2 \right]^{\alpha_m} \frac{S_P^2}{\sigma_{map}^2} \quad (2.1)$$

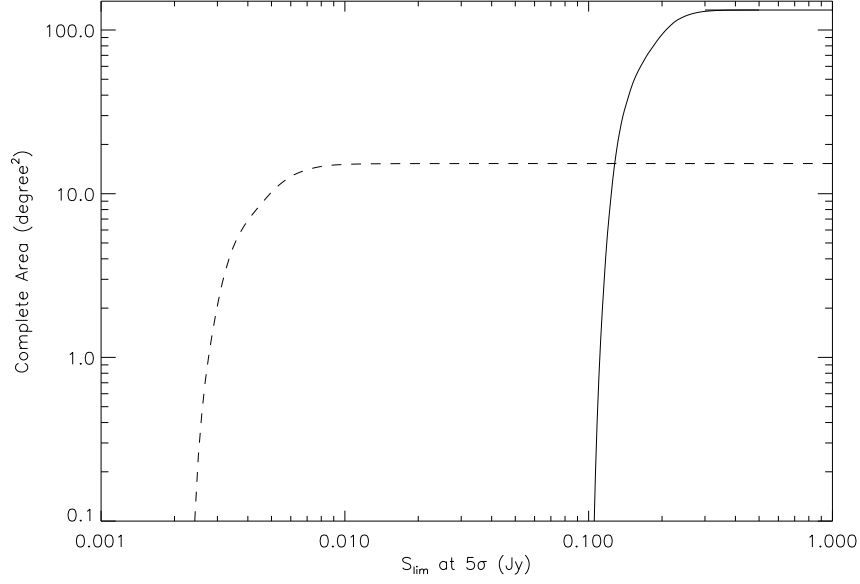


Figure 2.2: Area as a function of limiting flux density per beam at 5σ . The full line corresponds to the 74 MHz survey whereas the dashed one corresponds to the 325 MHz survey.

where θ_M and θ_m are fitted FWHMs of the major and minor axes, θ_N is the FWHM of the Gaussian correlation length of the image noise, corresponding to the FWHM of the synthesized beam, S_P is the peak flux density, and σ_{map}^2 is the local noise variance. $\{\alpha_M, \alpha_m\}$ have values determined empirically using Monte-Carlo simulations (Condon 1997, see Tab. 2.2). We have then calculated the errors of the fitted parameters as follows:

$$\begin{aligned} \frac{\sigma^2(S_P)}{S_P^2} &= 8 \ln 2 \frac{\sigma^2(x_0)}{\theta_M^2} = 8 \ln 2 \frac{\sigma^2(y_0)}{\theta_m^2} = \frac{\sigma^2(\theta_M)}{\theta_M^2} \\ &= \frac{\sigma^2(\theta_m)}{\theta_m^2} = \frac{\sigma^2(\phi)}{2} \left(\frac{\theta_M^2 - \theta_m^2}{\theta_M \theta_m} \right)^2 \approx \frac{2}{\rho^2} \end{aligned} \quad (2.2)$$

$$\frac{\sigma^2(S_T)}{S_T^2} \approx \frac{\sigma^2(S_P)}{S_P^2} + \left(\frac{\theta_N^2}{\theta_M \theta_m} \right) \left(\frac{\sigma^2(\theta_M)}{\theta_M^2} + \frac{\sigma^2(\theta_m)}{\theta_m^2} \right) \quad (2.3)$$

Here S_T is the total flux density, ϕ is the position angle of the major axis. $\sigma(x_0)$ and $\sigma(y_0)$ are related to the uncertainties in right ascension and declination (respectively $\sigma_{\alpha,fit}$ and $\sigma_{\delta,fit}$) by the

Table 2.2: Values of $\{\alpha_M, \alpha_m\}$ used for the calculation of error bars on individual parameters (Condon 1997).

Parameter	α_M	α_m
S_P	3/2	3/2
θ_M, x_0	5/2	1/2
θ_m, y_0, ϕ	1/2	5/2

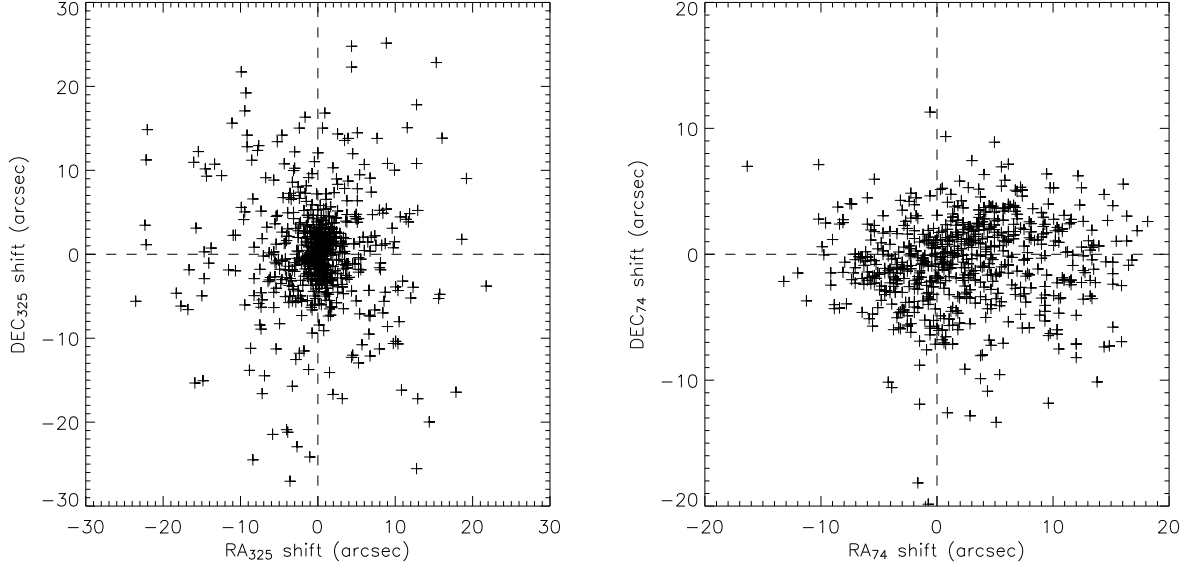


Figure 2.3: Positional differences in right ascension and declination between our source sample and NVSS at 325 (on the left) and 74 MHz (on the right). The 74 MHz source sample corresponds to a much brighter source population in NVSS than the 325 MHz source sample counterpart, so that the scatter in positional differences on the right reflects the 74 MHz dataset calibration errors. At 325 MHz, the scatter is dominated by the NVSS uncertainties.

relations given by Condon et al. (1998):

$$\sigma_{\alpha,fit}^2 = \sigma^2(x_0) \sin^2(\phi) + \sigma^2(y_0) \cos^2(\phi) \quad (2.4)$$

$$\sigma_{\delta,fit}^2 = \sigma^2(x_0) \cos^2(\phi) + \sigma^2(y_0) \sin^2(\phi) \quad (2.5)$$

2.3.3 Calibration errors

- *Position errors:* The imperfect phase calibration adds positional uncertainties. We can quantify these by comparing our astrometry measurements to a much more accurate source positioning catalog. Fig. 2.3 shows all the position differences between the NVSS survey and our source samples at both 74 and 325 MHz on both right ascension and declination. At 325 MHz, the mean value of the position differences do not show any significant offset, while at 74 MHz we measure an average offset of 2.25'' and -0.4'' on respectively right ascension and declination. We have removed these offsets in the final source list. The scatter around the NVSS positions is given by:

$$\sigma_{\alpha}^2 = \epsilon_{\alpha,calib}^2 + \epsilon_{\alpha,NVSS}^2 + \sigma_{\alpha,fit}^2 \quad (2.6)$$

$$\sigma_{\delta}^2 = \epsilon_{\delta,calib}^2 + \epsilon_{\delta,NVSS}^2 + \sigma_{\delta,fit}^2 \quad (2.7)$$

where $\epsilon_{\alpha,calib}$ and $\epsilon_{\delta,calib}$ are the calibration errors due to the ionosphere, $\epsilon_{\alpha,NVSS}$ and $\epsilon_{\delta,NVSS}$ are the calibration errors of the NVSS sources, and $\sigma_{\alpha,fit}$ and $\sigma_{\delta,fit}$ are the Gaussian fitting errors (eq 1-5).

At 325 MHz, the scatter in the distribution of the positional differences between the 325 MHz single source population and their associated NVSS counterpart contains the fitting errors of both ours and NVSS databases, as well as calibration errors. Therefore, selecting only the sources with higher signal-to-noise ratio lower the noise-dependent error contributions. Selecting the 325 MHz sources with associated NVSS counterparts having error bar lower than $0.6''$ gives a subsample of 41 sources with associated Gaussian fitting error contributions on the level of $0.05''$. For this high signal-to-noise ratio subsample, we find scatters of $\sigma_\alpha = 1.15''$ and $\sigma_\delta = 1.83''$. Compared with the NVSS noise-independent uncertainties of $\epsilon_{\alpha,NVSS} = 0.45''$ and $\epsilon_{\delta,NVSS} = 0.56''$, our values are much higher. We can explain this difference by the fact that we have used an NVSS-based model to phase calibrate the data which included low signal-to-noise NVSS sources, where noise-dependent uncertainties dominate noise-independent ones. Therefore, we consider the quadratic differences between our measurement of the position uncertainties of respectively $1.15''$ and $1.83''$ and the NVSS calibration errors to be a good estimate of our calibration errors. This leads to $\epsilon_{\alpha,calib} = 1.06''$ and $\epsilon_{\delta,calib} = 1.75''$

At 74 MHz, we get scatter values of $\sigma_\alpha = 6.8''$ and $\sigma_\delta = 3.7''$ for the whole population, which contains uncertainties coming from both Gaussian fitting errors and calibration errors, as for the 325 MHz data. Although the NVSS resolution is lower than ours, we assume the position errors from NVSS to be negligible, as the signal-to-noise ratio of NVSS is on average ~ 10 times greater (see Fig. 2.1). In order to quantify the calibration errors, we select sources with $\sigma_{\alpha,fit}$ and $\sigma_{\delta,fit}$ lower than $0.5''$, which makes a subsample of 43 sources detected at high signal-to-noise ratio. We find standard deviations in right ascension and declination of respectively $\sigma_\alpha = 3.43''$ and $\sigma_\delta = 2.14''$, which, subtracting the NVSS calibration error contribution, leads to $\epsilon_{\alpha,calib} = 3.37''$ and $\epsilon_{\delta,calib} = 2.00''$. We have quadratically added these errors to the Gaussian fitted ones.

- *Flux density errors:* For the flux density calibration, we have used 3C48, and 0137+331, at 74 and 325 MHz respectively. We have assumed the flux density of these sources to be reliable at the level of 5% (see Cohen et al. 2003). We therefore have an uncertainty at the level of 5% on the overall flux density scale. We have quadratically added that uncertainty value to the noise-based Gaussian fitting error, given for the peak and integrated flux densities.

- *Source size errors:* As discussed in detail by Cohen et al. (2003), at 74 MHz incompletely corrected ionospheric effects, which are similar to “seeing” effects in the optical domain, are hard to quantify, as we would need to know the actual source sizes. In order to evaluate the effects of the seeing we define the fitted size of resolved source of diameter θ_{source}^2 to be:

$$\theta_{fit}^2 = \theta_{source}^2 + \theta_{beam}^2 + \theta_{seeing}^2 \quad (2.8)$$

Here θ_{beam} is the beam size, and θ_{seeing} corresponds to the size of a point source, deconvolved from the beam and imaged with that level of seeing. Fig. 2.4 shows the scatter of the extendedness of the whole source population at 74 MHz as estimated by S_t/S_p .

Although we do not have any information on the actual source sizes of the individual sources, assuming the bulk of the source population is unresolved, we can directly get an upper limit on the actual value of the seeing. The median value $med(S_t/S_p) = 1.48$ gives an upper limit on the seeing of $20.7''$, and in order to be conservative, we have considered its lower limit to be $0''$.

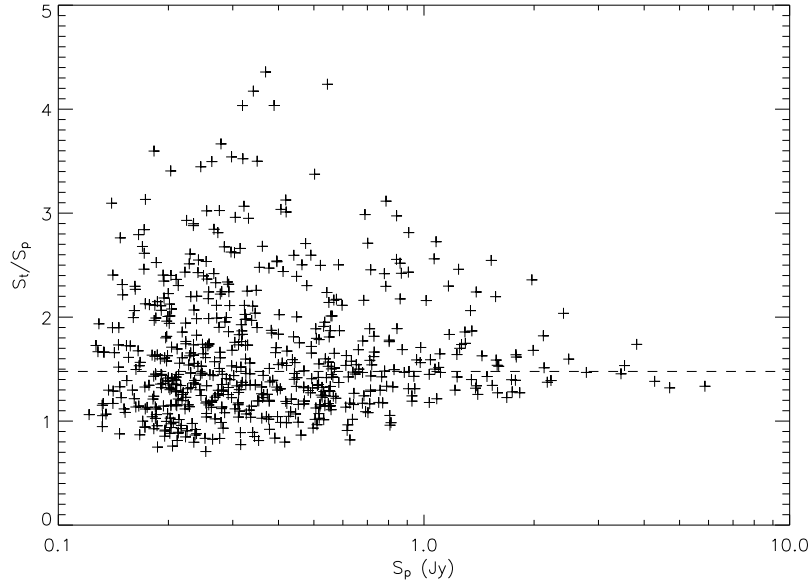


Figure 2.4: At 74 MHz: the ratio of the integrated to the peak flux density of each source vs. the peak flux density. Even if we cannot disentangle the discrepancy between the effects of seeing and physical size, for the seeing effect estimation we take the median value as a good upper limit (dashed line), assuming that the sources with that size are actually unresolved.

2.3.4 Completeness:

In order to quantify the source detection efficiency, we have computed a Monte-Carlo simulation, generating 1000 sources with peak flux densities between 4 and 12σ in a 2800×3100 pixel image, cut from the residual map. Fig. 2.5 shows the number of undetected sources as a function of the signal-to-noise ratio. A function of the following form, gives a fit to the Monte-Carlo outputs:

$$f_m(S_p/\sigma_l) = 1.13\left(\frac{S_p}{\sigma_l} - 3.67\right)^{-2.68} \quad (2.9)$$

where S_p is the peak flux density and σ_l is the local noise value. We can see that $\sim 95\%$ of the sources are detected above 7σ , and this value could be a reasonable estimation of the completeness level. Though assuming the missed fraction to be known, we can correct the source counts estimation by compensating down to the 5σ level the SAD detection inefficiency. We define an effective area element as the integration of a surface element weighted by the detection efficiency ($1 - f_m(S_p/\sigma_l)$). The total effective area at each flux density level S is the integration of that quantity over the domain where the local noise σ_l is as $\sigma_l < S/5$:

$$A_{eff}(S) = \int_{\sigma_l < S/5} [1 - f_m(S_p/\sigma_l)] dA \quad (2.10)$$

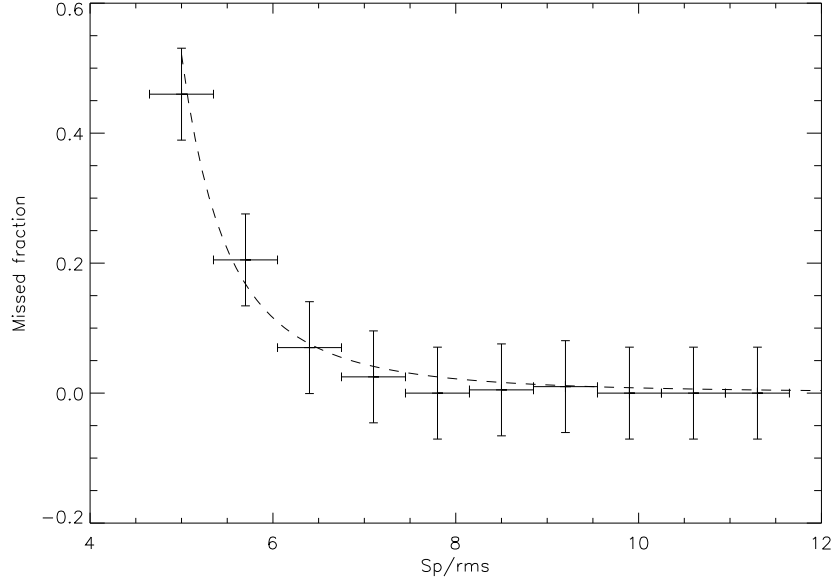


Figure 2.5: The fraction of the missed sources as a function of SNR, from Monte-Carlo simulation, and fitted curve (dashed line).

The source count estimator $N(> S_0)$ is then corrected as follows:

$$N_c(> S_0) = \int_{S_0}^{+\infty} \frac{n(S)dS}{A_{eff}(S)} \quad (2.11)$$

We have computed the uncertainties from the source counts, assuming Poisson statistics:

$$\sigma^2(N > S_0) = \sum_i \frac{1}{A_i^2} N_i$$

Here N_i is the number of sources per bin, and A_i is the area used in the source count calculation.

2.3.5 Extended flux density estimation

The source extraction method using Gaussian fitting algorithm can lead to an underestimation of the integrated flux densities, when significant part of the emission are extended. In order to quantify this effect, we derive another estimation of the integrated flux density inside a $60''$ diameter aperture, centered at the position of each Gaussian component. Then we have $S_{int} = \Sigma \times 4 \ln 2 / (\pi \cdot FWHM)$, where S_{int} is the integrated flux density, Σ is the sum of the pixels inside the aperture, and $FWHM$ is the Full Width at Half Maximum in pixels. Fig. 2.6 shows the cumulative probability distribution of the noise-normalized difference between the two flux density estimates for subsamples of unresolved point-like sources, and resolved, or multiple sources. Using a Kolmogorov-Smirnoff test, we compare both distributions with a purely Gaussian distribution. We derive probability values for the distributions to be Gaussian of $P_{KS} \sim 0.7$ for point like

sources and $P_{KS} \ll 10^{-4}$ for extended sources, indicating that the flux density estimates by the two methods are in agreement for point-like sources and obviously disagree for resolved sources. The median value of the ratio between the flux densities derived from the two methods for extended sources gives the average bias to be $\sim 7\%$. Therefore, at 325 MHz, since the error bars generated by the pixel based method are much higher, when the significance of the difference between the two estimates is above 2σ , we derive the integrated flux density following the pixel-based method, rather than summing over the Gaussian component individual flux densities. At 74 MHz, the resolution being much larger, most sources are unresolved and the Gaussian fitting based integrated flux density estimation is reliable.

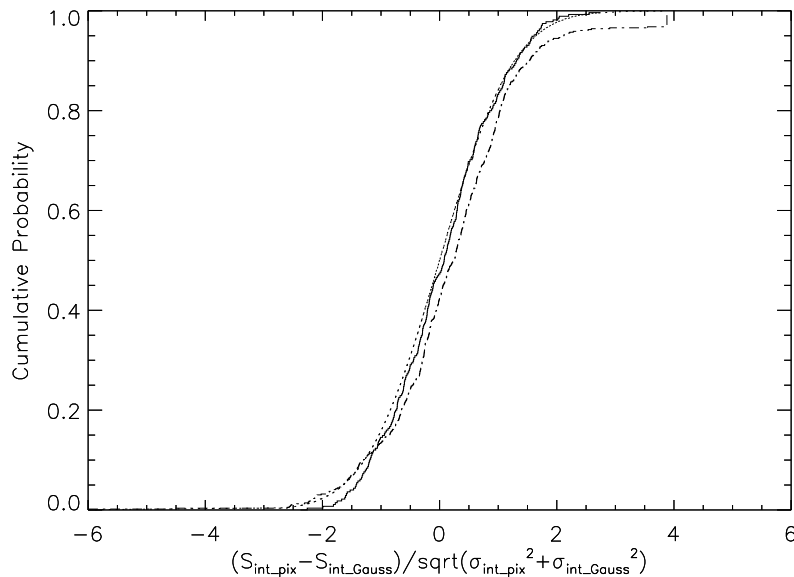


Figure 2.6: The cumulative probability distribution of the noise-normalized difference between the two flux density estimates derived by the Gaussian fitting method (“*int_Gauss*” label) and the pixel-based method (“*int_pix*” label). The solid line represents a subsample of single, unresolved sources, whereas the dash-dotted line represents the extended sources. The purely Gaussian distribution is over-plotted the dotted line.

2.4 RESULTS

2.4.1 325MHz Results

At 325 MHz using the extraction method described above, we extract 877 sources from the 15.3 degree² combined map. This sample contains a significant number of obviously false detections and by visual inspection, we rejected 30 that were close to the brightest sources where the noise is non-Gaussian.

We have defined as multiple sources those separated by less than 60'', and assuming Poissonian statistics this makes the probability of two independent sources to be classified as multiple lower

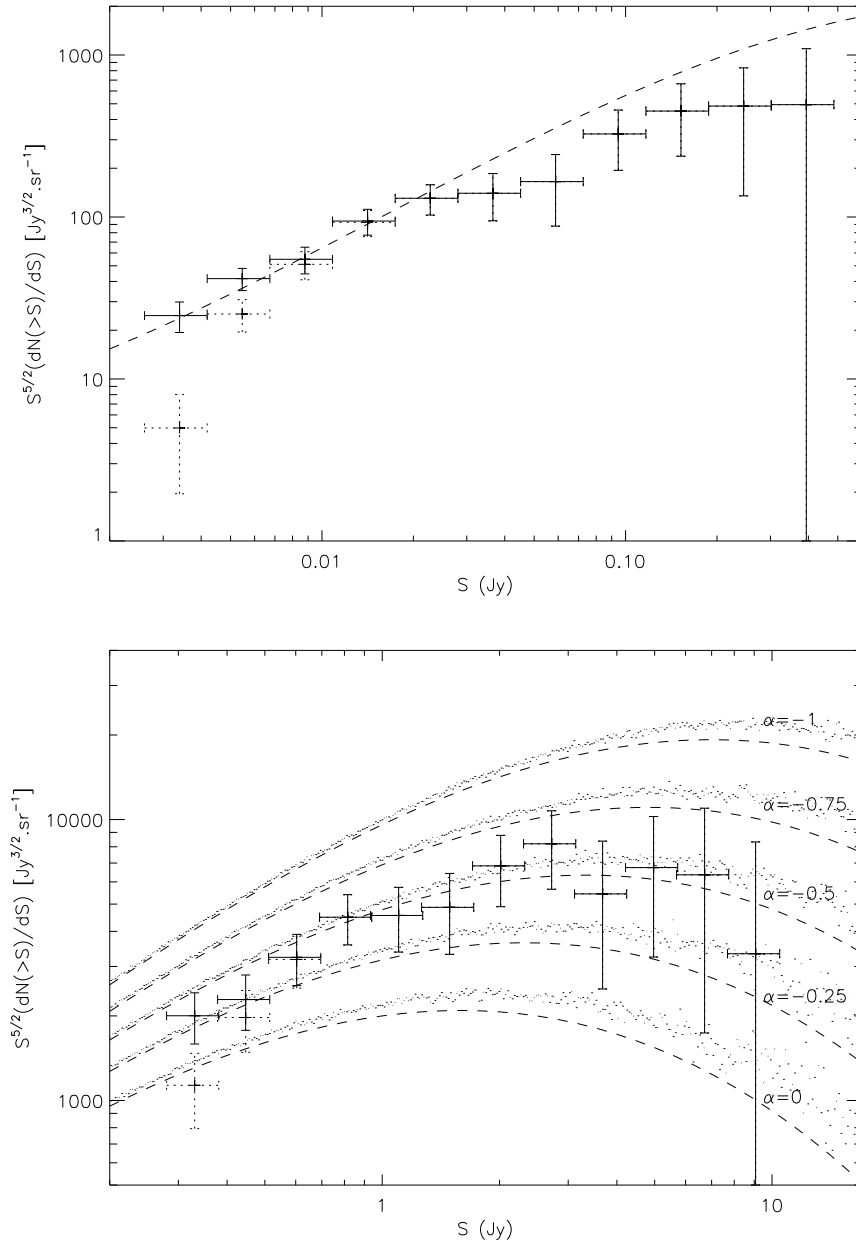


Figure 2.7: The top panel shows the Euclidean normalized differential source count at 325 MHz. The values with doted error bar are uncorrected, whereas the error bar in full line show the differential source count corrected from the noise variations within the map and from the source finding algorithm efficiency falling steeply bellow 10σ . The differential source count from deep 325 MHz survey (Wieringa 1991) is over plotted in dashed line. The bottom panel shows the Euclidean normalized differential source count at 74 MHz. The dashed lines shows the Wieringa (1991) differential source count extrapolated from 325 to 74 MHz using different spectral index in the 0 to -1 range. Dots are showing the differential source count extrapolation derived from Monte-Carlo simulation, taking in account spectral index dispersion $\sigma(\alpha_{325}^{74}) = 0.24$ of a typical radio source population (De Breuck et al. 2000).

than 1%. We finally arrive at a list of 847 sources in which 621 are single (“S”), and 226 are multiple³ (“M”). We have defined as unresolved sources the ones distinguishable from the beam size at the 2σ level, and on the 621 single component sources, 484 were unresolved. The final source list appears in Tab. A1⁴. Images of the multiple component sources larger than twice the beam size are shown in Fig. A1.

Since the Cohen et al. (2003) radio sources are all detected in our deeper and wider survey, at the same frequency, we can directly compare their flux densities. We found that Cohen et al. (2003) flux densities are on average higher than our flux densities by $\sim 20\%$. In order to address this issue, we built radio spectra of ~ 200 radio sources using the 74 MHz flux densities (that are in agreement with Cohen et al. 2003, see section 2.4.3), and 1.4 GHz flux densities retrieved from the NVSS database. Also, we considered two more measurements obtained in August 2004 by the Giant Meterwave Radio Telescope (GMRT) at 230 and 610 MHz, covering the same field at comparable depth (Tasse et al. in prep.). Selecting a sample of single, unresolved sources at 325 MHz, most often, when the general trend of the radio spectra doesn’t indicate any spectral aging or self absorption break, the flux density estimate by Cohen et al. (2003) is a poorer match to the physical synchrotron power law spectra, whereas the new flux density estimates and their associated error bars are well compatible with a power law spectra. We therefore conclude the flux densities published in Cohen et al. (2003) to be overestimated by $\sim 20\%$, and the flux densities presented here to be more reliable. Although not understood, the overestimation on the fluxes of Cohen et al. (2003) might be due to instrumental or algorithm errors.

Fig. 2.7 shows the Euclidean normalized differential source count. We have calculated the source density in each flux density bin as described in the previous section, compensating for noise inhomogeneities across the image. As the error bars have been computed considering the decreasing effective area, we claim that the derived source counts are correct down to the 5σ level, where σ is the minimum noise value in the noise map, so that $5\sigma \sim 2.5$ mJy/beam. Comparing the Euclidean normalized differential source count estimation from a deep Westerbork survey (Wieringa 1991), we find good agreement at low flux densities, where we have applied the efficiency corrections, but at flux densities higher than 30 mJy, they appear to differ by a factor of $\sim 2 - 3$, which we attribute to either cosmic variance or resolution difference.

We have compared our source list to the NVSS database, looking for 1.4 GHz counterparts within $45''$ of each source. The total integrated flux density used to derive the spectral index is calculated as described in section 2.3.5. The resolution difference between our data ($6.7''$) and NVSS ($45''$), makes the estimation of accurate spectral index less robust, as we can miss some of the extended emission seen in NVSS. This probably leads to a small over estimate of the spectral index for the extended sources, and we would need to match resolution to correct for this effect.

Out of the 847 detected sources at 325 MHz, we have found 566 sources to have NVSS counterparts, and for the 281 remaining sources we give an upper limit on their spectral index based on the NVSS detection limit. Fig. 2.8 shows the spectral index distribution, and the corresponding flux density and completeness limit of NVSS. We have derived the median spectral index $\alpha_{325}^{1400} \sim -0.66$, for the whole radio source sample, excluding the unidentified sources in NVSS,

³The largest multiple sources J0217.0-0449*, J0227.2-0325*, J0216.3-0245*, do not satisfy the $< 60''$ criteria, but regarding at the morphology it is obvious that are actually multiple, see Fig. A1.

⁴ In the electronic version of this paper only

and $\alpha_{325}^{1400}(S_{325} > 0.05 \text{ Jy}) \sim -0.72$, on the brightest sources subsample. Fig. 2.9 shows we find close agreement between the spectral index distributions of a $S > 0.05 \text{ Jy}$ subsample, and the De Breuck et al. (2000) Gaussian fit to the spectral index distributions derived from the WENSS/NVSS surveys flux densities ($S_{325} > 0.05 \text{ Jy}$ subsample).

2.4.2 A Radio halo candidate at 325 MHz

Giant radio halo and relic radio sources are generally diffuse low surface brightness sources with steep spectra and typical physical sizes of $\sim 0.1 - 1 \text{ Mpc}$. They are found in rich environment, showing signs of cluster merger activity (for extended reviews on the subject see Feretti 1999; Sarazin 2005).

An extended, low surface brightness object of $\sim 1.9'$ along the right ascension axis, and $\sim 0.9'$ along the declination axis is detected at 325 MHz at $\alpha(\text{J2000}) = 2^{\text{h}}19^{\text{m}}42^{\text{s}}$, $\delta(\text{J2000}) = -4^{\circ}00'30''$. Since that source is extended on the scale of the box being used for the local noise calculation, the peak flux density was below the 5σ level after the local noise normalization. We have therefore extracted the Gaussian components of that source on the original map, which appear together with the other sources in Tab. A2⁴. Using AIPS's task TVSTAT, we find its integrated flux density to be $150.7 \pm 12.5 \text{ mJy}$. We detect the diffuse emission counterparts at 74 MHz and 1.4 GHz (NVSS, Condon et al. 1998) at flux density levels of $1.34 \pm 0.2 \text{ Jy}$, and $27.7 \pm 1.8 \text{ mJy}$ respectively. This makes the spectral indexes to be $\alpha_{74}^{325} \sim -1.48 \pm 0.15$ and $\alpha_{325}^{1400} \sim -1.16 \pm 0.1$. We have looked for counterparts using the NED databases (NED Team 1992), and Fig. 2.10 shows the overlay between an image retrieved in the Digital Sky Survey (DSS) and the radio halo contours. We have found four objects classified as galaxies in Maddox et al. (1990).

Based on the morphology and the fairly steep spectral index, we suggest that this object is a good candidate for either a radio halo, a radio relic or both. The difference between the spectral indexes α_{74}^{325} and α_{325}^{1400} suggests the presence of more than one electron population. The contour lines on the east side of the object shows a steep fall-off of the surface brightness, which indicates the presence of a shock. A polarization observation of the halo could confirm the relic origin of its diffuse emission. Visually, it looks like a galaxy overdensity and this diffuse emission likely belongs to a galaxy group or cluster as discovered in recent, similarly observed objects at low frequencies (Kassim et al. 2001). The detection of diffuse X-ray emission would confirm the cluster identification, but unfortunately, the $\sim 5 \text{ degree}^2$ X-ray field does not overlap the source.

2.4.3 74MHz Results

At 74 MHz, on the criteria outlined above, we detect 686 sources. Matching the source list with NVSS 1.4 GHz objects, we find 20 sources to be false detections due to the correlated sidelobe noise close to bright sources. As for the 325 MHz data, any sources closer than $60''$ have been classified as multiple. Of the 666 remaining sources, 615 have been classified as single (S) and 51 as multiple (M) (see Fig. A2). Of the 615 simple sources, 465 were unresolved. Yet, as discussed in section ??, the size measurement at 74 MHz have very high uncertainties, as the seeing effect is poorly defined.

As for the 325 MHz dataset, we have checked for the consistency between our and Cohen et al. (2003) observed flux densities at 74 MHz. Results do not show any significant overall offsets in

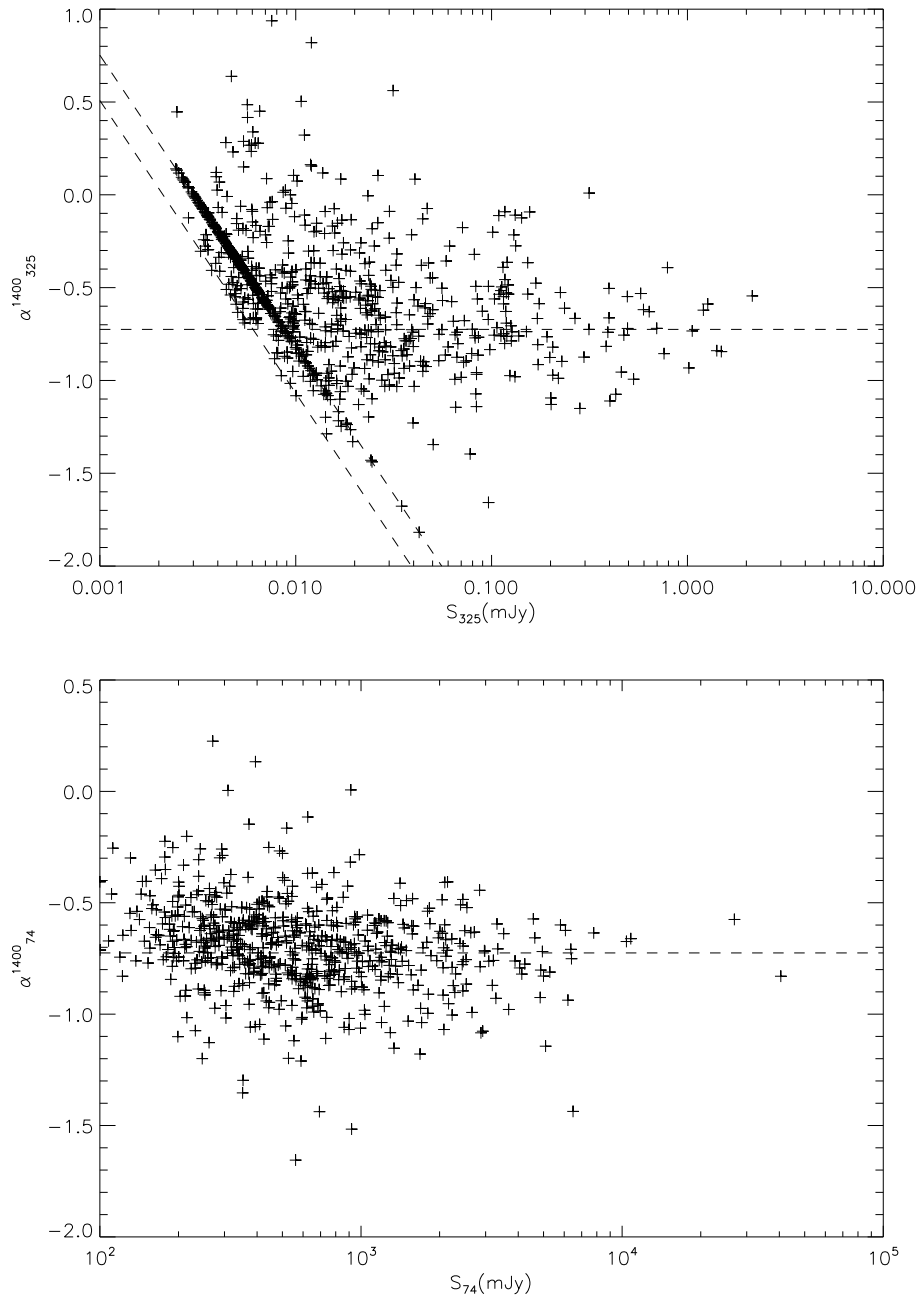


Figure 2.8: Spectral index distribution at 325 MHz (top panel) and 74 MHz (bottom panel), derived from comparison with flux density of each radio source counterpart at 1.4 GHz in the NVSS. The flat dashed lines on both plots represents the median value being respectively $\alpha_{325}^{1400} = -0.72$ and $\alpha_{74}^{1400} = -0.72$. In the 325 MHz spectral index distribution plot, the dashed lines on the left correspond to the spectral index reachable as a function of the 325 MHz flux density, with respect to the completeness, and flux density limit levels of NVSS.

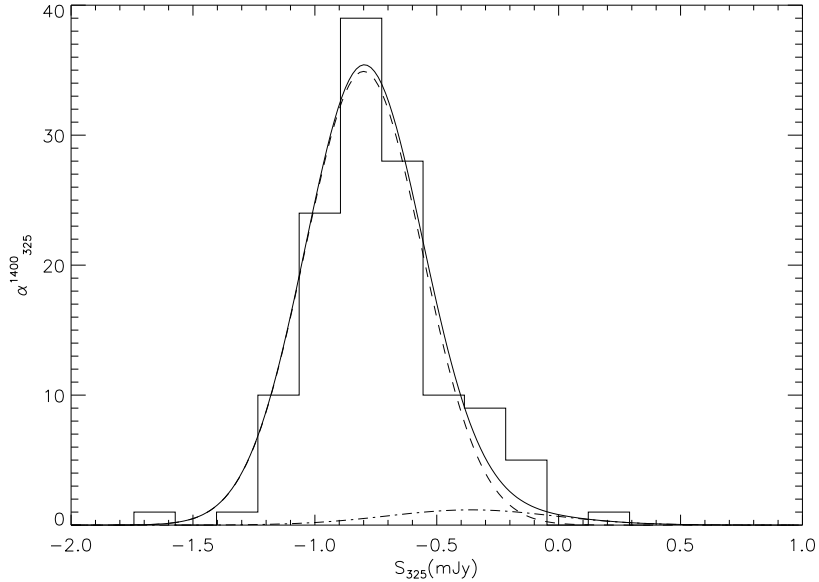


Figure 2.9: Spectral index distribution ($S > 0.05$ Jy) comparison with De Breuck et al. (2000) Gaussian fits, based on the WENSS/NVSS surveys. Dashed line and dashed-dotted line show the spectral index distribution of the steep-spectrum and the flat-spectrum radio source population respectively (De Breuck et al. 2000).

between the two measurement, as opposed to the 325 MHz observations. In addition, we compare our flux density estimates to the VLSS radio survey at 74 MHz (Cohen et al. 2006). Again, flux differences are compatible with the error bar estimates.

At 74 MHz, assuming $\alpha = -0.8$ the corresponding flux density limit at 1.4 GHz is about an order of magnitude higher than the NVSS flux density limit. Consequently, all the 74 MHz sources have a counterpart in the NVSS database within a $60''$ radius. Moreover our $30''$ resolution 74 MHz map roughly matching the NVSS resolution of $45''$, we expect the spectral index estimation to be highly reliable. The spectral index distribution is shown in fig. 2.8, and we find a spectral index median value of $\alpha_{74}^{1400} = -0.72$.

Fig. 2.7 shows the Euclidean normalized differential source count with and without applied corrections. In order to compare that result, we can analytically extrapolate the relation given by Wieringa (1991) from 325 MHz to 74 MHz, assuming various mean spectral indices ($\langle \alpha_{74}^{325} \rangle = \{-1.00, -0.75, -0.50, -0.25, 0.00\}$). Also, to take in account the spectral index dispersion of the radio source population at 325 MHz, we have conducted an extensive Monte-Carlo simulation, by generating a radio source population following the Wieringa (1991) source counts at 325 MHz, and then giving each source a random spectral index following a Gaussian distribution with mean values of $\langle \alpha_{74}^{325} \rangle$, and a dispersion of $\sigma(\alpha_{74}^{325}) = 0.24$ (De Breuck et al. 2000). Extrapolating the flux density of each source to 74 MHz, we can build the differential source count at 74 MHz. Fig. 2.7 shows that the analytical and Monte-Carlo extrapolated differential source counts are in close agreement. The Euclidean normalized differential source count of our sample roughly corresponds to the extrapolation done with $\alpha_{74}^{325} \sim -0.5$ which contrasts with the median \sim value $\alpha_{74}^{1400} = -0.72$ found between our 74 MHz sources and their NVSS counterparts at 1.4 GHz. This suggests a flat-

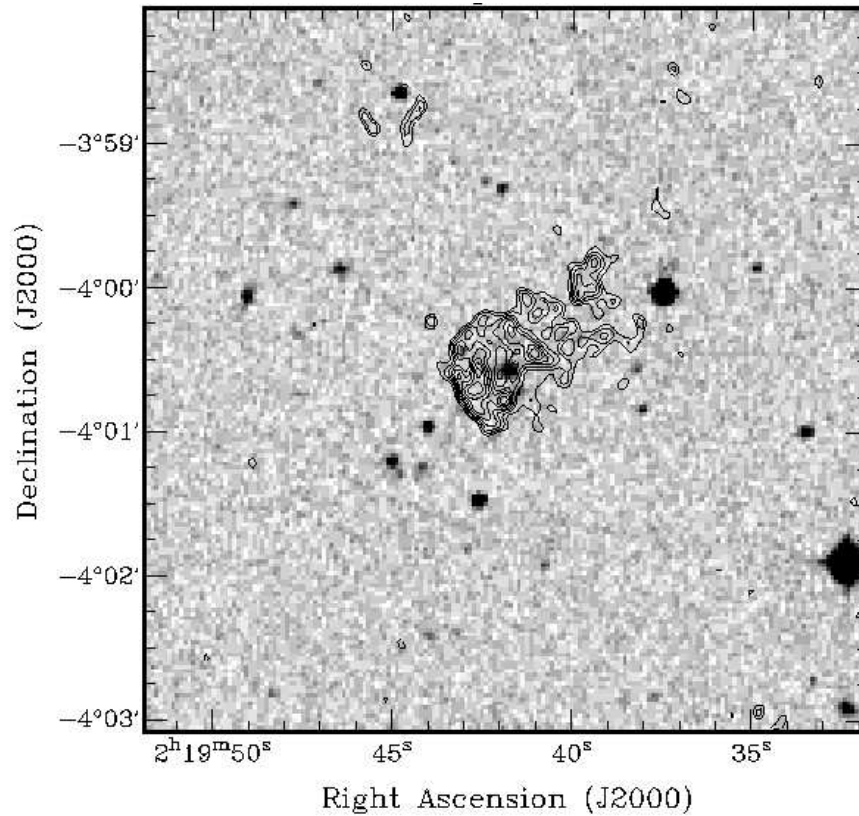


Figure 2.10: Radio contours of the giant radio halo candidate detected at 325 MHz overlaid with an image retrieved from Digitized Sky Survey. The contours corresponds to levels of $1.5 \text{ mJy/Beam} \times \{1, 1.4, 2, 2.8, \dots\}$

tening of the spectrum at $\nu < 325 \text{ MHz}$, likely due to the sources being synchrotron self absorbed.

2.4.4 Source Identification from Literature:

We have searched for published data on all objects we have detected at both frequencies, using the NASA/IPAC Extragalactic database (NED / NED Team 1992). We set the searching radius at $6''$ for the individual object search, and at $3'$ for the galaxy cluster search. On the 1460 detected objects at 74 and 325 MHz, 34 with known redshift have been identified optically as QSO, Galaxy, or are expected to belong to a galaxy cluster, and we have only selected the ones with their redshift determined (See Table 2.3). All of them have been identified at 74 MHz and only four have also been identified at 325 MHz. This appears to be a selection effect as the survey at 74 MHz probes a much brighter source population and an area which is ~ 7 times larger than at 325 MHz. Fig 2.11 shows the redshift distribution of our identified source sub-sample.

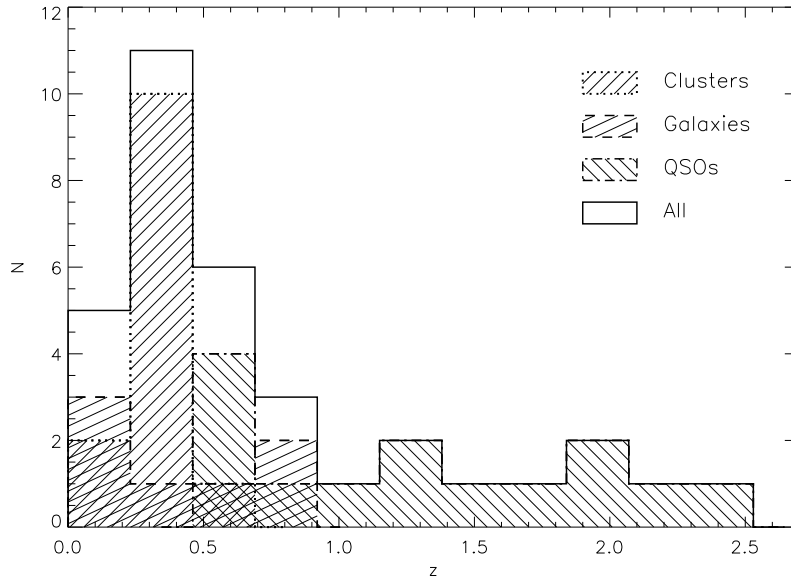


Figure 2.11: Redshift distribution of our whole radio source sample identified with NED, and with measured redshift for the QSOs, galaxies, and galaxy cluster.

2.5 CONCLUSION AND FUTURE WORK

We have mapped the XMM-LSS field over ~ 130 and ~ 15 squares degrees at 74 and 325 MHz respectively, detecting ~ 1500 sources in total. We detect one source of diffuse, steep-spectrum emission, which is a candidate for a radio halo or relic. The Euclidean normalized differential source counts at 74 MHz are consistent with previous studies assuming $\alpha_{325}^{74} \sim -0.5$, suggesting a flattening of the spectrum of radio source population for $\nu < 325$ MHz.

In the near future we will combine the VLA data at 74 and 325 MHz with observations from the GMRT (Giant Meterwave Radio Telescope) at 230 and 610 MHz of the XMM-LSS field, adding two additional frequencies. Cross-correlating this data with upcoming X-ray and optical observations will allow us to probe in detail the low frequency spectrum of a large radio galaxy sample, and to determine the influence of the small and large scale environment on the radio source properties, such as linear size, and radio power.

ACKNOWLEDGMENTS

The authors have made use of the NASA/IPAC Extragalactic Database (NED), which is operated by the Jet Propulsion Laboratory, Caltech, under contract with the National Aeronautics and Space administration. Basic research in radio astronomy at the Naval Research Laboratory is funded by the Office of Naval Research. The authors thank the referee for a number of helpful suggestions.

Table 2.3: Objects identified in NED database with known redshifts.

Name	R.A. Radio Source (J2000)	Decl. Radio Source (J2000)	Type	R.A. NED object	Decl. NED object	dist from object (")	Redshift	Reference
J0201.7–0211	02 01 43.10	–02 11 51.93	G	02 01 43.11	–02 11 47.6	4.33	0.19590	2
J0201.7–0211	02 01 47.18	–02 11 59.60	G	02 01 47.03	–02 11 55.7	4.50	0.19600 ± 0.00100	3
J0213.7–0256	02 13 46.93	–02 56 41.32	G	02 13 47.00	–02 56 37.5	3.96	0.35680 ± 0.00020	4
J0215.6–0222*	02 15 41.85	–02 22 54.27	QSO	02 15 42.02	–02 22 56.8	3.59	1.17800	5
J0216.2+0008	02 16 16.51	+00 08 59.32	GClstr	02 16 17.30	+00 11 37.0	158.12	0.21998	1
J0216.6–0444*	02 16 40.90	–04 44 05.12	QSO	02 16 40.65	–04 44 04.7	3.77	0.87000	6
J0217.4–0015	02 17 25.01	–00 15 47.02	GClstr	02 17 32.80	–00 15 52.0	116.95	0.31075	1
J0218.5–0923	02 18 34.50	–09 23 39.64	QSO	02 18 34.38	–09 23 38.5	2.13	0.47000	6
J0218.6–0015	02 18 39.78	–00 15 07.11	GClstr	02 18 39.40	–00 12 20.0	167.20	0.31075	1
J0220.0–0143	02 20 01.98	–01 43 49.67	QSO	02 20 02.31	–01 43 52.7	5.80	0.47000	6
J0220.5+0027	02 20 32.50	+00 27 59.65	GClstr	02 20 34.30	+00 27 56.0	27.24	0.26537	1
J0220.9–0156*	02 20 54.11	–01 56 53.07	G	02 20 54.25	–01 56 51.8	2.45	0.17500	7
J0223.0–0826	02 23 01.84	–08 26 09.02	QSO	02 23 01.55	–08 26 09.9	4.43	1.52070	8
J0224.3–0752	02 24 22.41	–07 52 58.85	QSO	02 24 22.39	–07 52 58.7	0.33	2.44920	8
J0225.1–0035	02 25 07.73	–00 35 32.50	QSO	02 25 08.09	–00 35 31.4	5.51	0.68700	9
J0227.6–0052	02 27 36.20	–00 52 58.03	GClstr	02 27 35.40	–00 54 05.0	68.03	0.34479	1
			GClstr	02 27 35.50	–00 51 32.0	86.66	0.33344	1
J0228.4+0032	02 28 25.01	+00 32 12.08	GClstr	02 28 26.50	+00 32 20.0	23.71	0.50000	10
J0228.6–0042	02 28 40.90	–00 42 55.03	GClstr	02 28 42.90	–00 43 20.0	39.03	0.42421	1
J0228.1–0115	02 28 07.50	–01 15 43.10	AbLS	02 28 07.79	–01 15 40.5	5.06	1.99760	11
			QSO	02 28 07.80	–01 15 40.6	5.14	2.03700	1
J0230.4+0108	02 30 26.25	+01 08 49.10	GClstr	02 30 27.40	+01 09 04.0	22.79	0.40000	10
J0231.0–0049	02 31 00.82	–00 49 44.42	GClstr	02 31 11.20	–00 49 21.0	157.45	0.39017	1
J0233.4+0015	02 33 25.37	+00 15 48.75	GClstr	02 33 28.10	+00 17 22.0	101.84	0.35613	1
			GClstr	02 33 27.90	+00 18 37.0	172.47	0.34479	1
J0233.5–0203	02 33 30.17	–02 03 22.19	G	02 33 30.34	–02 03 22.4	2.55	0.79400	9
J0234.3–0139	02 34 21.64	–01 39 00.25	G	02 34 21.83	–01 39 00.6	2.87	0.64500 ± 0.00200	12
J0234.9–0736	02 34 58.71	–07 36 17.98	QSO	02 34 58.44	–07 36 19.8	4.44	2.17260	8
J0235.5–0705	02 35 30.73	–07 05 01.43	QSO	02 35 30.71	–07 05 04.6	3.18	2.05980	8
J0235.5–0219	02 35 32.43	–02 19 31.19	QSO	02 35 32.51	–02 19 32.0	1.44	1.32100	9
J0237.9–0145	02 37 57.00	–01 45 10.77	G	02 37 57.09	–01 45 11.4	1.48	0.84000	9
J0239.2–0118	02 39 13.42	–01 18 15.01	QSO	02 39 13.68	–01 18 16.4	4.14	1.79400	9
J0239.7–0234	02 39 45.71	–02 34 39.93	QSO	02 39 45.47	–02 34 40.9	3.72	1.11600	9
J0242.6–0000	02 42 40.40	–00 00 45.21	G	02 42 40.71	–00 00 47.8	5.32	(1137 ± 3)km/s	13
			GClstr	02 42 32.10	+00 00 14.0	137.86	0.21998	1
J0242.7–0157	02 42 47.57	–01 57 46.54	QSO	02 42 47.65	–01 57 49.6	3.28	0.61700	9

An asterisk (*) after the source-name indicates the source has been detected at both frequencies.

REFERENCES:(1) Goto et al. (2002), (2) Crawford et al. (1999), (3) Crawford et al. (1995), (4) Owen et al. (1995), (5) Drinkwater et al. (1997), (6) Becker et al. (2001), (7) Hewitt & Burbidge (1991), (8) Schneider et al. (2003), (9) Dunlop et al. (1989), (10) Postman et al. (1996), (11) Junkkarinen et al. (1991), (12) Stanford et al. (2000), (13) Huchra et al. (1999)

REFERENCES

- Becker, R. H., White, R. L., Gregg, M. D., et al. 2001, *ApJS*, 135, 227
- Best, P. N., Kauffmann, G., Heckman, T. M., et al. 2005, *MNRAS*, 362, 25
- Blanton, E. L., Sarazin, C. L., McNamara, B. R., & Clarke, T. E. 2004, *ApJ*, 612, 817
- Bondi, M., Ciliegi, P., Zamorani, G., et al. 2003, *A&A*, 403, 857
- Cohen, A. S., Lane, W. M., Kassim, N. E., et al. 2006, in *Astronomical Society of the Pacific Conference Series*, 299
- Cohen, A. S., Röttgering, H. J. A., Kassim, N. E., et al. 2003, *ApJ*, 591, 640
- Condon, J. J. 1997, *PASP*, 109, 166
- Condon, J. J., Cotton, W. D., Greisen, E. W., et al. 1998, *AJ*, 115, 1693
- Cotton, W. D., Condon, J. J., Perley, R. A., et al. 2004, in *Proceedings of the SPIE*, Volume 5489, pp. 180-189 (2004), 180–189
- Crawford, C. S., Allen, S. W., Ebeling, H., Edge, A. C., & Fabian, A. C. 1999, *MNRAS*, 306, 857
- Crawford, C. S., Edge, A. C., Fabian, A. C., et al. 1995, *MNRAS*, 274, 75
- Croston, J. H., Hardcastle, M. J., Birkinshaw, M., & Worrall, D. M. 2005, in *X-Ray and Radio Connections* (eds. L.O. Sjouwerman and K.K Dyer) Published electronically by NRAO, <http://www.aoc.nrao.edu/events/xraydio> Held 3-6 February 2004 in Santa Fe, New Mexico, USA, (E7.06) 7 pages
- De Breuck, C., van Breugel, W., Röttgering, H. J. A., & Miley, G. 2000, *A&AS*, 143, 303
- Drinkwater, M. J., Webster, R. L., Francis, P. J., et al. 1997, *MNRAS*, 284, 85
- Dunlop, J. S., Peacock, J. A., Savage, A., et al. 1989, *MNRAS*, 238, 1171
- Fabian, A. C., Sanders, J. S., Allen, S. W., et al. 2003, *MNRAS*, 344, L43
- Fabian, A. C., Sanders, J. S., Taylor, G. B., & Allen, S. W. 2005, *MNRAS*, 360, L20
- Fanaroff, B. L. & Riley, J. M. 1974, *MNRAS*, 167, 31P
- Feretti, L. 1999, in *Diffuse Thermal and Relativistic Plasma in Galaxy Clusters*, 3
- Goto, T., Sekiguchi, M., Nichol, R. C., et al. 2002, *AJ*, 123, 1807
- Hewitt, A. & Burbidge, G. 1991, *ApJS*, 75, 297
- Hill, G. J. & Lilly, S. J. 1991, *ApJ*, 367, 1
- Huchra, J. P., Vogeley, M. S., & Geller, M. J. 1999, *ApJS*, 121, 287
- Junkkarinen, V., Hewitt, A., & Burbidge, G. 1991, *ApJS*, 77, 203
- Kassim, N. E., Clarke, T. E., Enßlin, T. A., Cohen, A. S., & Neumann, D. M. 2001, *ApJ*, 559, 785
- Kassim, N. E., Perley, R. A., Erickson, W. C., & Dwarakanath, K. S. 1993, *AJ*, 106, 2218
- Ledlow, M. J. & Owen, F. N. 1996, *AJ*, 112, 9
- Lonsdale, C. J., Smith, H. E., Rowan-Robinson, M., et al. 2003, *PASP*, 115, 897
- Maddox, S. J., Efstathiou, G., Sutherland, W. J., & Loveday, J. 1990, *MNRAS*, 243, 692
- McCarthy, P. J. 1993, *ARA&A*, 31, 639
- Owen, F. N., Ledlow, M. J., & Keel, W. C. 1995, *AJ*, 109, 14

- Perley, R. A. 1999, in ASP Conf. Ser. 180: Synthesis Imaging in Radio Astronomy II, 383
- Pierre, M., Valtchanov, I., Altieri, B., et al. 2004, *Journal of Cosmology and Astro-Particle Physics*, 9, 11
- Postman, M., Lubin, L. M., Gunn, J. E., et al. 1996, *AJ*, 111, 615
- Refregier, A., Valtchanov, I., & Pierre, M. 2002, *A&A*, 390, 1
- Rengelink, R. B., Tang, Y., de Bruyn, A. G., et al. 1997, *A&AS*, 124, 259
- Sarazin, C. L. 2005, in *X-Ray and Radio Connections* (eds. L.O. Sjouwerman and K.K Dyer) Published electronically by NRAO, <http://www.aoc.nrao.edu/events/xraydio> Held 3-6 February 2004 in Santa Fe, New Mexico, USA, (E8.00) 3 pages
- Schneider, D. P., Fan, X., Hall, P. B., et al. 2003, *AJ*, 126, 2579
- Stanford, S. A., Stern, D., van Breugel, W., & De Breuck, C. 2000, *ApJS*, 131, 185
- Wieringa, M. H. 1991, Ph.D. Thesis
- Yates, M. G., Miller, L., & Peacock, J. A. 1989, *MNRAS*, 240, 129
- Zirbel, E. L. & Baum, S. A. 1995, *ApJ*, 448, 521

APPENDIX

A RADIO IMAGES

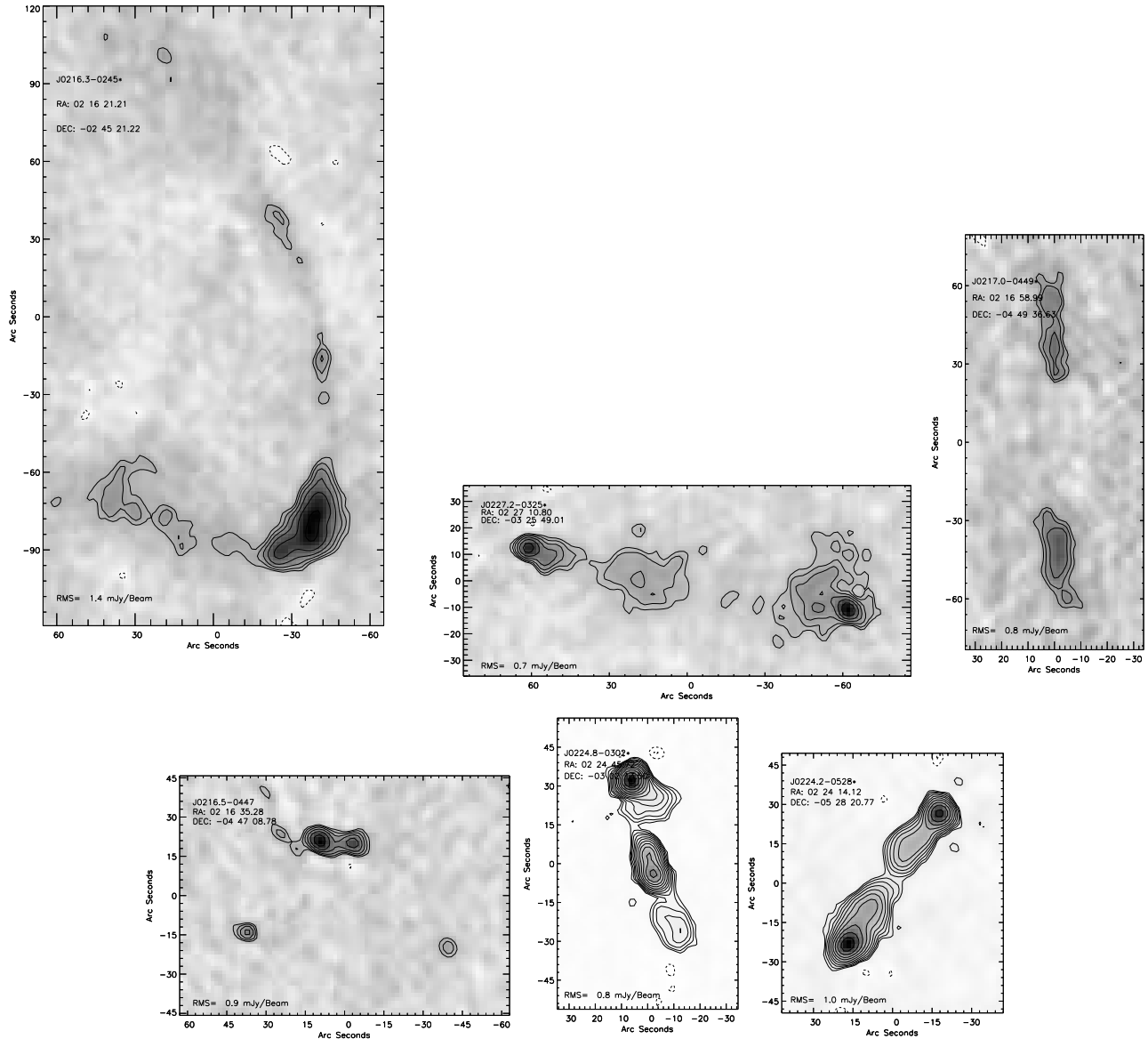


Figure A1: The multiple component sources in the 325 MHz source list larger than $13''$, sorted in decreasing angular size order. Contours corresponds to levels of $3\sigma \times (-1.4, -1, 1, 1.4, 2, 2.8, 4, 5.6, 8, 11, \dots)$ and greyscale is scaled from -3σ to the maximum value in the image. On the top-left corner of each images appears the name of the corresponding source in the source list, as well as its mean coordinate. The local noise level is shown on the bottom of each image.

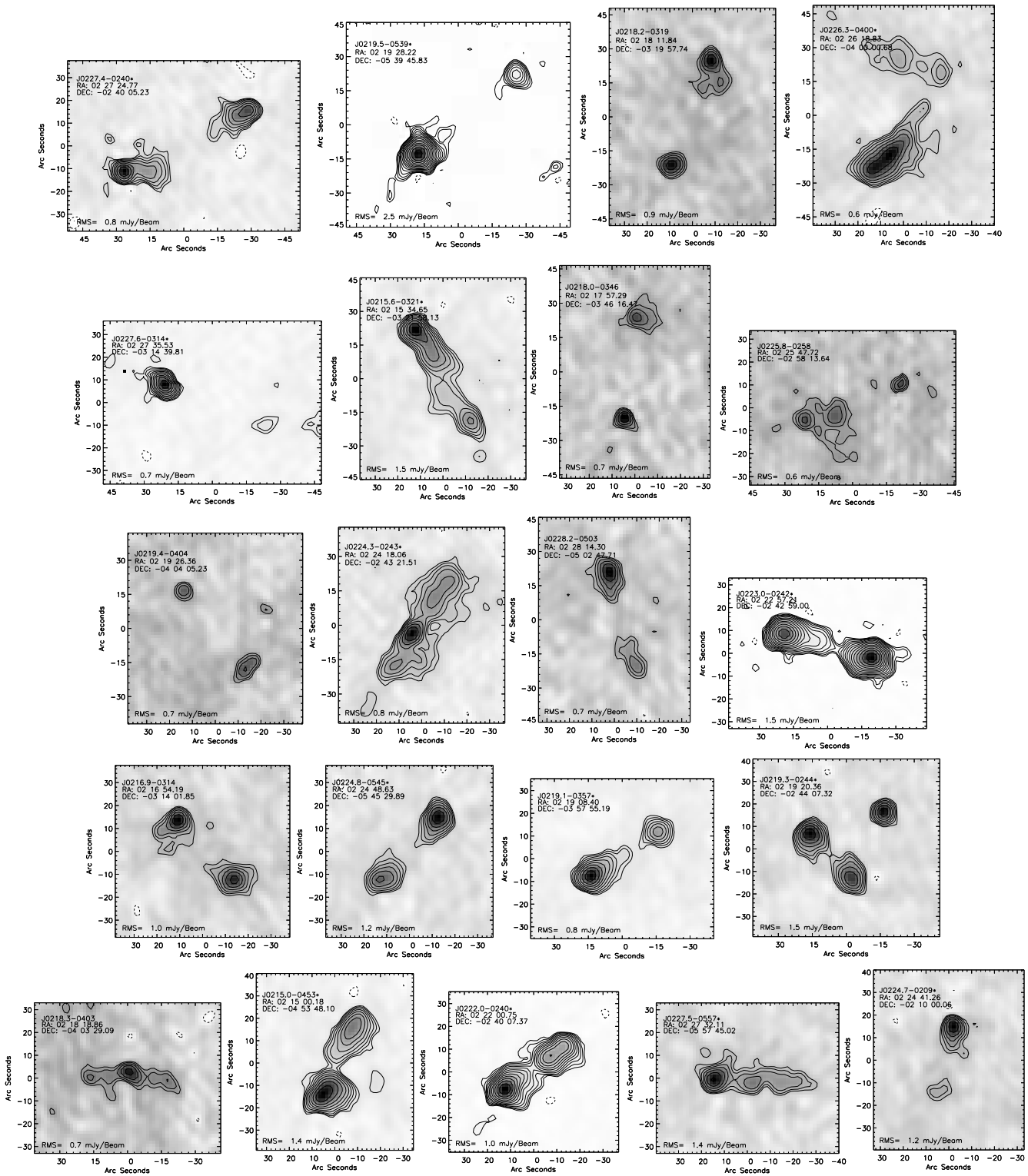


Figure A1: Continued.

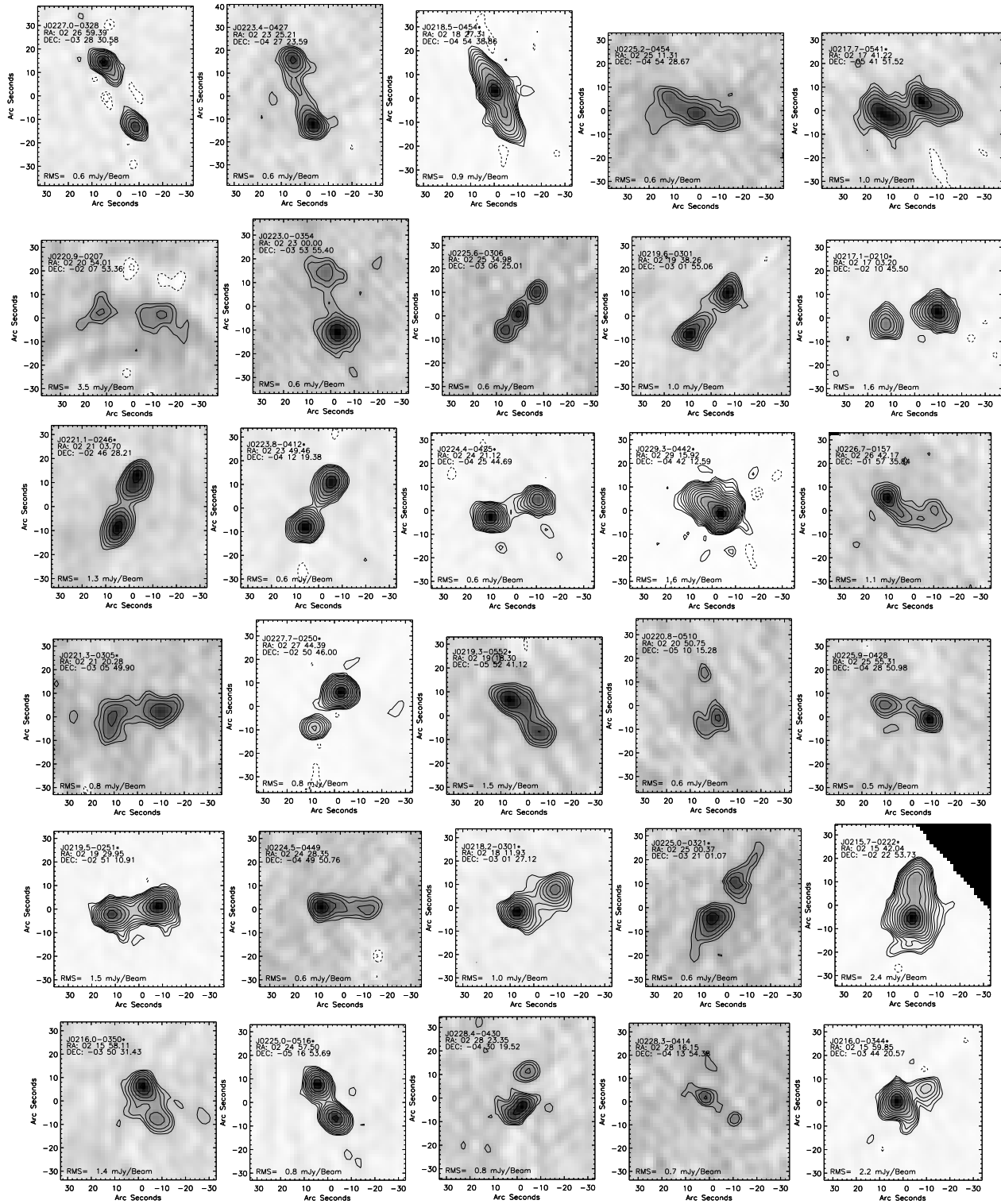


Figure A1: Continued.

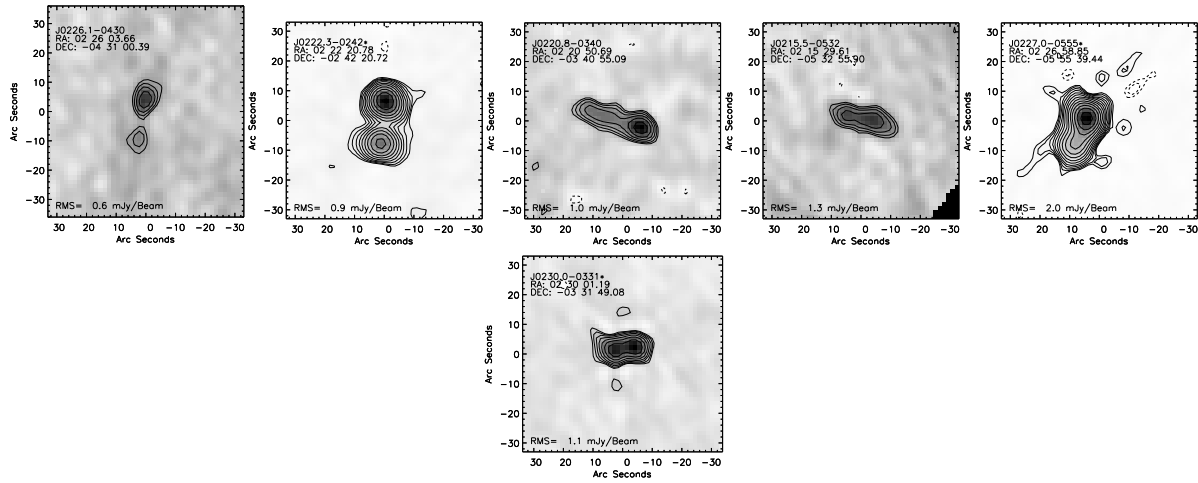


Figure A1: Continued.

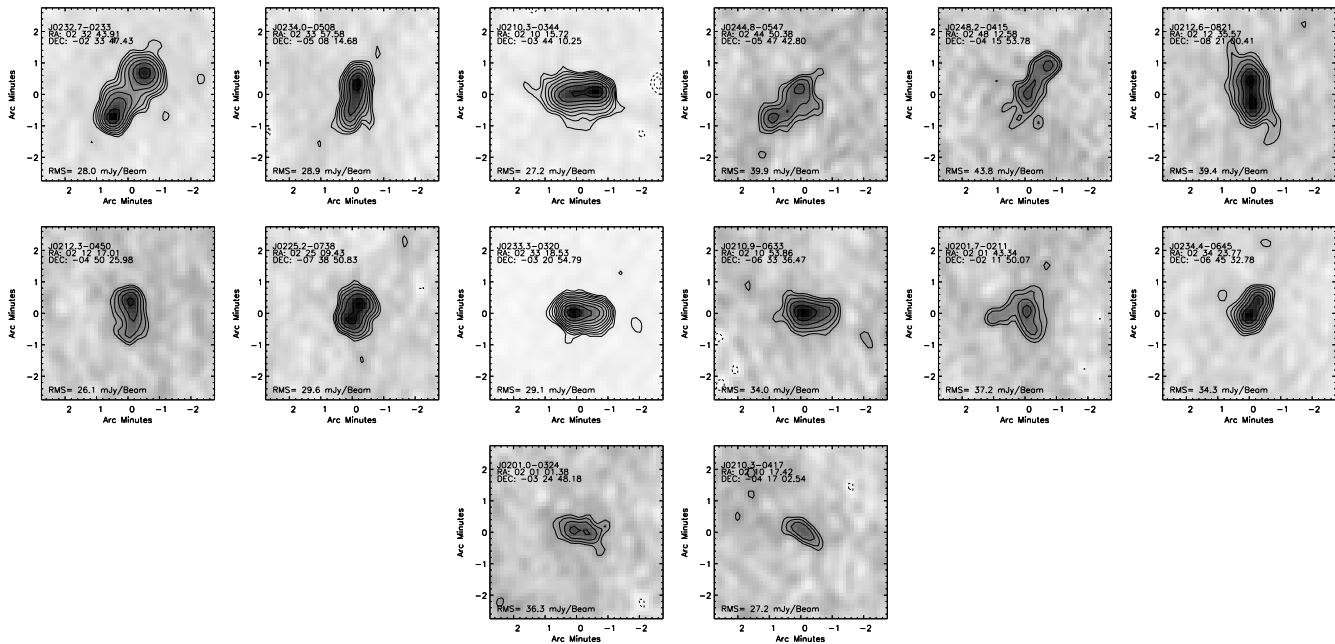


Figure A2: The multiple component sources in the 74 MHz source list larger than $60''$, sorted in decreasing angular size order. Contours corresponds to levels of $3\sigma \times (-1.4, -1, 1, 1.4, 2, 2.8, 4, 5.6, 8, 11, \dots)$ and greyscale is scaled from -3σ to the maximum value in the image. On the top-left corner of each images appears the name of the corresponding source in the source list, as well as its mean coordinate. The local noise level is shown on the bottom of each image.

CHAPTER 3

GMRT observations of the XMM large scale structure survey field

Cyril Tasse, H. J. A. Röttgering, P. N. Best, A. S. Cohen, M. Pierre, R. Wilman

Astronomy & Astrophysics 471, 1105, 2007

The low-frequency radio survey of the XMM-Large Scale Structure (XMM-LSS) field aims to study the connection between the extragalactic radio source populations and their environment as traced by X-ray and optical emission. In this paper we present new radio observations of the XMM-LSS field carried out using the Giant Meterwave Radio Telescope at 240 and 610 MHz. These observations complement the observations presented by Cohen et al. (2003) and Tasse et al. (2006) at 74 and 325 MHz with the Very Large Array. At 240 and 610 MHz, we reach noise levels of ~ 2.5 and ~ 0.3 mJy/beam, leading to the detection of 466 and 769 sources over 18.0 and 12.7 degree² with resolutions of 14.7'' and 6.5'' respectively. Combining these data with the available source lists at 74, 325 (Tasse et al. 2006) and 1400 MHz (NVSS), we build a multifrequency catalogue containing 1611 radio sources. We check for consistency of the astrometry and flux density estimates. We fit a simple synchrotron radiation model to the flux density measurements of the 318 radio sources being detected in at least 4 bands. While $\sim 26\%$ of them show signature of spectral ageing, $\sim 6\%$ show self absorption.

3.1 INTRODUCTION

The XMM-Large Scale Structure survey (XMM-LSS) is a 10 degree² X-ray survey designed to map out the large scale structure of the Universe through the detection of the X-ray emission of the diffuse intracluster medium (ICM). Spectroscopic follow-up of ~ 70 galaxy cluster candidates found in the first ~ 5 degree² is completed, leading to a galaxy cluster density of ~ 12 deg⁻² in the redshift range $z \lesssim 1$ (Pierre et al (2006), Pacaud et al (2006), in preparation). Also some 1000 deg⁻² X-ray active galactic nuclei have been detected.

The Canada France Hawaii Telescope Legacy Survey (CFHTLS¹) has observed the XMM-LSS field in 5 bands down to $i_{AB} \sim 25$, allowing for optical identification of X-ray sources and determination of photometric redshifts. Also, the XMM-LSS field was imaged in 7 bands from 3 to 160 μm as part of the Spitzer Wide-area Infrared Extragalactic Survey (SWIRE, Lonsdale et al. 2003). For a general overview of the XMM-LSS and associated surveys see Pierre et al. (2004).

Cohen et al. (2003) and Tasse et al. (2006) have conducted a deep low-frequency survey of the XMM-LSS field at 74 and 325 MHz with the Very Large Array (VLA), reaching flux density limits of ~ 162 and ~ 4 mJy/beam (5σ), leading to the detection of ~ 1500 radio sources over ~ 130 and ~ 15 degree² with resolutions of 30'' and 6.7'' respectively. The main scientific issues that such data can address include: (1) Where are various radio-loud active galactic nuclei (AGN) located with respect to the distribution of mass on cosmological scales as traced by the optical and X-Ray emission? (2) Can the radio loudness of optical and X-ray AGN be understood as due to environmental effects? (3) How does the hot IGM influence the physical properties of the radio sources such as linear size and radio power?

In order to increase the size of the low frequency radio sources sample (Tasse et al. 2006), we have conducted new observations of the XMM-LSS field at 240 and 610 MHz using the Giant Meterwave Radio Telescope (GMRT). As compared to the VLA, the GMRT has a collecting area a factor of 3 bigger. Integration time of ~ 20 hours at each frequency, lead to the detection of ~ 200 additional radio sources over ~ 15 degree², corresponding to an increase of the sample size of $\sim 25\%$.

In addition, for 41% of the radio sources detected at 325 MHz, our GMRT observations provide two additional flux density points giving the opportunity to study the links between host galaxy, environment, and observed radio spectra for large samples of radio sources. Specifically, within an evolutionary framework, the compact steep spectrum (CSS) and gigahertz peaked spectrum (GPS) radio sources showing signs of synchrotron self absorption at $\nu < 1$ GHz, are thought to be the progenitors of larger steep spectrum FRI and/or FR II (Fanaroff & Riley 1974) radio sources (eg Snellen et al. 2003; O'Dea 1998). When no more high energy electrons are injected into the synchrotron emitting lobes, spectral ageing feature appears in the radio spectra. If the link between these different classes of radio sources is effectively evolutionary, they should be found in similar environments, while the infrared and optical properties of the host galaxy should be evolving. The large multiwavelength dataset available on the XMM-LSS field, combined with the various radio surveys we have undertaken may allow us to address this issue in a consistent way.

In this paper we present the GMRT radio observations, and discuss their consistency. Using our multifrequency dataset and a simple model of synchrotron emission we build subsamples of sources showing self absorption and/or spectral ageing features. In subsequent papers, we will

¹for more information on the CFHT Legacy Survey, see <http://www.cfht.hawaii.edu/Science/CFHLS/>

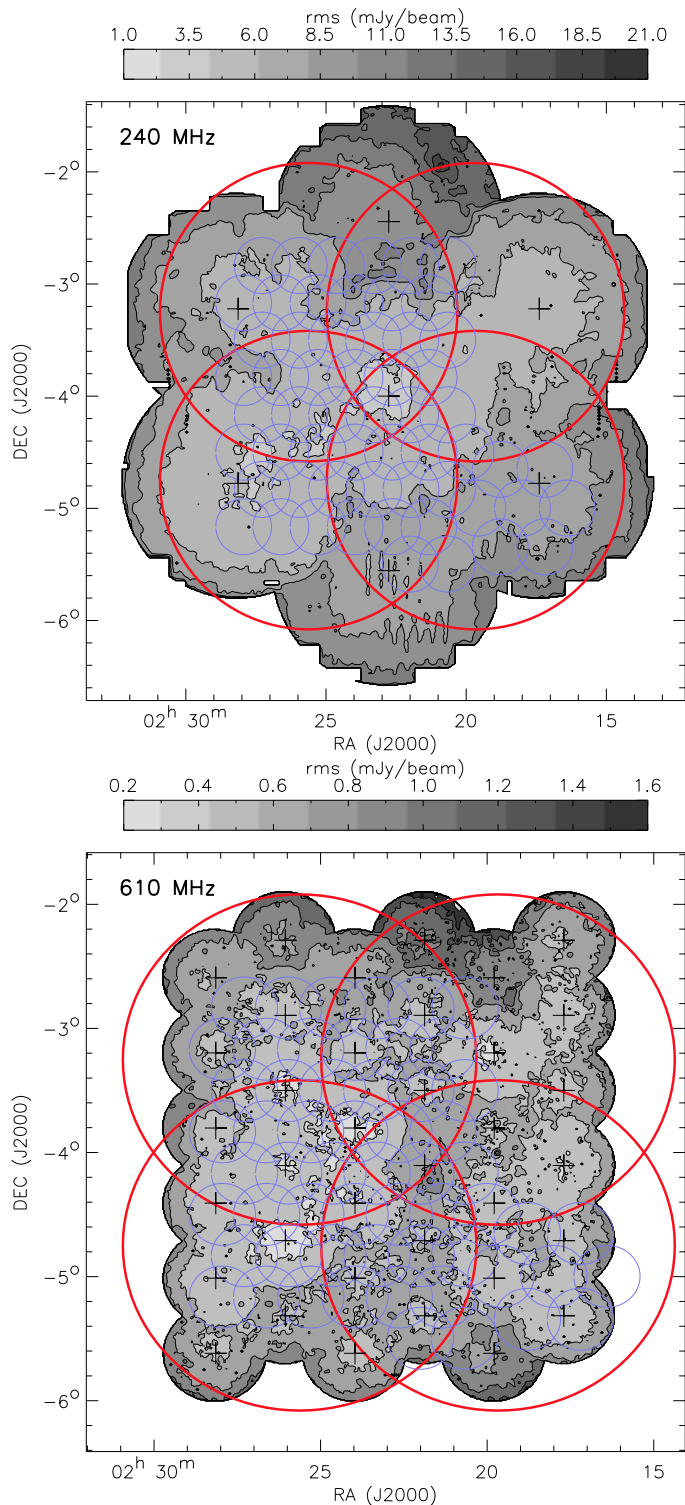


Figure 3.1: The noise maps at 240 and 610 MHz. On both panels, contours were plotted at level of $\sigma \times \{1, 1.4, 2, 2.8, 4, 5.6, 8, \dots\}$ with $\sigma = 1.0$ mJy and $\sigma = 0.2$ mJy at 240 and 610 MHz respectively. On both panels, the crosses show the location of each individual pointing center, the thick red line shows the four 325 MHz VLA pointings, and the blue circles show the location of the X-ray pointing. The primary beams at 240 MHz are counter intuitively smaller than those of the VLA at 325 MHz because the GMRT antennas are larger.

Table 3.1: Observational parameters for the XMM-LSS radio followup with GMRT.

Central Frequency	240 MHz	610 MHz
Obs. date	30, 31 Jul., 3 Aug. 2004	30, 31 Jul. 1, 2 Aug. 2004
Number of pointings	7	36
Int. time per pointing	~ 2.8 hrs	~ 0.5 hrs
Total obs. time (hrs)	~ 20	~ 18
Band Width	8 MHz	2×16 MHz
$N_{channel}$	128	2×128
UV range ($k\lambda$)	~ 0.3 – 18	~ 0.3 – 48
Band Pass Cal.	3C48	3C48
Phase Cal.	0116-208	0116-208

address the main scientific issues using the infrared, optical and X-ray data available on the XMM-LSS field.

This paper is organised as follow: in Section 3.2 we give details of the observations, and data reduction. In Section 3.3 we briefly describe the source extraction methods, and we present the error analysis in Section 3.4. The final source list is presented and analysed in Section 3.5. In Section 3.6 we build a multifrequency radio sample and we fit a simple synchrotron radiation model to the brightest sources to build the self absorbed and spectrally aged subsamples. We conclude in Section 3.7.

3.2 OBSERVATIONS AND DATA REDUCTION

3.2.1 Radio Continuum at 610 MHz

The XMM-LSS field centered at $\alpha(\text{J2000})= 2^{\text{h}}24^{\text{m}}00^{\text{s}}$, $\delta(\text{J2000})= -4^{\circ}09'47''$ was observed at 610 MHz from the 30th of July to the 2nd of August 2004 for a total of ~ 18 hours. We have used the full available bandwidth of 32 MHz, split into two intermediate frequencies (IFs), each IF being sampled into 128 channels. The first and second IF were covering the intervals 594 – 610 MHz and 610 – 626 MHz, respectively (See Tab. 3.1 for an overview). At 610 MHz the GMRT full width at half maximum (FWHM i.e. primary beam diameter) is $\theta_{FWHM} \sim 0.7^{\circ}$. In order to survey the ~ 15 degree² of the 325 MHz counterpart of the XMM-LSS field (Tasse et al. 2006), we spread the pointing centers over an hexagonal grid consisting of 36 pointings centers separated by 0.6° (Fig. 3.1). The pointing grid covers 78% of the area mapped at 325 MHz. For each pointing, we have used a total integration time of 30 minutes. Since the GMRT array consists of three arms, in the uv-plane the visibilities corresponding to each individual baseline come back to the same uv-location every 4 hours. In order to optimize the uv-plane coverage we split each 30 minutes observation of each individual pointing into three 10 minutes scans, separated by about 1.3 hours. For the flux and bandpass calibration we used 3C48 as flux density and bandpass calibrator, observed for 30 minutes at the beginning and the end of the run. We used 0116 – 208 as phase and amplitude calibrator, observed for 8 minutes every 30 minutes.

For the data reduction work, we made use of the Astronomical Image Processing System (AIPS). We reduced each IF independently. After a preliminary round of Radio Frequency Interference (RFI) removal using AIPS tasks SPFLG and UVFLG, the bandpass as well as the overall flux density scale were calibrated using 3C48, and the amplitudes of the gains of each antenna were calibrated using 0116 – 208. The expected resolution of $\sim 6.5''$ is similar to the $6.7''$ resolution obtained at 325 MHz with VLA. In order to calibrate the phases variation with time, we build from the Tasse et al. (2006) 325 MHz source list a catalog containing the positions and flux densities of all individual components brighter than 10 mJy. Most of these 325 MHz sources have positional uncertainties on the level of $1.5''$. By Fourier transforming this model of the sky plane, the AIPS task CALIB generates a corresponding model of the uv-plane that is used to calibrate the phase of each antenna every 3 minutes. This approach provides the advantage of suppressing all possible astrometry offsets between the different pointings.

In order to image the full primary beam, we have used a pseudo three dimensional Fourier transform technique (Perley 1999), where each pointing is divided into smaller fields (facets). We have used ~ 20 facets per pointing each $13'$ in size. Each facet was then imaged, and combined into a single image using AIPS task FLATN. The fitted size of the dirty beam is $\sim 6.5''$ along the major axis and $\sim 4.5''$ along the minor axis. In order to have a homogeneous beam across the different pointings in the combined map, the restoring beam was set to be a $6.5'' \times 6.5''$ circular Gaussian in each pointing, angular scale being $1.5'' \cdot \text{pixel}^{-1}$. After few standard phase only self-calibration steps, the synthesized images of the two IFs of each pointing have been averaged. Using a radial cutoff limit of 0.35° (corresponding to the FWHM), the 2IFs \times 36 pointings have been combined into a $\sim 13 \text{ degree}^2$ single image following the procedure described by Condon et al. (1998). In the final map the noise is as low as $\sim 0.2 \text{ mJy} \cdot \text{beam}^{-1}$ to as high as $\sim 1.5 \text{ mJy} \cdot \text{beam}^{-1}$ (Fig 3.1).

3.2.2 Radio Continuum at 240 MHz

The data at 240 MHz were obtained using the GMRT from the 30th of July to the 3rd of August 2004 for a total time of ~ 20 hours. As opposite to the 610 MHz setting, at 240 MHz, the 8 MHz wide bandwidth (128 channels) is centered at 240 MHz and consists of only one IF (See Tab. 3.1 for an overview). The primary beam diameter being 1.8° , in order to cover the 325 MHz counterpart of the XMM-LSS field, we made use of an hexagonal grid, consisting of 7 pointing centers, separated by 1.56° , as shown in Fig. 3.1. The pointing grid covers $\sim 93\%$ of the area mapped at 325 MHz. As for the 610 MHz observations, we used 3C48 at the beginning and the end of each run as flux density and bandpass calibrator, and 0116 – 208 as phase and amplitude calibrator. Also in order to optimize the uv-plane coverage, each pointing was observed for 10 minutes every ~ 1.4 hour, while the secondary calibrator was observed every 0.5 hour for 8 minutes. Each pointing has been observed ~ 2.8 hours in total. Table 3.1 shows a summary of the observational parameters we have been using.

We have synthesized the 240 MHz images as we did at 610 MHz. As for the 610 MHz data, we calibrated the phases using a model derived from the source list at 325 MHz by Tasse et al. (2006) (See Sec. 3.2.1). The restoring beam has been set to be $14.7''$ circular Gaussian in each map, with a pixel size of $3.5'' \cdot \text{pixel}^{-1}$. After a few phase-only self calibration steps we have combined the 7 pointings into a single map using a radial cutoff of 0.9° . The resulting noise varies from as low as $1.2 \text{ mJy}/\text{beam}$ and as high as $10 \text{ mJy}/\text{beam}$ close to bright sources.

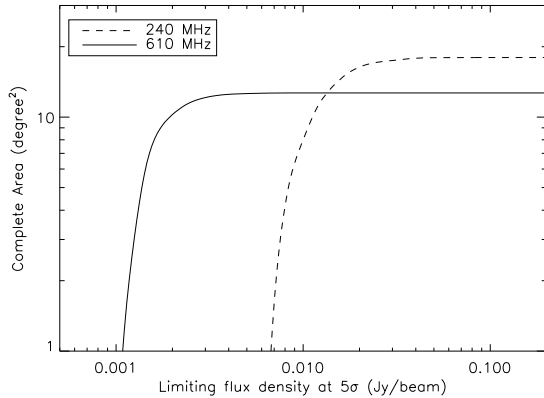


Figure 3.2: Area as a function of limiting flux density at 5σ . The full line corresponds to the 610 MHz survey whereas the dashed one corresponds to the 240 MHz survey.

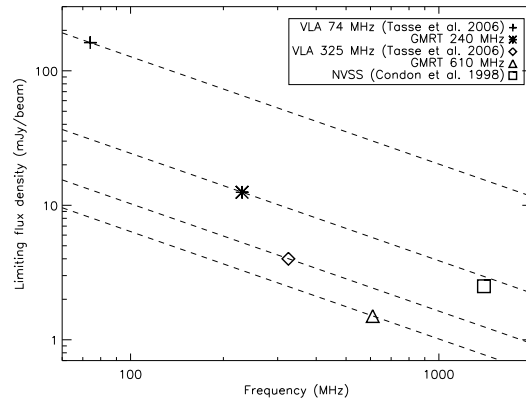


Figure 3.3: Flux density limits (5σ) reached at 240 and 610 MHz as compared to the flux density reached at 74 and 325 MHz with VLA. Dashed lines show the flux density of a source having a spectral index of $\alpha = -0.8$.

At both 240 and 610 MHz, Fig. 3.2 shows the complete area as a function of the sensitivity (5σ), and Fig. 3.3 shows the limiting flux density in the different available frequency bands.

3.3 SOURCE EXTRACTION

For a detailed discussion on the method we have used to extract the sources from the synthesized maps, see Tasse et al. (2006). We briefly describe that process below.

With the local noise being highly variable across the field (see Fig. 3.1 & 3.2), special attention was paid to the source finding method. First, a local noise map is generated using AIPS task RMSD, which derives a local noise value within a box. Given the noise distribution is non-Gaussian, the size of the box is critical. We set visually the size of this box to the scale over which the local noise varies significantly, which leads to values of 3' and 1' at 240 and 610 MHz respectively.

Then we normalize the combined map by the local noise map, and we extract the sources in that noise-normalized map using AIPS's Gaussian fitting algorithm Search And Destroy (SAD), giving an input cut on both the peak and the integrated flux densities of 5 (corresponding to $5\sigma_{local}$ in the original map). We then correct for the peak flux bias introduced by the noise normalization, and calculate the errors on each Gaussian fitting parameter following Condon (1997).

Following Tasse et al. (2006), we build a catalog by associating the components of the source list closer than 60". The number of Gaussian fitting components being 571 and 1024 at 240 and 610 MHz respectively, assuming a Poisson statistics, the probability of two components to be associated by chance is less than 1% in both cases. In the catalogs appearing in Tab. B1⁶ and B2⁶, we have tagged the brightest component of multiple sources with an "M", and the other components with a "C". Non associated components have been classified as Single sources (tag "S").

3.4 DETERMINATION OF SOURCE PARAMETERS AND ASSOCIATED ERRORS

3.4.1 Astrometry

The XMM-LSS field being fully covered at 1.4 GHz by the NVSS (Condon et al. 1998) we have looked for 1.4 GHz NVSS sources in a $45''$ radius around each individual radio source². For the sources identified in the NVSS, this provides 1.4 GHz astrometry, as well as a spectral index estimate. To assess the positional accuracy, in our catalog we have selected a subsample of single (“S”) sources with their NVSS counterpart being point-like and having positional uncertainties $\sigma_{\alpha,\delta}^{NVSS} < 0.7''$ on both right ascension and declination, which has the effect of selecting the radio sources that have the brightest 1.4 GHz counterparts. On this subsample containing 33 sources, we measure overall astrometrical offsets of $\Delta(\alpha_{610}) = 1.15''$ and $\Delta(\delta_{610}) = -1.50''$ at 610 MHz on right ascension and declination respectively, and $\Delta(\alpha_{240}) = 2.84''$ and $\Delta(\delta_{240}) = -1.85''$ at 240 MHz. These offsets are on the order of the pixel size at both 240 and 610 MHz. We have corrected for these astrometry shifts in the final catalog. In order to be conservative, given the fitted Gaussian major and minor axis and their associated error bars, we have classified as unresolved the sources that are indistinguishable from the restoring beam size at the 2σ level³.

From the same high signal-to-noise subsample, we measure the standard deviation of the position differences between fitted components and their NVSS counterpart to be $\sigma_{\alpha} = 0.70''$ and $\sigma_{\delta} = 1.78''$ at 610 MHz and $\sigma_{\alpha} = 1.31''$ and $\sigma_{\delta} = 2.37''$ at 240 MHz. These errors contain a contribution from the positional uncertainties in our catalog and a contribution from the NVSS positional uncertainties. In both these components, there is a contribution from the Gaussian fitting errors, which depends on the signal-to-noise ratio of the detection, and a contribution from the individual antenna calibration errors, which does not depend on the local rms value. In order to derive an estimate of the positional calibration errors in our GMRT data $\sigma_{GMRTcal}$ on both right ascension, and declination we write:

$$\sigma^2 = \sigma_{NVSScal}^2 + \sigma_{NVSSfit}^2 + \sigma_{GMRTcal}^2 + \sigma_{GMRTfit}^2 \quad (3.1)$$

For the NVSS the positional errors due to the antenna calibration has been measured to be $\sigma_{\alpha,NVSScal} = 0.45''$ and $\sigma_{\delta,NVSScal} = 0.56''$ (Condon et al. 1998). In the high signal-to-noise ratio subsample defined above, corresponding to the brightest sources in our source list, we measure the associated Gaussian fitting errors on position $\sigma_{GMRT,fit} \lesssim 0.1''$ at both 240 and 610 MHz making the Gaussian fitting error contribution to be negligible. We derive an upper limit to the residual systematic errors in the 610 MHz astrometry of $\sigma_{\alpha,GMRTcal} \lesssim (\sigma_{\alpha}^2 - \sigma_{\alpha,NVSScal}^2)^{1/2} = 0.53''$ and $\sigma_{\delta,GMRTcal} \lesssim 1.69''$. At 240 MHz we find $\sigma_{\alpha,calib} \lesssim 1.23''$ and $\sigma_{\delta,calib} \lesssim 2.31''$. We quadratically add these values to the error obtained from the Gaussian fits.

²Note that we can not use the deeper and higher resolution 1.4 GHz FIRST survey data (Becker et al. 1995) because it only partly covers the XMM-LSS field.

³If θ_N is the restoring beam diameter, θ_M the major axis diameter, and $\sigma(\theta_M)$ its associated error bar, then the fitted component is classified as unresolved if $(\theta_N - \theta_M)^2 / \sigma^2(\theta_M) < 2$. Same for the minor axis.

3.4.2 Flux densities

Various factors have to be taken into account in order to derive source lists having reliable flux densities estimates.

Contrarily to the VLA, at the GMRT the injection of calibrated noise at the front-end of each antenna to measure the system temperature has not been implemented. To calibrate the gains of each individual antenna, the system temperature T_{sys} is assumed to be sum of various components:

$$T_{sys} = T_r + T_a + T_{sky} \quad (3.2)$$

$$T_{sky} = 3 + 20(408/\nu)^{2.75} \quad (3.3)$$

where T_r is the receiver temperature, T_a is the antenna temperature, T_{sky} is the sky temperature and ν is the observed frequency. At each individual frequency, T_r , and T_a are assumed to be independent of the pointed position⁴. However, because of the Galactic diffuse radio emission, the sky temperature can vary greatly from one position to another, with T_{sky} being higher in the galactic plane. The gain by system temperature in units of K.Jy^{-1} used to calibrate the flux densities of the data, is based on the measurement T_{sys} at the position of the flux density calibrator. If T'_{sys} is the system temperature at the position of the field, then an overall multiplicative bias T_{sys}/T'_{sys} is introduced on the flux density estimates at the location of the field. The flux density calibrator 3C48 that we have used is situated at $b = 133.96^\circ$ and $l = -28.71^\circ$ (in Galactic coordinates), whereas the field is centered around $l \sim 173^\circ$ and $b \sim -57^\circ$. Using the Haslam et al. (1982) all-sky radio maps at 408 MHz, that have a resolution of 0.85° , we estimate using Eq. 3.3 that the flux densities need to be corrected by $\sim -2\%$ at 610 MHz and $\sim -18\%$ at 240 MHz. We have corrected for these overall offsets in the final source list.

In the case of resolved sources, calculating the integrated flux density by summing the individual Gaussian fitted flux density components produces a bias towards lower fluxes as compared to the real integrated flux density. Instead, following Tasse et al. (2006) we estimate the flux densities at both 240 and 610 MHz by summing the pixel values in $60''$ diameter apertures centered at the position of the individual Gaussian components. If S_{pix} is the flux density thereby computed, then $S_{pix} = \Sigma \times 4 \ln 2 / (\pi \cdot FWHM)$, and $\sigma_{pix} = N_{pix} \sigma_{loc}$, where Σ is the sum of the pixels inside the aperture, N_{pix} is the number of pixel over which the summation is done, σ_{loc} is the local noise at the location of the source and $FWHM$ is the Full Width at Half Maximum of the restoring beam in pixels. Because this flux density estimator does not use any *a priori* knowledge on the restoring beam shape, the error bars associated to the integrated flux density estimate are much bigger than those associated with the Gaussian fitting method. Given the values and error bars estimates for the two methods, we consider the pixel-based estimate of the integrated flux density only when the difference is significant at the 2σ level⁵.

Finally, because we have used the secondary calibrator 0116 – 208 to calibrate the gains of individual antennas, we quadratically add a standard 10% overall flux density scale error to the noise-based Gaussian fitting uncertainties. This value takes into account any systematic error in the GMRT measurement, like small elevation dependant errors (for a more detailed discussion see Mohan et al. 2001; Chandra et al. 2004).

⁴see <http://www.gmrt.ncra.tifr.res.in> for more information on the estimation of each of these temperature

⁵With σ being computed as $\sigma = (S_{pix} - S_{gauss}) / \sqrt{\sigma_{pix}^2 + \sigma_{gauss}^2}$

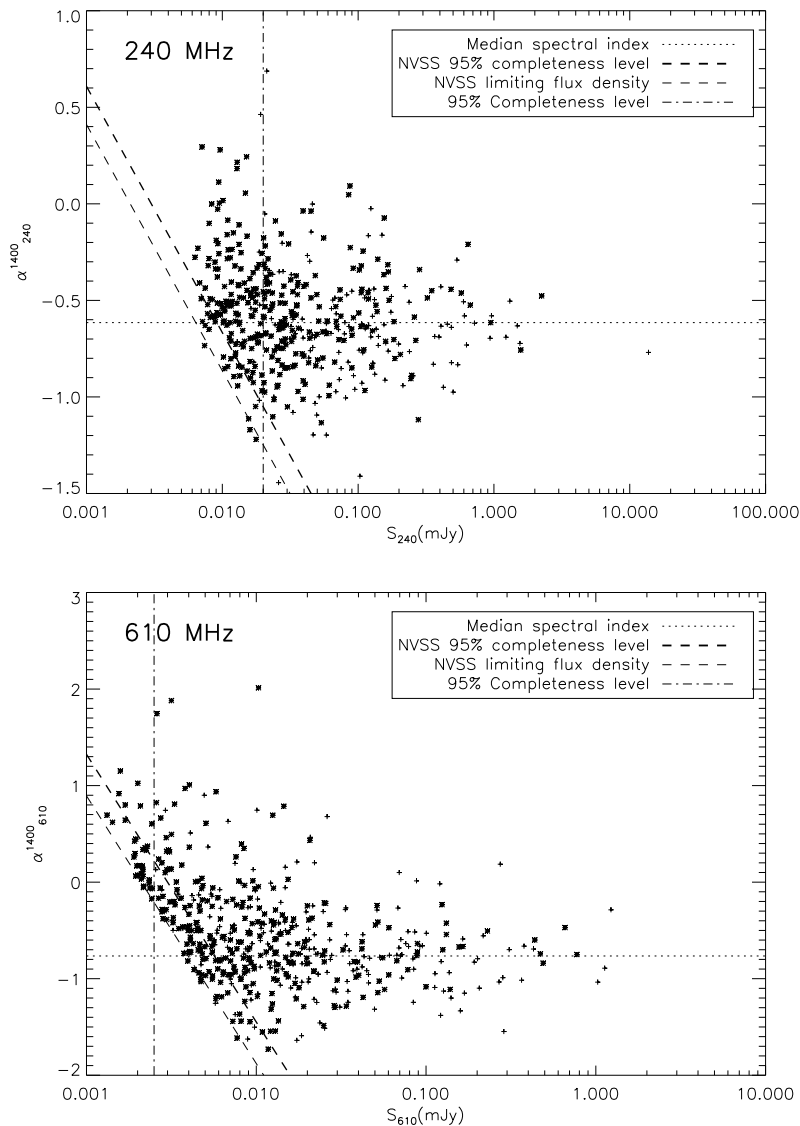


Figure 3.4: The spectral index distribution at 240 and 610 MHz, derived from flux density comparison with NVSS. The resolution differences at both frequencies (14.7'' and 6.5'' respectively as compared to 45'' for NVSS) leads to an overestimate of the spectral indices for extended and resolved sources, as we may miss a significant fraction of the total flux density. Simple crosses stand for the resolved sources, whereas thick stars are the point-like sources, where no extended emission is expected to bias the spectral index estimate toward higher values. On both panels, the vertical dash-dotted line indicates the 95% completeness level. On both graphs, horizontal dotted lines indicate the median spectral index value derived from subsamples having integrated flux density $S_{240}^{int} > 63$ mJy and $S_{610}^{int} > 30$ mJy, corresponding to a limiting integrated flux density at 325 MHz of $S_{325}^{int} > 50$ mJy. Diagonal dashed lines indicate the bias introduced by the limiting flux density and the 95% completeness limit (thick dashed) of NVSS respectively (Condon et al. 1998). We have given the sources that are not detected in the NVSS, a spectral index upper limit. These points are not plotted, but lie along the 95% completeness limit of NVSS.

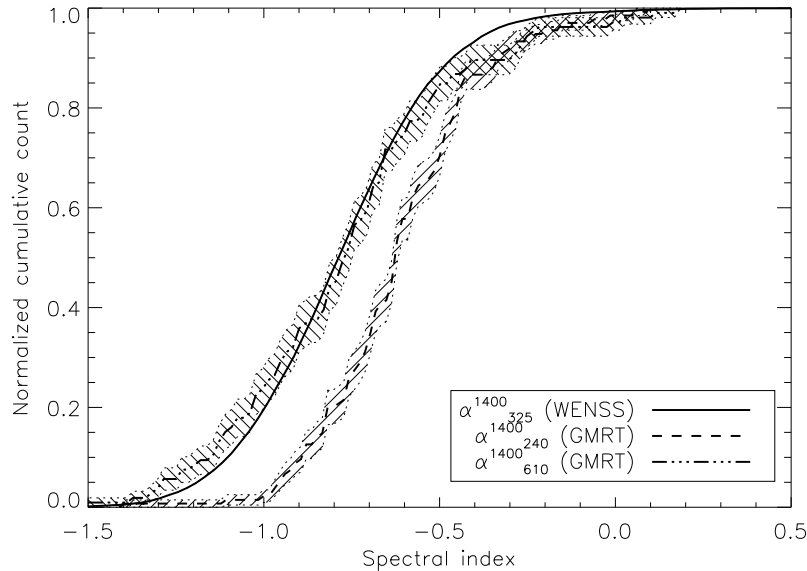


Figure 3.5: The distribution of the spectral index α_{240}^{1400} and α_{610}^{1400} derived from flux comparison between our surveys flux density estimates at 240 and 610 MHz, and the NVSS at 1.4 GHz. The full line stands for the spectral index distribution α_{325}^{1400} of the radio sources in the WENSS radio survey (De Breuck et al. 2000). To match the 5σ flux density limit of WENSS, we have applied a flux density cut $S_{240}^{int} > 63$ mJy and $S_{610}^{int} > 30$ mJy at 240 MHz and 610 MHz respectively.

3.5 RESULTS

The main characteristics of the 240 and 610 MHz surveys are given in Table 3.2. The associated source lists are given in Tab. B1⁶ and B2⁶ respectively. Contour plots are shown in Fig. A1 at 240 MHz and in Fig. A2 at 610 MHz for the brightest extended sources.

Table 3.2: Main results in both 240 and 610 MHz bands.

Frequency	240 MHz	610 MHz
Resolution	14.7''	6.5''
Area (degree ²)	18.0	12.7
Rms (mJy/Beam)	~ 2.5	~ 0.3
Single sources ‘‘S’’	388	592
Single unresolved	96%	75%
Multiple sources ‘‘M’’	79	175

Of the sources detected at 325 MHz (Tasse et al. 2006), ~ 50% and ~ 67% are detected at 240 and 610 MHz respectively. The fraction of the 325 MHz area surveyed at 240 and 610 MHz, is ~ 93% and ~ 78% respectively. Of the sources detected at 325 MHz and covered by the 240 and 610 MHz surveys, ~ 55% and ~ 80% are detected at 240 and 610 MHz respectively. Although, the

⁶ Available in the electronic version of this paper only.

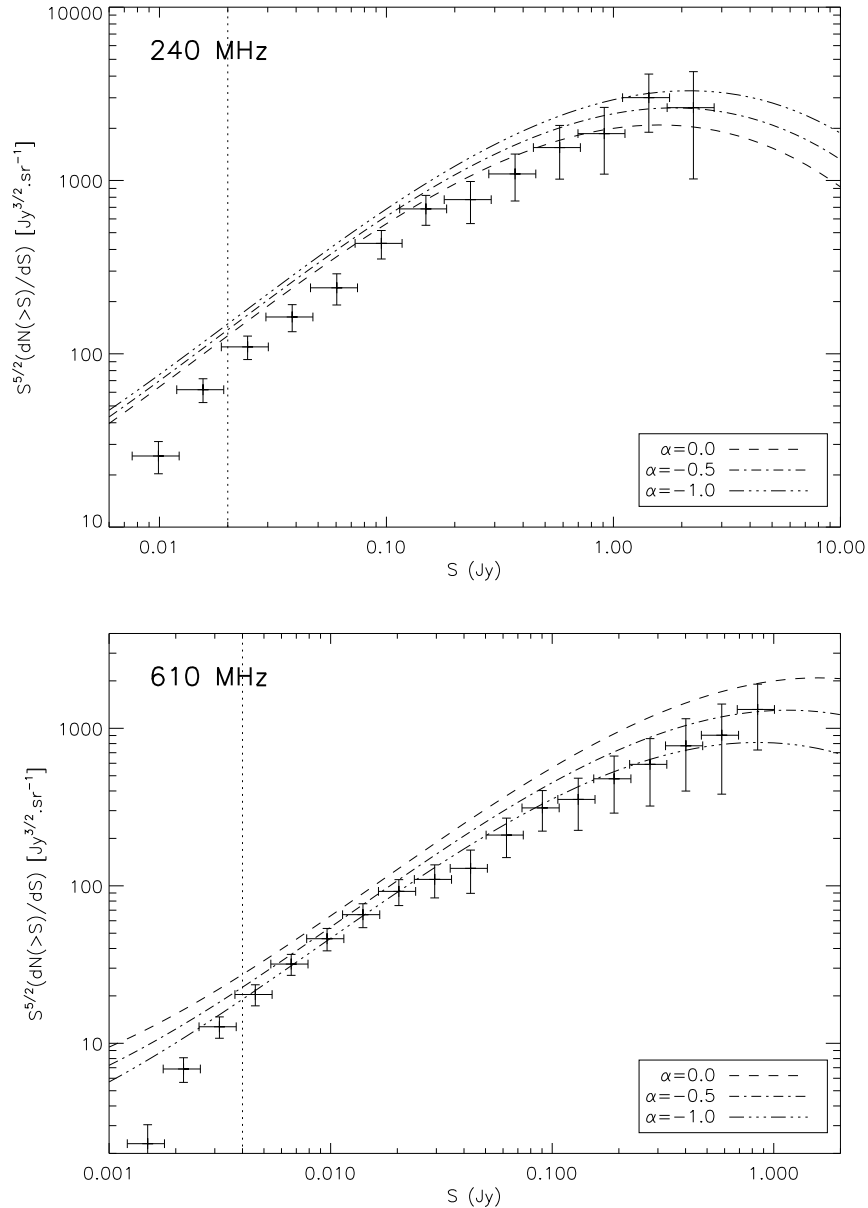


Figure 3.6: Both panel show the Euclidean normalized differential source count at 240 MHz (top panel), and 610 MHz (bottom panel). The curves shows the extrapolated Wieringa (1991) 325 MHz differential source count, assuming different spectral index values. The vertical dotted line show the 95% completeness level.

610 MHz survey is on average deeper by a factor of ~ 1.5 than the 325 MHz survey (Fig. 3.3), the fact that we miss $\sim 20\%$ of the 325 MHz sources at 610 MHz is explainable because the 325 MHz sources that are missed at 610 MHz are the faintest ones. In order to check for the consistency of the amount of the 325 MHz sources detected at 240 and 610 MHz, we first generate a 325 MHz catalog in which each source is given a random flux density value according to their measured flux density and associated error bars. Then each of these source is given a random spectral index

following a normal law with mean value $\langle\alpha\rangle = -0.8$ and dispersion $\sigma(\alpha) = 0.24$ (De Breuck et al. 2000). We extrapolate the flux density of each of these 325 MHz radio source to 240 and 610 MHz, and add up the local noise corresponding to their individual position at 240 and 610 MHz. From these simulated 240 and 610 MHz catalog, we extract the respective source lists using a $5\sigma_{local}$ cut as we did on the actual maps (Sec. 3.3). We observe that such a 325 MHz population would lead to the detection of $\sim 55\%$ and $\sim 76\%$ of the of 325 MHz sources at 240 and 610 MHz respectively, in agreement with our observations.

Fig. 3.4 shows the spectral index distribution derived from the flux density comparison with NVSS. The sources without a 1.4 GHz counterpart have been given an upper limit on their spectral index, using the NVSS 95% completeness limit at 5σ . At both frequencies the resolutions being $14.7''$ and $6.5''$ are smaller than the $45''$ resolution of NVSS (Condon et al. 1998). Such differences make the estimation of spectral index to be less reliable for extended radio emission.

In order to compare the spectral index distribution of the 240 and 610 MHz sources to the spectral index distribution of the WENSS 325 MHz radio sources (Rengelink et al. 1997), we assume a mean spectral index of $\alpha_{325}^{1400} = -0.8$ (De Breuck et al. 2000). We extrapolate the limiting integrated flux density of WENSS being $S_{325}^{lim} = 50$ mJy to 240 and 610 MHz, which makes $S_{240}^{lim} = 63$ mJy and $S_{610}^{lim} = 30$ mJy. We derive median spectral index values of $\alpha_{240}^{1400} = -0.62$ and $\alpha_{610}^{1400} = -0.76$. Fig. 3.5 shows the spectral index distribution of the subsamples defined above ($S_{240} = 65$ mJy and $S_{610} > 30$ mJy) to the WENSS spectral index distribution at 325 MHz (De Breuck et al. 2000). At 240 MHz, the spectral index distribution has the same width but is shifted towards shallower spectral indices. This is likely to be due to the combination of the resolution differences ($14.7''$ at 240 MHz, against $\sim 55''$ for WENSS), and the natural tendency of radio sources to be synchrotron self absorbed at low frequency. At 610 MHz, we find close agreement in the distribution centroid, but we note an excess of flat spectrum sources, whose presence might be due to the resolution difference being even bigger, and the shallower effective depth of WENSS to flat spectrum sources.

Below the corresponding flux density limit of WENSS, we detect a few $\alpha > 0$ inverted spectral index for unresolved sources at rather small flux densities (Fig. 3.4). This is expected when synchrotron self absorption occurs in compact radio sources such as compact steep spectrum (CSS) and gigahertz peaked spectrum sources (GPS).

Fig. 3.6 shows the Euclidean normalized differential source counts at 240 and 610 MHz as well as the WENSS differential source counts extrapolated from from 325 MHz (Wieringa 1991). In principle, in order to derive reliable estimates of the differential counts over the whole flux density range, biases and incompleteness correction have to be taken into account: (i) the incompleteness introduced by the variation of the complete area with flux density (Fig. 3.3) (ii) the incompleteness due to the efficiency of the source finding algorithm SAD that decreases with the signal-to-noise ratio and (iii) the bias introduced by SAD flux density overestimation at low flux densities (see Seymour et al. 2005, for a detailed discussion on these biases). All these biases occur at low flux densities. We do not correct for any of these but plot the 95% completeness level estimated from the noise maps. Above this flux density, the differential counts are reliable. At 240 MHz, the differential counts agree with the WENSS differential counts until a flux density level of ~ 100 mJy. At lower fluxes, the factor of ~ 2 difference with the expected values could be due to cosmic variance: at 325 MHz in the same field the differential source count shows the same offset with the Wieringa (1991) differential source count at $\gtrsim 20$ mJy (Tasse et al. 2006). At 610

MHz, the Euclidean normalized differential source counts follow the Wieringa (1991) extrapolated differential source counts, consistently with a mean spectral index value of $\alpha \sim -1$.

3.6 RADIO SPECTRA ANALYSIS

3.6.1 The multi frequency radio sample

For each individual source, when comparing the flux density estimates obtained at the different frequencies, several issues have to be considered.

First, the sky plane has been imaged using different instruments, at different frequencies. In each frequency band, the uv plane coverage can be significantly different from one observation to another. This can lead to a variation in the flux estimate, shorter baselines being sensitive to larger angular scale radio emission. After the RFI flagging step, the shortest baselines in the uv plane are $\sim 0.3 \text{ k}\lambda$ at 240 and 610 MHz, $\sim 0.5 \text{ k}\lambda$ at 325 MHz, $0.2 \text{ k}\lambda$ at 74 MHz, and $\sim 0.05 \text{ k}\lambda$ at 1400 MHz, corresponding to angular scales of $\sim 11.5'$, $6.9'$, $20'$ and $\sim 1.2^\circ$ respectively. The largest extended radio emission detected in the XMM-LSS field is the $\sim 1'$ radio halo candidate described in Tasse et al. (2006) and is smaller than the maximum angular scale detectable at 325 MHz. This effect is therefore assumed to have a negligible impact on the integrated flux density estimates.

Secondly, through the various frequency bands, the size of the synthesized beam varies from $6.5''$ at 610 MHz to $45''$ at 1.4 GHz. As described in Sec. 3.4.2, since the Gaussian fitting method may miss a significant part of the extended flux in some cases, we also extract the integrated flux density based on pixel values within a $60''$ diameter aperture (see Sec. 3.4.2). This second estimation corrects for that effect.

Finally, the overall flux density calibration is reliable on the level of $\sim 5\%$ for the VLA and $\sim 10\%$ for the GMRT. These systematics have been taken into account within the error bar calculation. We discuss the effect of these systematics on the radio spectra fits in Sec. 3.6.4.

In order to study the shape of the low frequency radio spectra, we build a 5-frequency band catalog on the basis of the source lists at 74, 240, 325, 610, and 1400 MHz (Tasse et al. 2006; Condon et al. 1998), by associating their Gaussian fitted components that are closer than $60''$. Considering the sum of all the number density of these various radio surveys, this radius makes the probability of two components to be associated by mistake to be less than 2%.

3.6.2 Comparison with VLA data

For testing the 610 MHz source list flux densities, we select the ones being detected at 325 and 1400 MHz. In order to be not affected by the angular extend of the radio sources in any way, we select only the sources being unresolved in all frequency bands. We define the spectral curvature as $\alpha_{325}^{610} - \alpha_{610}^{1400}$. The spectral curvature expresses whether the synchrotron slope shows any difference on the two sides of the 610 MHz point. In Fig. 3.7 we plot the spectral curvature as a function of the flux density at 610 MHz. The mean spectral curvature value is $\langle \alpha_{325}^{610} - \alpha_{610}^{1400} \rangle = -0.15$, becomes ~ 0 if we correct the overall flux density scale on the level of 6%, in agreement with the $\sim 10\%$ error on the flux scale used to calculate the error bars. At low fluxes though, we see the mean spectral curvature to reach negative values of ~ -0.8 , which is due to a selection effect: we

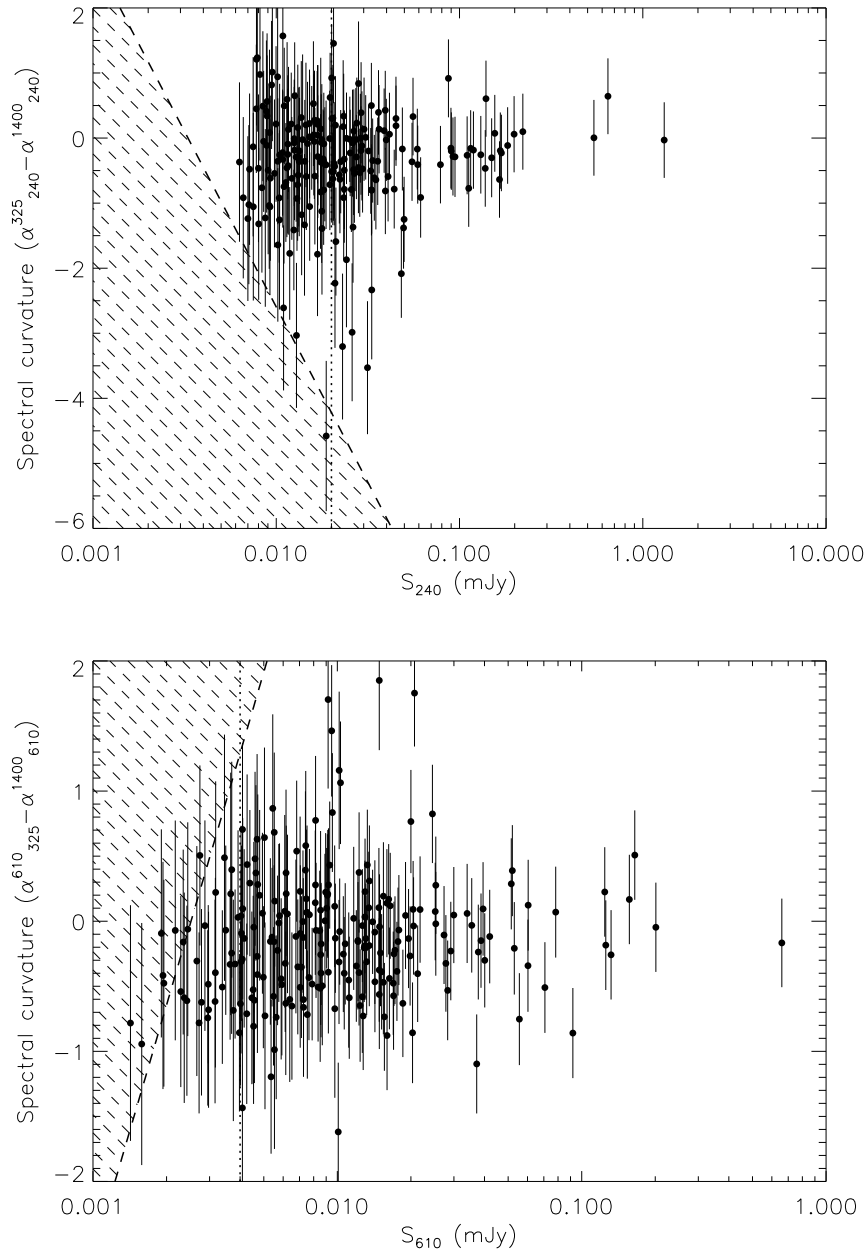


Figure 3.7: These plots show the consistency of the flux density measurements of the VLA and the GMRT instruments. Top panel: for the sources detected at 240, 325, and 1400 MHz, the spectral curvature $\alpha_{240}^{325} - \alpha_{240}^{1400}$ is plotted as a function of the flux density at 240 MHz. The overall shift is explainable in term of flux density calibration being accurate on the level of $\sim 10\%$ on true spectral curvature. The bottom panel similarly shows the spectral curvature $\alpha_{610}^{325} - \alpha_{610}^{1400}$ as a function of the 610 MHz flux density. Because each survey is flux density limited, a range of spectral curvature is *not* reachable at a given 240 or 610 MHz flux density level (dashed area). This explains the apparent decreasing of the spectral curvature at low 610 MHz flux densities. Some points stand with the dashed area because the flux density limit is not homogeneous in the radio maps, both at 325 and 1400 MHz. Vertical dotted lines stand for the 95% completeness limit.

have selected the point-like 610 MHz sources being detected at both 325 and 1400. Therefore at a given 610 MHz flux density, and given the 325 and 1400 MHz flux density limit (Fig. 3.3), a range of spectral curvature values is not observable. If we compute the observable spectral curvature range as a function of the 610 MHz flux density, we clearly see how biased the spectral curvature measurement is for faint 610 MHz sources.

We carry out the same analysis at 240 MHz (Fig. 3.7, left panel). The mean spectral curvature value is $\langle \alpha_{240}^{325} - \alpha_{240}^{1400} \rangle = -0.11$ corresponding to the 240 MHz flux density being overestimated. Nevertheless, a correction of the overall flux density scale on the level of $\sim 4\%$ brings the averaged spectral curvature value to ~ 0 , in agreement with the 10% error on the gain calibration. The agreement between flux density estimates at 240, 325, and 1400 MHz seems to hold until the 5σ level although we note the presence of sources showing very low spectral curvature values. The bias introduced by the different flux density limits at 325 and 1400 MHz do not seem to have much influence. That is because assuming a spectral index of -0.8 the 240 MHz flux density limit is higher than the ones at 325 and 1400 MHz by a factor of ~ 2 (see Fig. 3.3).

3.6.3 Spectral fits

Theoretically, the classical power law spectrum of synchrotron emission is understood as a zero aged relativistic electron population, having a power-law energy distribution, and being optically thin to its own radiation (Kardashev 1962). Deviation from the power law occurs with (1) a low frequency turnover due to synchrotron self absorption at low frequency and (2) a steepening at high frequencies due to particle energy losses. When the major fraction of the flux density is emitted by one, single electron population the radio spectra are well approximated by a simple synchrotron radiation model, including self absorption and spectral ageing features. The presence of different synchrotron emitting electron population will make the integrated radio spectra significantly deviate from the simple synchrotron spectrum. For example FRI radio sources (Fanaroff & Riley 1974) show a compact flat spectrum core and steep spectrum extended lobes.

For a crude modeling of the synchrotron emission, we approximate the integrated radio spectra to be emitted by a single electron population, following the continuous injection model described above. It is well known that under these assumptions the synchrotron spectrum $S(\nu)$ has a standard shape (Kardashev 1962), modified by low frequency self-absorption (Pacholczyk 1970) as follows:

$$S(\nu) = S_0(\nu/\nu_1)^{5/2-\alpha}(1 - e^{-(\nu/\nu_1)^{\alpha-5/2}})S_{aged} \quad (3.4)$$

$$S_{aged} = \begin{cases} \nu^\alpha & : \nu < \nu_c \\ \nu^{\alpha-1/2} & : \nu > \nu_c \end{cases} \quad (3.5)$$

where S_0 is a normalization factor, ν_1 is the self absorption frequency break, α is the zero aged spectral index in the transparent frequency range and ν_c is the break frequency above which the power-law breaks to be spectrally aged. Our free parameter space for the spectral fit is composed of $\{S_0, \alpha, \nu_1, \nu_c\}$. The initial condition of the fitting routine are set on a $15 \times 21 \times 21 \times 21$ parameter grid. The ν_1 and ν_c initial condition ranges are ~ 50 -250 MHz and ~ 300 -2000 MHz respectively whereas the initial condition ranges for S_0 and α depend on individual flux density levels and error bars.

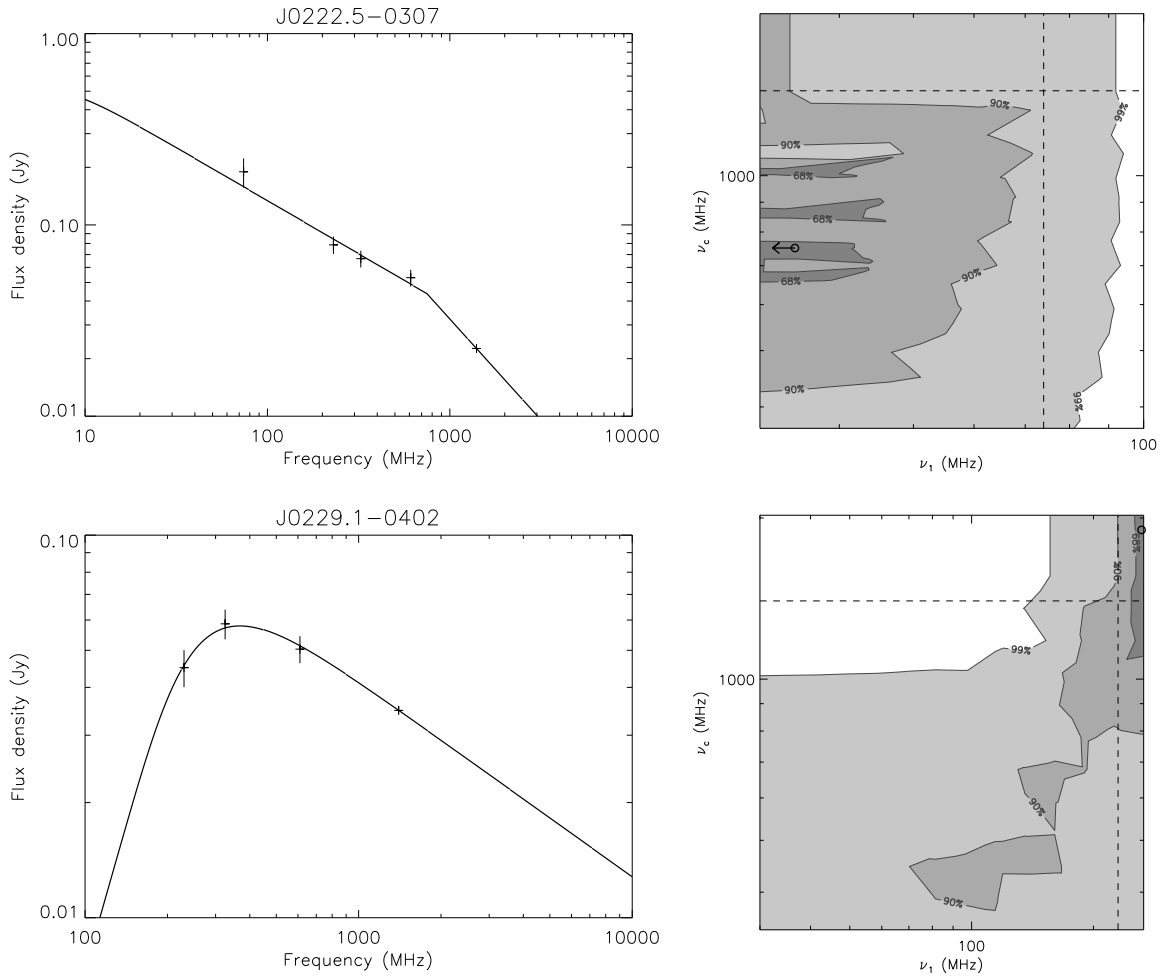


Figure 3.8: Examples of two radio sources, showing spectral ageing (top) and self absorption signatures (bottom). Left panels show the flux density measurement at 74, 240, 325, 610 and 1400 MHz together with their associated error bars. The full line shows the best fit spectrum described by equations 3.4 and 3.5. The right panels show the dependence of the χ^2 on the parameters ν_1 and ν_c , that are used for the radio spectral type classification. The parameters corresponding to the best fit is marked with a thick open circle. The different contour lines show the $\chi^2_{min} + 1$, $\chi^2_{min} + 2.71$ and $\chi^2_{min} + 6.63$ levels corresponding to the 68%, 90% and 99% confidence intervals respectively (Avni 1976). The vertical and horizontal dashed lines correspond to the lowest and highest available frequency respectively. In the final fitted parameters table, we consider the best fit parameter together with the 68% confidence interval covering also the degenerated solution. In these examples, based on the 68% confidence interval for ν_1 and ν_c , we can see the model fits the flux density points only if spectral ageing and self-absorption are present in the first and second case respectively.

3.6.4 Subsample definition

Because we want to build samples of sources showing clear signatures of spectral ageing and/or self-absorption, we select in the multi radio frequency catalog described in Sec. 3.6.1 the objects having been detected at least at 240, 325, 610, and 1400 MHz, which makes the total number of fitted sources to be 318 (38% of the sources detected at 325 MHz). When the object is not detected

at 74 MHz, we have used the flux limit at 74 MHz to constrain the fitting parameters.

In order to reject the objects that could not be well fitted we choose a reduced⁷ χ^2 cut above which the model described with Eq. 3.5 is assumed to be irrelevant. Fig. 3.9 shows that if we select the spectral fits with an associated $\chi^2_{reduced} < 4.3$ then the observed $\chi^2_{reduced}$ distribution follows the theoretical distribution⁸, meaning we can consider the model to be relevant for these objects. We visually inspected the radio images of the objects having an associated $\chi^2_{reduced} > 4.3$ ($\sim 25\%$ of the selected sample). They are found to be mainly resolved, having a few to many radio emitting components. For these objects, the assumptions of a single synchrotron emitting electron population (Sec. 3.6.3) is wrong, and the simple model we have used is most probably irrelevant. In order to be conservative, we list the fitted parameters for all objects in Tab. B3⁶ (including the $\chi^2_{reduced} > 4.3$ objects).

The minimum χ^2 is recorded in the 4-parameter space, and the errors on the fitted parameters are derived from the 68% confidence interval calculated at $\chi^2_{min} + 1$ (Avni 1976). In the case of degenerated solutions, instead of considering the list of all the χ^2 minima with their respective associated error bars, only the best fit parameters are considered, and the error bar associated with them is the interval including all the multiple χ^2 minima (See Fig. 3.8). This method allows us to define a robust sample of sources having detected self absorption of spectral ageing feature. A source is considered to be showing self absorption if and only if the 68% confidence interval of ν_1 falls within the frequency range $[\nu_{low}, 1.4 \text{ GHz}]^9$ probed by our survey, meaning good solutions cannot be found without observed self absorption. We proceed the same way for the ν_c free parameter. This allows us to define robust subsamples of radio spectra showing self absorption, or spectral ageing or both.

The best fit parameters with their associated 68% confidence interval as well as their classification appear in table B3⁶.

On the subsample of fitted spectra, $\sim 68\%$ are found to show no significant signs of spectral ageing or self absorption, $\sim 6\%$ show self absorption only, $\sim 26\%$ show spectral ageing only, and none show both. It has been suggested in the past that compact steep spectrum (CSS) and gigahertz peaked spectrum (GPS) may correspond to the early stages of evolution of classical FRI and FRII radio sources, consistent with the observed subarcsecond angular size of CSS and GPS radio sources (Fanti et al. 1995; O’Dea & Baum 1997; Snellen et al. 2000). Conversely, the radio sources showing spectral ageing in their radio spectra are the ones in which no high energy electron is injected into the radio emitting lobes. These radio sources should correspond to the latest evolutionary stage of radio sources. In order to test the consistency of the three radio spectral classes¹⁰, we compare their respective angular size distribution. As the resolution at 325 and 610 MHz is higher, we estimate the angular size of the objects in the sample based on the Gaussian fitting components positions and their elongation deconvolved from the beam size at these two frequencies. Fig. 3.10 shows the cumulative distribution of the angular sizes for the three subsample. $\sim 60\%$ of the steep spectrum sources are unresolved, compared to $\sim 40\%$

⁷To calculate the reduced χ^2 we have used the formula $\chi^2_{reduced} = \chi^2_{min}/(n - p)$ where n is the number of data points and p is the number of parameter in the model. The value of p depends on whether the parameters ν_c and ν_1 of Eq. 3.5 have to be used to fit the radio spectra. For example if we use a single power law then $p = 2$

⁸The reduced χ^2 distribution theoretically follows a normal distribution with one degree of freedom.

⁹Because we have the objects detected in at least 4 bands, the lower available frequency ν_{low} value depends on whether the object is detected at 74 MHz. In all cases, if this is not the case then $\nu_{low} = 240 \text{ MHz}$.

¹⁰Steep spectrum, Self absorbed and Spectrally aged

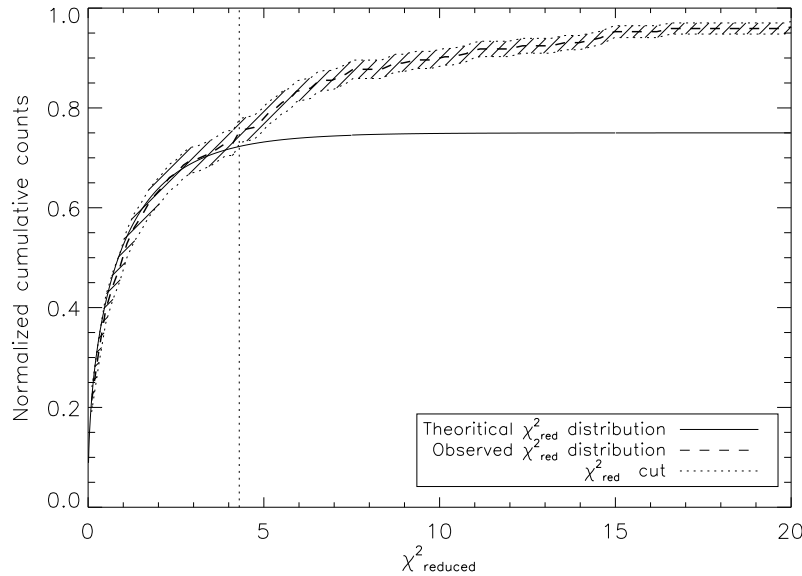


Figure 3.9: The cumulative distribution of the reduced χ^2 . Choosing a χ^2_{red} cut of 4.3, we see that $\sim 75\%$ of the population behaves like the adjusted theoretical χ^2_{red} distribution (black line).

and $\sim 80\%$ for the sources showing signatures of spectral ageing and self-absorption respectively. Consistently, the distribution of spectrally aged sources is clearly biased towards sources having larger angular sizes than the single power law sources by a factor of $\sim 1.5 - 2$. In the subsample of sources showing signs of self absorption, we note the presence of three sources having large angular diameters $\gtrsim 10''$ (J0217.0-0308, J0218.3-0403, J0219.7-0448)¹¹.

In principle we should be allowed to compare a parameter distribution only for a homogeneously selected sample. Nevertheless, we have built subsamples of radio sources based on their radio spectral shape, selecting the objects that are detected at 240, 325, 610, and 1400 MHz at least, the various surveys having different flux density limits (see Fig. 3.3). For example let us consider a source at a given redshift and 325 MHz luminosity: in the observer frame, a self absorbed source is more likely not to appear in the subsamples because its 240 MHz flux density may be below the flux density limit of the associated survey. A similar effect acts on the spectrally aged subsample. These preliminary results on the angular size distribution in the various radio source classes have to be taken with caution because selection effect may play an important role.

3.7 CONCLUSION AND FUTURE WORK

We have imaged the low frequency 325 MHz counterpart (Tasse et al. 2006) of the XMM-LSS field at 240 and 610 MHz with the GMRT, leading to the detection of 467 and 667 radio sources

¹¹Detailed inspection of the radio images at 240, 325 and 610 MHz, show that the extended source J0217.0-0308 has its 240 MHz position in between two facets, likely making the flux to be badly estimated and the source to be classified as self absorbed. J0218.3-0403 and J0219.7-0448 have an FRI-like morphology, suggesting the flux density of the central component might dominates the overall flux density emission. Self absorption might therefore happen within the central core of these sources although they are measured to be extended.

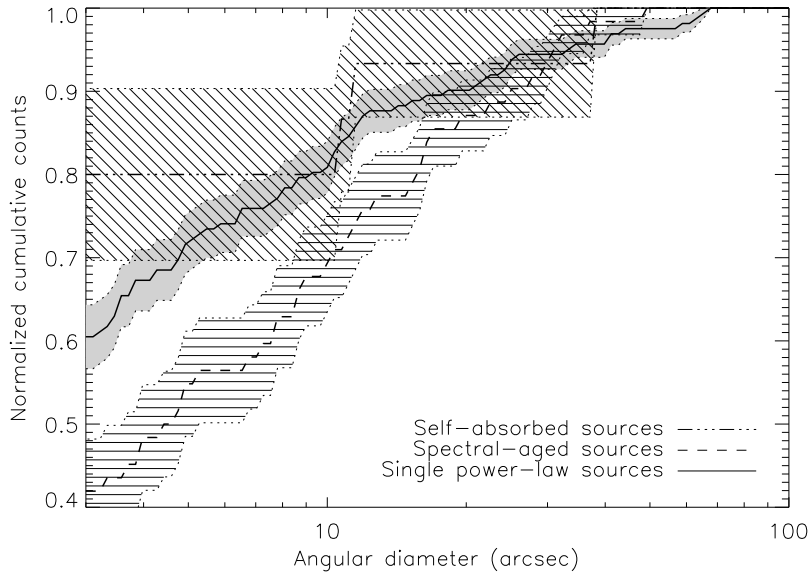


Figure 3.10: The angular diameter of the radio sources classified as spectrally aged or self absorbed. Spectrally aged sources appear larger on average than single power law sources and self-absorbed sources.

respectively. The GMRT survey covers 18.0 degree^2 at 240 MHz and 12.7 degree^2 at 610 MHz, with average flux density limits of 12.5 and 1.5 mJy/Beam (5σ) respectively. We have corrected for the various systematic errors introduced by the instrument and the data reduction procedure on both astrometry and flux density scale. Comparison between the catalogs at 240 and 610 MHz with other datasets at 325, and 1400 MHz show good agreement, although the spectral index distribution suggests a spectral index flattening below 240 MHz.

We have fitted a simple continuous injection synchrotron emission model to the flux density measured at 74 and 325 MHz by Tasse et al. (2006), 240 and 610 MHz presented in this paper, and 1.4 GHz (NVSS, Condon et al. 1998). On the basis of fitted parameters and error bars estimates, we define a sample of radio sources showing signatures of self absorption or spectral ageing feature in their radio spectra. Consistent with other studies suggesting a link between radio spectra shape and radio source evolution, we found that spectrally aged sources have larger angular sizes, whereas sources showing self-absorption are smaller.

In the near future, on the basis of the available X-ray and optical data we will study the effect of environment on the fundamental properties of the various classes of radio sources.

ACKNOWLEDGMENTS

We thank the staff of the GMRT that made these observations possible. GMRT is run by the National Center for Radio Astrophysics of the Tata Institute of Fundamental Research. We thank Ishwara Chandra, Walter Jaffe, Dave Green, Niruj Mohan Ramanujam, Amitesch Omar, Ignas Snellen for useful discussion on the data reduction and analysis.

REFERENCES

- Avni, Y. 1976, *ApJ*, 210, 642
- Becker, R. H., White, R. L., & Helfand, D. J. 1995, *ApJ*, 450, 559
- Chandra, P., Ray, A., & Bhatnagar, S. 2004, *ApJ*, 612, 974
- Cohen, A. S., Röttgering, H. J. A., Kassim, N. E., et al. 2003, *ApJ*, 591, 640
- Condon, J. J. 1997, *PASP*, 109, 166
- Condon, J. J., Cotton, W. D., Greisen, E. W., et al. 1998, *AJ*, 115, 1693
- De Breuck, C., van Breugel, W., Röttgering, H. J. A., & Miley, G. 2000, *A&AS*, 143, 303
- Fanaroff, B. L. & Riley, J. M. 1974, *MNRAS*, 167, 31P
- Fanti, C., Fanti, R., Dallacasa, D., et al. 1995, *A&A*, 302, 317
- Haslam, C. G. T., Salter, C. J., Stoffel, H., & Wilson, W. E. 1982, *A&AS*, 47, 1
- Kardashev, N. S. 1962, *Soviet Astronomy*, 6, 317
- Lonsdale, C. J., Smith, H. E., Rowan-Robinson, M., et al. 2003, *PASP*, 115, 897
- Mohan, R., Dwarakanath, K. S., Srinivasan, G., & Chengalur, J. N. 2001, *Journal of Astrophysics and Astronomy*, 22, 35
- O'Dea, C. P. 1998, *PASP*, 110, 493
- O'Dea, C. P. & Baum, S. A. 1997, *AJ*, 113, 148
- Pacholczyk, A. G. 1970, *Radio astrophysics. Nonthermal processes in galactic and extragalactic sources* (Series of Books in Astronomy and Astrophysics, San Francisco: Freeman, 1970)
- Perley, R. A. 1999, in *ASP Conf. Ser. 180: Synthesis Imaging in Radio Astronomy II*, 383–+
- Pierre, M., Valtchanov, I., Altieri, B., et al. 2004, *Journal of Cosmology and Astro-Particle Physics*, 9, 11
- Rengelink, R. B., Tang, Y., de Bruyn, A. G., et al. 1997, *A&AS*, 124, 259
- Seymour, N., McHardy, I., Gunn, K., & Moss, D. 2005, in *The Dusty and Molecular Universe: A Prelude to Herschel and ALMA*, ed. A. Wilson, 323–324
- Snellen, I. A. G., Lehnert, M. D., Bremer, M. N., & Schilizzi, R. T. 2003, *MNRAS*, 342, 889
- Snellen, I. A. G., Schilizzi, R. T., Miley, G. K., et al. 2000, *MNRAS*, 319, 445
- Tasse, C., Cohen, A. S., Röttgering, H. J. A., et al. 2006, *A&A*, 456, 791
- Wieringa, M. H. 1991, Ph.D. Thesis

APPENDIX

A RADIO IMAGES

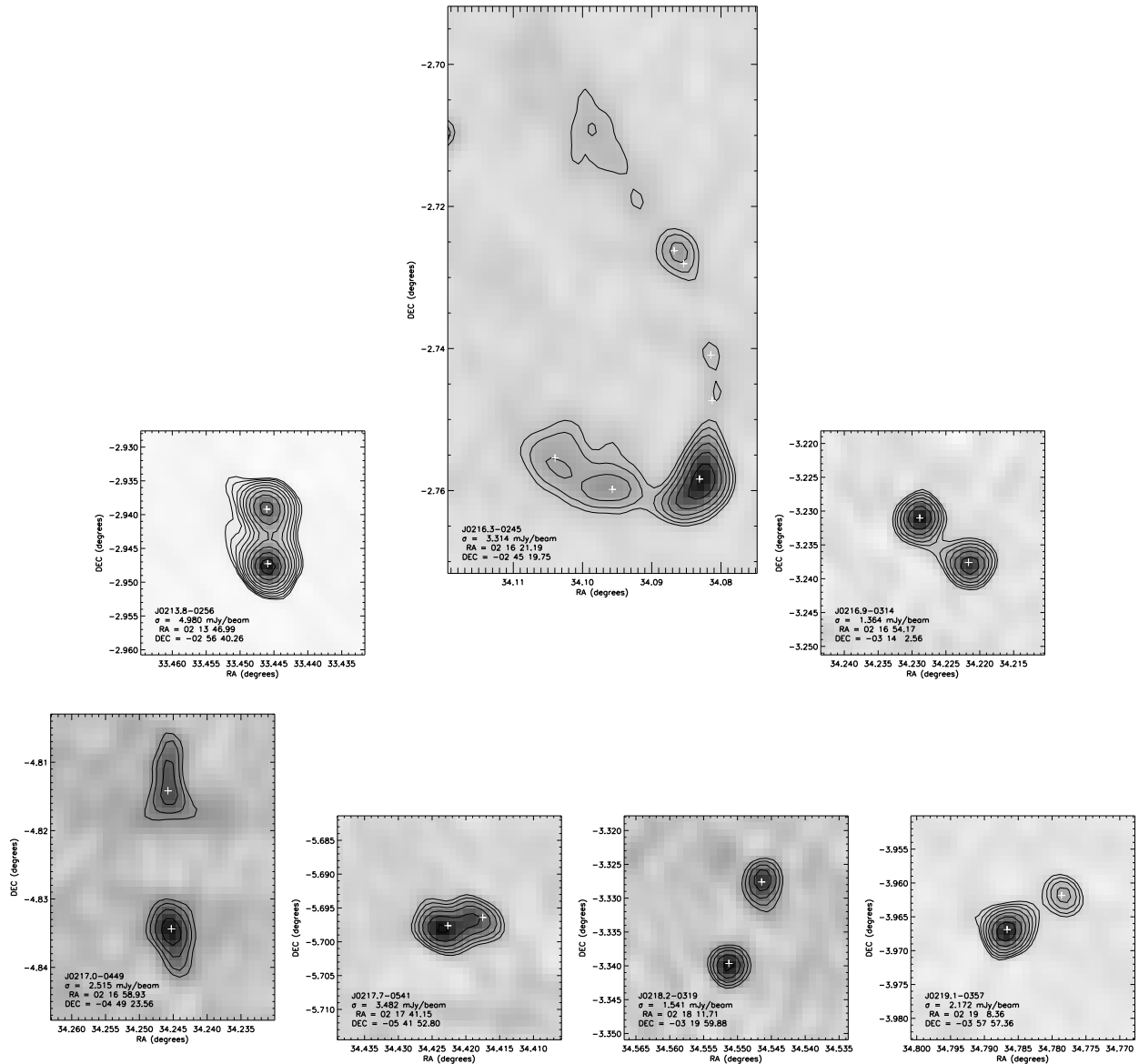


Figure A1: At 240 MHz, the 20 largest sources. Sorting order is increasing right ascension. Contours correspond to levels of $3\sigma \times (-1.4, -1, 1, 1.4, 2, 2.8, 4, 5.6, 8, 11, \dots)$ and grayscale is scaled from -3σ to the maximum value in the image. On the bottom-left corner of each image appears the name of the corresponding source in the source list, its flux weighted coordinate as well as the local noise level. The crosses are marking the Gaussian fitting components.

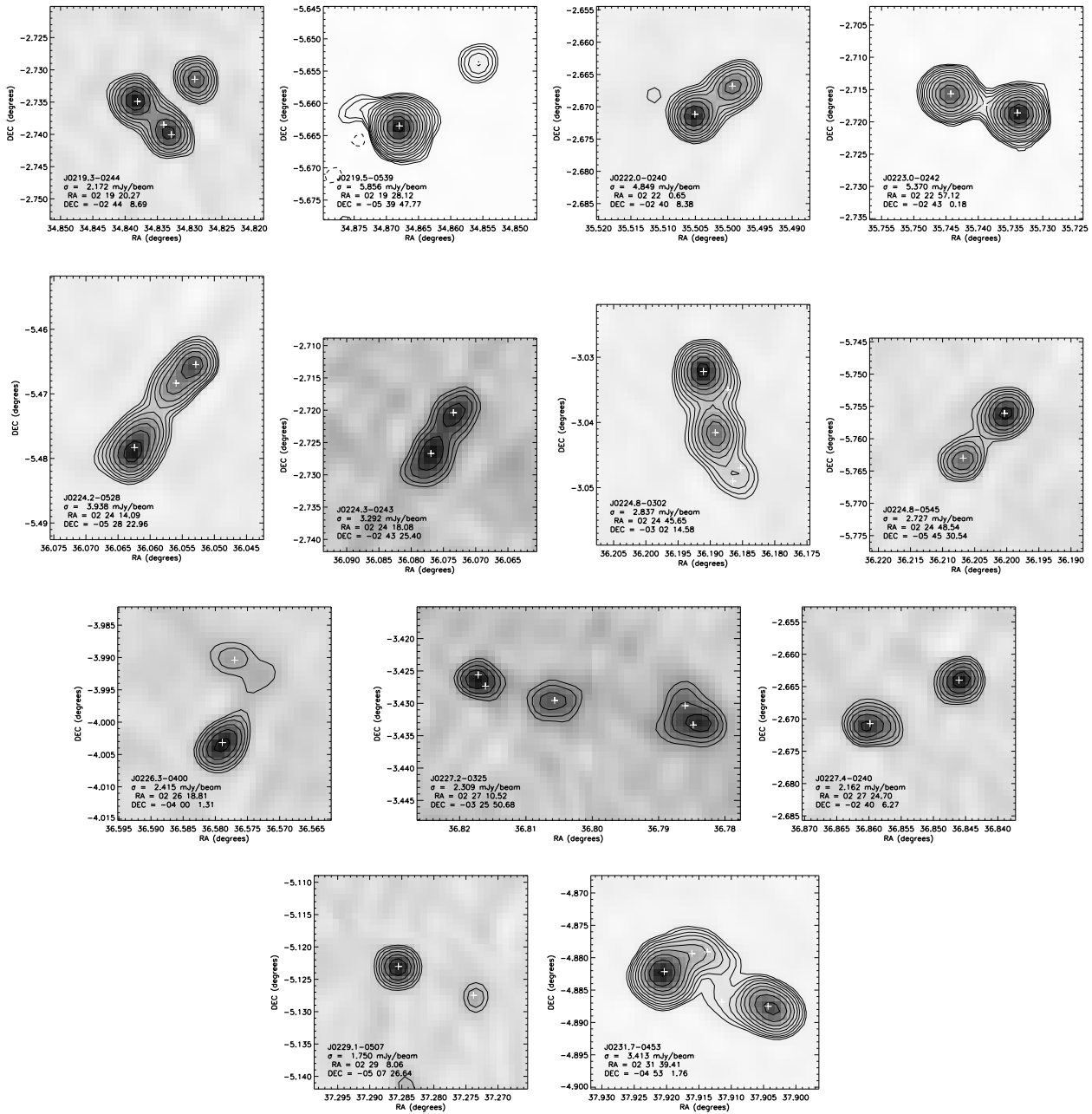


Figure A1: Continued.

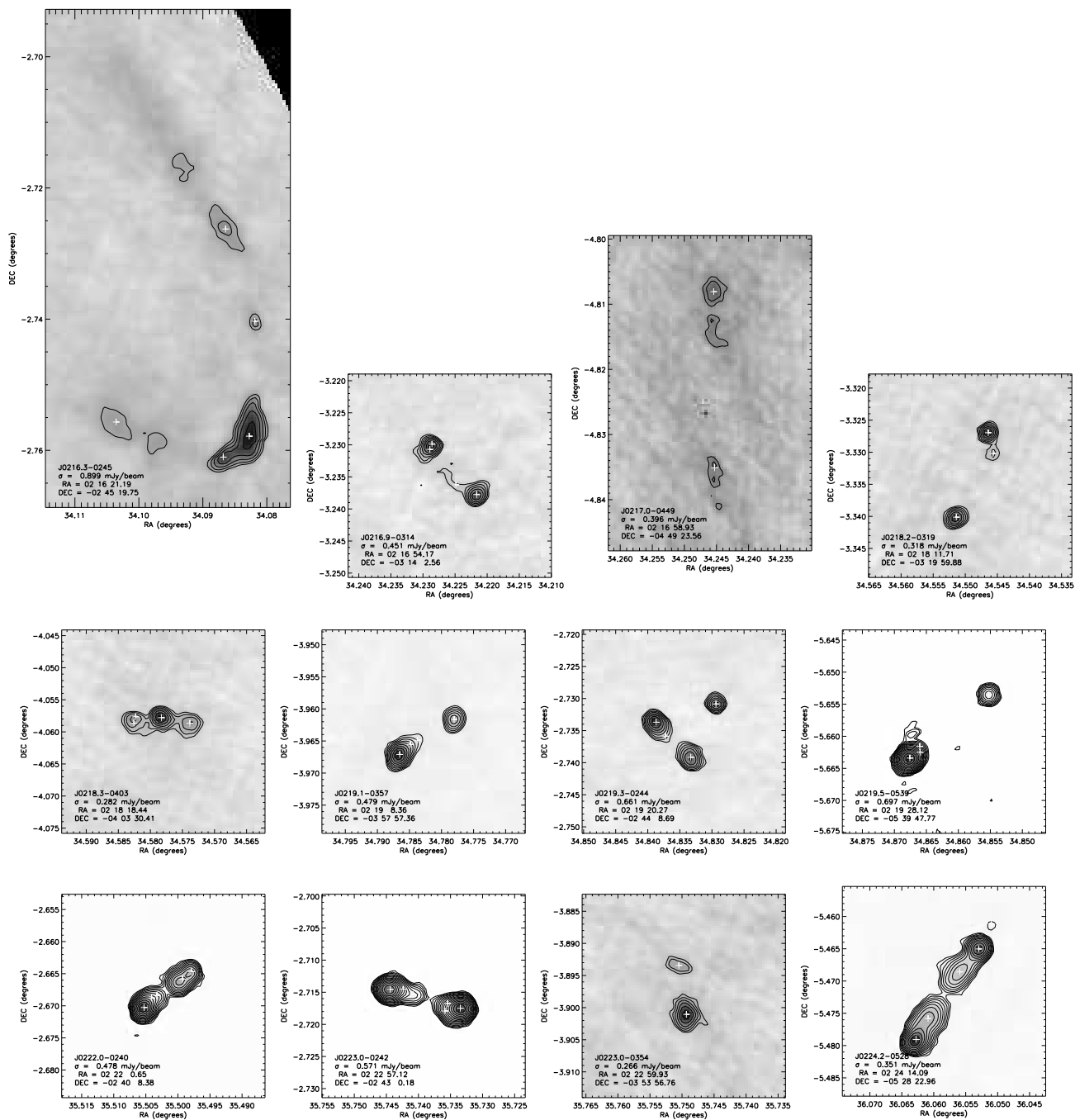


Figure A2: At 610 MHz, the 20 largest sources. Sorting order is increasing right ascension. Contours correspond to levels of $3\sigma \times (-1.4, -1, 1, 1.4, 2, 2.8, 4, 5.6, 8, 11, \dots)$ and grayscale is scaled from -3σ to the maximum value in the image. On the bottom-left corner of each image appears the name of the corresponding source in the source list, its flux weighted coordinate as well as the local noise level. The crosses are marking the Gaussian fitting components.

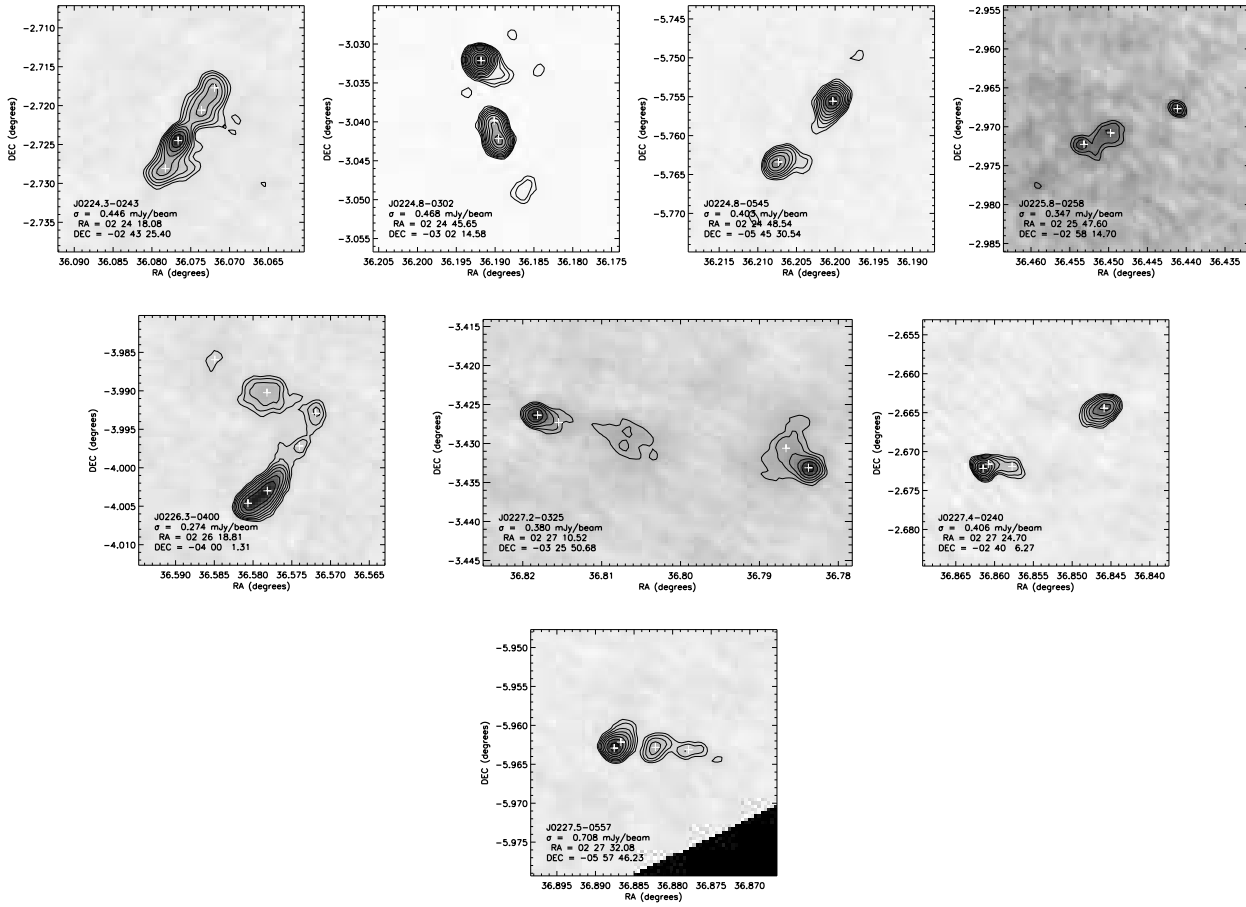


Figure A2: Continued.

CHAPTER 4

Radio-loud AGN in the XMM-LSS field: optical identification and sample selection

C. Tasse, D. Le Borgne, H. Röttgering, P. N. Best, M. Pierre, B.
Rocca-Volmerange

Submitted

The XMM-Large Scale Structure survey field (XMM-LSS) is an extragalactic window surveyed in the X-ray with the XMM-Newton satellite. It has also been observed in the optical with the Canada-France Hawai Telescope (CFHTLS survey), and in the infrared with the Spitzer Space Telescope (SWIRE survey). These surveys have been carried out to study the structure and evolution of the baryonic as well as dark matter on cosmological scales. In two previous papers, we have presented deep low frequency radio surveys of the XMM-LSS field. These radio surveys were motivated by the need to understand the various connections between radio sources' hosts and their environments.

Using the Very Large Array (VLA) and the Giant Meterwave Radio Telescope (GMRT), radio observations were carried out at 74, 230, 325 and 610 MHz (Tasse et al. 2006, Tasse et al. 2007). In paper, we proceed to identify optical counterparts to the low frequency radio sources, using the CFHTLS optical catalogue and images. We use a likelihood ratio method and estimate that $\sim 75\%$ of the radio sources have a detected optical counterpart. Using the CFHTLS and SWIRE data, we derive photometric redshifts for the galaxies that are identified with a radio source, as well for those that are not. We discuss the selection of a sub-sample of host galaxies of radio sources, wherein we estimate the remaining contamination by Type-1 AGN to be $\sim 2\%$.

4.1 INTRODUCTION

With the recent achievement of large surveys it becomes possible to study in great detail the relationship between the various classes of active galactic nuclei (AGN), their host galaxies and their environments (see Heckman & Kauffmann 2006, for a review). Recent findings indicate that the criteria used to select AGN have a significant influence on the observed properties of the AGN population. In the local $z \lesssim 0.3$ universe, AGN as selected using optical emission line criteria have rather high accretion rates, and are preferentially situated in massive galaxies (Kauffmann et al. 2003; Heckman et al. 2004). Quite strikingly, it appears that samples of AGN selected based on radio luminosity, are statistically independent at low radio power ($P_{1.4GHz} < 10^{25} \text{ W.Hz}^{-1}$), from samples of emission-line selected AGN (Best et al. 2005). This suggests that those two populations are fundamentally different.

It has been suggested by many authors, that the unified scheme is not always satisfying for the low-power radio-loud AGN. Specifically, Hine & Longair (1979) have observed that many radio galaxies do not have the luminous emission lines expected in the framework of the unified scheme (see also Laing et al. 1994; Jackson & Rawlings 1997). These low-excitation radio galaxies (LERGs) are very common at low radio power, but some of the powerful FR II radio galaxies are LERGs as well. In addition the expected infrared emission from a dusty torus is in general not observed (Whysong & Antonucci 2004; Ogle et al. 2006) nor is an accretion related X-ray emission (Hardcastle et al. 2006; Evans et al. 2006).

Altogether these arguments suggests that the AGN phenomena actually enclose two distinct classes of AGN: a radiatively efficient accretion mode (the ‘‘Quasar mode’’), and a radiatively inefficient accretion mode (the ‘‘Radio mode’’) for which there is no evidence that the unified scheme applies. The physical reasons for the rise of these two accretion modes are still speculative. It has been suggested that the quasar mode is produced by the accretion of cold gas onto the super-massive black hole, while the accretion of hot gas might drives a radiatively inefficient accretion (see Hardcastle et al. 2007, for a discussion). These two accretion modes might rise as due to the nature of the process that brings the gas to the central super-massive black-hole. In that framework, galaxy mergers trigger a cold gas, radiatively efficient accretion. In contrast, the hot intergalactic medium gas that is seen to be cooling in the atmosphere of massive elliptical galaxies (see Mathews & Brighenti 2003; Best et al. 2005, and references therein), triggers a hot gas accretion, that is radiatively inefficient. A good way of testing this scenario in which the nature of the triggering process drives the accretion type, is to study the properties and environment of quasar mode and radio mode AGN.

The XMM-Large Scale Structure (XMM-LSS) field is surveyed at low radio frequencies, infrared, optical, UV, and X-rays over $\sim 10 \text{ degree}^2$ (for a general presentation of the associated surveys see Pierre et al. 2004). This combination of data is well suited for testing the possible link between triggering process and accretion mode: the near infrared data may provides information on the presence of hot dust (radiatively efficient accretion), while the combination of width and depth of the optical data allows for a detailed study of the influence of the environment on the AGN activity, that might constrain the nature of the triggering mechanisms. In this third paper of the series, we build a sample of radio-loud AGN that may contain both quasar and radio mode AGN. In the next paper of the series, we will study their properties including the stellar mass function, radio luminosity function, and environmental dependence down to low $10^{9-10} M_{\odot}$ stellar mass.

The outline of the paper is as follows. In Sec. 4.2 we briefly present the radio and optical data used throughout this paper. In Sec. 4.3 we describe the optical and infrared identifications. In Sec. 4.4, we derive the photometric redshifts and in Sec. 4.5 we define a subsample of radio sources' hosts for which the estimated physical parameters are reliable. The uncertainties on these parameters are discussed in Sec. 4.6. We discuss the results and their consistency in Sec. 4.7 and conclude our results in Sec. 4.8.

4.2 SURVEYS OF THE XMM-LSS FIELD

4.2.1 VLA Radio data at 74 and 325 MHz

We use the radio data described in detail in Tasse et al. (2006). The observations were carried out using the Very Large Array (VLA) at 74 and 325 MHz simultaneously (4P mode). The radio survey consists of four pointings, observed in June, July and August 2003 in the A configuration and in June and July 2002 in the B configurations (see Fig. 4.1). The total integration time was ~ 60 hours in total, split over 4 pointing centers. The extended A configuration provides the high angular resolution needed for any optical identification work, whereas the B configuration is necessary to detect any low surface brightness radio emission. Great attention has been paid to properly calibrate any corrupting influence of the ionosphere (Cohen et al. 2003).

The different pointings have been assembled into single maps covering ~ 130 degree² and ~ 15 degree² at 74 and 325 MHz respectively. Since the noise is highly variable over the fields, we extracted the sources in the maps normalised by the local noise.

At 325 MHz, we have an angular resolution of $6.7''$, a median 5σ sensitivity limit of 4.0 mJy/beam, and we detect ~ 850 sources ($> 5\sigma$). At 74 MHz, the angular resolution is $30''$, with a 5σ sensitivity limit of ~ 160 mJy/beam, and we detect 650 sources. The position accuracy at 325 MHz of $\sim 2''$ is good enough for the optical identification of radio sources.

4.2.2 GMRT Radio data at 230 and 610 MHz

Low-frequency radio observations of the XMM-LSS field have been carried out with the Giant Meterwave Radio Telescope (GMRT) at 230 and 610 MHz (Tasse et al. 2007). These data provide two additional flux density measurements for 41% of the radio sources detected at 325 MHz with the VLA. These observations were motivated by the need of study the influence of the optical host galaxy and environmental properties on the observed radio spectra for large samples of radio sources.

At 610 MHz, the coverage is 12.7 degree², reaching an average noise level of ~ 0.3 mJy/beam, leading to the detection of 767 sources. At 230 MHz, we reach an average noise level of ~ 2.5 mJy/beam, leading to the detection of 467 radio sources over ~ 18.0 degree². The position accuracies are typically $3''$ and $2''$ at 230 and 610 MHz respectively.

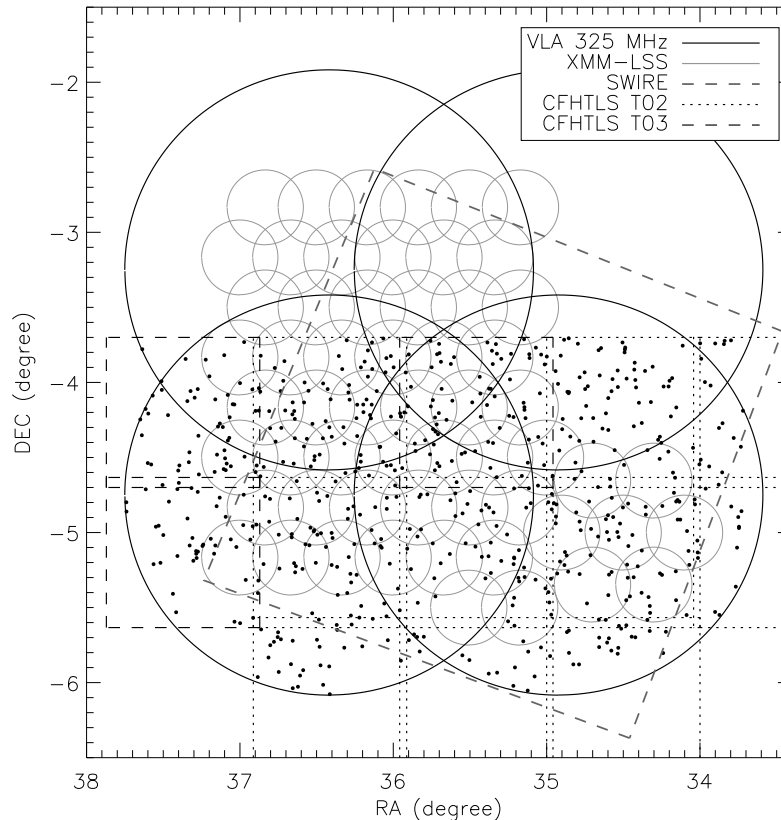


Figure 4.1: The location of the various available surveys in the XMM-LSS field. The thin, grey circles show the positions of the observed XMM X-ray pointings. The four solid thick circles show the 325 MHz pointings observed with the VLA, and the dots are at the positions of the sources detected at 325 MHz (Tasse et al. 2006). The CFHTLS-Wide optical observations are indicated by the dotted lines for the T02 release and dashed lines for the T03 release. The SWIRE field is indicated by dashed lines.

4.2.3 CFHTLS-W1 optical data

The aim of the Wide component of the Canada France Hawaii Telescope Legacy Survey¹ (CFHTLS) is to cover 170 square-degrees spread over 3 areas of the sky (W1, W2, W3). The W1 field patch covers 7×7 square degrees and is centered at $\alpha(\text{J2000}) = 02^{\text{h}}18^{\text{m}}00^{\text{s}}$, $\delta(\text{J2000}) = -07^{\circ}00'00''$, and partly covers the XMM-LSS field (Fig. 4.1). The observations are carried out through queued service observing, using the 1 degree^2 MegaCam CCD detector. Typical exposure time are ~ 1 hour in each u^* , g^* , r^* , i^* and z^* band, leading to a limiting magnitude of $i_{AB} \sim 25$. The observations were carried out between June 1, 2003 and Sept. 12, 2005. Of the 13 degree^2 of CFHTLS data used throughout this paper, 10 were part of the Terapix T02 release, and the 3 others were part of the Terapix T03 release (see Fig. 4.1). The 13 degree^2 catalog contains $\sim 3 \times 10^6$ objects.

The $u^*g^*r^*i^*z^*$ magnitudes and associated error bars are Kron-like, in the AB magnitude system. Also, for each object the Terapix catalog contains a flag indicating whether:

¹<http://www.cfht.hawaii.edu/Science/CFHLS/>

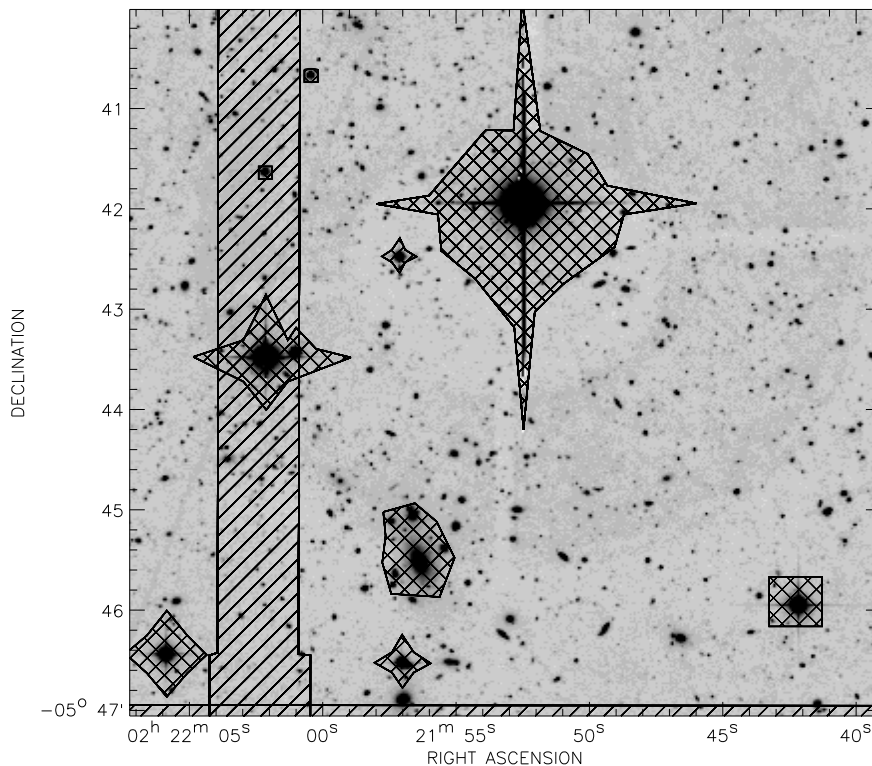


Figure 4.2: The masks designed by Terapix being very restrictive, we have redesigned new masks by suppressing some of the Terapix masks. The original masks are hashed, with the masks we kept for our purpose are double hashed.

- it is an extended or a point-like source. This flag is extracted from the SExtractor “flux-radius” parameter, which measures the radius enclosing 50% of the flux. This classification cannot be applied to objects fainter than $i = 21$, due to low signal-to-noise.
- it is masked or not. The masks are built on the basis of the i -band images, and their role is to reject the field boundary, surrounding zones of saturated stars, satellite tracks, and image defects.
- it is saturated or not. An object is flagged as saturated when its i -band magnitude satisfies $i < 17.8$.

The masks have been designed to be optimal for weak lensing studies. They are therefore very restrictive. On the basis of the i -band images we have redesigned new, less restrictive masks by suppressing the less relevant Terapix masks (see Fig. 4.2). These zones unmasked are mainly the ones situated between the 36 CCDs of the MegaCam detector. We have also included a new flag in the catalog. The new masks typically mask $\sim 20 - 25\%$ of the total surveyed area, against $\sim 50\%$ for the original Terapix masks.

4.2.4 SWIRE survey data

The Spitzer Wide-area InfraRed Extragalactic legacy survey (SWIRE, Lonsdale et al. 2003) is a ~ 50 degree² high galactic latitude, imaging survey. The SWIRE survey is spread over 6 regions observed in 4 bands with the IRAC instrument from 3.6 to 8.0 μm and in 3 bands with MIPS from 24 to 160 μm . Spitzer space observatory has observed 9.1 degree² of the XMM-LSS field as part of the SWIRE legacy survey in July 2004 (See Fig. 4.1). Throughout this paper we have used the data release 2 (DR2 hereafter) band-merged catalog available online² containing the flux density measurements at 3.6, 4.5, 5.8, 8.0 and 24 μm for a total of $\sim 2.5 \times 10^5$ objects. This catalog contains the sources detected above 5σ from 3.6 to 8.0 μm and above 3σ at 24 μm , corresponding to sensitivities of 14, 15, 42, 56, and 280 μJy respectively, and positional accuracies better than 0.5'' (2σ). Following Rowan-Robinson et al. (2005) we have used the Kron flux density estimates for the IRAC bands objects brighter than $S(3.6)_{\text{Kron}} > 1$ mJy, and the aperture flux density for the fainter ones as well as for all the objects at 24 μm . The data reduction and quality assessment is extensively discussed in Surace et al. (2004).

4.2.5 Field selection

The optical T02/T03 and infrared DR2 data do not entirely cover the radio maps of the XMM-LSS field (Fig. 4.1). Since our approach is based on photometric redshift estimates for $z \lesssim 1$ radio sources hosts, the u*g*r'i'z' optical data is of primary importance for our purpose. We therefore include the radio sources from the multifrequency radio catalog (Tasse et al. 2007) only when they are in an area covered by at least 3 optical bands. This leads to a remaining fraction of 56.6%, 59.1%, and 56.1% at 230, 325 and 610 MHz respectively. Furthermore we have restricted the area of study to the 325 MHz field which leads to an additional 6.0% and 0.2% of the objects to be rejected at 230 and 610 MHz respectively. No sources in that sample are detected only at 230 MHz. The resulting sample contains 604 radio sources.

4.3 OPTICAL AND INFRARED IDENTIFICATION OF RADIO SOURCES

We quantify the probability of an optical object to be the true host of a given radio source, by using the likelihood ratio method which was first described by Richter (1975), and subsequently modified by de Ruiter et al. (1977), Prestage & Peacock (1983), Benn (1983), and Wolstencroft et al. (1986). The version of the likelihood ratio method we use in this paper allows us to derive for each optical candidate, an association probability, which potentially takes into account their magnitude, location, colour, etc (Sutherland & Saunders 1992).

Prior to the likelihood ratio estimate, we proceed with a visual inspection of the i'-band images, and classify their radio morphologies into different classes (Sec. 4.3.1). In Sec. 4.3.2, we describe the likelihood ratio method, and based on the magnitude of each optical candidate, we estimate a probability of association with a given radio source. We show in Sec. 4.3.3 that this technique drives a contamination caused by the background sources. Using Monte-Carlo simulations, we

²see <http://swire.ipac.caltech.edu/swire/> for more information.

correct the estimated probabilities for that effect. We address the issue of completeness and reliability in Sec. 4.3.4. We associate the optical candidates with their infrared IRAC counterparts in Sec. 4.3.5.

4.3.1 Visual inspection and classification

All the optical images of radio sources have been inspected visually. When needed, the Gaussian fitting components of multiple component sources (Tasse et al. 2006, 2007) have been considered separately. This occurred for example in the case of a radio source having each of its component lying close to a bright optical source. In such cases we have renamed the source following the convention used by Tasse et al. (2006) and Tasse et al. (2007). Table C1 gives the correspondence between the original name and the new names. The resulting number of sources to be identified is 621. For all³ sources, we present the i-band images overlaid with the radio contours in Fig. D1.

Preliminarily to the likelihood ratio calculation presented in Sec. 4.3.2, a strong subjective *a priori* was given on the relation between the radio emission position and the position of its optical counterpart.

- *Class 1*: Sources are classified as Class 1 when *the radio emission is assumed to be produced at the physical location of an optical emission (detected or not)*. This occurs in sources such as starbursts, compact core dominated radio sources or radio sources where the radio core can be clearly identified. In these cases, knowing the errors on the radio and optical positions, a statistical approach can directly be used to identify the optical progenitor of a considered radio source at a given position (Sec. 4.3.2).

- *Class 2*: When no radio core is identified, as often in classical double lobes FR II (Fanaroff & Riley 1974) radio sources, only a weak *a priori* can be considered for the optical host position. Following Best et al. (2003) we have used a case-to-case approach: when the morphology does not give any clue on the location of the optical host, we classify the radio source as Class 2. This aspect is described in Appendix A and discussed in greater detail in Best et al. (2003).

- *Class 3*: When the environment has a large effect on the radio morphology, the flux weighted radio centroid and associated error bars can be very far from the real optical host. When suggested by the combination of radio and optical properties (such as an elongated lobe pointing at a bright object), we use the radio morphology to determine the position of the optical counterpart and we classify the object as Class 3. Note that, because of that case-to-case approach, we cannot calculate the completeness and reliability level of the Class 3 subsample as we do for Class 1 and 2 objects in Sec. 4.3.4. Comments on the Class 3 individual sources are given in Appendix B1.

- *Class 4*: We have classified as Class 4 the resolved radio sources for which the morphology does not suggest the presence of jets. Radio halos and relics are a part of this class. Comments on

³Irrespective of whether the identified host is saturated or flagged. Six of the identified radio sources do not appear (J0220.5-0348, J0220.4-0350, J0226.0-0542, J0225.9-0545, J0229.9-0447 and J0230.0-0440) in Fig. D1 because the i-band image was either totally corrupted or not available at this location.

these sources can be found in Appendix ??.

- *Class 5*: When the radio source overlaps a bright saturated source, or a satellite track for example, we have classified the source as Class 5, meaning we cannot proceed with the identification. The Class 5 category should in principle correspond to a masked region with overlapping objects being flagged (see Sec. 4.2.3)

4.3.2 Optical identification: the likelihood ratio method

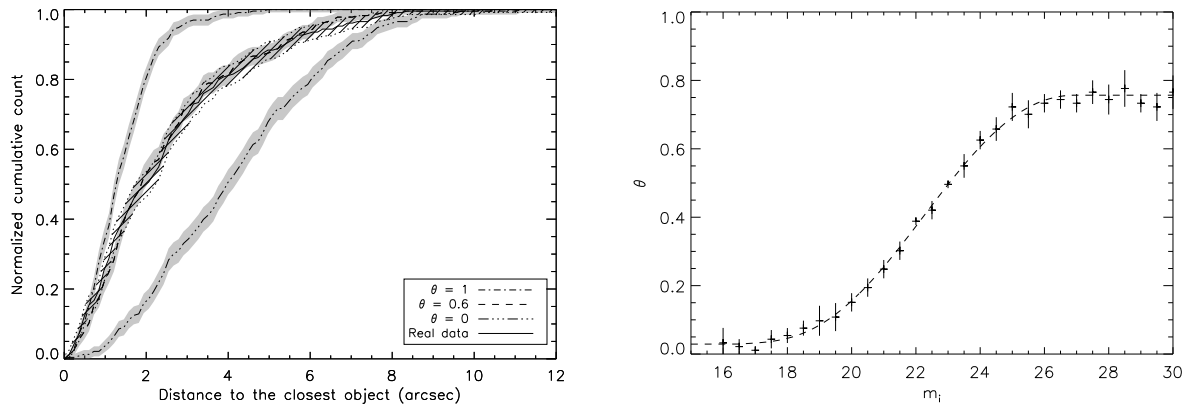


Figure 4.3: Left panel: the cumulative distribution of the angular distance from the radio source centroid to the closest neighbour in the optical catalog. In the simulated catalog, the magnitude cut is $m_i = 24$, and the fraction $\theta(m)$ of radio sources having an optical counterpart is a variable. The first dash-dotted line on the left correspond to $\theta = 100\%$, while dash-dotted line on the right corresponds to $\theta = 0\%$. In this case, the best fit to the distribution of the actual data is obtained with $\theta = 60\%$. The right panel shows the best values of θ found for different limiting magnitudes. We model $\theta(m)$ as being constant above $i = 27$ and below $i = 17$ and fit by a polynomial between these values (dashed line).

We quantify the probability that an optical candidate is the true optical counterpart of a given radio source, by calculating the likelihood ratio as described in (Sutherland & Saunders 1992):

$$LR(r, m, x_1, x_2, \dots) = \frac{\theta(< m, x_1, x_2, \dots) \exp(-\frac{r^2}{2})}{2\pi\sigma_\alpha\sigma_\delta\rho(< m, x_1, x_2, \dots)} \quad (4.1)$$

where m is the i -band magnitude of the optical candidate, and the values $\{x_1, x_2, \dots\}$ stand for a list of parameters $\{X_1, X_2, \dots\}$ that can be any numerical quantity considered as relevant, such as the optical colours, or derived photometric redshifts. $\theta(m, x_1, x_2, \dots)$ is the *a priori* probability that a radio source has an observed optical counterpart with magnitude $< m$ and values $\{x_1, x_2, \dots\}$. $\rho(m, x_1, x_2, \dots)$ is the surface number density of objects having their magnitude $< m$ and values $\{x_1, x_2, \dots\}$. The parameter r is the uncertainty-normalised angular distance between the radio core and the optical host candidate in the band merged $u^*g'r'i'z'$ optical catalog, defined as $r = ((\Delta_\alpha/\sigma_\alpha)^2 + (\Delta_\delta/\sigma_\delta)^2)^{1/2}$, where Δ stands for the positional difference, σ for the uncertainty, and α and δ for right ascension and declination respectively. On the axis α and δ , the uncertainty is the quadratic sum of the uncertainty on the radio position and on the optical position $\sigma_\alpha^2 = \sigma_{\alpha,radio}^2 + \sigma_{\alpha,opt}^2$ and $\sigma_\delta^2 = \sigma_{\delta,radio}^2 + \sigma_{\delta,opt}^2$.

We adopt the T02/T03 astrometry accuracy estimate $\sigma_{opt} \sim 0.3''$ being independent on the magnitude m . The accuracy on radio position σ_{radio} is different for every source depending on various parameters such as local noise level in the radio data, and Gaussian fitting parameters (Tasse et al. 2006). As explained in Sec. 4.3.1, we take into account the radio source morphology class to estimate σ_{radio} .

Using the formula given by Sutherland & Saunders (1992), the probability $P_{id}(i)$ of the i^{th} candidate to be a true identification is:

$$P_{id}(i) = \frac{LR_i(r, m, x_1, x_2 \dots)}{\sum_j LR_j(r, m, x_1, x_2 \dots) + (1 - \theta(m_{lim}))} \quad (4.2)$$

where $\theta(m_{lim})$ is the fraction of radio sources having a detected optical counterpart at the limiting magnitude of the survey, i refers to the candidate under consideration and j runs over the set of all possible candidates. Contrary to the formulae given by de Ruiter et al. (1977), Benn (1983) and Wolstencroft et al. (1986), this equation includes information from the other candidates, and is self consistent in the sense that $\sum_i P_{id}(i) < 1$ and $\langle \sum_i P_{id}(i) \rangle = \theta(m_{lim})$ (Sutherland & Saunders 1992).

We give a first estimate of the probability of association by assuming θ and ρ depend only on the object magnitude m . In practice, m is taken as the i-band magnitude of the optical candidate, and for each radio source we calculate the function $\rho(m)$ in a $2'$ square centered on the radio source centroid. This has the advantage of potentially taking into account the effect of clustering, *ie* the variation of the surface density, as a function of position. At the limiting magnitude of the survey, $\rho \sim 2 \times 10^{-2} \text{ arcsec}^{-2}$. We estimate the values of the function $\theta(m)$ as follows. We consider i-band magnitude cuts in the interval $16 < i < 30$ with an increment $\Delta i = 0.5$. For each of these cuts we generate a radio catalog having uniformly distributed positions, and a corresponding optical catalog in which a given fraction $\theta(m)$ of radio sources have an optical counterpart. The optical hosts of radio sources have their position scattered by the radio and optical positional uncertainties. We then consider the distribution of the angular distance between radio sources and their closest object in the optical catalog. For each value of the limiting magnitude m , we compare the distributions of the smallest angular distance for the random catalog and the actual dataset through a Kolmogorov-Smirnov test. The retained fraction $\theta(m)$ is the one corresponding to the maximum Kolmogorov-Smirnov probability (see left panel of Fig. 4.3 for an example). For each i-band magnitude cut, the test is repeated 10 times, so that we can estimate an error bar on $\theta(m)$. The right panel of Fig. 4.3 shows the variation of $\theta(m)$ with the limiting magnitude. We model $\theta(m)$ using a fit composed of two linear parts and a polynomial of degree 5. We assume the function $\theta(m)$ we have derived for the Class 1 sources is valid for the extended Class 2 sources as well.

For each of the 621 radio sources, we have derived the likelihood ratio of the optical counterparts situated in a $20''$ radius around the assumed radio centroid. For each radio source, we have retained the 5 objects having the highest likelihood ratios. The total number of radio sources having an optical counterpart is $\sum P_{id} \sim 482$. Thus $\sim 76\%$ of radio sources have a detected optical counterpart. For comparison, Simpson et al. (2006) probe radio quiet AGN and/or closeby starburst radio sources, found that 90% of their faint radio source population ($S_{1.4GHz}^{lim} \sim 100 \mu\text{Jy.beam}^{-1}$) have a detected optical counterpart in the Subaru/XMM-Newton Deep Field that has an i-band limiting magnitude $m_i \sim 27.5$ (Kashikawa et al. 2004). In the CENSOR survey, Best et al. (2003) found that 63% of their brighter radio sample ($S_{1.4GHz}^{lim} \sim 7.8 \text{ mJy.beam}^{-1}$) that are uniquely com-

posed of radio-loud AGN have an optical counterpart in the optical i-band limited ($m_i^{lim} \sim 23$) images. Considering the i-band limiting magnitude of our survey is $m_i^{lim} \sim 25$, our fraction $\sim 76\%$ seems reasonable.

4.3.3 Contamination correction

As explained in the introduction, we aim to study the properties and environment of radio sources' hosts over a wide range of stellar mass. In order to derive a reliable estimate of stellar mass function, it is important to understand the effect of contamination by miss-identifications. As show in Fig. 4.4, using the probability estimates from the previous section, we find that $\sim 8\%$ of radio sources have a host galaxy with a stellar mass in the range $\lesssim 10^8 M_\odot$. Running a Monte-Carlo simulation (described bellow), show that most of this fraction is due to contamination from background sources. In order to derive the probability of association we have only taken into account the magnitude of the optical hosts candidates, and not their u*g'r'i'z' magnitude measurements of which the stellar mass, star formation rate and photometric redshifts estimates depend on. Therefore the distribution of the radio sources optical host population along other dimensions than the i-band magnitude may be contaminated by the normal galaxies parameter distributions (See Fig. 4.4 for example). In this section, we address this issue statistically by estimating the dependence of the probability density functions θ and ρ mentioned in Sec. 4.3.2, on the stellar mass, redshift, and specific star formation rate (that we derive in Sec. 4.4). We use this *a priori* knowledge to derive a new estimate of the association probability $P_{id}^i(j)$. As shown in Fig. 4.4, this approach minimises the effect of contamination by miss-identification.

The parameter space $\{z_{ph}, M, sSFR\}$ is first gridded onto: i-band optical magnitude m ($15 < z_{ph} < 30$), redshift ($0 < z_{ph} < 2$), stellar masses ($6 < \log(M/M_\odot) < 13$) and specific star formation rates ($-13 < \log(sSFR/yr^{-1}) < -7$), with steps of $\Delta m = 1$, $\Delta z = 0.2$, $\Delta \log(M/M_\odot) = 0.5$, and $\Delta \log(sSFR/yr^{-1}) = 0.3$ respectively.

We estimate the values of the function ρ over the parameter space $\{m, z_{ph}, M, sSFR\}$ as follows. For a random subsample of normal galaxies, we calculate the observed number of galaxies in each cell of the parameter space. One obtains $\rho(m, z_{ph}, M, sSFR)$ by normalising the total number of sources in such a parameter space to the surface density at the limiting magnitude.

For the radio sources' hosts, in each cell C of the parameter space, the observed number of sources is $n_{obs}(C) = \sum_{\Omega_{i,j}(C)} [P_{id}^i(j)]$, where $P_{id}^i(j)$ is the association probability between the j^{th} optical candidate and the i^{th} radio source (Sec. 4.3.2), and the $\Omega_{i,j}(C)$ is the set of $\{i, j\}$ optical candidates which are located within the cell C . One can write the observed number of sources $n_{obs}(C)$ as $n_{obs}(C) = n_{true}(C) + n_{mID}(C)$, where $n_{true}(C)$ and $n_{mID}(C)$ are the true and miss-identified observed sources in the cell C respectively. The function $\theta(m, M, sSFR, z)$ is estimated in each cell by removing the miss-identified contribution, and by normalising the total number of radio sources in the $\{z_{ph}, M, sSFR\}$ parameter space to unity. In order to estimate $n_{mID}(C)$, we generate 10 simulated radio catalogs in which we associate a fraction $\theta(m_i)$ of radio sources with galaxies of magnitude m_i (see Sec. 4.3.2), introducing a scatter between the radio and optical positions corresponding to the astrometrical errors of the individual sources in the original radio catalog. We proceed with the optical identification for these simulated catalogs, and derive the association probabilities as described in Sec. 4.3.2. Knowing the input *true* optical counterpart, and removing them from our catalog, we can compute the miss-identification contribution $n_{mID}(C)$ (see Fig. 4.4).

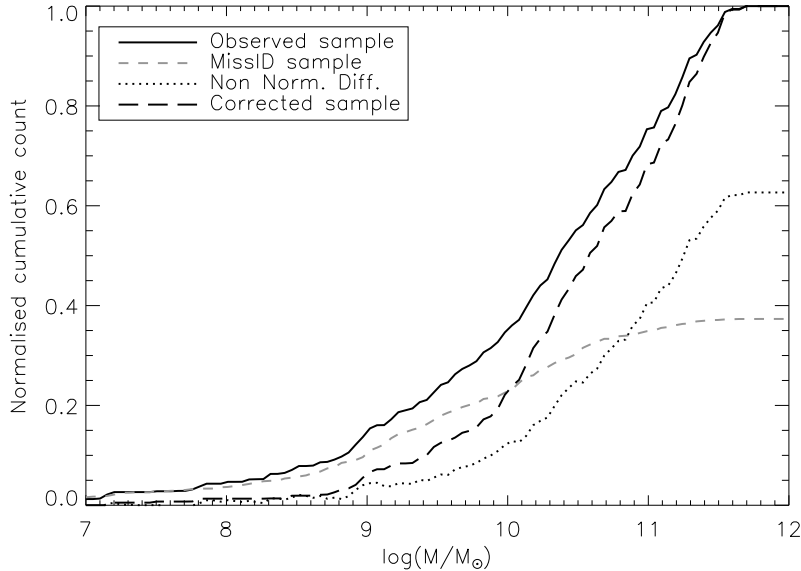


Figure 4.4: Stellar mass distributions in the redshift range $0.1 < z < 1.2$, for the observed radio sources’ hosts (solid line) and for the estimated contribution from the miss-identifications (grey dashed line). The dotted line (‘Non Normalised Difference’) corresponds to the difference between these two distributions. We have used such a miss-identification contribution subtraction to estimate $\theta(m, M, sSFR, z)$, and give estimates of the association probabilities corrected from the miss-identification contribution.

We have re-computed the probabilities of association using these estimates of θ and ρ . Fig. 4.4 shows the miss-identifications have been properly removed from the observed mass distribution of radio sources’ hosts. For example while the contribution of low stellar mass galaxies with $\log(M/M_\odot) < 8.5$ was as high as 8% and was mainly due to miss-identification, the corrected number is $\sim 2\%$. Results appear in Tab. C2.

4.3.4 Completeness and reliability

In this section, we discuss the completeness and reliability of the identified sample presented in Tab. C2. In practice it is useful to define two samples from the association probabilities we have defined in Sec. 4.3.3. The first (S1 hereafter) contains for each radio source *all* the optical candidates and their individual association probabilities and is used to estimate the radio sources’ optical host *density* in the parameter space. In the next paper of the series, we will mostly use the S1 sample, to estimate comoving number density down to low stellar mass. In a given region R of the parameter space we estimate the mean number $\langle n_{id}(R) \rangle$ of radio sources optical counterparts as $\langle n_{id}(R) \rangle = \sum_{\Omega_{i,j}(C)} [P_{id}^i(j)]$ where $P_{id}^i(j)$ is the association probability between the j^{th} optical candidate and the i^{th} radio source (Sec. 4.3.2), and $\Omega_{i,j}(C)$ is the set of all $\{i, j\}$ optical candidates which are located in the region R of the parameter space. The second sample (S2) is derived from S1, and contains for each radio source the optical candidate that has the highest likelihood ratio. S2 is handy for displaying discrete properties of radio sources’ hosts (see for example Fig. 4.9).

In practice, the S1 sample is an extensive list of optical candidates. Many of those have low or

negligible probability of association with a given radio source. In order to reject the most unlikely optical candidates from the table presented in this paper (Tab. C2), we apply a likelihood ratio cut LR_{cut} to the samples S1 and S2. The completeness and reliability of such a selected source list will be affected by the value of LR_{cut} , since a fraction of candidate that are true optical identifications will be filtered out. Given an LR_{cut} , the completeness and reliability levels can be written as:

$$C(LR_{cut}) = 1 - \left(N_{rej} + \sum_{LR_i < LR_{cut}} P_{id}(i) \right) / N_{id} \quad (4.3)$$

$$R(LR_{cut}) = 1 - (1/N_{id}) \sum_{LR_i \geq LR_{cut}} (1 - P_{id}(i)) \quad (4.4)$$

where N_{rej} is the number of true optical identifications rejected prior to the likelihood ratio cut, N_{id} is the total number of true optical identifications, and $P_{id}(i)$ is estimated following Eq. 4.2. For the S1 sample we have $N_{rej} = 0$, while the S2 sample, prior to the likelihood ratio cut a number $N_{rej} = \sum_{i \neq i_0} P_{id}(i)$ of true identification has been rejected, where for each radio source i_0 is the optical candidate that has the highest likelihood ratio. We estimate N_{id} as $\sum_i \sum_j [1 - P_{id}^i(j)]$, where i runs over all radio sources and j over the individual optical identification candidates.

In Fig. 4.5, the completeness and reliability levels for the samples S1 and S2 are plotted as a function of LR_{cut} for Class 1 and Class 2 sources. The lower completeness level for the Class 2 sources is due to the error on the *a priori* positions of their optical host being higher. For the S2 sample, for both classes we choose $LR_{cut} = 0.5$ corresponding to completeness levels of $\sim 88\%$ and $\sim 83\%$, and reliability levels of $\sim 87\%$ and $\sim 83\%$ for the classes 1 and 2 respectively. As shown in Fig. 4.5, this value for LR_{cut} allows us to reject $\sim 75\%$ of all optical candidates from the original optical counterpart candidates source list, without affecting the reliability and completeness level of the most likely optical identification source list.

As mentioned in Sec. 4.3.1, because Class 3 sources are identified subjectively, completeness and reliability level cannot be derived. All the information about each radio source optical identification appears in Tab. C2. A flag allows to construct the S2 sample.

4.3.5 Infrared association

Following Surace et al. (2004), we associate to the optical candidates the infrared objects of the SWIRE DR2 that are closer than $1.5''$. This provides flux density measurements at 3.6, 4.5, 5.8, 8.0 and $24 \mu\text{m}$ (Sec. 4.2.4) for the radio source optical hosts identified above. Considering the source density in the SWIRE DR2 band merged catalog being $\sim 3.2 \times 10^4 \text{ deg}^{-2}$, and assuming a Poisson statistics, the chance of association with a random background source is $\sim 2\%$. In the case of detection of more than one source within the search radius we have only considered the closest object.

Of the sample of radio sources optical counterparts, $\sim 61\%$ have been associated with an infrared counterpart at 3.6 and $4.5 \mu\text{m}$, against $\sim 33\%$, $\sim 27\%$ and $\sim 18\%$ at 5.8, 8.0 and $24 \mu\text{m}$ respectively.

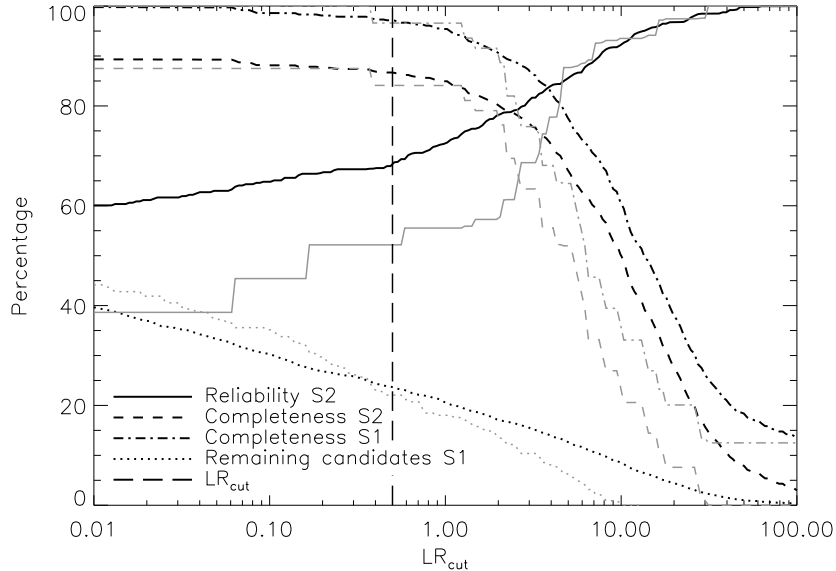


Figure 4.5: Reliability level for the S2 sample and Completeness for the S1 and S2 samples as a function of the likelihood ratio cutoff LR_{cut} . These quantities are displayed for the Class 1 (black) and Class 2 (grey) sources. The dotted lines indicate the fraction of optical candidates from the original source list that remain in the S1 source list

4.4 SPECTRAL ENERGY DISTRIBUTION FITTING

The photometric redshift method consists of fitting spectral energy distribution (SED) templates to the observed magnitude measurements and their associated error bars using a standard χ^2 minimisation. Such galaxy templates can be built from stellar synthesis code, and physical properties such as age, stellar mass, or star formation rate can be inferred. However, the radio selected galaxy population is dominated by a population of AGNs, whose optical emission can dominate over the contribution from the stellar population to the overall SED, such as in the extreme case of an optical quasar.

In this section, we use two photometric redshift approaches, the combination of which allows us to (i) derive physical quantities related to the observed galaxies in our survey, (ii) address the issue of Type-1 AGN contamination, and (iii) assess the reliability of the photometric redshifts. The first method (Sec. 4.4.1) uses the ZPEG stellar synthesis code (Le Borgne & Rocca-Volmerange 2002), which yields quantitative information on the physics of these objects, such as stellar masses, and star formation rates. Dust emission has not been included in these models, and hence this method can only be used in the wavelength range $\lambda \lesssim 1 \mu\text{m}$. The second method (Sec. 4.4.2) uses SED templates built mostly from observations, which will provide us a more qualitative understanding. This method has the advantage of covering a large wavelength range from far infrared to soft uv light, as well as probing a wide range of objects from normal galaxies to Quasars. In Sec. 4.5 we select a subsample of galaxies for which the ZPEG output parameters are reliable.

4.4.1 Theoretical approach: ZPEG

In this section, we compute photometric redshifts for $\sim 3 \times 10^6$ galaxies of the T02/T03 release by using the photometric redshift code ZPEG⁴ (Le Borgne & Rocca-Volmerange 2002).

The ZPEG template library is synthesised from nine evolutionary scenarios defined by a minimum number of free parameters. Assuming an universal Initial Mass Function (IMF, Kroupa 2002), the time scale τ of star formation is derived from both a star formation efficiency associated with a Schmidt law and an e-folding time scale for the infall of gas onto the galaxy. The epoch of galactic winds in the galaxy's history is also a free parameter in the models. Details of these physical parameters defining the various scenarios can be found in Le Borgne & Rocca-Volmerange (2002). The templates used by ZPEG are constructed from these models for ages ranging from 10 Myr to 14 Gyr after the birth of the first stars, with an additional constrain on the age of the universe at every redshift. For example, for an age > 10 Gyr, a short star formation timescale ($\tau < 1$ Gyr) is more appropriate for an early type galaxy while $\tau \sim 2$ Gyr corresponds to a typical spectrum of an Sb galaxy (see Bruzual A. & Charlot 1993; Fioc & Rocca-Volmerange 1997). Effects such as metal enrichment, dust extinction, and nebular emission lines are coherently taken into account depending on evolution scenarios (see Le Borgne & Rocca-Volmerange 2002, for more details). As mentioned earlier, the infrared emission from dust is not taken into account within the model, and hence this approach is used only in the optical and near infrared domains (CFHTLS $u^*g'r'i'z'$ bands).

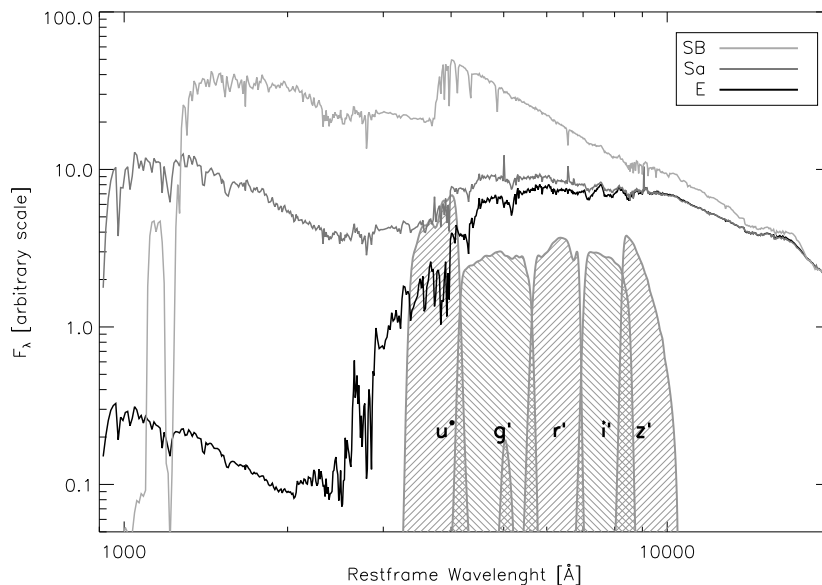


Figure 4.6: Examples of the synthetic templates used by ZPEG. Because the stellar synthesis model does not include dust emission, we only use the CFHTLS magnitude points in the $u^*g'r'i'z'$ bands. These templates correspond to spiral (Sa), elliptical (E) and starburst (SB) galaxies.

In each of the nine scenarios, 57 time steps were used between 10 Myr and 14 Gyr, for the age of the galaxy template. The stellar mass varies between 10^6 and $10^{13} M_{\odot}$. Assuming a Λ CDM

⁴The ZPEG code is available online at <http://www2.iap.fr/cgi-bin/pegase/zpeg.pl>

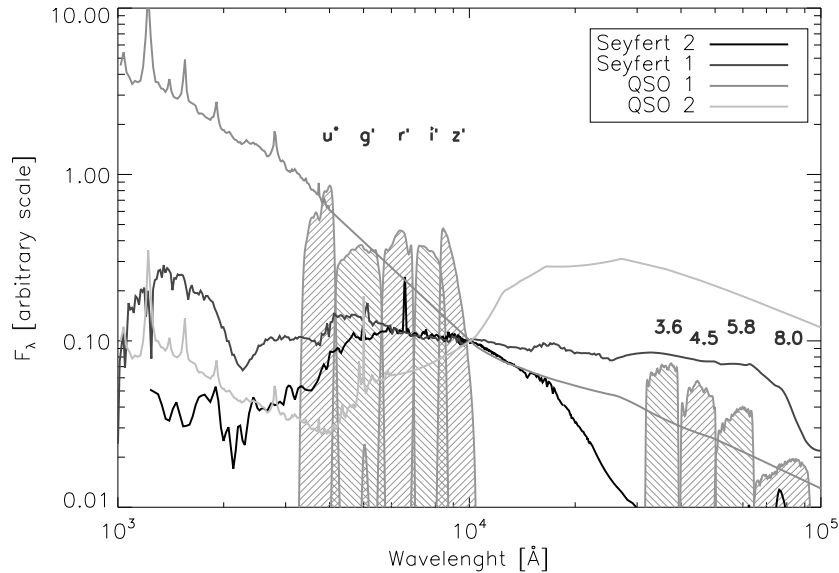


Figure 4.7: Examples of SED templates of optically active AGNs retrieved from the SWIRE template library (Polletta et al. 2007) that we have used to derive photometric redshifts and spectral types. Because these SEDs include the infrared dust emission in addition to the $u^*g^*r^*i^*z^*$ optical data we could use the infrared flux density measurements to constrain the best fit associated parameters.

cosmology, the SEDs are k and e -corrected (*cosmologically* and *evolutionary* respectively). The redshift varies between $z = 0$ and $z = 2$, in steps of $\Delta z = 0.01$. Fig. 4.6 shows examples of synthetic templates used by ZPEG. The value of the χ^2 is recorded in the parameter space of the input parameters of the model. Error bars on best fit parameters are taken at $\chi^2_{min} + 1$ if $\chi^2_{min} < 1$ and at $2 \times \chi^2_{min}$ if $\chi^2_{min} > 1$ (see Sullivan et al. 2006, for a detailed discussion on these estimates). In addition, assuming a given object is located in the redshift range probed within the redshift grid, the function $\chi^2(z)$ is directly translatable into $p(z)$ the *redshift probability function*. Multiplied by dz , $p(z)$ gives the probability of an object to be located between z and $z + dz$. In the next paper, we will use this information to derive an overdensity parameter, and study the environment of radio sources.

The ZPEG output parameters that are specially relevant to our study are the estimates and associated error bars of the redshift, the stellar mass, and the star formation rate. However, the true star formation history of a galaxy can deviate from the idealised scenarios outlines above. In order to give a reliable estimate of the star formation rate, this quantity is averaged over 0.5 Gyr ($SFR_{0.5}$ hereafter). The uncertainties associated with these quantities are discussed in more detail in Sec. 4.6 and Sullivan et al. (2006).

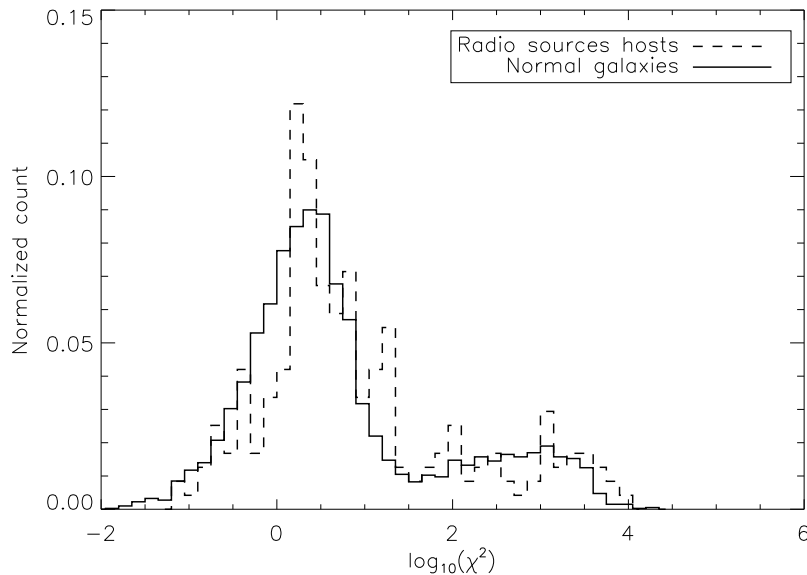


Figure 4.8: The reduced χ^2 distribution from SED fitting using SWIRE template library. The secondary bump at $\chi^2 \gtrsim 100$ shows $\sim 30\%$ of the population is not properly fit. Assuming this does not drive any selection effect, we have rejected these sources from the spectral type distribution study.

4.4.2 Semi empirical approach

The SWIRE template library⁵ (Polletta et al. 2007) contains 25 templates including three ellipticals, seven spirals, six starbursts, seven AGN (three Type-1 AGNs, four Type-2 AGNs), and two composite (starburst+AGN) templates. These templates cover the wavelength range between 1000 Å and 1000 μm, including spectral features such as stellar emission, emission and absorption lines, dust extinction and emission. These are partly based on theoretical SED models, as for elliptical, spiral and starburst templates (GRASIL, Silva et al. 1998), and partly on observations, as in the case of the AGN templates. For more information on the SWIRE template library see Polletta et al. (2007).

Using a standard χ^2 minimisation procedure with the redshift and the SED normalisation as free parameters, we have fitted the u*g*r'i'z' and IRAC flux density measurements of the radio source sample defined in Sec. 4.3. The redshift varies in the range $0 < z < 3$ with steps of 0.05, and the SED normalisation is unconstrained. The value of the χ^2 has been recorded in the space $\{t, z\}$, where t stands for the template type. Assuming the statistics to be normal, the probability density p of observation of a given χ^2 follows $p \propto \chi^{r-2} \exp(-\chi^2/2)$ where r is the number of degrees of freedom. Converting the χ^2 in the $\{t, z\}$ -space to probability, and normalising to unity, and integrating through the z -axis at t , we obtain the probability of a template t to be the true SED. We will make full use of these probability estimates in Sec. 4.5.2.

Fig. 4.8 shows that the reduced χ^2 distribution of the best fit templates is bimodal: $\sim 26\%$ of the normal galaxy population have a $\chi^2_{red} > 100$ against $\sim 34\%$ for the radio sources' hosts. This effect

⁵The SWIRE template library is available online at http://cass.ucsd.edu/SWIRE/mcp/templates/swire_templates.html

can be caused by the underlying true SED of the objects having $\chi_{red}^2 > 100$ being represented by one or more SED templates that are very different from the SEDs present in the SWIRE template library. We have investigated that issue by comparing the ZPEG output parameter distribution of the $\chi_{red}^2 > 100$ objects, to the rest of the population. The stellar mass, redshift and star formation rate distribution look similar for these two populations, suggesting that this bi-modality is due to variability that is higher in infrared than in optical: if the objects having $\chi_{red}^2 > 100$ would be constituting a special SED type population, one would expect to find biased optical properties, which is not the case. Therefore, in the following, we only include the galaxies having spectral fits with $\chi_{red}^2 < 100$, assuming this does not drive any selection effect on the observed properties of radio sources.

Results from the SED fitting appear in Tab. C2.

4.5 SUBSAMPLE SELECTION

As discussed in the introduction, our goal is to build a sample of radio-loud AGN with reliable physical parameter estimates, as derived using the stellar synthesis code ZPEG, and study their properties and environment. However, many AGN (mostly Type-1) have their SED dominated by the central core light in the optical domain, in the form of optical and UV continuum emission, or luminous emission lines, such as in the extreme case of optical quasars. The presence of such objects within our dataset introduce a contamination, as their physical parameter estimates are corrupted. In this section, we pay special attention to select a subsample of Type-2 radio-loud AGN for which the physical parameter estimates are reliable. The result of the following selection is encapsulated into a single flag that appears in Tab. C2.

4.5.1 Selection of the basic sample

We first proceed with basic selections based on the u*g*r'i'z' optical data. A given optical object at a location $\{\alpha_0, \delta_0\}$, being detected in N_b optical bands, having an i-band magnitude i , and a stellaricity flag s is included if it satisfies *all* of the following conditions:

- 1- $i < 24$
- 2- $N_b \geq 3$
- 3- $i > 18$
- 4- $\{\alpha_0, \delta_0\}$ corresponds to a non-masked area
- 5- $s = 0$ (non point-like, Sec. 4.2.3)
- 6- $0.1 < z_{ph}(ZPEG) < 1.2$
- 7- $0.1 < z_{ph}(SWIRE) < 1.2$

The selection criterion (1) removes faint objects having large flux density error bars as well as false detections close to bright stars. (2) filters out the objects for which too few flux density measurements are available. The selection criteria (3) and (4) remove the saturated and masked objects respectively, for which the magnitude measurements are corrupted. We remove point-like objects, corresponding to a contribution from $i < 21$ contaminating Type-1 quasars using (5). Finally, the 4000\AA break of the stellar population being the most constraining feature of SEDs in the optical regime, we restrict our study to the redshift range $z_{ph} < 1.2$, corresponding to the 4000\AA break being in z' filter (6-7). Furthermore, we restrict our study to $z > 0.1$, as we expect significant radio emission from starbursts at $z < 0.1$ (this aspect is further discussed in Sec. 4.5.3)

4.5.2 Type-1 AGN contamination

In order to reject the remaining contaminating Type-1 AGN, we have used a combination of criteria based upon (i) the optical colours, and (ii) the goodness of the SWIRE library SED template fits.

The optical colour classification criteria is based on the g-r versus r-i colour-colour diagram (bottom panel of Fig. 4.9). Computing the tracks of a Type-1 AGN, a starburst, and an elliptical galaxy in that colour-colour space, it is clearly seen that the Type-1 AGN occupy a restricted area. This is due to the SED of Type-1 objects being a power law in the optical domain, while the SED of normal galaxies show a high to moderate 4000\AA break. We classify a source as contaminating if it lies in the region $R(g', r', i')$ defined as follows:

$$R(g', r', i') \equiv \begin{aligned} &(g' - r' < 0.38 \wedge r' - i' < 0.5) \\ &\vee (g' - r' > 0.38 \wedge r' - i' < 0.2) \end{aligned} \quad (4.5)$$

where \wedge and \vee stand for the AND and OR logical connectives.

For the SED-type criteria, we first classified the SWIRE templates in two groups. The first group contains the SEDs in which there is either no contribution, or moderate contribution from an AGN (“N/NL” for *Normal/Narrow Line*), while the second class contains the templates with strong AGN contribution such as the QSOs (“BL” for *Broad Line*). Tab. 4.1 shows how the SWIRE templates have been classified in these two categories. We have classified an object as BL when its probability P_{BL} (Sec. 4.4.2) of being a BL-type object satisfies:

$$C_{BL}(P_{BL}) \equiv (P_{BL} > 60\%) \quad (4.6)$$

Finally, combining the two selection criteria (Eq. 4.5 and 4.6) gives: $[C_{BL}(P_{BL})] \vee [R(g', r', i')]$. We investigate below the consistency of the selection.

Stern et al. (2005), from the study of a large sample of spectroscopically identified sources in the AGN and Galaxy Evolution Survey (AGES, Cool 2006), have shown that broad line AGN can be well separated from the mean galaxy population in the $[3.6]-[4.5]$ versus $[5.8]-[8.0]$ colour-colour space. In Fig. 4.9 we plot the location of radio source hosts in this colour-colour plot. Of the 10 objects classified as BL, 1 (10%) lies outside the area given by Stern et al. (2005), in good agreement with the 9% given by that author. In the g-r vs r-i colour-colour diagram, the area defined by $R(g', r', i')$ includes $\sim 5\%$ of the objects classified as N/NL using SED fitting, against

Table 4.1: The distribution of the original SWIRE template name through our classification (see Sec. 4.4.2).

N/NL				BL		
E113	Sb	N6090	Spi4	I19254	BQSO1	Torus
E112	Sc	N6240	I20551	Mrk231	QSO1	TQSO1
E115	Sdm	Sey18	I22491			
S0	Sd	Sey2	M82			
Sa	Arp220	QSO2				

80% of the objects classified as BL sources. Furthermore, we show in Fig. 4.10 of Sec. 4.6 that the ZPEG photometric redshift estimates are in good agreement with the SWIRE template fits for the N/NL, but not for the contaminating BL objects ($\sigma(z) \sim 0.1$ against $\sigma(z) \sim 0.3$). This coherence suggests that when all IRAC and optical bands are available, we are able to detect the contaminating broad line AGN in an efficient way.

However, only $\sim 37\%$ of our radio sources' hosts are detected in 9 bands, and it is likely that band availability affects the effectiveness of our SED-type selection technique. In order to address this, we assume that for the sample of sources detected in all 9 bands, we have effectively detected all the true contaminating Type-1 sources. For this bright sample, we recalculate the photometric redshifts using the SWIRE template library only with their (1) u*g'r'i'z' + 5.8 and 8.0 μm (2) u*g'r'i'z' and (3) g'r'i' flux density measurements. It can be seen from Fig. 4.9 that the removal of infrared data has a large influence on the SED-type classification. In the cases where only optical data are available, it appears that our selection criteria leads to a remaining contamination of $2/37 \sim 5.4\%$, while there should be no remaining contamination when infrared data is available. The fraction of radio sources not having infrared IRAC measurements being $\sim 39\%$, we estimate the remaining contamination to be $\sim 2\%$.

Results of the N/NL/BL classification for the S1 and S2 samples appears in Tab. C2.

4.5.3 Starburst selection

The intense star formation occurring in starburst galaxies is known to produce a significant amount of radio emission. Since our purpose is to study the triggering processes and the evolution of the radio-loud AGN population there is a need to identify and remove these starbursts.

Fig. 4.11 shows the relation between the SFR and 1.4 GHz radio power given by Cram (1998), as well as the location of our sources in that plane. We have used the ZPEG star formation rate estimator $\text{SFR}_{0.5}$ and the 1.4 GHz radio power as estimated using the ZPEG photometric redshift and the spectral index (Tasse et al. 2006, 2007). We reject a source if the contribution from star formation to the radio luminosity is higher than 10%, which leads to the selection of 5 radio sources within the subsample selected in Sec. 4.5. As mentioned in Sec. 4.4.1, the ZPEG SFR estimate is averaged over 0.5 Gyr, while a starburst may occur on time scales ~ 0.1 Gyr. We investigate this issue by estimating the number of starbursts we should observe within our dataset. To do this we consider a starburst radio luminosity function given by Oliver et al. (1998), combined with the starburst luminosity function evolution as given by Pozzi et al. (2004) up to $z = 1$. Given our flux

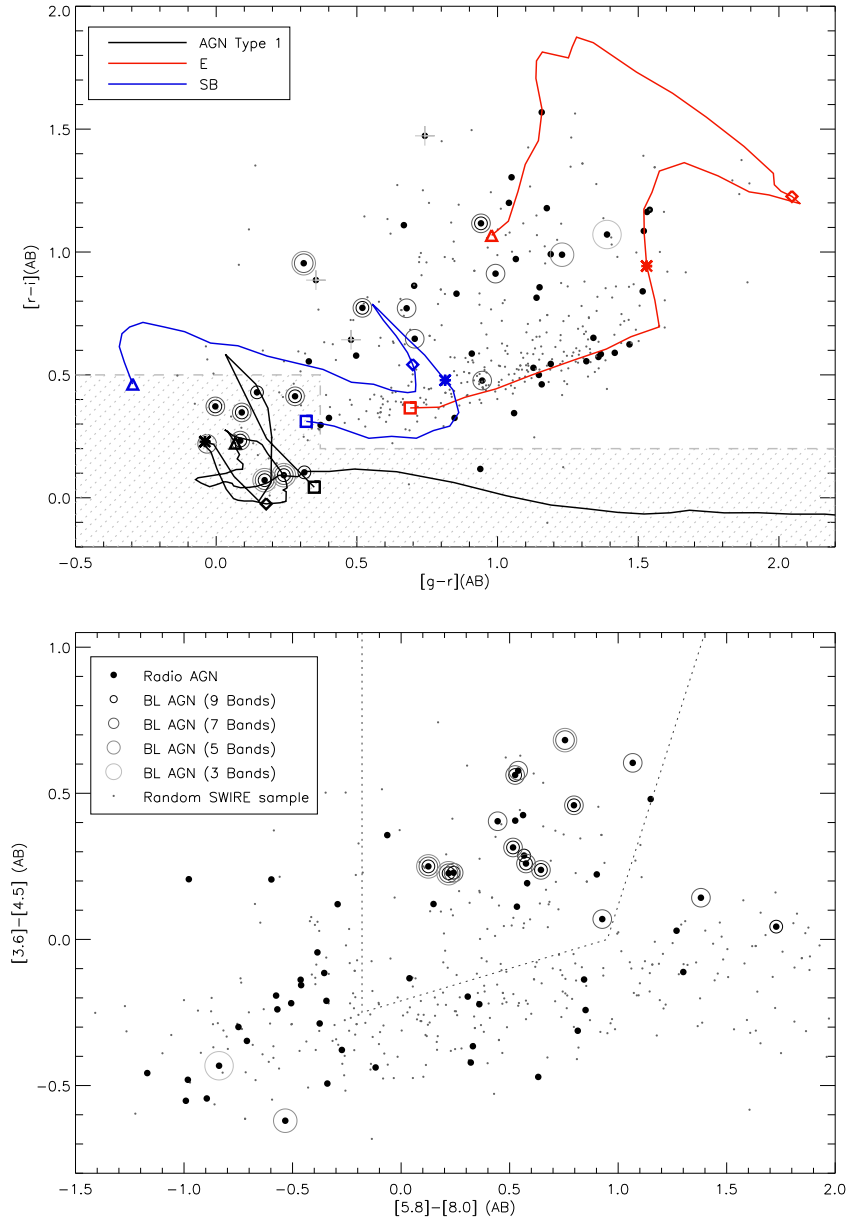


Figure 4.9: *Top panel:* The $g-r$ vs $r-i$ colour-colour plot for the S2 sample detected in all the $u^*g'r'i'z'$ and IRAC bands (black dots), and for a subsample of normal galaxies similarly selected (grey dots). We classify as contaminating those objects which lie in the hashed area. The open circles indicate the classification based on the SED-type criteria (See *Bottom panel*). We plot the colour-colour tracks for a Type-1 QSO, an elliptical, and a starburst galaxy. The square, star, diamond and triangle symbols stand for redshifts 0, 0.5, 1.5, and 2 respectively. *Bottom panel:* The $[3.6]-[4.5]$ versus $[5.8]-[8.0]$ colour-colour plot for the sources of the same sample. The grey dotted line indicates the region in which Stern et al. (2005) finds $\sim 90\%$ of the spectroscopically identified broad-line AGN. Based on the SWIRE template library, the objects best fit by a BL AGN templates are plotted with small black circle. The bigger circles indicate the sources classified as BL contaminating AGN when progressively removing the information on the infrared bands.

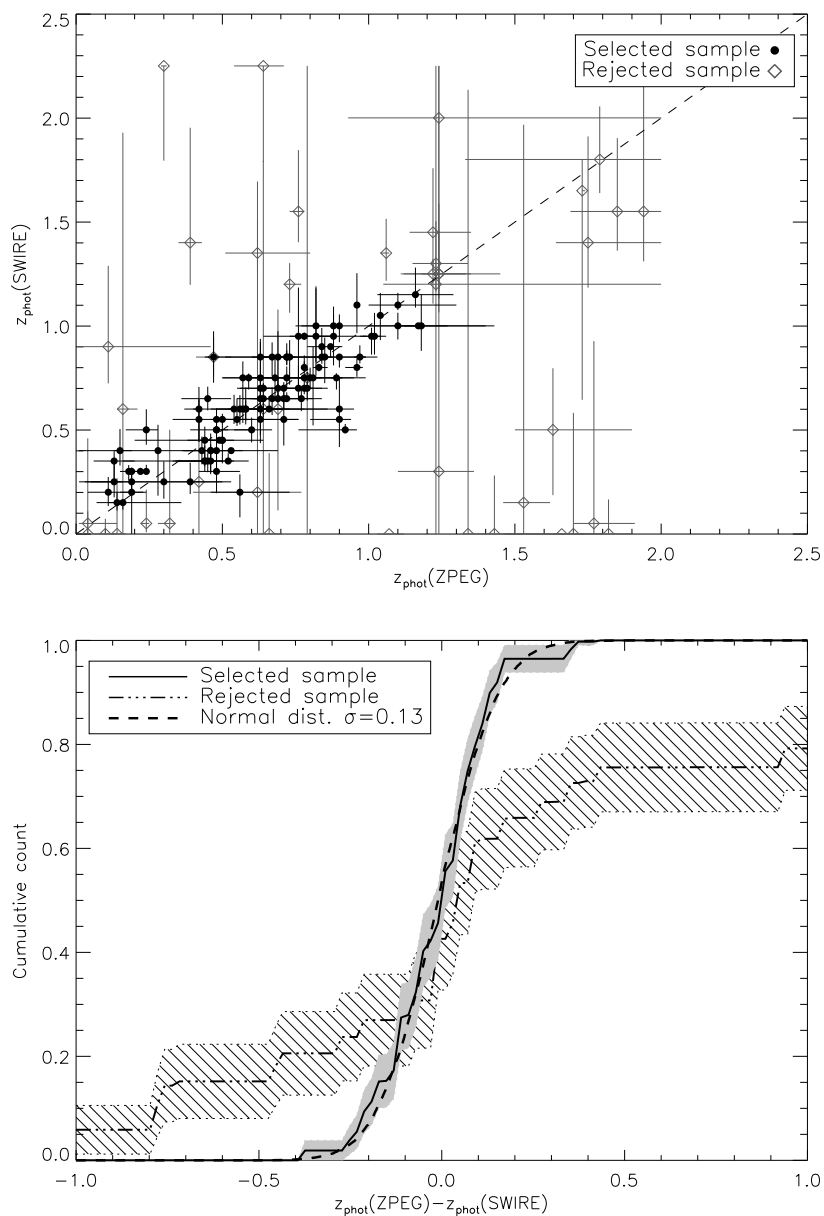


Figure 4.10: For a subsample of sources detected at 3.6 and $4.5\mu\text{m}$, we can compare the photometric redshifts as estimated by the methods. The top panel shows the photometric redshift z_{ZPEG} against z_{SWIRE} as estimated using ZPEG and the SWIRE template library respectively, for the contaminating sources (“rejected”) and for the selected sources. The bottom panel shows the cumulative distribution of $z_{\text{ZPEG}} - z_{\text{SWIRE}}$. The agreement is $\sigma \sim 0.13$ for the selected sample, suggesting the physical parameters as estimates by ZPEG will be reliable for these objects.

density limit at 1.4 GHz of ~ 1.5 mJy, we calculate there should be 6.2 starburst galaxies within our sample. This good correspondence with the number of sources classified as starbursts suggests that the remaining sources are radio-loud AGN.

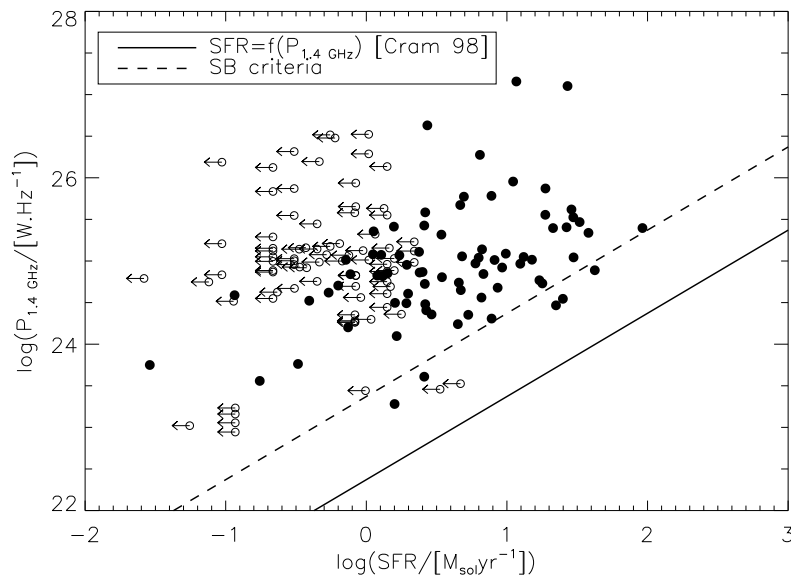


Figure 4.11: The distribution of the radio sources in the $P_{1.4}$ - SFR plane. The open circles indicate upper limits. The solid line is the SFR- $P_{1.4}$ relation given by Cram (1998). Below the dashed line, the contribution by star formation to the radio power is higher than 10%. In order to retrieve a purely radio-loud AGN sample, in the final source list, we have flagged these sources as being starburst-like.

4.6 OUTPUT PARAMETERS ACCURACIES

4.6.1 ZPEG standards

In this section we discuss the uncertainties of ZPEG output parameters for the sample of radio sources' hosts selected in Sec. 4.5.

As part of the SNLS (SuperNovae Legacy Survey), Sullivan et al. (2006) have discussed the uncertainties of ZPEG physical estimates in great detail. Their photometric dataset is very similar to ours as they use the broad band CFHTLS-D1 and D4 *deep* survey data, while we use the CFHTLS-W1. These fields were imaged in the same $u^*g^*r^*i^*z^*$ filters, but the observations differ in that the *Deep* surveys are deeper by a factor of ~ 2 , which should not give rise to any systematic differences between the accuracy of their photometric redshifts and ours.

Using a sample of 116 galaxies having measured spectroscopic redshift Sullivan et al. (2006) estimate the uncertainties of the ZPEG photometric redshifts and associated parameters. Specifically, the distribution of $\Delta z = z_{spec} - z_{phot}$ has a median (or 50% *quantile*) offset of $q_{0.5}(\Delta z) = 0.02$, and a 90% quantile of $q_{90}(\Delta z) = 0.15$. Assuming the distribution to be normal, this corresponds to a standard deviation $\sigma(\Delta z) = 0.09$. In order to check that this estimate is compatible with our

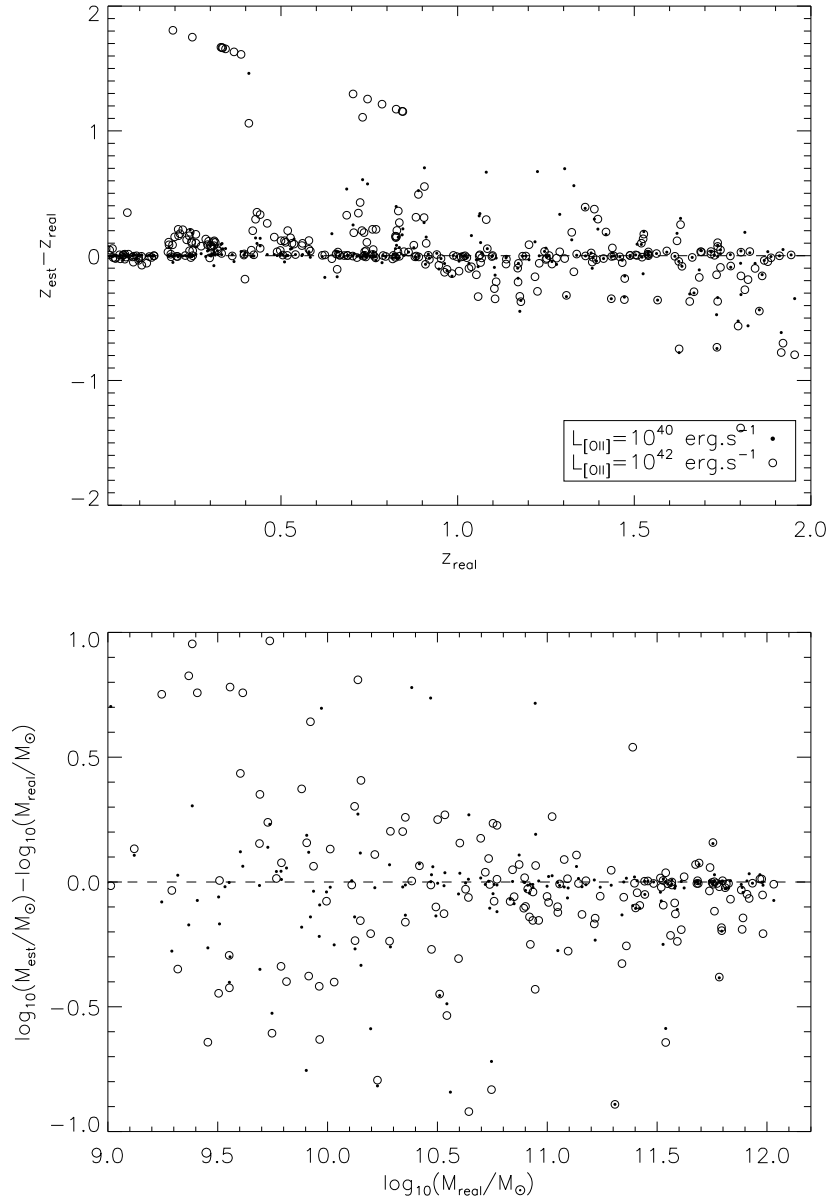


Figure 4.12: Effects of the AGN activity in the form of emission lines on the ZPEG estimate of the photometric redshifts derived from Monte-Carlo simulation for $L_{[OII]} = 10^{40} \text{ erg.s}^{-1}$ (dots), and $L_{[OII]} = 10^{42} \text{ erg.s}^{-1}$ (open circles). The top panel shows the $z_{est} - z_{real}$ versus z_{real} , where the z_{real} is the real redshift and z_{est} is the estimated photometric redshift. In the plot of the bottom panel, we proceed to the same analysis with the stellar mass estimates.

dataset, we plot the distribution $\Delta z' = z_{ZPEG} - z_{SWIRE}$ of photometric redshifts as estimated by the ZPEG and SWIRE template libraries respectively for the normal (N/NL) and contaminating (BL) objects being detected in at least 7 bands (Fig. 4.10). Although the ZPEG and SWIRE libraries are built in a very different manner (Sec. 4.4), for the N/NL sources the distribution of $\Delta z'$ fits a normal distribution with a standard deviation of $\sigma(\Delta z') = 0.13$. This higher value is expected

as we compare two independent photometric redshift estimates, corresponding to a difference of factor $\sqrt{2}$ between $\sigma(\Delta z)$ and $\sigma(\Delta z')$, in agreement with the factor ~ 1.4 observed.

Sullivan et al. (2006) also discussed in detail the accuracies of the $SFR_{0.5}$ and stellar mass estimates. In the most extreme case of galaxies experiencing recent star formation events, they derive $q_{90}(\Delta \log(M/[M_{\odot}])) \sim 0.3$ and $q_{90}(\Delta \log(SFR/[M_{\odot}.yr^{-1}])) \sim 0.6$ for the stellar mass and SFR respectively, corresponding to standard deviations of $\sigma(\Delta \log(M/[M_{\odot}])) \sim 0.14$ and $\sigma(\Delta \log(SFR/[M_{\odot}.yr^{-1}])) \sim 0.28$. More importantly, the error bars as estimated by ZPEG based on the χ^2 statistics are consistent with the observed errors, suggesting that the uncertainties for the individual objects are properly estimated.

Using the stellar masses and photometric redshifts estimates, in the next paper of the series (Tasse et al. 2007 in prep), we will show that the stellar mass function, and radio luminosity function derived using our dataset are all consistent with previous results.

4.6.2 The influence of emission lines

The activity in the central core of powerful radio-loud AGN is known to produce luminous emission lines with $L_{[OII]} \sim 10^{40} - 10^{44} \text{erg.s}^{-1}$ (e.g. McCarthy 1993; Zirbel & Baum 1995).

In order to investigate whether these emission lines can influence the photometric redshift estimates, we generate a catalog of galaxies with SED taken randomly from the ZPEG SED library, corresponding to random stellar masses, age, star formation rate, and redshift. To each SED, we add emission lines with [OII] line luminosities between 10^{38} and $10^{44} \text{erg.s}^{-1}$, while other lines are generated considering the emission lines luminosity ratios given by McCarthy (1993). We generate the corresponding $u^*g'r'i'z'$ magnitudes, and estimate the photometric redshifts using ZPEG. In Fig. 4.12 we compare the true redshifts and stellar masses to the estimated ones, while Tab. ?? shows the statistics of the photometric redshifts and stellar masses. At $L_{[OII]} < 10^{40} \text{erg.s}^{-1}$, the influence of emission lines is negligible, and although there are a few outliers that is comparable to case in which there are no emission lines. As shown in Fig. 4.12, for $L_{[OII]} > 10^{42} \text{erg.s}^{-1}$, a systematic redshift offset seems to be introduced for some sources, while there are no systematic deviation on the stellar mass estimates. However, by using the photometric redshifts estimates by ZPEG, we estimate the radio power range of the sources in our selected sample (Sec. 4.5) to be $\log_{10}(P_{1.4GHz}/W.Hz^{-1}) \lesssim 26$ for $\sim 90\%$ of the sources. Using the [OII] line luminosity - radio power relation (McCarthy (1993), Best et al. (2005)), this radio power corresponds to $L_{[OII]} \lesssim 10^{40} - 10^{41} \text{erg.s}^{-1}$. We conclude that within the radio power range probed by our survey, the presence of emission lines should not significantly affect the photometric redshift estimates.

4.7 RADIO SOURCES' HOSTS PROPERTIES

In this section, we compare the distribution of the radio sources' optical hosts and normal galaxies in the parameter space.

Table 4.2: Influence of the presence of emission lines at the level L[OII] on the estimates of photometric redshifts and stellar masses. $q_{0.5}$ refers to the median value, while $q_{0.9}$ refers to the 90% quantile.

L[OII] [erg.s ⁻¹]	Δz		$\Delta \log(M/M_{\odot})$	
	$q_{0.5}$	$q_{0.9} - q_{0.5}$	$q_{0.5}$	$q_{0.9} - q_{0.5}$
< 38	-0.003	0.09	-0.03	0.45
40	-0.004	0.09	-0.04	0.45
42	0.008	0.20	-0.04	0.76
44	-0.027	0.34	-0.68	0.64

4.7.1 Basic observed properties

4.7.1.1 Optical properties

Fig. 4.13 shows the cumulative distribution of the i-band magnitude and z-r colour for the mean galaxy population and for the S1 radio selected sample (corrected for contamination as described in Sec. 4.3.3). The distribution of the m_i and $m_z - m_r$ parameters are very different for the true identifications and for the mean population. As expected $\theta(m_i)$ is well matched by the magnitude distribution of the identified sample, although there are more $m_i < 20$ galaxies than expected. Inspecting Fig. 4.3 we see that the error bars on $\theta(m)$ are quite large in that magnitude range. These results confirm that the optical identification has been conducted properly since the identified hosts are different from the mean population. Specifically, in the left panel, the m_i distribution of the radio sources' optical hosts is, on average, brighter than the mean population in the optical catalog by $\sim 2 - 3$ magnitudes. In the right panel, it can be seen that the radio sources' optical hosts are redder by a ~ 0.5 magnitudes.

Two effects can contribute to the differences between these distributions: (i) radio sources are known to be preferentially hosted by massive elliptical galaxies (eg. Best 1998) and (ii) the co-moving density of powerful radio sources is known to increase from the local universe to redshifts $z \sim 2 - 3$ by $\sim 2 - 3$ order of magnitude (Dunlop & Peacock 1990). These two effects cause the colour of radio sources to redden as seen in the right panel of Fig. 4.13.

4.7.1.2 Infrared properties

For the S2 sample, Fig. 4.9 shows the distribution of radio sources' hosts in the [3.6]-[4.5] versus [5.8]-[8.0] colour-colour space. Inside the region marked by dotted line, Stern et al. (2005) find 7% of normal galaxies, $\sim 40\%$ of the narrow-line AGN and $\sim 90\%$ of the broad-line AGN.

In order to compare the distribution of the radio sources' optical hosts in this diagram to non radio loud objects, we select a random sample of infrared sources in the SWIRE DR2 catalog with which we associate the u*g*r'i'z' optical objects closer than $1.5''$ (see Sec. 4.3.5). On this combined optical and infrared sample, we apply the same basic selection criteria described in Sec. 4.5.2 corresponding to a magnitude selection $18 < i < 24$. Retaining the objects that are detected in all the IRAC bands, we are left with 300 and 37 objects classified as N/NL and BL types respectively. Out of the BL and N/NL objects, 30 ($81 \pm 19\%$) and 36 ($12 \pm 2\%$) lie in the broad-line AGN area defined in Stern et al. (2005). These estimates are slightly different to the

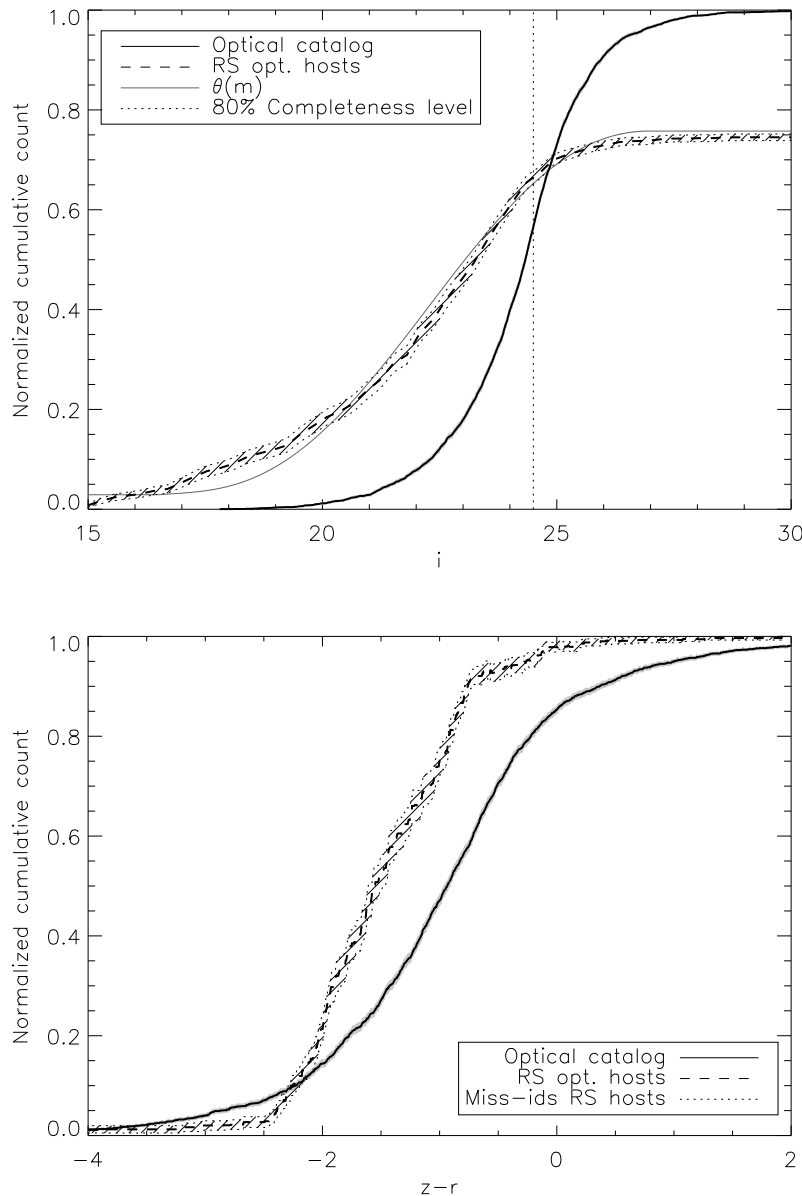


Figure 4.13: The top panel shows the i -band magnitude distribution for the true radio source optical identifications and for the mean galaxy population in the optical catalog. The overplotted grey line shows the function $\theta(m)$ that has been used to the likelihood ratios and reliability levels. The bottom panel shows the $m_z - m_r$ colours for these two samples.

fraction given by Stern et al. (2005). However, differences are expected as their optical magnitude selection criterion $R < 20$ is different from ours ($i > 18$, corresponding to $R \gtrsim 19$). Our samples populating the [3.6]-[4.5] versus [5.8]-[8.0] diagram have little optical overlap. Specifically we expect to select galaxies having higher redshifts on average.

The statistics of the radio sources' hosts classified as BL-type is in agreement with Stern et al. (2005) with 1 object over 10 (90%) lying in the broad-line AGN region. Out of the 38 N/NL-type

radio source hosts, 8 are in the broad-line AGN region, corresponding to a fraction of $\sim 21 \pm 8\%$, which is more than the $12 \pm 2\%$ found above for the normal galaxy population. This indicates that the mid-infrared spectrum of the radio selected population may be different from the normal galaxy population.

4.7.2 ZPEG outputs

We use the S1 sample selected as described in Sec. 4.5. Contamination from Type-1 AGN has been removed as discussed in Sec. 4.5.2. The normal galaxy comparison sample is built from a random sample of normal galaxies, to which we apply the basic cuts outlined in Sec. 4.5.1.

Since the SED templates used in ZPEG are defined using a common stellar population synthesis scheme, the observed output templates synthesised for different scenarios can overlap. For example, a young E and an old S0 look similar. Instead of relating template type to galaxy type, following Sullivan et al. (2006) we classify the galaxies into three groups on the basis of their specific star formation rate (*ie* the SFR per unit stellar mass). The specific SFR (sSFR) is a measure of how quickly the stars will be formed in a galaxy. Starburst galaxies will have high sSFR, whereas passively elliptical galaxies will have a zero sSFR. The first category contains the passively evolving galaxies with $sSFR \sim 0$ (*Class A*), and basically contains the early type galaxies of the Hubble classification. The second group is defined to comprise late type galaxies having an old evolved stellar population as well as young stars. We set the criterion on the sSFR as $-12 \leq \log(sSFR/[\text{yr}^{-1}]) \leq -9.5$ (*Class B*). The third and final class has $-9.5 \leq \log(sSFR/[\text{yr}^{-1}])$, and contains galaxies actively forming stars, such as dwarf and starburst galaxies (*Class C*).

The upper panel of Fig. 4.14 shows the distribution of the parameters derived with ZPEG for the radio source optical hosts and for the normal galaxies, for the three different $sSFR_{0.5}$ classes. The mean galaxy population is composed of $\sim 16\%$ of Class A (passively evolving galaxies), $\sim 21\%$ of Class B and $\sim 63\%$ of class C (actively evolving galaxies).

According to the results from the previous section, the radio source host galaxy population is largely biased towards passively evolving systems: $\sim 61\%$ are class A, $\sim 22\%$ are class B and $\sim 17\%$ are class C. Also, inside class B for instance, the radio loud galaxy population is biased towards lower sSFR than the average population.

In all the classes, the redshift distribution of the radio sources' hosts is found to be biased toward higher redshifts on average, than the normal population. The shape of the stellar mass distribution of all radio sources' hosts is similar in all A, B, and C classes while being significantly different to the normal galaxy population. Consistently with previous studies, the radio sources tend to be found in galaxies more massive than the average by a mean factor of $\sim 5 - 10$, with stellar masses between $\sim 10^{10}$ and $\sim 10^{11.5} M_{\odot}$. This confirms the validity of the stellar synthesis code used for our sample.

4.8 CONCLUSION

In this paper we have carried out the identification of 621 low frequency radio sources (Tasse et al. 2006) overlapping with the CFHTLS-W1 field (T02/T03 release). A proper use of the likelihood ratio method (Sutherland & Saunders 1992) and a good control over both the optical and radio

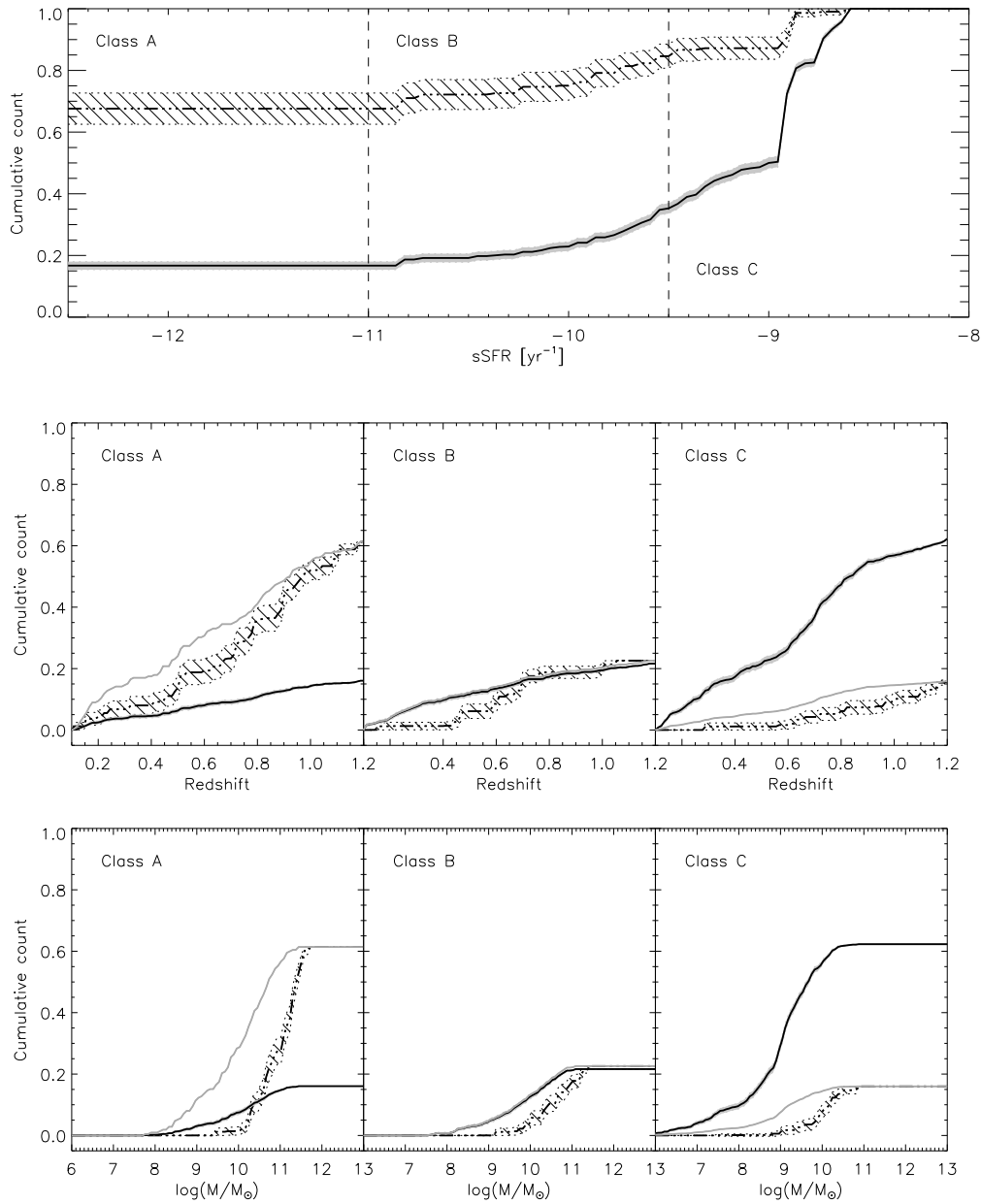


Figure 4.14: Upper panel: The specific star formation rate distribution of radio source identified hosts (dashed-dotted line), and the same distribution for the normal galaxy population (thick solid line). We have classified the population in three groups (Class A, B and C, see Sec. 4.7) on the basis of their $\text{sSFR}_{0.5}$ (specific star formation rate). ZPEG does not give $\text{sSFR}_{0.5}$ estimates below $\text{sSFR}_{0.5} \sim 10^{-11} \text{ yr}^{-1}$. The plots showing the redshift and mass distributions (middle and bottom panel), are normalised in each class to the fraction of galaxies in that class. In order to compare the shape of the distributions, the grey line shows the average galaxy population whose fraction is scaled to the radio emitting population. The radio emitter hosts are largely biased towards low sSFR. The middle panel shows the redshift distribution for the three classes of galaxies. The radio sources' hosts seem to be located in average at higher redshifts than the normal galaxies. The mass distribution shows the radio sources' hosts are largely biased towards higher stellar mass systems.

catalog quantities, allow us to derive estimates of probability of association with a given optical candidate. About 75% of the radio sources have been associated with an optical counterpart, which is a result consistent with both our Monte-Carlo estimate and previous results from other surveys. Using the infrared SWIRE survey catalogs, we have associated the radio sources' optical counterparts with their flux density measurements at 3.6, 4.5, 5.8 and 8.0 μm . Within our sample, radio sources' hosts are different from the average: they are redder and brighter, thereby showing that the optical identification has been conducted properly.

In order to have a good overall understanding of the identified sample, we have fitted SED templates to the flux density measurements using two very different approaches: the first is theoretical and gives quantitative information, the second is empirical and gives qualitative insights. In order to obtain a sample with reliable estimates of physical parameters, we reject the bright Type-1 AGN contaminating sources, and estimate the remaining contamination by faint Type-1 AGN to be $\sim 2\%$. Using the Stern et al. (2005) [3.6]-[4.5] versus [5.8]-[8.0] diagnostic diagram, we have shown that radio sources' hosts are mostly narrow-line Type-2 galaxies.

The physical parameters as estimated by ZPEG for the radio sources' hosts and the normal galaxies show strong differences. Specifically, the radio sources' hosts population is largely biased towards (i) passively evolving systems, and (ii) galaxies more massive than the average by a factor of $\sim 5 - 10$. These results are all consistent with previous studies of radio sources' hosts in low frequency radio surveys (Best et al. 1998; McLure & Dunlop 2000).

In the near future, we will study the influence and evolution of both the intrinsic and environmental host galaxy properties on the radio source fundamental properties.

ACKNOWLEDGMENTS

The authors have made use of the NASA/IPAC Extragalactic Database (NED), which is operated by the Jet Propulsion Laboratory, Caltech, under contract with the National Aeronautics and Space administration. The optical images were obtained with MegaPrime/MegaCam, a joint project of CFHT and CEA/DAPNIA, at the CFHT which is operated by the National Research Council (NRC) of Canada, the Institut National des Sciences de l'Univers of the Centre National de la Recherche Scientifique (CNRS) of France and the University of Hawaii. This work is based on data products produced at TERAPIX and at the Canadian Astronomy Data Centre as part of the CFHTLS, a collaborative project of NRC and CNRS. The authors thank Herve Aussel for useful discussions on the Terapix data release.

REFERENCES

- Benn, C. R. 1983, *The Observatory*, 103, 150
- Best, P. 1998, in ASP Conf. Ser. 146: *The Young Universe: Galaxy Formation and Evolution at Intermediate and High Redshift*, 482–+
- Best, P. N., Arts, J. N., Röttgering, H. J. A., et al. 2003, *MNRAS*, 346, 627
- Best, P. N., Kauffmann, G., Heckman, T. M., et al. 2005, *MNRAS*, 362, 25
- Best, P. N., Longair, M. S., & Roettgering, H. J. A. 1998, *MNRAS*, 295, 549
- Bruzual A., G. & Charlot, S. 1993, *ApJ*, 405, 538

- Cohen, A. S., Röttgering, H. J. A., Kassim, N. E., et al. 2003, *ApJ*, 591, 640
- Cool, R. J. 2006, in *American Astronomical Society Meeting Abstracts*, Vol. 209, American Astronomical Society Meeting Abstracts, 193.06–+
- Cram, L. E. 1998, *ApJ*, 506, L85
- de Ruiter, H. R., Arp, H. C., & Willis, A. G. 1977, *A&AS*, 28, 211
- Dunlop, J. S. & Peacock, J. A. 1990, *MNRAS*, 247, 19
- Evans, D. A., Worrall, D. M., Hardcastle, M. J., Kraft, R. P., & Birkinshaw, M. 2006, *ApJ*, 642, 96
- Fanaroff, B. L. & Riley, J. M. 1974, *MNRAS*, 167, 31P
- Fioc, M. & Rocca-Volmerange, B. 1997, *A&A*, 326, 950
- Hardcastle, M. J., Evans, D. A., & Croston, J. H. 2006, *MNRAS*, 370, 1893
- Hardcastle, M. J., Evans, D. A., & Croston, J. H. 2007, *MNRAS*, 376, 1849
- Heckman, T. M. & Kauffmann, G. 2006, *New Astronomy Review*, 50, 677
- Heckman, T. M., Kauffmann, G., Brinchmann, J., et al. 2004, *ApJ*, 613, 109
- Hine, R. G. & Longair, M. S. 1979, *MNRAS*, 188, 111
- Jackson, N. & Rawlings, S. 1997, *MNRAS*, 286, 241
- Kashikawa, N., Shimasaku, K., Yasuda, N., et al. 2004, *PASJ*, 56, 1011
- Kauffmann, G., Heckman, T. M., Tremonti, C., et al. 2003, *MNRAS*, 346, 1055
- Kroupa, P. 2002, *Science*, 295, 82
- Laing, R. A., Jenkins, C. R., Wall, J. V., & Unger, S. W. 1994, in *Astronomical Society of the Pacific Conference Series*, Vol. 54, *The Physics of Active Galaxies*, ed. G. V. Bicknell, M. A. Dopita, & P. J. Quinn, 201–+
- Laing, R. A., Riley, J. M., & Longair, M. S. 1983, *MNRAS*, 204, 151
- Le Borgne, D. & Rocca-Volmerange, B. 2002, *A&A*, 386, 446
- Lonsdale, C. J., Smith, H. E., Rowan-Robinson, M., et al. 2003, *PASP*, 115, 897
- Mathews, W. G. & Brighenti, F. 2003, *ARA&A*, 41, 191
- McCarthy, P. J. 1993, *ARA&A*, 31, 639
- McLure, R. J. & Dunlop, J. S. 2000, *MNRAS*, 317, 249
- Ogle, P., Whysong, D., & Antonucci, R. 2006, *ApJ*, 647, 161
- Oliver, S., Gruppioni, C., & Serjeant, S. 1998, *ArXiv Astrophysics e-prints*
- Pierre, M., Valtchanov, I., Altieri, B., et al. 2004, *Journal of Cosmology and Astro-Particle Physics*, 9, 11
- Polletta, M., Tajer, M., Maraschi, L., et al. 2007, *ArXiv Astrophysics e-prints*
- Pozzi, F., Gruppioni, C., Oliver, S., et al. 2004, *ApJ*, 609, 122
- Prestage, R. M. & Peacock, J. A. 1983, *MNRAS*, 204, 355
- Richter, G. A. 1975, *Astronomische Nachrichten*, 296, 65
- Rowan-Robinson, M., Babbedge, T., Surace, J., et al. 2005, *AJ*, 129, 1183
- Silva, L., Granato, G. L., Bressan, A., & Danese, L. 1998, *ApJ*, 509, 103
- Simpson, C., Martínez-Sansigre, A., Rawlings, S., et al. 2006, *MNRAS*, 372, 741

- Stern, D., Eisenhardt, P., Gorjian, V., et al. 2005, ApJ, 631, 163
- Sullivan, M., Howell, D. A., Perrett, K., et al. 2006, AJ, 131, 960
- Surace, J. A., Shupe, D. L., Fang, F., et al. 2004, VizieR Online Data Catalog, 2255, 0
- Sutherland, W. & Saunders, W. 1992, MNRAS, 259, 413
- Tasse, C., Cohen, A. S., Röttgering, H. J. A., et al. 2006, A&A, 456, 791
- Tasse, C., Röttgering, H. J. A., Best, P. N., et al. 2007, A&A, 471, 1105
- Whysong, D. & Antonucci, R. 2004, ApJ, 602, 116
- Wolstencroft, R. D., Savage, A., Clowes, R. G., et al. 1986, MNRAS, 223, 279
- Zirbel, E. L. & Baum, S. A. 1995, ApJ, 448, 521

APPENDIX

A CENTROID UNCERTAINTIES FOR CLASS 2 SOURCES

For the class 2 sources (Sec. 4.3.1), no strong *a priori* can be assumed on the location of the radio source optical hosts. The position of the optical host is estimated using the flux weighted radio position of the various Gaussian fitting components. The error bars associated with these positions are estimated using *a priori* statistical knowledge of the geometry of the radio lobes with respect to the radio core.

From the 3CR radio sources (Laing et al. 1983), Best et al. (2003) retrieved the mean asymmetry angle $\langle\phi\rangle = 6.8^\circ$, defined as 180° minus the angle between the radio core and the two radio lobes, and the mean separation quotient $\langle Q\rangle = \langle\theta_1/\theta_2\rangle = 1.42$, where θ_1 and θ_2 are the angular distances between the core and the two lobes. If ϕ is small then the angular distance between the two radio lobes R can be written as $R = \theta_1 + \theta_2$. The errors on the position of the radio source core are then:

$$\sigma_{\parallel} = \frac{1}{2}(\theta_1 - \theta_2) = \frac{1}{2}R \left(\frac{\langle Q\rangle - 1}{\langle Q\rangle + 1} \right) \quad (\text{A1})$$

and

$$\sigma_{\perp} = \frac{1}{2}R \tan \frac{\langle\phi\rangle}{2} \quad (\text{A2})$$

where σ_{\parallel} refers to the error on the position of the radio source host parallel to the radio axis (the line passing by the two radio lobes), and σ_{\perp} is the position error orthogonally to the radio axis. These estimates relate to the uncertainties on right ascension and declination as:

$$\sigma_{\alpha,radio}^2 = (\sigma_{\parallel} \sin PA)^2 + (\sigma_{\perp} \cos PA)^2 \quad (\text{A3})$$

and

$$\sigma_{\delta,radio}^2 = (\sigma_{\parallel} \cos PA)^2 + (\sigma_{\perp} \sin PA)^2 \quad (\text{A4})$$

where PA is the position angle of the radio axis on the sky, as estimated using the Gaussian fitted components. For a more detailed discussion, see Best et al. (2003).

B COMMENTS ON INDIVIDUAL SOURCES

B1 Class 3 sources

In this section, we give comments on the radio sources classified as Class 3 and Class 4 sources (see Sec. 4.3.1 for the classes definitions).

J0216.6-0527 (Fig. D1): Although only the eastern lobe has been detected by Tasse et al. (2007), a 3σ level component is clearly elongated along an east-west axis, suggesting the optical host to be an $m_r = 19.2$ galaxy.

J0217.6-0513 (Fig. D1): Only the east side 5σ lobe appears in the Tasse et al. (2006) source list, but radio contours at 3σ suggest the source is extended in the east-west direction. The non-detected west-side lobe corresponds to a $m_r = 20.51$ object that we chose as the optical identification.

J0217.7-0541 (Fig. D1): The radio source appear to be a small head-tail radio galaxy. The weighted radio position is $\sim 6 - 8''$ off the bright $m_i \sim 21$ galaxy that lies within the two radio lobes. We have identified this object as being the progenitor.

J0218.9-0401 (Fig. D1): Only the eastern lobe appears in the Tasse et al. (2006) 325 MHz catalog, although there appears to be a second lobe at the 4σ level. We have chosen the $m_r = 24.21$ object lying at the center to be the optical counterpart.

J0219.1-0357 (Fig. D1) The asymmetry angle of this source is obviously negligible, but the luminosity of the two radio lobes is quite different. This shifts the radio source centroid towards the south-east of the region. We choose the faint $m_i \sim 25.02$ source to be the optical host.

J0219.5-0507 (Fig. D1): As for J0216.6-0527, only one of the two lobes present in the data is detected by Tasse et al. (2007). Two objects might be considered to be possible candidates: the one overlapping with the lobe on the north-east and the $m_r = 21.1$ object lying in the middle of the two lobes. Since the radio morphology being likely an FR II, we have considered this later object to be the host.

J0219.9-0518 (Fig. D1): For this double lobe radio source, the flux weighted radio position is too far from the obvious very bright $m_i \sim 16$ host galaxy.

J0220.6-0417 (Fig. D1): This radio source appears to be a double lobe with the second undetected on the east-side of the image. The detected lobe points at an $m_r \sim 22$ galaxy that we have considered to be the optical counterpart.

J0223.4-0427 (Fig. D1): As for J0217.7-0541 the flux weighted central position is well off the obvious $m_i = 20.6$ optical counterpart.

J0224.2-0528 (Fig. D1): Although the identification is obvious, the flux weighted centroid does not lead to the selection of that candidate. We have chosen the bright $m_r = 20.8$ galaxy to be the optical host.

J0225.5-0524 (Fig. D1): Only the western radio component appears in the radio catalog, the eastern lobe being too faint. We consider the $m_r = 22.51$ object at the center to be the optical counterpart.

J0227.1-0543 (Fig. D1): This elongated east-west lobe points at a $m_r = 22.58$ object that we have considered to be the progenitor.

J0228.0-0400 (Fig. D1): This object, elongated along the north-south axis, has only one of its component detected. We have considered the bright object lying at the center to be the optical

counterpart.

J0228.2-0503 (Fig. D1): Similar to the case of J0219.1-0357 the asymmetry of the flux inside the two radio lobes makes the flux weighted centroid to be shifted towards the north, whereas the optical host is obviously the bright candidate lying at the center.

B2 Class 4 sources

J0219.7-0400 (Fig. D2): This object has been reported to be a promising radio halo or radio relic candidate in Tasse et al. (2006). The overlay with the i-band imaging shows that the diffuse radio emission corresponds to an overdensity of optical galaxies.

J0217.0-0449 (Fig. D2): This object is one of the most extreme radio sources in the combined radio sample. Its angular size is almost $2'$ and its spectral index is one of the steepest in the sample with $\alpha_{1400}^{325} = -1.65$. The two lobes are separated by almost $1'$ and no bright optical counterpart is present in that area. The most likely candidate has an r-band magnitude $m_r = 24.5$ and a photometric redshift estimate of $z_p = 0.88_{-0.08}^{+0.04}$, which would make the physical diameter at the radio source location to be $D_p \sim 0.92$ Mpc. We suggest that this radio source might correspond to the latest stage of the evolution of a radio source, when no more high energy electrons are injected into the IGM.

C TABLES

Table C1: The 15 objects for which the Gaussian fitting components were splitted and renamed. Positions appearing in columns 3 and 4 are the flux density weighted ones.

Original name	New name	RA	DEC
J0215.0-0458	J0215.0-0458	02 14 59.04	-04 58 11.32
	J0215.0-0457	02 14 58.92	-04 57 41.24
J0219.5-0539	J0219.5-0539	02 19 28.22	-05 39 48.21
	J0219.4-0539	02 19 25.20	-05 39 11.99
J0224.4-0425	J0224.4-0425	02 24 21.45	-04 25 48.22
	J0224.3-0425	02 24 20.47	-04 25 42.94
J0216.5-0447	J0216.6-0447a	02 16 35.06	-04 47 01.11
	J0216.6-0447b	02 16 37.30	-04 47 36.35
	J0216.5-0447	02 16 32.23	-04 47 41.59
J0218.0-0346	J0218.0-0346a	02 17 57.03	-03 46 02.64
	J0218.0-0346b	02 17 57.51	-03 46 48.95
J0219.4-0404	J0219.4-0404	02 19 25.75	-04 04 18.15
	J0219.4-0403	02 19 24.98	-04 03 52.49
	J0219.5-0403	02 19 27.49	-04 03 44.90
J0220.8-0510	J0220.8-0510	02 20 50.67	-05 10 17.85
	J0220.8-0509	02 20 50.98	-05 09 59.93
J0227.5-0411	J0227.6-0411	02 27 35.55	-04 11 22.83
	J0227.5-0411	02 27 30.45	-04 11 16.20
J0228.1-0408	J0228.2-0408	02 28 11.29	-04 08 42.76
	J0228.1-0408	02 28 08.72	-04 08 49.35
J0228.4-0435	J0228.4-0434	02 28 25.38	-04 34 39.56
	J0228.4-0435	02 28 22.18	-04 35 04.12
J0229.1-0507	J0229.1-0507a	02 29 08.64	-05 07 24.59
	J0229.1-0507b	02 29 05.75	-05 07 39.30
J0221.5-0402	J0221.5-0402a	02 21 30.20	-04 02 28.39
	J0221.5-0402b	02 21 27.44	-04 02 33.69
J0224.3-0505	J0224.3-0505	02 24 19.99	-05 05 25.03
	J0224.3-0506	02 24 18.19	-05 06 04.19
J0226.1-0459	J0226.1-0459a	02 26 04.56	-04 59 32.41
	J0226.1-0459b	02 26 03.65	-04 59 02.42
J0229.0-0504	J0229.0-0505	02 28 58.57	-05 05 21.97
	J0229.0-0504	02 28 57.44	-05 04 48.92

Table C2: The optical counterparts properties.

Name	Optical Properties							ZPEG			Infrared Properties				Radio properties					
	RA	DEC	u	g	r	i	z	z_p	$\log(M)$	$\log(S)$	3.6 μ m	4.5 μ m	5.8 μ m	8.0 μ m	74	240	325	610	$\log(P_{1.4})$	$\log(D_p)$
J0214.9-0451	02 14 54.91	-04 51 27.26	26.16	24.82	23.66	23.02	21.68	1.18	10.64	-∞	NC	NC	NC	NC	< 126.7	< 15.0	6.4	NC	25.0	.
J0215.0-0506	02 15 02.06	-05 06 00.32	> 25.30	23.94	22.16	21.38	20.65	0.99	10.92	-∞	NC	NC	NC	NC	< 121.1	134.1	116.6	NC	26.2	2.1
J0215.2-0449	02 15 11.20	-04 49 38.57	22.70	21.66	21.00	20.74	20.52	0.15	9.13	-9.89	NC	NC	NC	NC	< 128.2	25.5	9.2	NC	23.6	.
J0215.4-0344	02 15 22.92	-03 44 40.71	26.33	23.75	22.24	20.97	20.40	0.78	11.31	-∞	0.00	0.00	0.00	0.00	< 129.2	28.4	16.0	NC	25.1	.
J0215.6-0344	02 15 36.20	-03 44 22.79	24.82	24.20	23.88	22.35	21.38	1.10	10.57	-∞	19.60	19.63	> 19.84	> 19.53	< 130.1	61.4	45.0	NC	25.9	1.9
J0215.8-0433	02 15 45.67	-04 33 32.96	24.54	23.77	22.76	21.77	21.19	0.84	10.96	-10.85	19.23	19.44	> 19.84	19.61	< 118.5	< 11.5	4.5	NC	24.5	.
J0215.9-0442	02 15 51.15	-04 42 26.18	> 25.30	26.39	24.31	23.13	22.38	0.85	10.49	-∞	20.23	20.48	> 19.84	> 19.53	< 111.6	20.7	13.3	NC	25.3	1.6
J0216.1-0507	02 16 03.60	-05 07 56.24	22.97	22.57	21.97	21.12	20.49	1.01	10.85	-9.58	19.16	19.39	> 19.84	> 19.53	< 115.5	48.7	45.7	NC	25.9	1.8
J0216.1-0446	02 16 08.36	-04 46 43.86	23.95	22.43	21.04	19.97	19.42	0.90	11.23	-∞	18.55	18.92	19.03	19.16	< 109.5	38.9	28.8	NC	25.7	1.6
J0216.6-0454	02 16 34.80	-04 54 33.27	22.30	20.88	19.72	19.26	18.92	0.15	10.29	-∞	18.59	18.67	19.21	17.94	< 119.0	< 10.1	4.4	2.7	23.2	.
J0216.6-0447a	02 16 35.09	-04 47 00.69	25.07	24.16	> 24.90	22.62	22.28	0.72	10.28	-9.87	> 21.03	> 20.96	> 19.84	> 19.53	< 118.5	70.8	49.3	32.0	25.6	2.0
J0216.8-0427	02 16 49.55	-04 27 37.98	24.63	22.04	20.52	19.43	19.07	0.63	11.39	-∞	18.13	18.62	19.11	19.42	< 124.5	< 12.2	4.4	< 2.0	24.4	.
J0217.0-0516a	02 17 02.66	-05 16 18.44	> 25.20	24.91	23.43	22.36	21.77	0.94	10.35	-∞	20.34	20.70	> 19.84	> 19.53	< 121.5	< 13.1	4.6	2.7	24.5	.
J0217.1-0430	02 17 03.20	-04 30 40.35	> 25.60	24.04	22.66	21.12	20.58	0.73	11.25	-∞	0.00	0.00	0.00	0.00	< 126.5	< 11.0	4.8	< 1.7	24.4	.
J0217.7-0541	02 17 41.02	-05 41 50.22	26.38	24.33	22.43	21.14	20.42	0.83	11.35	-∞	18.76	19.19	19.10	> 19.53	535.9	212.4	171.2	168.2	26.3	2.5
J0217.8-0541	02 17 46.99	-05 41 36.39	22.99	22.14	20.91	19.92	19.49	0.69	11.38	-10.85	18.41	18.93	19.38	19.32	< 118.7	39.9	32.8	19.7	25.3	1.5
J0217.9-0512	02 17 54.09	-05 12 49.83	22.96	21.75	20.36	19.71	19.53	0.53	10.64	-∞	19.06	19.48	> 19.84	> 19.53	< 117.6	19.5	15.2	10.2	24.6	.
J0218.0-0346a	02 17 57.30	-03 46 00.73	22.42	21.54	20.70	19.98	19.55	0.56	11.09	-9.99	19.89	20.22	> 19.84	> 19.53	< 128.4	15.7	11.0	8.6	25.0	1.6
J0218.0-0344	02 18 01.20	-03 43 57.27	24.42	22.60	21.22	19.98	19.41	0.80	11.54	-∞	0.00	0.00	0.00	0.00	< 122.4	14.2	11.4	7.4	25.0	1.4
J0218.1-0538	02 18 03.34	-05 38 29.58	26.13	25.24	24.96	23.73	24.33	0.76	8.97	-8.92	> 21.03	> 20.96	> 19.84	> 19.53	< 115.9	26.1	27.0	20.6	25.4	1.4
J0218.2-0459	02 18 09.46	-04 59 45.79	22.40	22.15	21.65	21.08	20.90	0.71	10.20	-9.27	19.10	18.59	17.71	16.52	< 127.8	< 10.8	6.2	3.5	24.5	.
J0218.4-0516	02 18 22.45	-05 16 48.65	24.94	22.23	20.69	19.79	19.31	0.50	11.35	-∞	18.67	19.02	19.19	> 19.53	< 126.7	< 13.0	5.4	4.7	24.3	.
J0218.4-0542	02 18 22.64	-05 42 14.57	> 25.20	24.06	22.32	20.92	20.28	0.78	11.46	-∞	18.64	19.15	> 19.84	> 19.53	< 123.4	33.1	32.8	17.3	25.6	1.9
J0218.4-0525	02 18 23.50	-05 25 00.54	26.60	22.30	20.75	19.58	22.02	0.15	7.20	-8.74	18.11	18.56	18.78	19.25	< 119.0	< 13.8	5.7	6.8	23.7	.
J0218.9-0509	02 18 51.22	-05 09 08.61	27.62	23.79	22.36	21.37	20.84	0.92	10.64	-∞	20.16	20.55	> 19.84	> 19.53	< 126.4	71.8	53.9	40.1	25.8	.
J0218.9-0401	02 18 55.07	-04 01 34.44	> 25.60	25.77	24.30	23.40	23.39	0.67	9.27	-∞	> 21.03	> 20.96	> 19.84	> 19.53	< 126.2	9.9	10.5	5.6	24.7	1.9
J0219.0-0355	02 19 00.60	-03 55 56.57	24.55	24.36	23.58	22.90	22.33	0.99	10.36	-9.67	19.70	19.65	> 19.84	> 19.53	< 124.4	58.2	32.9	27.3	25.8	1.4
J0219.1-0459	02 19 06.65	-04 59 01.88	23.08	21.27	19.75	18.91	18.51	0.49	11.56	-∞	18.11	18.46	18.71	19.23	< 124.1	< 10.9	4.0	< 1.4	24.4	.
J0219.3-0552	02 19 18.31	-05 52 44.51	25.88	23.69	22.16	20.94	20.46	0.72	11.19	-∞	19.28	19.77	> 19.84	> 19.53	305.4	203.0	118.9	71.0	25.9	2.3
J0219.4-0539	02 19 25.49	-05 39 11.45	24.24	23.63	23.07	22.29	22.00	0.72	10.15	-9.48	> 21.03	> 20.96	> 19.84	> 19.53	< 135.4	97.7	76.7	44.2	25.7	.
J0219.4-0404	02 19 25.68	-04 04 20.46	> 25.60	23.50	21.60	20.24	19.64	0.78	11.66	-∞	18.27	18.85	19.02	> 19.53	< 123.7	12.3	11.7	6.4	25.1	1.7
J0219.5-0403	02 19 27.50	-04 03 43.27	25.79	23.14	21.67	20.44	20.01	0.71	11.16	-∞	19.01	19.52	> 19.84	> 19.53	< 124.0	NC	7.4	5.9	24.8	.
J0219.7-0448	02 19 44.53	-04 48 49.09	> 25.20	26.27	24.86	23.40	22.78	0.78	10.46	-∞	> 21.03	> 20.96	> 19.84	> 19.53	< 118.7	14.2	16.4	13.8	25.2	1.9
J0219.8-0437	02 19 50.63	-04 37 18.58	21.87	20.44	19.50	19.02	18.71	0.15	10.31	-∞	17.84	17.65	17.23	15.83	< 121.7	< 9.4	3.3	2.2	23.1	.
J0219.9-0444	02 19 51.63	-04 44 37.64	> 24.70	24.30	25.07	23.45	23.54	0.89	9.19	-9.04	> 21.03	> 20.96	> 19.84	> 19.53	< 119.0	< 12.5	6.2	2.7	24.6	.
J0220.2-0404	02 20 10.58	-04 04 20.04	> 25.40	24.59	22.80	21.50	20.90	0.79	10.99	-∞	19.52	19.95	> 19.84	> 19.53	< 117.5	< 7.9	5.0	3.5	24.5	.
J0220.3-0346	02 20 16.93	-03 46 04.26	> 25.40	24.67	24.22	22.86	23.23	0.79	9.33	-8.92	20.42	20.41	> 19.84	> 19.53	< 127.4	< 6.8	5.4	4.0	24.7	.
J0220.3-0557	02 20 18.80	-05 57 31.25	25.43	25.02	24.37	23.99	23.56	0.99	9.65	-9.27	> 21.03	> 20.96	> 19.84	> 19.53	< 134.6	< 13.9	7.5	< 3.5	25.1	.
J0220.4-0448	02 20 24.81	-04 48 13.91	24.55	24.91	> 25.00	22.77	21.93	1.06	10.31	-∞	> 21.03	> 20.96	> 19.84	> 19.53	< 119.6	< 9.6	3.2	< 1.3	24.5	.
J0220.5-0422	02 20 27.86	-04 22 50.88	22.06	20.35	19.16	18.62	18.35	0.19	10.77	-∞	18.58	18.79	19.54	19.03	< 126.2	< 8.0	5.2	4.2	23.2	.
J0220.5-0450	02 20 32.09	-04 50 04.74	23.21	23.08	22.74	21.98	21.49	1.02	10.10	-8.92	> 21.03	> 20.96	> 19.84	> 19.53	< 118.9	< 8.4	5.5	3.7	24.8	.
J0220.6-0409	02 20 34.84	-04 09 52.66	25.06	23.84	22.30	20.79	20.28	0.72	11.42	-∞	18.72	19.09	> 19.84	> 19.53	< 129.4	< 7.4	3.9	2.5	24.2	.
J0220.6-0408	02 20 36.06	-04 08 06.81	25.45	24.67	23.17	22.00	21.28	0.87	10.90	-∞	19.47	19.87	> 19.84	> 19.53	< 125.5	< 7.4	6.9	4.5	24.8	1.3
J0220.8-0510	02 20 50.62	-05 10 18.50	24.59	24.75	22.88	21.46	20.60	0.88	11.51	-∞	18.53	18.85	19.21	> 19.53	< 114.6	15.1	8.7	5.2	25.2	1.6
J0221.3-0457	02 21 18.41	-04 57 22.33	26.79	26.48	24.51	23.84	23.49	0.40	9.45	-∞	> 21.03	> 20.96	> 19.84	> 19.53	< 121.6	< 13.0	16.3	24.5	24.8	.
J0221.3-0344	02 21 19.41	-03 44 41.86	23.19	21.22	20.75	18.92	18.52	0.48	11.53	-∞	18.38	18.61	19.14	> 19.53	< 125.5	24.8	15.8	13.9	24.9	.
J0221.4-0405	02 21 21.38	-04 05 34.89	> 25.40	24.61	24.21	23.65	> 24.00	1.07	10.03	-9.35	> 21.03	> 20.96	> 19.84	> 19.53	< 133.1	< 6.9	4.9	< 1.7	24.8	.
J0221.4-0424	02 21 23.94	-04 24 16.34	24.98	24.26	23.23	22.65	21.74	1.16	10.48	-8.90	> 21.03	> 20.96	> 19.84	> 19.53	< 123.9	< 8.2	6.8	8.5	25.4	.
J0221.5-0504	02 21 27.44	-05 04 01.05	24.57	23.46	22.11	20.93	20.40	0.90	10.84	-∞	19.18	19.55	> 19.84	> 19.53	< 130.7	< 12.5	6.9	3.9	24.8	.
J0221.6-0409	02 21 33.28	-04 09 01.69	> 25.40	24.37	23.50	22.87	22.59	0.58	9.84	-9.73	> 21.03	> 20.96	> 19.84	> 19.53	< 123.7	25.9	23.2	18.5	25.1	1.3
J0221.7-0413	02 21 43.04	-04 13 43.65	24.04	24.06	23.37	21.86	21.80	0.82	9.97	-8.90	19.51	19.71	19.39	> 19.53	2405.6	1595.6	1269.7	1127.9	27.2	1.8
J0221.7-0404	02 21 43.71	-04 04 27.55	24.85	24.47	23.73	23.47	23.63	0.56	8.82	-8.61	> 21.03	> 20.96	> 19.84	> 19.53	< 120.1	< 7.3	7.0	< 1.8	24.4	.
J0221.9-																				

Name	Optical Properties							ZPEG			Infrared Properties				Radio properties					
	RA	DEC	u	g	r	i	z	z_p	$\log(M)$	$\log(S)$	3.6 μ m	4.5 μ m	5.8 μ m	8.0 μ m	74	240	325	610	$\log(P_{1.4})$	$\log(D_p)$
J0222.1-0448	02 22 03.99	-04 48 34.84	> 24.70	23.15	22.11	20.80	20.48	0.84	10.62	-∞	18.30	18.63	18.84	19.13	< 115.8	< 7.8	5.7	5.1	24.8	.
J0222.7-0402	02 22 44.33	-04 02 34.55	21.67	20.08	18.89	18.27	17.90	0.45	11.50	-10.85	> 21.03	> 20.96	> 19.84	> 19.53	< 121.6	< 5.8	3.4	8.9	24.2	.
J0222.8-0348	02 22 47.63	-03 48 13.78	25.09	24.94	24.36	23.88	22.60	1.19	9.95	-8.91	> 21.03	> 20.96	> 19.84	> 19.53	< 132.0	53.7	32.6	30.0	26.0	.
J0222.9-0432	02 22 51.12	-04 32 13.84	24.11	24.02	23.52	22.52	22.12	0.96	9.83	-8.92	19.76	19.89	> 19.84	> 19.53	< 117.1	< 6.9	5.6	3.6	25.0	.
J0222.9-0416	02 22 52.09	-04 16 46.47	23.96	23.26	22.58	21.81	21.44	0.70	10.43	-9.60	18.86	18.13	17.14	16.02	< 126.3	11.8	9.7	8.7	24.8	.
J0222.9-0525	02 22 54.11	-05 25 30.85	27.14	25.03	24.65	23.72	23.53	0.81	9.39	-9.01	21.01	20.84	> 19.84	> 19.53	< 109.6	< 10.5	7.0	< 1.7	24.7	.
J0222.9-0424	02 22 56.39	-04 24 48.05	23.91	23.35	22.22	21.42	21.06	0.60	10.45	-10.25	20.36	20.49	> 19.84	> 19.53	189.9	91.4	70.0	49.7	25.4	2.0
J0223.0-0407	02 22 58.03	-04 07 01.71	22.13	20.21	18.85	18.26	17.92	0.45	11.26	-∞	18.23	18.49	19.06	19.42	< 121.9	8.5	4.2	5.4	24.3	.
J0223.0-0409	02 23 01.11	-04 09 35.81	26.30	24.72	22.96	21.82	20.97	1.17	11.30	-∞	19.04	19.39	19.69	> 19.53	< 127.5	< 6.5	6.6	6.2	25.3	.
J0223.3-0458	02 23 16.66	-04 58 43.77	> 24.70	24.51	24.30	23.72	> 24.10	0.86	9.03	-8.63	> 21.03	> 20.96	> 19.84	> 19.53	< 116.3	< 9.7	5.7	3.9	24.7	.
J0223.4-0541	02 23 22.82	-05 41 48.18	24.43	24.17	23.78	23.13	> 24.20	1.12	9.91	-8.92	> 21.03	> 20.96	> 19.84	> 19.53	< 117.2	< 10.4	5.1	3.9	25.1	.
J0223.4-0427	02 23 25.30	-04 27 24.44	25.16	23.34	21.81	20.65	20.25	0.63	10.96	-∞	19.13	19.47	19.12	19.21	< 117.3	71.2	46.0	35.2	25.4	2.4
J0223.5-0401	02 23 32.33	-04 01 45.30	25.20	24.63	23.64	22.73	21.67	1.15	10.53	-∞	18.26	17.69	17.29	16.69	< 127.0	< 5.9	3.5	4.1	25.1	.
J0223.8-0551	02 23 48.09	-05 51 14.36	23.92	23.06	21.83	20.59	19.97	0.95	11.08	-∞	NC	NC	NC	NC	< 122.9	201.5	129.9	164.9	26.5	1.1
J0223.8-0531	02 23 49.80	-05 31 05.46	24.64	23.59	22.55	21.35	20.77	0.96	10.66	-∞	19.14	19.52	19.37	20.00	< 118.5	< 10.4	8.1	6.3	25.1	.
J0224.2-0350	02 24 10.79	-03 50 16.66	24.96	25.04	24.30	23.09	22.11	1.09	10.17	-8.90	19.60	19.66	> 19.84	> 19.53	< 117.9	31.3	18.7	13.2	25.6	.
J0224.2-0355	02 24 12.15	-03 55 57.42	22.00	20.83	19.70	19.17	18.84	0.44	10.98	-10.25	18.41	18.56	18.54	18.86	< 113.7	8.1	4.5	4.4	24.4	.
J0224.2-0528	02 24 13.94	-05 28 19.37	25.08	23.17	21.99	20.81	20.33	0.70	11.06	-∞	19.30	19.72	19.44	18.86	1309.1	765.3	494.5	308.9	26.5	2.7
J0224.5-0449	02 24 28.31	-04 49 52.08	> 25.00	21.30	19.91	19.06	18.67	0.50	11.44	-∞	18.28	18.60	18.86	> 19.53	< 129.4	27.4	24.2	17.2	25.0	2.1
J0224.5-0504	02 24 29.31	-05 04 22.08	24.26	24.56	24.20	23.32	24.31	0.78	8.98	-8.93	19.81	19.40	18.72	18.84	< 123.5	29.3	20.9	9.6	25.1	.
J0224.6-0354	02 24 32.95	-03 54 37.58	> 25.60	25.84	23.27	22.02	21.34	0.82	10.97	-∞	19.26	19.65	> 19.84	19.87	< 112.3	< 6.9	6.0	5.5	25.0	.
J0224.7-0347	02 24 39.41	-03 47 13.80	25.09	23.50	21.95	20.70	20.03	0.83	11.54	-∞	18.52	19.05	19.05	> 19.53	< 112.1	19.8	15.4	8.9	25.2	1.6
J0224.7-0357	02 24 39.68	-03 57 41.84	22.44	21.38	20.24	19.38	19.07	0.58	11.20	-10.73	17.90	18.32	18.27	18.31	< 112.7	< 6.9	3.2	1.7	23.9	.
J0224.8-0431	02 24 50.84	-04 31 40.47	24.80	23.21	21.78	20.46	19.89	0.78	11.51	-∞	18.61	19.09	19.32	> 19.53	< 108.6	< 6.5	5.0	2.3	24.4	.
J0225.0-0435	02 24 59.46	-04 35 36.21	25.40	24.95	23.58	22.42	21.49	1.10	10.68	-∞	19.98	20.35	> 19.84	> 19.53	< 118.6	< 6.9	5.0	3.5	25.0	.
J0225.1-0536	02 25 05.11	-05 36 47.97	23.29	22.23	21.17	20.20	19.73	0.69	11.28	-10.85	18.51	18.71	18.60	18.53	1464.9	876.3	596.3	429.5	26.6	1.4
J0225.1-0519	02 25 05.89	-05 19 59.33	24.47	23.84	22.67	21.36	20.87	0.89	10.57	-∞	19.47	19.84	> 19.84	> 19.53	< 121.7	13.2	9.0	7.7	25.1	.
J0225.1-0406	02 25 08.37	-04 06 54.18	24.32	23.60	22.91	22.62	22.28	0.28	8.99	-9.48	21.15	21.17	> 19.84	> 19.53	< 110.9	< 6.9	2.9	3.1	23.4	.
J0225.2-0401	02 25 09.15	-04 01 02.30	24.75	23.25	21.97	20.75	20.30	0.72	11.05	-∞	18.81	19.27	19.31	> 19.53	< 109.1	30.7	24.0	15.4	25.2	.
J0225.2-0509	02 25 09.71	-05 09 49.15	21.94	20.16	18.80	18.23	17.90	0.24	11.15	-∞	18.12	18.31	18.91	19.17	< 116.9	< 8.0	3.6	2.4	23.5	.
J0225.3-0424	02 25 16.39	-04 24 25.79	21.73	20.92	20.25	19.96	19.75	0.24	9.92	-9.51	19.35	19.55	> 19.84	18.84	< 111.0	< 6.4	3.9	2.0	23.2	.
J0225.3-0417	02 25 18.00	-04 17 53.43	21.98	21.57	21.09	20.45	20.16	0.72	10.55	-9.15	18.47	18.70	18.76	18.81	< 108.1	< 6.5	2.5	2.1	24.0	.
J0225.5-0524	02 25 27.14	-05 24 57.59	26.42	24.10	22.52	21.12	20.66	0.68	11.19	-∞	19.43	20.00	> 19.84	> 19.53	< 119.2	< 8.8	3.8	2.7	24.2	.
J0225.7-0417	02 25 40.10	-04 17 56.43	> 25.60	24.17	22.55	21.18	20.57	0.78	11.21	-∞	19.11	19.64	> 19.84	> 19.53	< 111.4	11.2	6.0	3.4	24.8	.
J0225.8-0415	02 25 45.80	-04 15 27.92	25.33	24.64	23.51	22.35	21.74	0.97	10.28	-∞	19.92	20.09	> 19.84	> 19.53	< 111.2	8.7	5.5	5.3	25.0	.
J0225.9-0500	02 25 53.14	-05 00 18.55	24.02	24.28	23.73	22.95	21.79	1.16	10.24	-8.91	19.60	19.68	> 19.84	19.86	< 113.5	11.3	14.0	3.3	25.4	.
J0225.9-0428	02 25 55.33	-04 28 49.44	26.90	25.90	24.29	23.13	22.33	0.99	10.70	-∞	> 21.03	> 20.96	> 19.84	> 19.53	< 109.5	29.9	23.5	16.5	25.5	2.3
J0226.0-0512	02 26 01.35	-05 12 07.96	21.81	20.00	18.68	18.13	17.87	0.22	11.09	-∞	18.06	18.27	18.70	18.95	< 118.9	< 7.0	3.5	1.9	23.5	.
J0226.1-0416	02 26 06.57	-04 16 32.07	23.33	22.25	20.90	20.25	19.99	0.46	10.72	-10.85	19.18	19.25	18.44	17.46	< 114.8	< 6.7	2.8	< 1.1	23.7	.
J0226.2-0403	02 26 12.68	-04 03 19.38	20.46	19.49	18.64	18.31	17.93	0.16	10.55	-10.35	17.57	17.42	17.18	16.00	< 110.2	9.5	8.4	5.0	23.3	.
J0226.3-0425	02 26 19.93	-04 25 35.76	26.19	25.56	24.70	23.57	22.67	1.08	10.04	-∞	19.26	19.20	19.70	> 19.53	301.8	171.6	115.1	72.0	26.3	1.9
J0226.4-0554	02 26 21.13	-05 55 04.43	24.81	24.18	23.84	22.79	22.11	1.05	10.03	-8.91	NC	NC	NC	NC	< 123.7	< 17.1	5.1	NC	24.8	.
J0226.6-0411	02 26 35.02	-04 11 26.58	25.33	25.31	24.57	23.10	22.12	1.08	10.23	-∞	18.98	18.99	19.21	19.54	< 115.1	< 7.5	3.7	< 1.2	24.6	.
J0226.6-0432	02 26 35.82	-04 32 28.13	25.68	24.55	22.87	21.85	21.41	0.77	10.47	-∞	19.78	20.30	> 19.84	> 19.53	< 113.3	< 7.0	3.7	2.0	24.5	.
J0226.8-0351	02 26 50.42	-03 51 28.77	21.48	19.87	18.99	18.52	18.26	0.11	10.22	-∞	NC	NC	NC	NC	< 110.7	< 11.5	5.8	< 1.2	22.7	1.3
J0227.0-0555	02 26 59.20	-05 55 46.48	24.11	24.03	23.31	21.97	21.36	0.99	10.33	-8.90	NC	NC	NC	NC	2462.8	NC	1017.2	NC	27.1	2.2
J0227.3-0549	02 27 15.25	-05 49 59.24	22.18	20.33	19.03	18.43	18.05	0.45	11.24	-∞	NC	NC	NC	NC	< 122.4	NC	6.3	< 2.5	24.3	.
J0227.4-0433	02 27 22.74	-04 33 50.74	21.92	21.25	20.35	19.76	19.45	0.55	11.05	-9.70	18.45	18.82	18.76	18.48	< 115.7	10.3	6.4	3.9	24.3	.
J0227.4-0512	02 27 23.07	-05 12 42.88	24.68	25.88	24.06	22.88	22.67	0.79	9.69	-∞	19.69	19.97	> 19.84	> 19.53	< 114.1	22.8	3.6	3.5	24.8	.
J0227.9-0343	02 27 53.52	-03 43 54.77	NC	24.61	24.18	23.78	NC	0.67	8.72	-8.86	NC	NC	NC	NC	< 126.7	23.5	19.3	12.1	25.0	1.6
J0228.1-0408	02 28 08.53	-04 08 49.59	NC	24.75	24.07	23.47	NC	0.65	9.33	-9.26	NC	NC	NC	NC	< 117.5	14.1	11.9	7.9	24.8	.
J0228.2-0503	02 28 14.07	-05 02 59.55	NC	20.18	18.71	18.09	NC	0.39	11.51	-∞	17.72	17.94	18.28	18.59	< 117.7	53.6	50.0	22.0	25.0	1.9
J0228.2-0433	02 28 14.15	-04 33 30.89	NC	21.81	20.28	19.35	NC	0.51	11.25	-∞	NC	NC	NC	NC	< 119.3	< 6.6	5.3	3.5	24.1	.
J0228.4-0453	02 28 22.39	-04 53 36.54	NC	23.09	21.98	21.36	NC	0.60	9.99	-9.58										

Name	Optical Properties							ZPEG			Infrared Properties				Radio properties					
	RA	DEC	u	g	r	i	z	z_p	$\log(M)$	$\log(S)$	3.6 μ m	4.5 μ m	5.8 μ m	8.0 μ m	74	240	325	610	$\log(P_{1.4})$	$\log(D_p)$
J0228.6-0505	02 28 38.47	-05 05 12.65	NC	20.74	19.22	18.58	NC	0.32	11.26	-∞	NC	NC	NC	NC	< 128.6	< 7.0	5.8	3.8	24.3	.
J0228.6-0406	02 28 38.51	-04 06 48.28	NC	21.11	19.80	19.11	NC	0.63	10.86	-8.90	NC	NC	NC	NC	< 129.3	37.5	30.0	25.6	25.4	.
J0229.1-0421	02 29 05.01	-04 21 22.25	NC	21.61	20.36	19.46	NC	0.67	10.86	-∞	NC	NC	NC	NC	< 129.8	32.2	21.4	12.7	25.1	.
J0229.1-0510	02 29 07.80	-05 10 14.67	NC	21.51	20.43	19.89	NC	0.46	10.89	-9.99	NC	NC	NC	NC	< 131.6	17.0	8.4	3.2	24.3	.
J0229.3-0403	02 29 17.22	-04 03 28.37	NC	22.27	21.05	20.00	NC	1.04	11.45	-∞	NC	NC	NC	NC	< 137.7	36.1	24.3	14.8	25.6	1.4
J0229.6-0440	02 29 35.64	-04 40 11.08	NC	22.89	21.38	20.16	NC	0.76	11.37	-∞	NC	NC	NC	NC	< 122.4	< 7.8	5.3	NC	24.5	.
J0229.7-0531	02 29 39.86	-05 31 53.72	NC	21.76	20.49	19.62	NC	0.66	10.77	-∞	NC	NC	NC	NC	< 125.4	< 10.6	5.7	< 2.6	24.7	.
J0230.0-0359	02 30 02.72	-03 59 35.12	NC	24.20	22.77	21.75	NC	0.59	10.37	-∞	NC	NC	NC	NC	< 129.6	< 9.5	5.5	NC	24.3	.
J0230.1-0512	02 30 04.47	-05 12 09.69	NC	23.49	22.06	20.89	NC	0.70	10.95	-∞	NC	NC	NC	NC	< 127.2	36.5	24.7	NC	25.1	1.3
J0230.1-0457	02 30 07.15	-04 57 16.12	NC	22.64	21.16	20.19	NC	0.53	10.90	-∞	NC	NC	NC	NC	< 125.0	43.6	25.2	NC	25.2	1.8
J0230.2-0457	02 30 11.47	-04 57 44.03	NC	22.77	21.86	20.96	NC	0.69	10.66	-9.89	NC	NC	NC	NC	< 124.9	22.1	13.1	NC	25.0	1.6
J0230.5-0442	02 30 27.33	-04 42 44.57	NC	22.66	21.09	19.94	NC	0.91	11.36	-∞	NC	NC	NC	NC	< 130.2	9.1	6.6	NC	25.0	.
J0230.5-0410	02 30 27.48	-04 10 36.60	NC	22.58	21.74	21.43	NC	0.60	9.60	-8.93	NC	NC	NC	NC	< 132.4	< 11.3	13.9	NC	24.6	1.3

Description of columns:

1. Radio source Name.
2. Optical counterpart right Ascension (J2000).
3. Optical counterpart declination (J2000).
4. u-band magnitude. Quote 'NC' means the field has not been observed in that band.
5. g-band magnitude.
6. r-band magnitude.
7. i-band magnitude.
8. z-band magnitude. Quote 'NC' means the field has not been observed in that band.
9. Photometric redshift as estimated by ZPEG.
10. Stellar mass as estimated by ZPEG in logarithm base-10 scale.
11. Specific SFR as estimated by ZPEG in logarithm base-10 scale.
12. 3.6 μ m magnitude (AB). Tag 'NC' (standing for 'Not Covered') has been used when the location of the object is not overlapping with the SWIRE field. Tag 'NI' stands for 'Not investigated', and is used when the object has no optical counterpart, so we didn't investigate if either the radio source has an IRAC counterpart. We have used the same notation for the columns below.
13. 4.5 μ m magnitude (AB).
14. 5.8 μ m magnitude (AB).
15. 8.0 μ m magnitude (AB).
16. Total flux density of the radio source at 74 MHz in mJy.
17. Total flux density of the radio source at 240 MHz in mJy.
18. Total flux density of the radio source at 325 MHz in mJy.
19. Total flux density of the radio source at 610 MHz in mJy.
20. Radio power in W/Hz in logarithm base-10 scale.
21. Physical diameter in kpc in logarithm base-10 scale.

D OVERLAYS

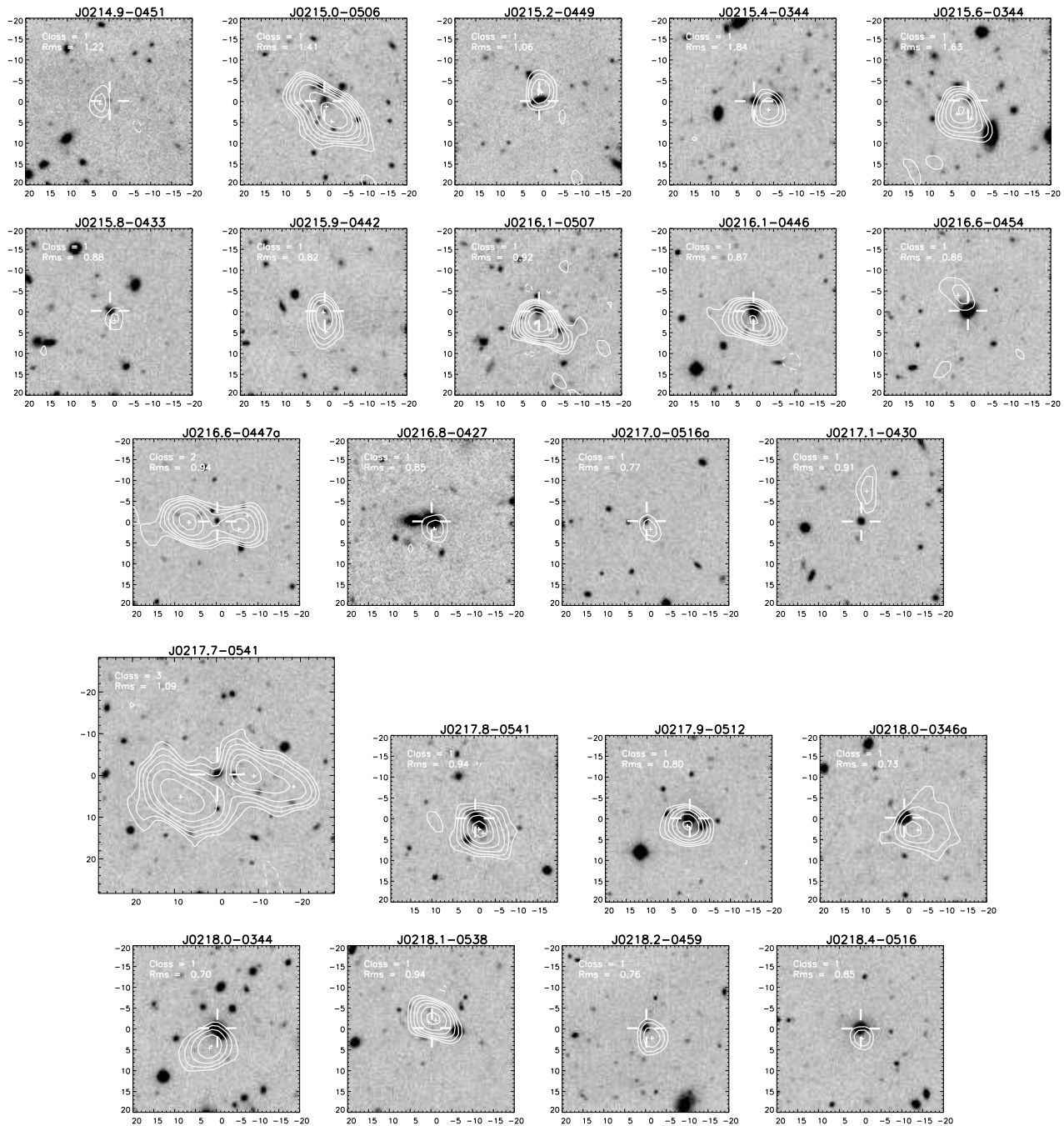


Figure D1: The optical identifications in the S2 sample. Greyscale: The i-band image image. Axes are labeled in arcsecond. In contour: The radio contours drawn for the 325 of 610 MHz maps at levels of $3\sigma_{local} \times 1, 1.4, 2, 2.8, 4, \dots$. The local noise σ_{local} appears in each overlay, and is in units of mJy.beam^{-1} . The cross indicates the position of the optical identification. Small crosses indicate the positions of the Gaussian fitting components appearing in Tasse et al. (2006) source list, used for the centroid position calculation.

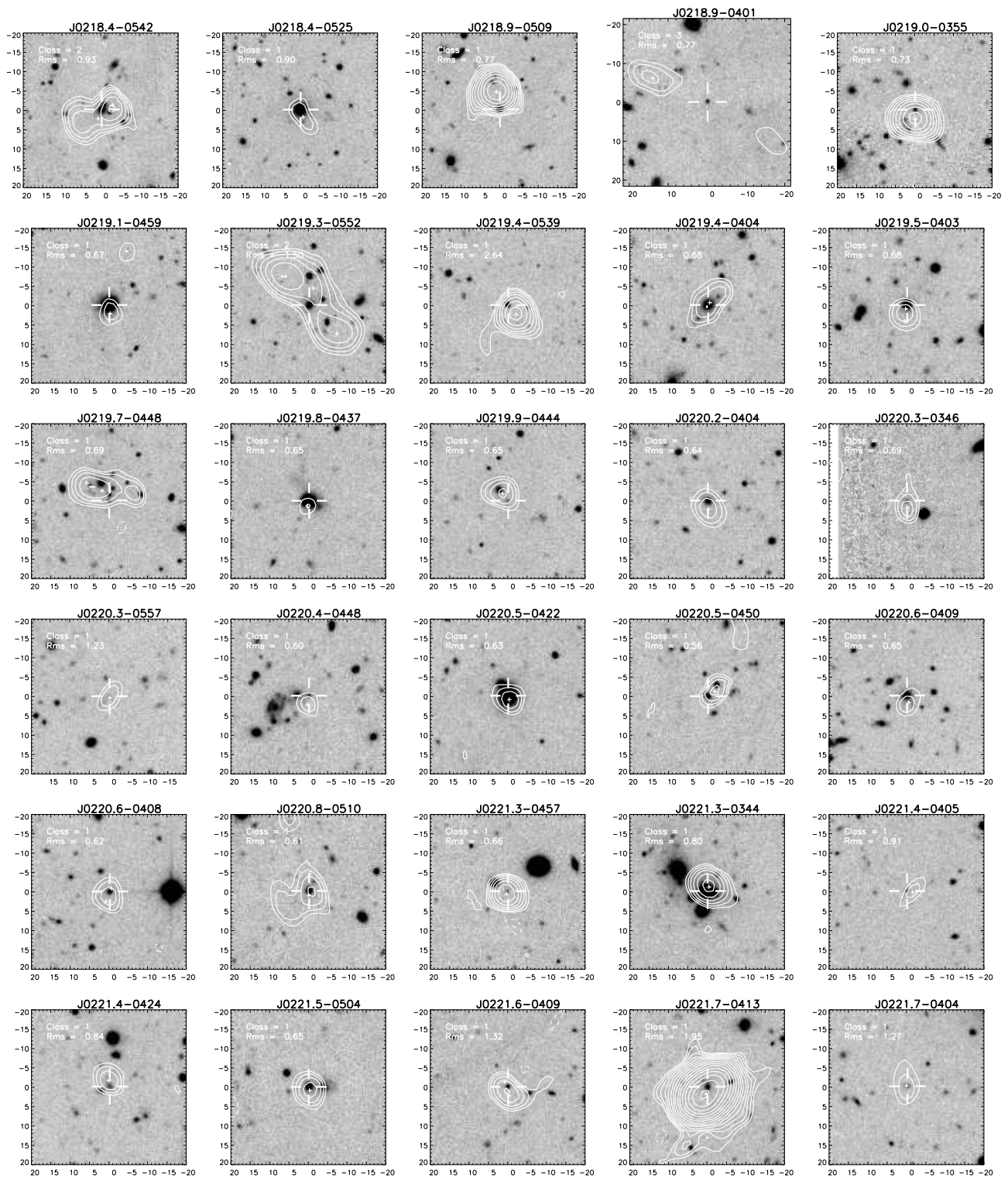


Figure D1: Continued.

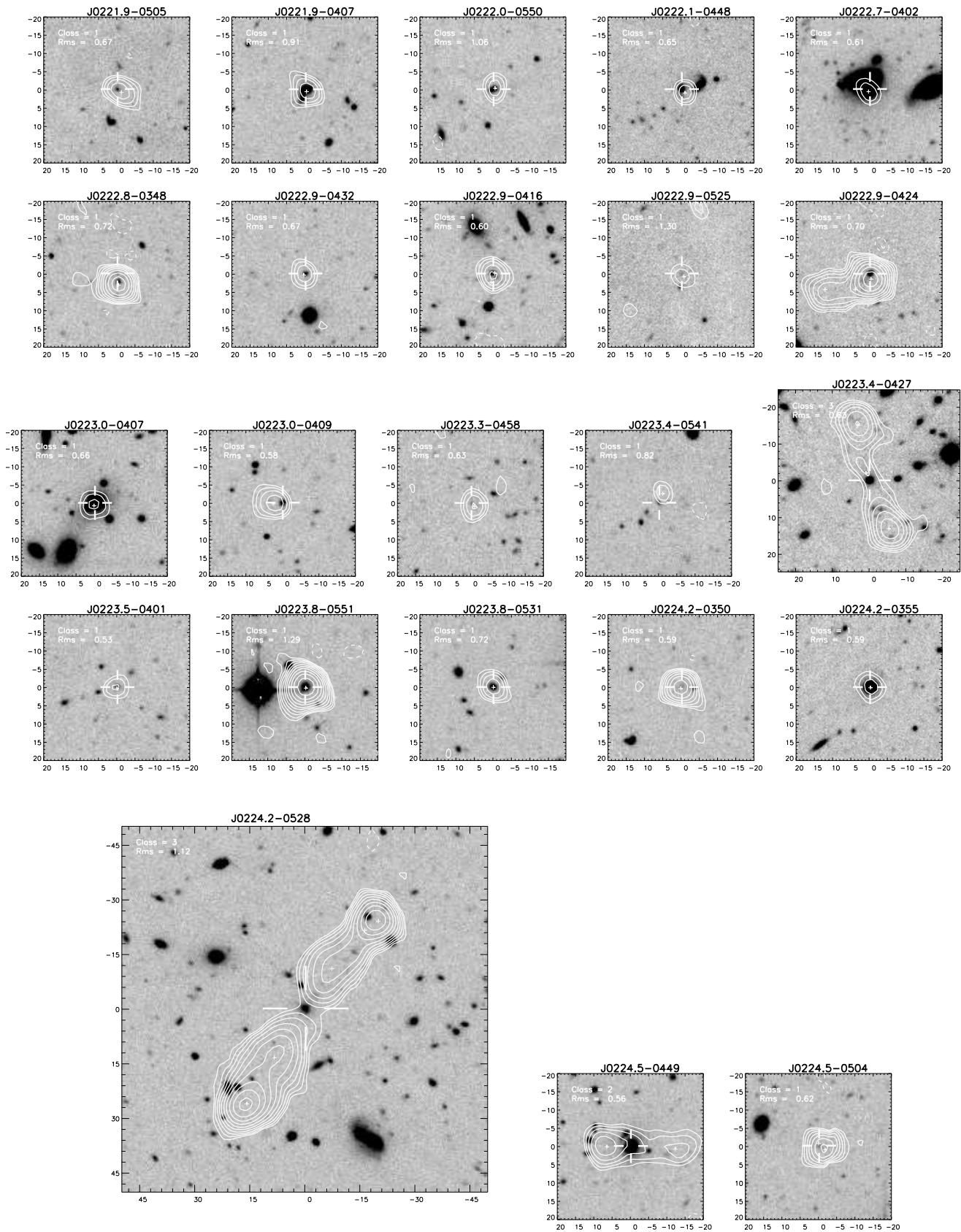


Figure D1: Continued.

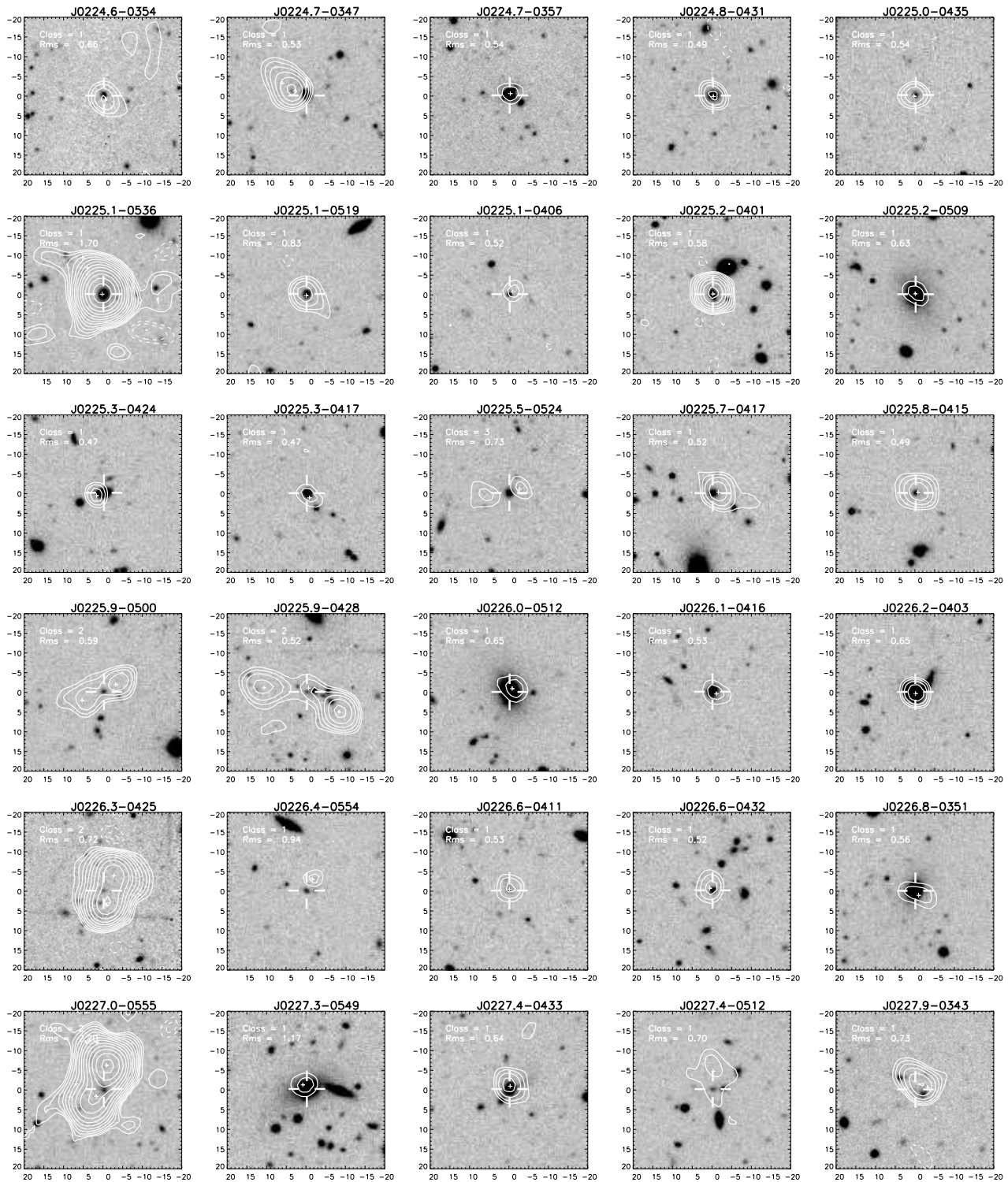


Figure D1: Continued.

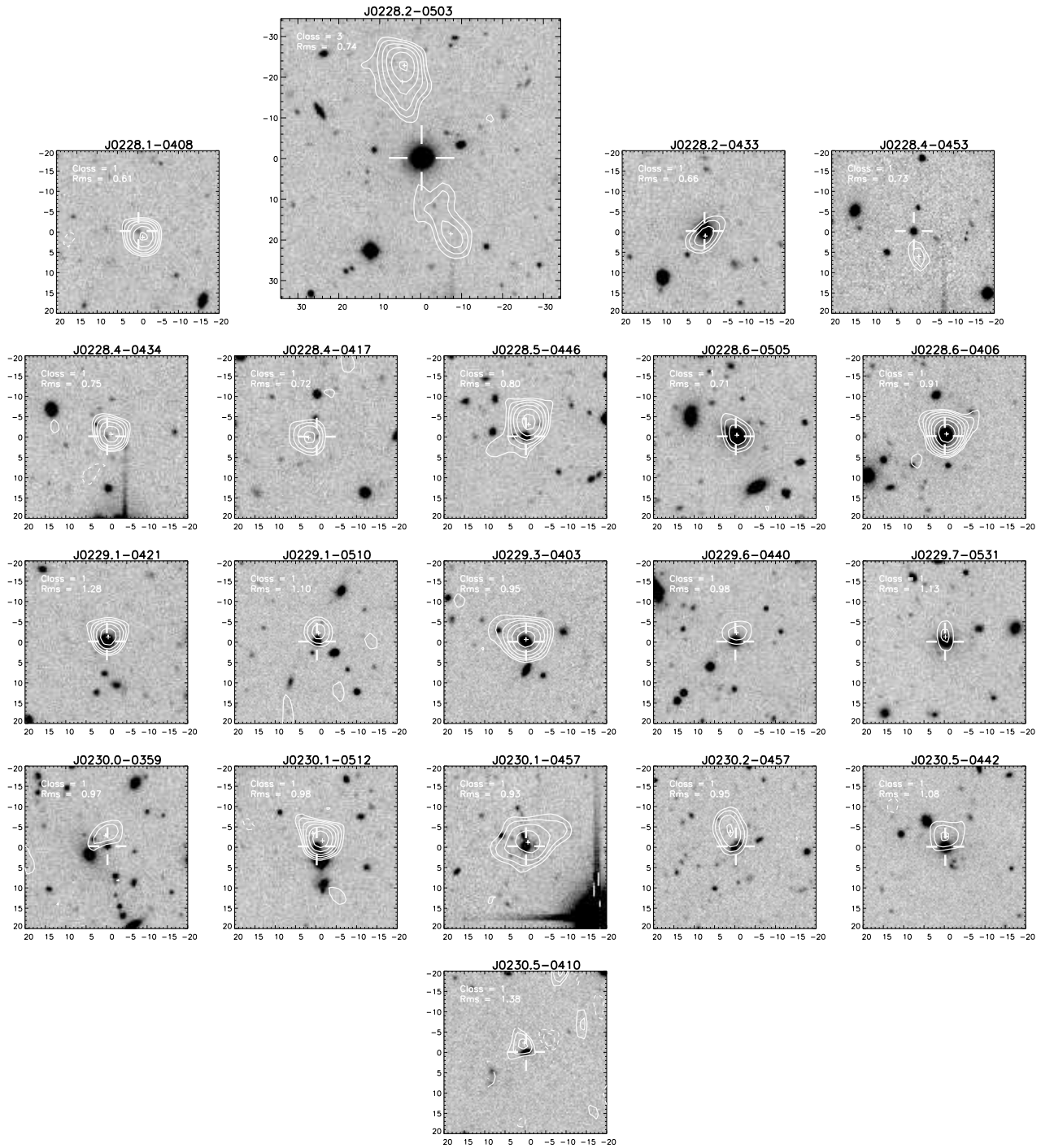


Figure D1: Continued.

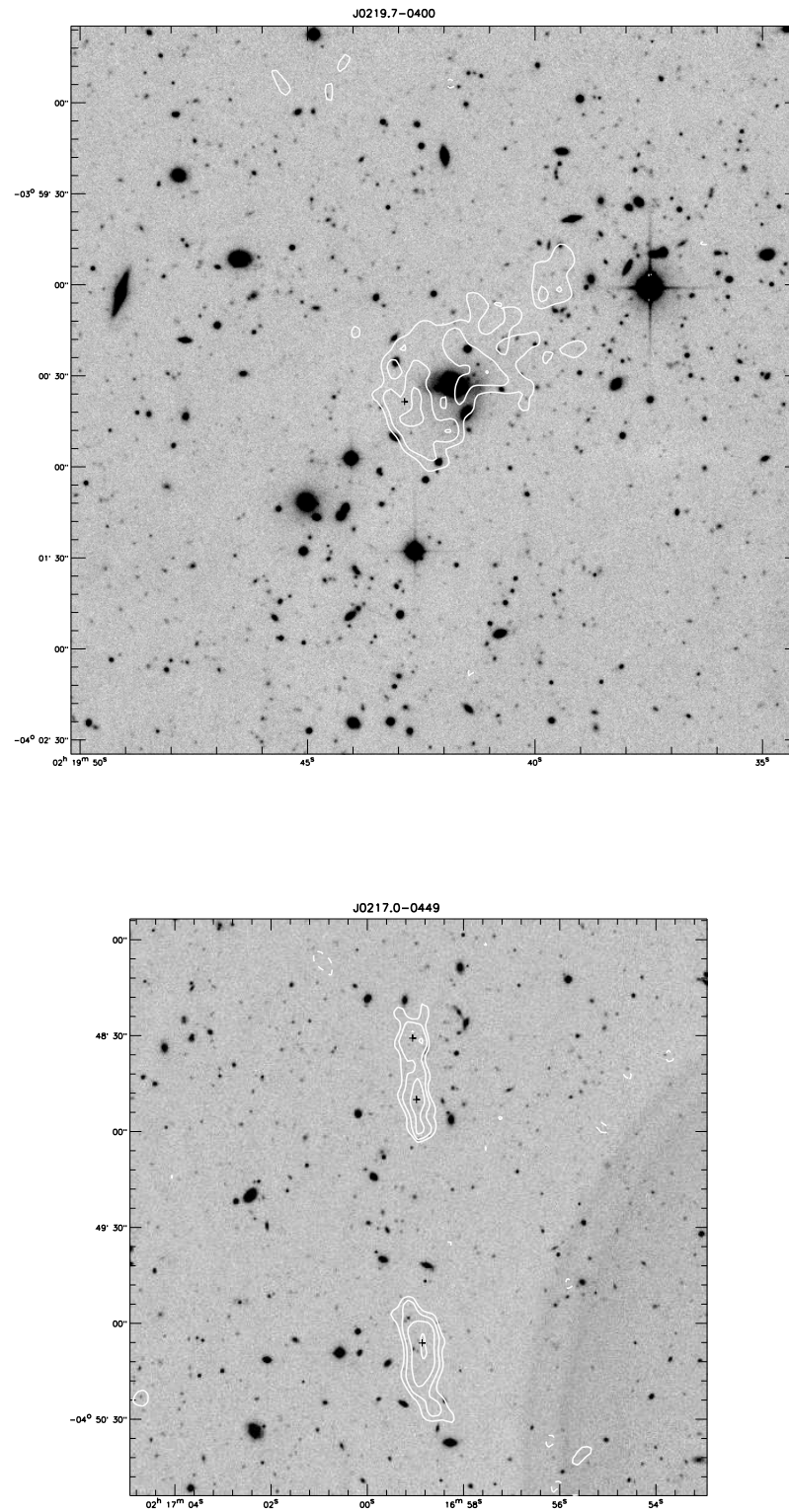


Figure D2: Greyscale: The *i*-band image. In contour: The 325 MHz contours drawn at levels of $3\sigma_{local} \times 1, 1.4, 2, 2.8, 4, \dots$. Small crosses indicate the positions of the Gaussian fitting components appearing in Tasse et al. (2006) source list, used for the centroid position calculation. The object on the top is the radio halo/relic candidate reported in Tasse et al. (2006). The objects on the bottom image have a spectral index $\alpha_{1400}^{325} = -1.65$.

CHAPTER 5

Radio-loud AGN in the XMM-LSS field: a dichotomy on environment and accretion mode?

C. Tasse, P. N. Best, H. Röttgering, D. Le Borgne

Submitted

Although the unified scheme of active galactic nuclei (AGN) gives a good description of the observed properties of radio quiet AGN, it does not explain many features of radio loud AGN. Several authors have argued that optically active and radio loud AGN correspond to different modes of accretion (“Quasar mode” versus “Radio mode”) that are triggered by different physical mechanisms.

In this third paper of the series we independently study the internal and environmental properties of the radio sources’ optical hosts sample described in Tasse et al. (2007). We do this by building a comoving scale dependent overdensity parameter, based on the photometric redshifts probability functions, and use it to constrain the small (~ 75 kpc) and large (~ 450 kpc) scale environments of radio sources independently from their stellar mass estimates. We compare our results with other surveys, confirming the robustness of our stellar mass and photometric redshifts estimates. The results of this paper support the picture in which the comoving evolution of radio sources in the redshift range $\lesssim 1$ is caused by two distinct galaxy populations, where radio loudness is triggered by two different mechanism. The first component of this population is made of massive elliptical galaxies, lying in galaxy groups or clusters. Their radio loudness is triggered by the cooling of the hot gas in their atmosphere. The second population are star forming, low stellar masses ($M \lesssim 10^{11} M_{\odot}$) systems, and lie in large scale underdensities.

5.1 INTRODUCTION

Active galactic nuclei (AGN) have regained attention in the last decade since they are thought to play a major role in the framework of galaxy formation. During their short lifetime, the enormous amount of energy they produce in the form of ionising radiation or relativistic jets can have a significant effect on their small-scale (internal) and large scale (external) surroundings. It appears from semi-analytical models and high resolution numerical simulations that the AGN energetic feedback is a vital ingredient for reproducing some of the observed features of the Universe, such as the stellar galaxy mass function (Croton et al. 2005; Best et al. 2006), or the black hole mass versus bulge mass relationship (Gebhardt et al. 2000; Springel et al. 2005a).

The unified scheme gives a good description of the observed properties of radio-quiet AGN. In this picture, the nuclear activity is produced by matter accreted onto a super-massive black hole, with an optically thick dusty torus surrounding it. The most powerful radio sources also follow the unified scheme, but there is a subset of radio loud AGN (especially at low radio power) for which the unified scheme does not seem appropriate: these sources lack infrared emission from the dusty torus (Whysong & Antonucci 2004; Ogle et al. 2006), as well as luminous emission lines (Hine & Longair 1979; Laing et al. 1994; Jackson & Rawlings 1997) and accretion related X-ray emission (Hardcastle et al. 2006; Evans et al. 2006). These observations are supported by recent results from large surveys (Best et al. 2005) indicating that low-luminosity radio-loud and radio-quiet AGN phenomenon are statistically independent. Many authors have argued that the low luminosity radio-loud and the optically active AGN correspond to two different accretion modes (“Radio mode” vs “Quasar mode”). In this picture, the quasar mode is radiatively efficient, and is caused by accretion of cold gas onto the super-massive black hole, while the radio mode results from the accretion of hot gas and is radiatively inefficient (see Hardcastle et al. 2007, for a discussion). As we show in this paper, the nature of the processes that trigger the black hole activity might be important in giving rise to these two AGN modes.

It has often been proposed that galaxy mergers and interactions both trigger a starburst and fuel the central super-massive black hole. Although the situation remains controversial for the low luminosity optically active AGN (Veilleux 2003; Schmitt 2004), observations of large samples of optically-selected AGN from the Sloan Digital Sky Survey show clear evidence that the luminous optically active AGN are associated with young stellar populations (Kauffmann et al. 2003). At the extreme end, this scenario is supported by observations of ultra-luminous infrared galaxies (ULIRGs, Sanders & Mirabel 1996), that are in general associated with galaxy mergers, and have bolometric luminosities and luminosity function similar to that of quasars (Sanders et al. 1988a), while some ULIRGs hide a buried AGN in their nucleus (eg. Sanders et al. 1988b). High resolution numerical simulations (Springel et al. 2005a,b) have consistently shown that the AGN activity remains obscured during most of the starburst and AGN activity phase. However, at low redshift, low-luminosity radio-loud AGN are seen to be preferentially hosted by massive elliptical galaxies, that tend to be found in richer, cold-gas poor environments, where gas-rich galaxy mergers are less likely to occur. The cooling of the hot X-ray emitting gas observed in the atmospheres of massive elliptical galaxies (Mathews & Brighenti 2003) has been proposed as an alternative triggering process to galaxy mergers. Based on a large sample of radio sources in the SDSS, Best et al. (2005) argued that the gas cooling rate has the same dependence on stellar mass as the fraction of low luminosity radio-loud galaxies. This suggests that the gas that has radiatively cooled from the X-ray emitting atmosphere may trigger the AGN activity.

In this paper, we study the properties of a well-controlled sample of ~ 110 radio loud AGN situated at $z \lesssim 1.2$, to put constraints on the triggering mechanisms, and the evolution of the radio-loud AGN population. Our results support the picture in which galaxy mergers and gas cooling from the hot atmosphere of massive ellipticals compete to trigger the quasar and the radio mode respectively (Hardcastle et al. 2007). The evolution of these two processes through cosmic time might play an important role in the evolution of the radio luminosity function.

In Section 5.2, we present the sample, and its associated parameters. In Section 5.3, we build the stellar mass function of normal galaxies and radio sources' hosts, and derive a radio loud fraction (f_{RL}) versus stellar mass relation equivalent to that which has been estimated at low redshift in the SDSS (Best et al. 2005). In Section 5.4, we construct a scale dependent overdensity parameter that allows us to study the environment of radio sources independently from their intrinsic properties estimates. We discuss the results in Section 5.5.

5.2 A SAMPLE OF RADIO SELECTED AGN IN THE XMM-LSS FIELD

In this section we briefly introduce the XMM-LSS survey, and the sample of radio sources that has been described in full detail in Tasse et al. (2007a).

The XMM-Large Scale Structure field (XMM-LSS) is a 10 square degree extragalactic window observed by the XMM-Newton X-ray satellite in the 0.1 – 10 keV energy band. The XMM-LSS area has been followed up with a broad range of extragalactic surveys. The Wide-1 component of the Canada France Hawai Telescope Legacy Survey (CFHTLS-W1) will image 7×7 degree² in the 5 broad band u*g*r'i'z' filters, reaching an i-band magnitude limit of $i_{AB} \sim 25$. As part of the Spitzer Wide-area InfraRed Extragalactic legacy survey (SWIRE, Lonsdale et al. 2003), the XMM-LSS field was imaged in 7 infrared bands from 3.6 to 160 μm over ~ 9 degree² (see Pierre et al. 2004, for a layout of the associated surveys). Low frequency radio surveys of the XMM-LSS field have been carried out with the Very Large Array (Tasse et al. 2006) at 74 and 325 MHz, and with the Giant Meterwave Radio Telescope (GMRT) at 230 and 610 MHz (Tasse et al. 2007b).

In Tasse et al. (2007a) we derived estimates of photometric redshifts, stellar masses (M), and specific star formation rates $sSFR_{0.5}$ (averaged over the last 0.5 Gyr) for $\sim 3 \times 10^6$ galaxies in the CFHTLS-W1 field, using the ZPEG photometric redshift code (Le Borgne & Rocca-Volmerange 2002). We estimated the uncertainties were typically $\sigma(z) \sim 0.1$, $\sigma(\log(M/[M_{\odot}])) \sim 0.15$ and $\sigma(\log(sSFR_{0.5}/[\text{yr}^{-1}])) \sim 0.3$.

We matched the radio sources detected at 230, 325, and 610 MHz (Tasse et al. 2006, 2007b) with their optical counterpart using the the CFHTLS optical images. To do this we used a modified version of the likelihood ratio method described in great detail in Sutherland & Saunders (1992), which allows us to derive for each radio source i , a probability $P_{id}^i(j)$ of association with a given optical candidate j . Using Monte-Carlo simulations, we have quantified and corrected for the contamination from missidentifications. Each optical candidate was also cross-identified with infrared SWIRE sources at 3.6, 4.5, 5.8, 8.0 and 24 μm .

In order to select a subsample of objects having reliable photometric redshifts estimates, we applied a few basic cuts to the identified sample, rejecting the masked, saturated, and point-like objects. Furthermore, the objects that did not satisfy the following properties were rejected:

$$- 18 < i < 24$$

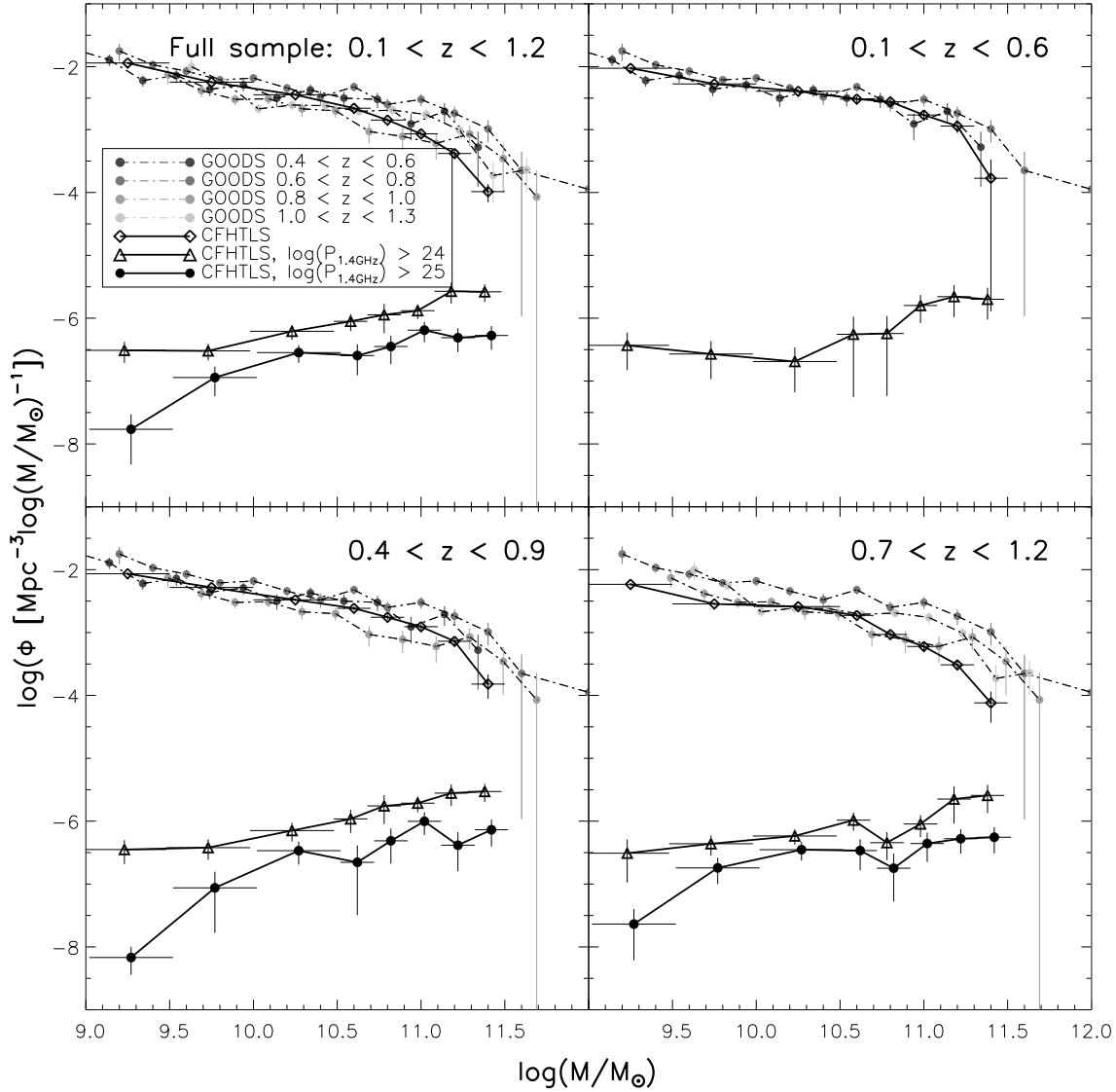


Figure 5.1: Using the $1/V_{max}$ comoving number density estimator, we have derived the stellar mass function for normal galaxies and for radio sources' hosts in different redshift bins. For the normal galaxies, at all redshifts our estimate of the stellar mass function is in good agreement with its measurement in the GOODS surveys (Fontana et al. 2006), which suggests the stellar masses estimates are reliable. The underestimate of the mass function at low stellar masses in the redshift bins $0.4 < z < 0.9$ and $0.7 < z < 1.2$ is due to incompleteness. The stellar mass function of the radio sources' hosts shows a very different, evolving shape.

- $N_b \geq 3$
- $0.1 < z_{ph} < 1.2$

where N_b is the number of bands the object is detected in, and z_{ph} is the photometric redshift estimate.

We also rejected the Type-1 AGN objects, since these will have corrupted physical parameter estimates. To do this, we fitted the u*g*r'i'z' and IRAC magnitude measurements with SED

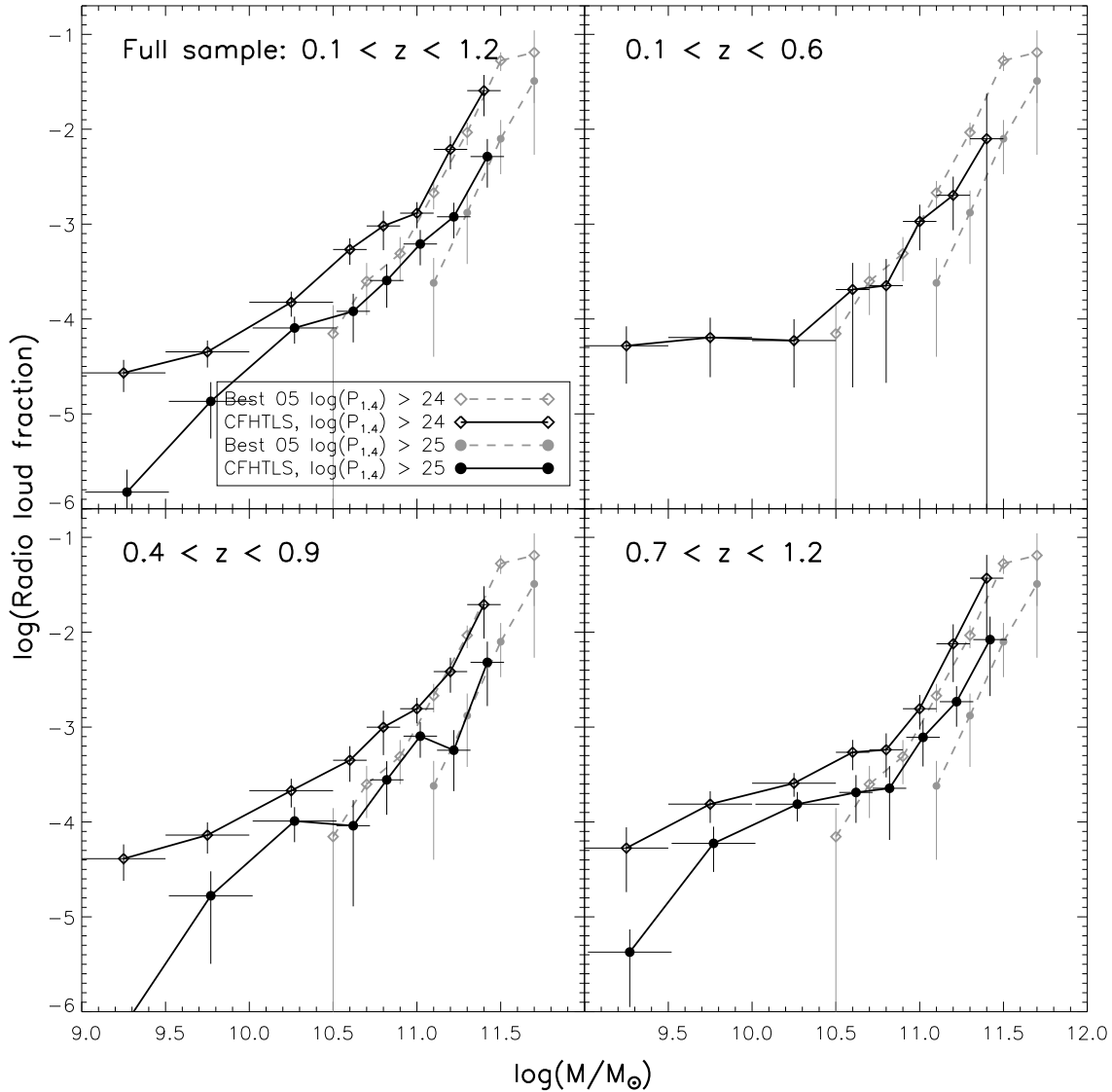


Figure 5.2: These plots show the fraction of radio sources that are radio loud as a function of the stellar mass in a given comoving volume. These relations have been derived using the mass function estimates of the normal and radio loud galaxies presented in Fig. 5.1. In the lower redshift bins, our measurement of the $f_{RL} - M$ relation matches its SDSS/NVSS $z \lesssim 0.3$ estimate (Best et al. 2005) both on normalisation and shape. Whereas the fraction of high stellar mass object $M \gtrsim 10^{11} M_{\odot}$ stays fairly constant with redshift, it seems the fraction of lower stellar masses objects ($10^{10.0} M_{\odot} < M < 10^{10.5} M_{\odot}$) undergoes a strong evolution.

templates retrieved from the SWIRE library (Polletta et al. 2006). These templates contain both normal galaxies and AGN. We rejected the objects best-fitted by a template having a strong AGN contribution, and those selected with a selection criteria in the g-r vs r-i color-color diagram. We estimate that only $\sim 2\%$ of the remaining objects are contaminating type-1 AGN. In addition, for our purpose, we reject the radio emitting starburst galaxies, since these would contaminate our radio loud AGN sample.

5.3 INTRINSIC PROPERTIES OF THE HOST GALAXIES OF RADIO SOURCES

In this section, we study the intrinsic properties of the radio sources' hosts sample described above. Specifically, in Section 5.3.1 we compare their stellar mass function to that of the normal galaxies in different redshift bins and in Section 5.3.2 we address the evolution of radio sources using the V/V_{max} estimator. In Section 5.3.3, we compute an infrared excess estimator.

5.3.1 Stellar mass functions

We derived the stellar mass function for normal galaxies (ϕ_{Opt}) and for the radio sources' hosts (ϕ_{Rad}) by using the $1/V_{max}$ estimator (Schmidt 1968), which corrects for the fact that our sample is magnitude limited. This procedure is described in detail in Appendix A. Fig. 5.1 show the stellar mass functions in the redshift ranges: $0.1 < z < 1.2$, $0.1 < z < 0.6$, $0.4 < z < 0.9$, and $0.7 < z < 1.2$.

A number of authors have estimated the galaxy mass function using different techniques, in various redshift ranges (see Fontana et al. 2006, for a general review). We compare our estimates of ϕ_{Opt} to the stellar mass function as estimated by Fontana et al. (2006) in the redshift intervals $\{0.4, 0.6, 0.8, 1.0, 1.3\}$, using the GOODS-MUSIC catalogs (Grazian et al. 2006), which contains broad band photometry from the optical to infrared regime, as well as a spectroscopic data for $\sim 27\%$ of the sample. At all redshifts, our estimates of ϕ_{Opt} show good agreement with Fontana et al. (2006) over the full mass range, both on normalisation and shape. The low values obtained at low stellar masses in the higher redshift bin are discussed below.

As expected from the SDSS-NVSS analysis (Best et al. 2005), the shape of ϕ_{Rad} is different from ϕ_{Opt} , with the radio sources' hosts being biased towards more massive systems. Interestingly, while the comoving number density of normal galaxies decreases with redshift, the radio sources' hosts having $M < 10^{11} M_{\odot}$ show strong positive redshift evolution. In the redshift bin $0.7 < z < 1.2$, the stellar mass function is rather flat.

This effect is clearly shown in Fig. 5.2 which displays the fraction of galaxies that are radio-loud galaxies ($f_{RL} = \phi_{Rad}/\phi_{Opt}$), as a function of stellar mass in the four redshift bins. At low redshift and at $M \gtrsim 10^{10.5} M_{\odot}$, the shape and normalisation of our estimate of f_{RL} matches $f_{RL} \propto M^{2.5}$ as found by Best et al. (2005) in the redshift range $z \lesssim 0.3$. However, we find evidence that the $f_{RL}(M)$ relation flattens at $M \lesssim 10^{10.5-11.0} M_{\odot}$. In the higher redshift bins the fraction of radio-loud objects agrees with the low redshift measurements for high stellar masses, but the lower stellar masses $M \lesssim 10^{10.5-11.0} M_{\odot}$ show a strong evolution. The physical implication of these results are discussed in Section 5.5.

We investigate below the possibility that this effect is caused by (i) an incompleteness effect caused by our flux limited survey and (ii) the scatter along the stellar mass axis, due to the uncertainties on that parameter.

Fontana et al. (2004) have extensively discussed a common incompleteness effect arising when computing comoving number densities from flux limited surveys. The $1/V_{max}$ estimator corrects for the number densities of the galaxies detected in each given stellar mass bin. However, these galaxies have different spectral types and may have very different mass-to-light ratios. Therefore, at high redshifts especially, galaxies of some spectral type may just not be detected, and the comoving number density estimate although corrected using the $1/V_{max}$ estimator, will still be an

underestimate. Radio sources' hosts may be significantly different from normal galaxies, hence may have mass-to-light ratios that differ on average to those of the normal galaxy population, leading to a different incompleteness for ϕ_{Opt} and ϕ_{Rad} , thereby driving a bias of f_{RL} . We investigate the possibility that this effect causes the flattening of the $f_{RL} - M$ relation by estimating an upper limit to that bias. In the most extreme case all radio sources' hosts are detected, but not all normal galaxies. The good match between our mass function for the normal galaxies and that of Fontana et al. (2006) indicates that this effect should not significantly affect ϕ_{Opt} in the redshift bin $0.1 < z < 0.6$ and $0.4 < z < 0.9$. However, the lower estimate of the comoving number density for $M < 10^{10} M_{\odot}$ in the higher redshift bin indicates that the effect of incompleteness may affect our comoving number density estimate by a factor of ~ 2 . The bias should therefore be less than a factor of ~ 2 , while the flattening involves differences by factor of ~ 100 . We therefore conclude that this effect cannot explain the observed flattening.

We investigate the possibility that this flattening is produced by the uncertainty on the stellar masses estimate, that are higher at higher redshift. For this, we generate radio sources' hosts mass functions corresponding to a fraction $f_{RL} = C_{11}M^{\alpha}$, where α is the slope of the relation and C_{11} is its normalisation at $10^{11}M_{\odot}$. We assume that the V_{max} within a given stellar mass bin will be similar for all galaxies of that bin. Given the average V_{max} of the objects of a given stellar mass, we estimate the true number of sources to be observed in a given stellar mass bin for each α . In order to generate the catalog corresponding to a $f_{RL} \propto M^{\alpha}$ relation, we have to scatter the true stellar mass estimates. Each object in a given stellar mass bin is given the stellar mass of the i^{th} object of the S1 sample with a probability $p_i = P_{id}(i) \times p_i(\Delta M)$, where P_{id} is the identification probability (Tasse et al. 2007a) and $p_i(\Delta M)$ is the probability that the true stellar mass of object i is in the mass bin ΔM . The operation is repeated 10 times, and the fraction f_{RL} is re-evaluated in each mass bin. As expected the mass scatter has the effect of increasing the observed fraction of low stellar mass objects. We quantify this effect by calculating the χ^2 on a grid where the free parameters are α and C_{11} , and associated error bars are taken at $\chi^2_{min} + 1$ (Avni & Bahcall 1976). Fig. 5.3 shows the best fit parameters in different redshift slices. The normalisation C_{11} of f_{RL} stays roughly constant through redshift. At low redshift, the slope measurement gives a good fit to the $\alpha \sim 2.5$ found by Best et al. (2005), while it progressively flattens towards higher redshift. This shows that the effect of the stellar masses uncertainty cannot explain the flattening of the fraction-mass relation at low stellar masses.

As a check, we have computed the radio luminosity function (RLF) of the radio loud AGN in our sample by using the comoving number density estimator described in Appendix A. The RLF (Fig. 5.4) of radio sources' hosts in our sample is in good agreement with the Willott et al. (2001) RLF estimates of the 7CRS, 3CRR, and 6CE radio sources samples selected at 150 MHz.

5.3.2 V/V_{max} statistics

In this section we address the issue of the evolution of radio sources' hosts within our sample using the V/V_{max} test (Schmidt 1968), where V is the comoving volume corresponding to the observed redshift of the radio sources' hosts, and V_{max} is the maximum available volume, described in Appendix A. If the radio source population is not evolving, then V/V_{max} is uniformly distributed over the interval $[0, 1]$ and $\langle V/V_{max} \rangle = 0.5 \pm (12N)^{-0.5}$ where N is the number of sources in the sample. Values of $\langle V/V_{max} \rangle > 0.5$ implies a higher comoving number density at high redshifts,

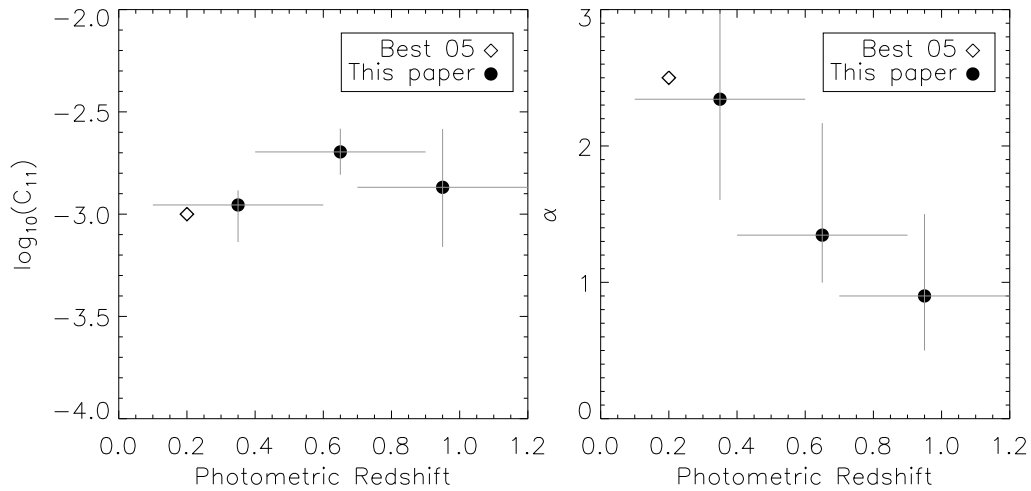


Figure 5.3: In order to investigate the possibility of the flattening seen in Fig. 5.2 to be due to the uncertainty on stellar mass estimates, we generate radio sources' hosts samples being characterised by a relation $f_{RL} = C_{11}M^\alpha$. We set C_{11} and α to be free variables, and after introducing a scatter on the stellar mass estimate, we measure the χ^2 corresponding to each C_{11} and α . This figure shows (i) the scatter introduced by the stellar mass uncertainty cannot explain the flattening of the $f_{RL} - M$ relation, and (ii) our sample agrees with the Best et al. (2005) measurement at low redshift.

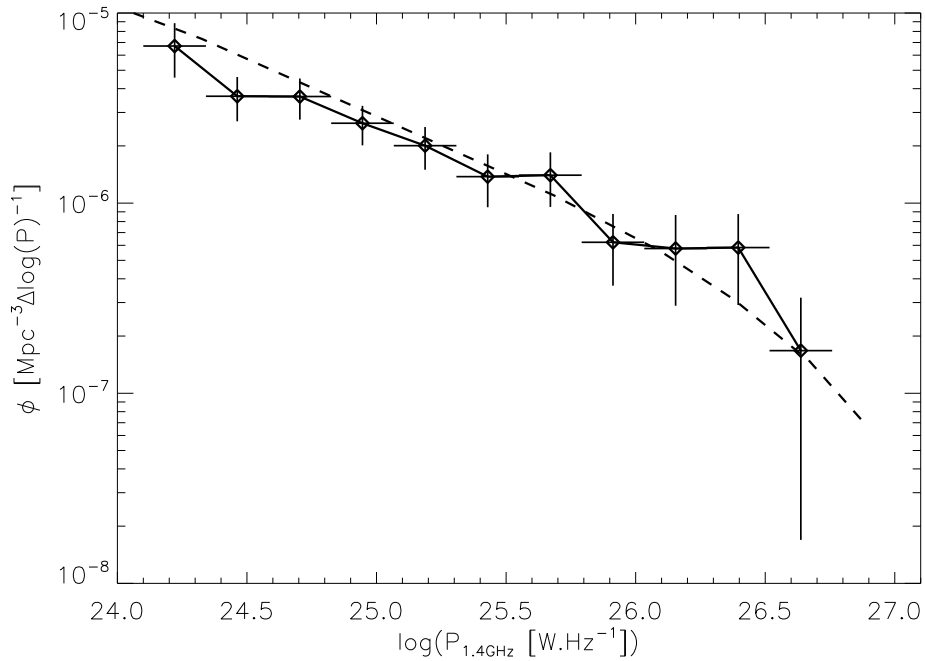


Figure 5.4: In this figure, we compare our estimate of the radio luminosity function in $0.1 < z < 1.2$ with the Willott et al. (2001) RLF estimate at $z = 0.9$. Both the normalisation and slope are in good agreement confirming the photometric redshifts are reliable.

and therefore a negative evolution with cosmic time, whereas $\langle V/V_{max} \rangle < 0.5$ indicates a positive evolution. A number of authors have used this estimator to address the cosmological evolution of radio sources selected at low frequency (Dunlop & Peacock 1990; Willott et al. 2001).

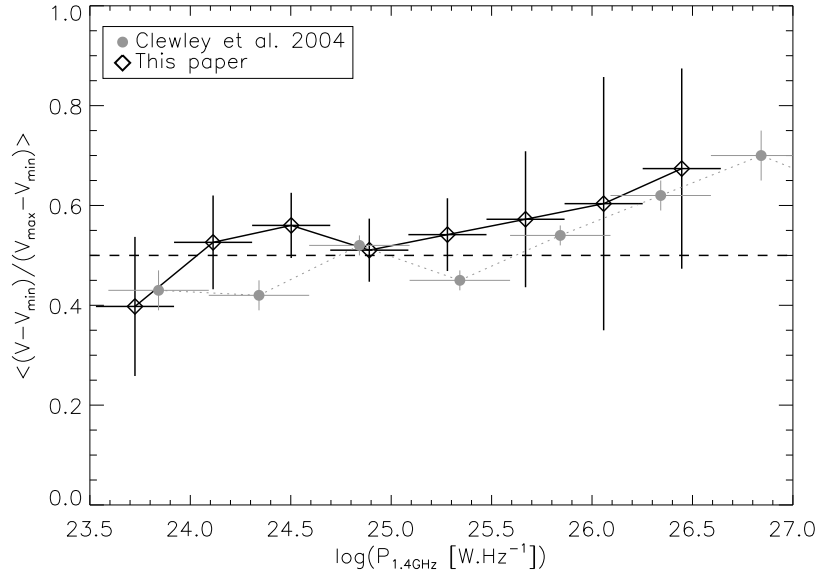


Figure 5.5: We compute $\langle V/V_{max} \rangle$ in different radio power ranges. Our measurement is in good agreement with Clewley & Jarvis (2004), with the low power radio sources ($P \lesssim 10^{25} \text{ W}\cdot\text{Hz}^{-1}$) evolving positively with cosmic time, whereas the higher power evolve negatively.

Fig. 5.5 shows the comparison between the $\langle V/V_{max} \rangle$ radio power relation for our sample and that of Clewley & Jarvis (2004), which was built from SDSS galaxies selected at 325 MHz. There is a good agreement between the two estimates.

In Fig. 5.6 we compute the $\langle V/V_{max} \rangle$ in different stellar mass bins. Although radio sources are seen to evolve more than normal galaxies on average, their respective evolution show a similar trend with the stellar mass: low stellar mass systems evolve more than high stellar mass ones. These results are further discussed in Section 5.5.

5.3.3 Infrared properties of radio sources' hosts

As described in Tasse et al. (2007a), we have associated to each radio source the infrared IRAC flux density measurements at 3.6, 4.5, 5.8 and 8.0 μm . Because ZPEG does not include infrared dust emission, the photometric redshifts have been computed from the magnitude measurements in the $u^*g'r'i'z'$ bands. We define an infrared excess parameter as:

$$\Delta_{IR} = \log(F_v(\lambda_{IRAC})/F_v^{ZPEG}(\lambda_{IRAC})) \quad (5.1)$$

where $F_v(\lambda_{IRAC})$ is the IRAC flux density measurement at λ_{IRAC} and $F_v^{ZPEG}(\lambda_{IRAC})$ is the flux density measurement from the ZPEG best fit template at λ_{IRAC} . The infrared excesses are computed in the observer frame.

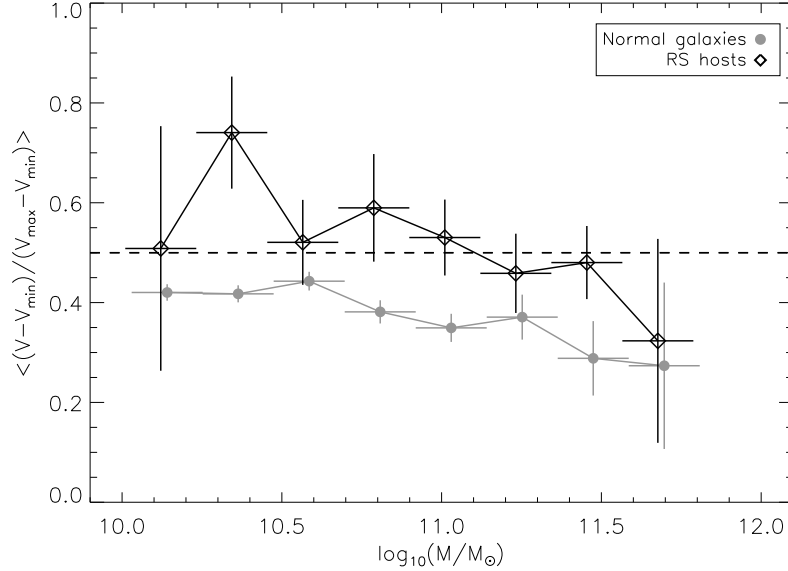


Figure 5.6: The averaged V/V_{\max} in different stellar mass bins, for the normal galaxies, and for the radio sources' hosts. The high stellar mass radio sources' hosts show a similar evolution to the non radio loud galaxies of the same mass, while the low stellar masses galaxies show strong evolution.

Fig. 5.7 shows the infrared excess at $3.6 \mu\text{m}$ computed for the normal galaxy population and for radio sources' host galaxies. The infrared excess is higher for the radio sources' hosts than for the normal galaxies, especially at low stellar masses. Yet the radio sources' hosts and the normal galaxies population have different properties, notably in terms of redshift and magnitude distribution. In order to compare the infrared properties of these two distinct population, for each galaxy we compute the quantity $\Delta_{IR}^R - \langle \Delta_{IR}^N(dz, dM) \rangle$, where Δ_{IR}^R is the infrared excess of the given radio source host, that is in the mass bin dM and in the redshift bin dz , and $\langle \Delta_{IR}^N(dz, dM) \rangle$ is the averaged value of the infrared excess for the normal galaxies that lay in the same mass and redshift bin. Fig. 5.7 shows that an infrared excess remains observed for the low stellar mass radio sources' hosts. The high stellar mass radio sources' hosts do not show an infrared excess. This result is further discussed in Section 5.5.

5.4 THE ENVIRONMENT OF THE HOST GALAXIES OF RADIO SOURCES

In order to study the environment of radio sources, we use a scale-dependent estimator of the overdensity around a given galaxy, which is based on the photometric redshift probability functions. The overdensity estimator is described in detail in Appendix B. This estimator has the advantage of (i) having a physical comoving scale as input, (ii) fully using the information contained within the photometric redshift probability function, and (iii) controlling edge effects. Overdensities found on large scales may refer to galaxy clusters, whereas smaller scales may refer to small groups of galaxies, or pairs of galaxies.

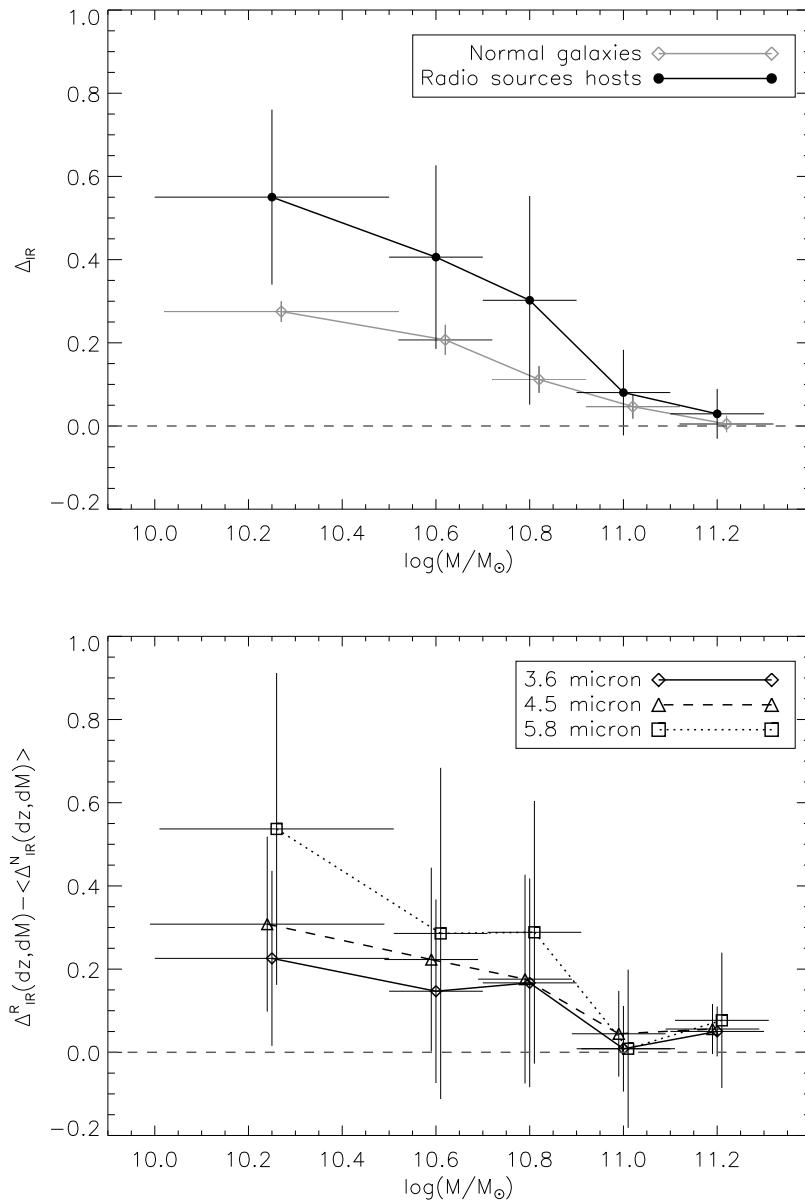


Figure 5.7: In order to retrieve information of the infrared emission of radio sources' hosts, we compute the infrared excess Δ_{IR} . The top panel shows the infrared excess at $3.6 \mu\text{m}$ for the radio sources' hosts and for the normal galaxies. In order not to bias the observation, in the bottom panel, we compare the infrared excess of individual radio sources' hosts with normal galaxies that are in the same mass and redshift range. The low stellar masses radio sources' hosts present an infrared excess in all the 3.6, 4.5, 5.8 μm bands, while the high stellar mass $M \gtrsim 10^{10.8-11} M_\odot$ do not.

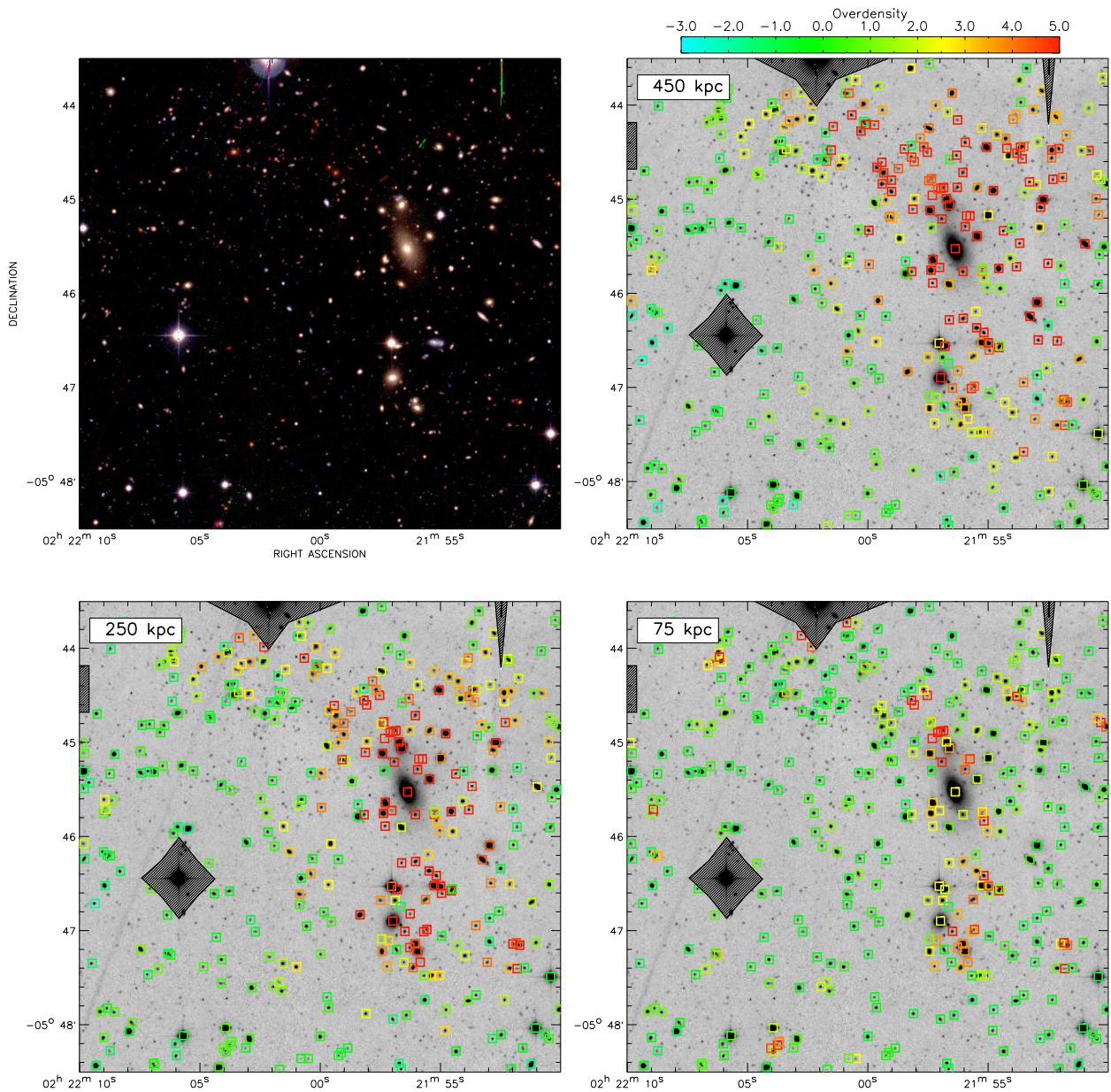


Figure 5.8: We have derived an overdensity estimator based on the individual photometric redshifts probability functions. The top left panel show a given region of the CFHTLS field in which we have computed the overdensity parameter at different scales for the objects brighter than $i = 23$. The other panels show the overdensity for each object on 450, 250 and 75 kpc scales, following the color code of top right panel. The clustering at the different scales looks different. The galaxy cluster that appears visually obvious in the i -band image is detected with a 450 kpc scale giving many galaxies an overdensity parameter $\rho_{450} \gtrsim 5$. Decreasing the overdensity scale enhances small groups of galaxies or even galaxy mergers.

5.4.1 The overdensity parameter

The derivation of the overdensity parameter is described fully in Appendix B, but we summarised here the basic idea. The $\chi^2(z)$ that were available for all the objects of the CFHTLS-W1 field (Tasse et al. 2007a) are first converted into probability functions $p(z)$. Given an object, its associated $p(z)$, and a comoving scale R_{kpc} , we estimate the number of objects n enclosed in the co-cone of radius R_{kpc} . Because the optical survey is flux limited, the estimate of n strongly depends on the probability function of the considered object: if the object is at high redshift, the probability of detecting nearby object is low, which biases the number density towards lower values. Therefore, we define the overdensity parameter by the significance of a given observed n . For doing this, we generate 20 catalogs containing the same objects, with uniformly distributed positions (no clustering). In each of these catalogs, the number density n_{unif} around the given object is calculated and the mean $\langle n_{unif} \rangle$ and standard deviation $\sigma(n_{unif})$ are estimated. The overdensity ρ is then computed as $\rho = (n - \langle n_{unif} \rangle) / \sigma(n_{unif})$.

We have derived the overdensity parameter on 75, 250, and 450 kpc scales for both the radio sources' host sample and for the normal galaxies. Fig 5.8 shows an example of the overdensity parameters estimates derived for the $i < 23$ objects within a $5' \times 5'$ field. We chose this location because it contains galaxies belonging to a galaxy cluster as well as field galaxies. Qualitatively, our algorithm looks efficient: a high overdensity parameter corresponding to an overdense region is seen at the location where the overdensity is obvious in the sky plane.

5.4.2 The environment of radio sources

The overdensity parameter is likely to be quite sensitive to redshift, since the optical survey is flux limited. Comparing the overdensity distribution of two population having different magnitude and redshift distribution can therefore be misleading. Therefore, in the following, we compare the environment of radio sources' hosts given galaxy to the normal galaxy population that are in the same mass and redshift range. We do this by computing the quantity $\Delta\rho_i = \rho_i - q_{0.5}[\rho^N(dz, dM)]$, where ρ_i is the overdensity of the given galaxy being in the redshift and mass bins (dz, dM) , while $q_{0.5}[\rho^N(dz, dM)]$ is the median overdensity parameter of normal galaxies in the same redshift and stellar mass interval. In practice, dM is taken to be the stellar mass bin, and we set $dz = 0.1$.

Fig. 5.9 shows the median value of $\Delta\rho$ in different stellar mass bins and at different scales. The observed relations were quite bin dependent, therefore we smooth the observation with a box of width $\Delta M = 0.4$. In order to quantify the uncertainty in the median value estimate, we follow a Monte-Carlo approach. We assume the $\Delta\rho$ distributions have the same shape in all stellar mass bins. By generating samples of n sources following the same distribution we estimate the error bar on the median as the standard deviation between the estimated median and the true median.

A stellar mass dichotomy appears in Fig. 5.9, with the two different environmental regimes occurring above and below a stellar mass range of $\sim 10^{10.5-10.8} M_\odot$. The higher stellar mass radio sources' hosts lie in a 450 kpc scale environment that is on average denser than the environment of the non-radio-loud galaxies of the same mass by $\Delta(\rho) \sim 0.7$, while their small scale environment has $\Delta(\rho) \sim 0$. An inverse relation is observed for the low stellar masses objects: their small scale 75 kpc scale environment is denser than the average by $\Delta\rho \sim 0.3$, while their large scale environment is significantly underdense on average, with $\Delta\rho \sim -0.5$. However, the estimated

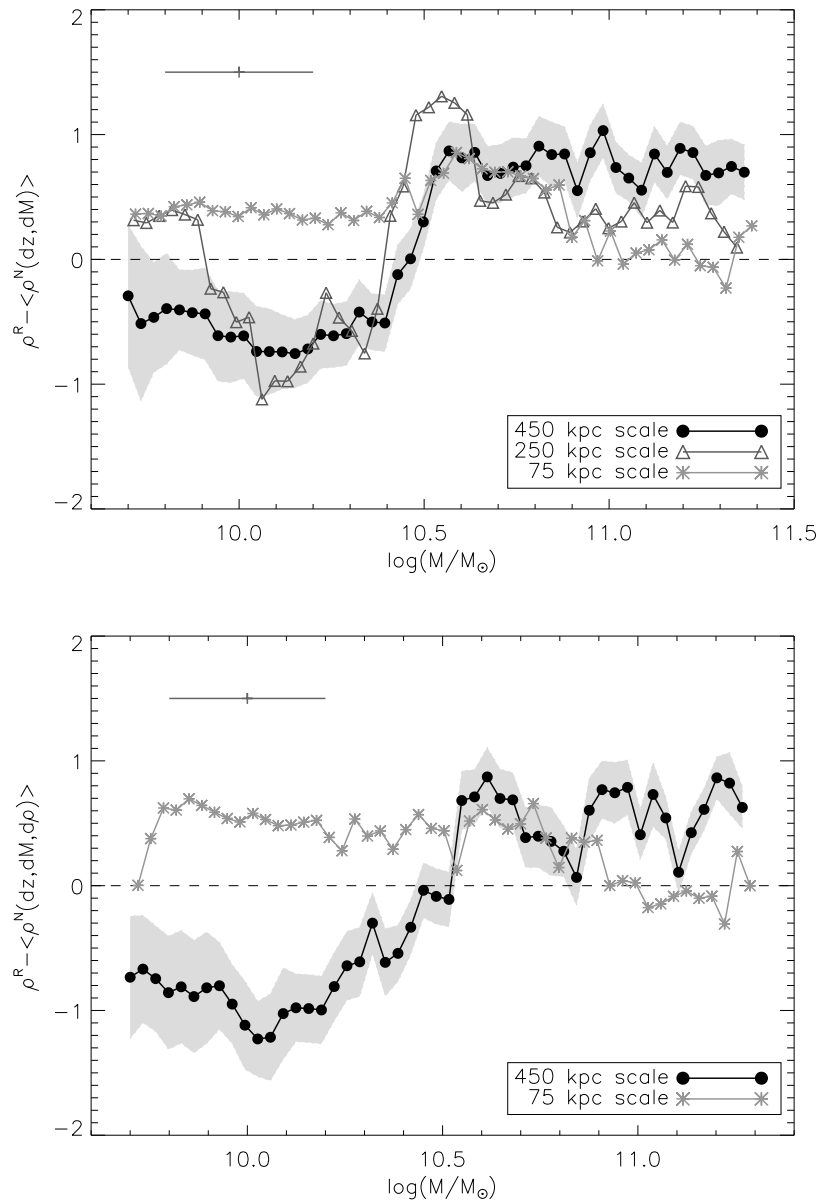


Figure 5.9: The top panel shows the difference in overdensity parameter $\Delta\rho$ between the radio sources' hosts, and the normal galaxies, as a function of the stellar mass. Because these two populations are significantly different in terms of redshift and magnitude distribution notably, we compare the overdensity of each radio source to the overdensity around normal galaxies in the same mass and redshift bin. This quantity is plotted for different input scales. The massive radio sources' hosts preferentially lie in large scale (~ 450 kpc) overdensities, while the less massive ones lie in large scales underdensities, and small scales (~ 75 kpc) overdensities. However, the overdensity estimates on a given scale may depend on the overdensity estimate on another scale. In order to address that issue, in the bottom panel we compute the overdensity differences $\Delta\rho$ on small and large scale for galaxies situated in similar large and small scale environment respectively (see discussion in the text). The environmental dichotomy remains observed.

overdensities may be dependent at the different scales: high 450 kpc scale overdensities may lead to higher 75 kpc scale overdensities. In order to study the 75 kpc overdensities of radio sources' hosts independently from their large 450 kpc environment, we compute the quantity $\Delta\rho(75|450) = \rho_{i,75} - q_{0.5}[\rho_{75}^N(dz, dM, d\rho_{450})]$, where $q_{0.5}[\rho_{75}^N(dz, dM, d\rho_{450})]$ is the median overdensity of non-radio-loud galaxies that lie in similar large scale environment and that have comparable stellar mass, and redshift estimates. Similarly, we compute $\Delta\rho(450|75)$, and we take $d\rho = 0.3$. Fig. 5.9 shows $\Delta\rho(75|450)$ and $\Delta\rho(450|75)$: the environmental dichotomy remains observed with the stellar mass cut in the range $\sim 10^{10.8-11.0} M_{\odot}$. These results are further discussed in Section 5.5.

5.4.3 Comparison with X-ray selected galaxy clusters

In this section, we compare the overdensities found around radio sources to the overdensity estimates of the galaxies aligned with X-ray groups and clusters. Studying the dependence of the overdensity estimate on the bolometric luminosity of these clusters (ie their dark matter halo mass), allows us to put further constrains on the environment of radio sources determined in Section 5.4.2.

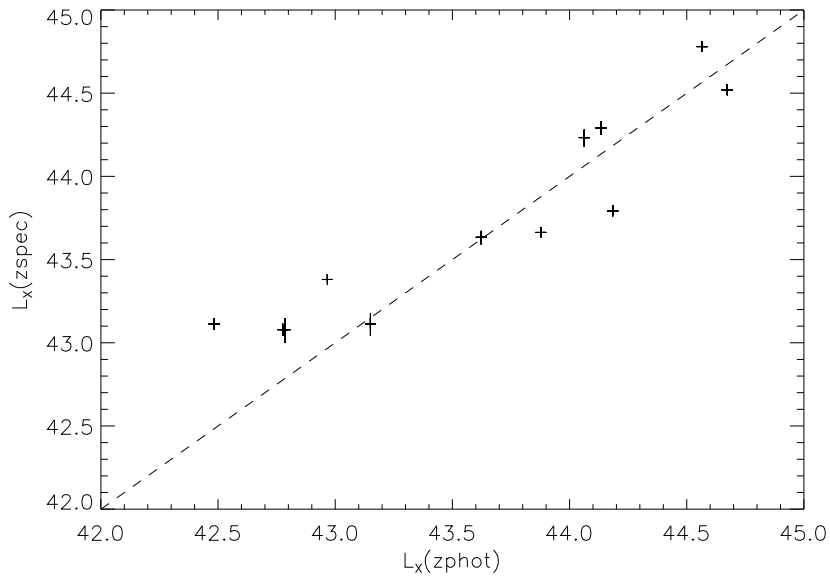


Figure 5.10: This figure shows the comparison between our estimate of the bolometric luminosity ($L_X(z_{\text{phot}})$) with the bolometric luminosity $L_X(z_{\text{spec}})$ as deduced using spectroscopic redshift and X-ray spectral fits. Except for one source, the two estimates are in agreement.

We here consider the sample of X-ray clusters detected as extended X-ray emission (Pacaud et al. 2006) in the initial ~ 5 degree² of the XMM-LSS field (Pierre et al. 2004). By fitting a model of free-free emission to the X-ray spectra of 29 sources, Pierre et al. (2006) and Pacaud et al. (2007) measured bolometric luminosities as well as temperatures. Only 12 of those sources overlap with the CFHTLS-W1 field. In order to increase the size of the X-ray cluster sample, we also consider the X-ray sources classified as extended by the X-ray pipeline, but have not been spectroscopically confirmed. The final sample of extended X-ray sources contains 35 sources in

the redshift range $z \lesssim 1.2$. We describe below how we derived a crude estimation of the redshifts and bolometric luminosities of these clusters.

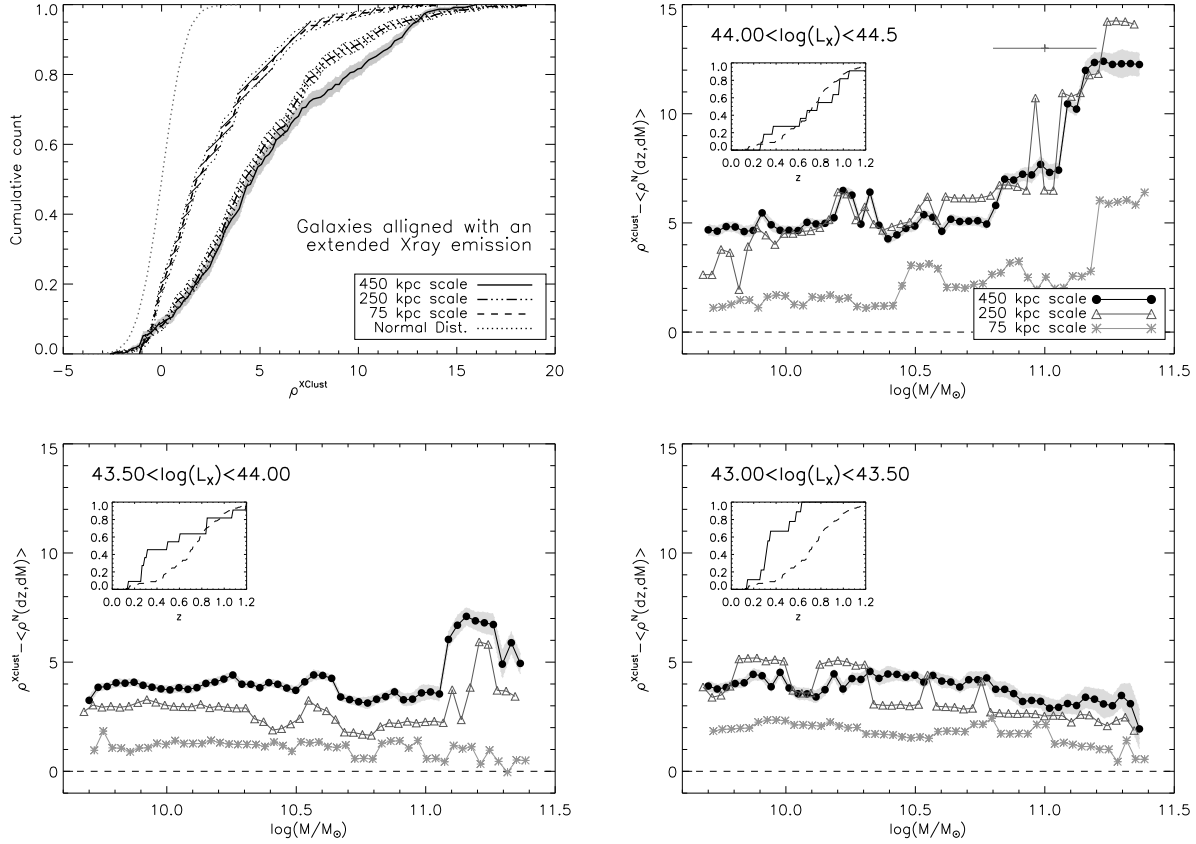


Figure 5.11: Top left panel: the overdensity parameter for the galaxies aligned with X-ray cluster emission and field galaxies in the same redshift ranges. The overdensity parameter appears to be quite efficient. Top right to bottom right: the difference on overdensity parameter between the radio sources’ hosts, and the normal galaxies for different X-ray luminosities. In each panel, the estimated redshift distribution of the X-ray clusters is indicated (full line), and compared to the redshift distribution of the radio sources’ hosts (dashed line). Although our overdensity parameter is biased by redshift, it seems that the increase of the halo mass leads to a higher overdensity parameter estimate. Comparing this with Fig. 5.9, it seems that massive radio sources lie in rather small clusters on average.

We estimated the overdensity on 75, 250 and 450 kpc scales for the galaxies that lie within $30''$ the galaxy clusters detected as extended X-rays sources. In most cases, inspecting the $\rho_{450} - z$ plane we can see a peak in the redshift distribution of the galaxies aligned with a given extended X-ray source, and having a high $\rho_{450} > 2$ overdensity estimate. If a redshift peak was detected, we assigned a redshift to the extended X-ray emission, otherwise we rejected the X-ray source. We estimated the bolometric luminosity using the X-ray pipeline XSPEC. We have modelled the X-ray emission with a bremsstrahlung emission model (named “APEC” in XSPEC), and by assuming a temperature of 3 keV, at each redshift in $0 < z < 2$ we have derived a [0.5-2] keV flux to bolometric luminosity conversion factor. Allowing the temperature to vary from 0.5 to 10 keV, affects the conversion factor by a factor of ~ 3 . For the extended X-ray sources confirmed spectroscopically

(Pacaud et al. 2007), Fig. 5.10 shows the comparison between the bolometric luminosities as estimated using (i) the combination of photometric redshift and overdensity parameter and (ii) the spectroscopic redshifts and spectral fits (Pacaud et al. 2007). The agreement is quite good on average.

Fig. 5.11 shows the averaged values of $\Delta\rho$ (see Section 5.4.1) in different galaxy stellar mass and bolometric luminosity ranges. Galaxies aligned within a luminous X-ray cluster, have higher overdensity estimates: in the luminosity range $L_X > 10^{43.5}$ erg.s⁻¹, $\Delta\rho$ is as high as ~ 9 whereas $\Delta\rho \sim 3$ at $L_X < 10^{43.0}$ erg.s⁻¹. We interpret this effect as being caused by an increase of the *true* overdensity with increasing X-ray luminosity as it is well known that the bolometric luminosity of the X-ray emitting gas correlates with the dark matter halo mass (Popesso et al. 2005).

Although the overdensity parameter might be biased by redshift effects, and probes number density rather than mass, it seems we can further constrain the environment of radio sources. We can already see from the overdensities estimates of the galaxies in the brightest ($L_X > 10^{43.5}$ erg.s⁻¹) X-ray clusters that, although they have a similar redshift distribution to the radio sources' hosts, their overdensities are far higher. The overdensity around radio sources is rather similar to the overdensity found within the lower luminosity clusters, whose halo masses are on the order of $M \sim 10^{14} M_\odot$ (Popesso et al. 2005). These results are consistent with previous studies in which radio sources' hosts were found to be preferentially located in environment of moderate density (eg. Hill & Lilly 1991; Best 2000).

5.5 DISCUSSION AND CONCLUSIONS

In this paper we have carried out a series of analyses giving further evidence that our estimates of photometric redshifts and stellar masses for the radio sources' hosts sample built in Tasse et al. (2007a) are reliable. Specifically, our estimate of the radio luminosity function as derived using the $1/V_{max}$ estimator (Fig. 5.4) shows a good fit with the Willott et al. (2001) radio luminosity function that has been estimated using a complete sample of radio sources selected at 150 MHz. Furthermore our estimate of the V/V_{max} vs radio power relation fits the SDSS measurement of (Clewley & Jarvis 2004), suggesting there should be no systematics between the radio luminosity and the accuracies of the photometric redshifts. For the sample of normal galaxies, our estimate of the stellar mass function is similar to the Fontana et al. (2006) stellar mass function from the GOODS survey. Also, in the lowest redshift bin $0.1 < z < 0.6$, the relation between the fraction of radio-loud galaxies and the stellar mass relation is in good agreement with the SDSS $z \lesssim 0.3$ measurement in the radio power range $P_{1.4} > 10^{24}$ W.Hz⁻¹ from Best et al. (2005).

In Section 5.3 and 5.4, we investigated the intrinsic and environmental properties of radio sources' hosts as compared to the normal galaxy population. The sample extends up to $z \sim 1.2$, and across the radio power range 10^{24-27} W.Hz⁻¹. The main results are as follows:

- (i) The relationship between the fraction of radio-loud galaxies and the stellar mass shows a break in the range $M \sim 10^{10.8-11} M_\odot$ and $z \gtrsim 0.5$.
- (ii) The low stellar mass radio source host galaxies show a stronger evolution than the high stellar mass galaxies. At $z \sim 1$, the mass function of radio sources' hosts appears to be significantly flatter than in the local universe.

- (iii) High stellar mass radio sources are seen to be preferentially located in poor clusters of galaxies.
- (iv) The environment of the low stellar mass radio sources is biased towards large-scale underdensities, and small-scale overdensities.
- (v) At $M \lesssim 10^{10.8-11} M_{\odot}$, galaxies have a hot dust component observed as an infrared excess, while the galaxies with $M \gtrsim 10^{10.8-11} M_{\odot}$ do not.

These results suggest the existence of dichotomy in the nature of both the hosts and environment of radio sources. We argue below that the observed dichotomy might be caused by the different ways of triggering the black hole activity as discussed in Section 5.1.

Best et al. (2005) used a large sample of low luminosity radio sources in the SDSS ($z \lesssim 0.3$) to show that the fraction f_{RL} of radio loud galaxies scales with the galaxy stellar mass as $f_{RL} \propto M^{2.5}$, and argued that the IGM gas cooling rate \dot{M} that has the same dependence on stellar mass ($\dot{M}_{cool} \propto M^{2.5}$), provides a way of feeding the black hole and triggering the AGN. For our dataset, in the redshift range $0.1 < z < 0.6$ the fraction of radio loud galaxies show a similar dependence on the stellar masses of galaxies. Furthermore, our results (iii) supports this picture as the high stellar mass systems that are radio-loud are preferentially located in large 450 kpc scale overdense environments as compared to non-radio-loud galaxies of the same mass. This environment resembles small clusters of galaxies with $M \sim 10^{14} M_{\odot}$, in agreement with observations of low redshift radio sources lying in moderate groups to poor clusters (Best 2004, and references therein). In contrast, Best et al. (2007) found that the radio-loud fraction versus stellar mass relation flattens to $f_{RL} \propto M^{1.5}$ for a sample of brightest cluster galaxies (BCGs), while there is evidence that the radio sources observed at high redshift lie in rich cluster environment (Best et al. 2003; Kurk et al. 2004; Venemans 2006). Interestingly, in the redshift bin $0.6 < z < 1.2$, the radio sources with $P_{1.4} > 10^{25} \text{ W.Hz}^{-1}$ show a dependence of f_{RL} with the stellar mass that flattens to $f_{RL} \propto M^{-1.8}$, which could be due to a greater fraction of radio-loud galaxies that are located at the center of galaxy clusters by $z \sim 1$.

Result (iv) suggests that the low stellar mass, strongly evolving component of the radio sources' hosts population inhabit a different environment than the radio-loud AGN with high stellar mass host galaxies discussed above. Compared to normal galaxies of the same mass, radio-loud galaxies preferentially lie in large scale underdensities (450 kpc comoving), and overdensities at small scales (75 kpc), suggesting their AGN activity may be triggered by galaxy mergers and interactions. Similarly, ULIRGs are found to be associated with galaxy interactions or galaxy mergers (Section 5.1), and star forming galaxies have been shown to be preferentially located in underdense environments, where the low velocity dispersion conditions favour the galaxy mergers and interactions (Gómez et al. 2003; Best 2004). Furthermore the low mass radio-loud AGN in our sample have a significant infrared excess at $3.6 \mu\text{m}$ (observer frame) as compared to non-radio-loud galaxies of the same mass. Seymour et al. (2007) have already observed such infrared excesses in high redshift radio galaxies, and concluded on the presence of hot ($\sim 0.5 - 1 \times 10^3 \text{ K}$) dust, heated by an obscured, highly accreting AGN. This is consistent with AGN unified schemes whereby these objects are radiatively efficient radio-loud quasars viewed edge-on. The infall of the cold IGM gas in the potential well of those low stellar mass systems AGN might provide an alternative triggering process to the galaxy mergers discussed above. In such scenarios, the tendency of those quasar mode AGN to be located in underdense environment may indicate that the black hole accretes cold

gas as well since the IGM gas in underdense regions has a lower temperature than in overdense regions.

As discussed in Hardcastle et al. (2007), the state of the gas that reaches the black hole might play an important role in triggering the quasar and the radio modes (Section 5.1). The observed environmental dichotomy reported here, with the low stellar mass ($M < 10^{11} M_{\odot}$) systems having a hot infrared excess, support the picture in which the galaxy mergers or the cold IGM gas infall trigger high efficiency accretion, while the hot IGM gas cooling from the atmosphere of massive galaxies trigger the radiatively inefficient accretion of low luminosity radio-loud AGN. It might be that the number density of low-mass radio-loud AGN is low in the nearby Universe because the combination of fairly massive black hole and a galaxy merger or interaction which can supply cold gas, are quite rare. However, these conditions will be more common in the gas-rich early Universe, which might explain the higher number density of low stellar mass radio-loud AGN at higher redshift. As the large scale structure forms and the environment of galaxies changes, the competing mechanisms discussed in this paper may play an important role in the evolution of the AGN activity.

ACKNOWLEDGMENTS

The optical images were obtained with MegaPrime/MegaCam, a joint project of CFHT and CEA/DAPNIA, at the CFHT which is operated by the National Research Council (NRC) of Canada, the Institut National des Sciences de l'Univers of the Centre National de la Recherche Scientifique (CNRS) of France and the University of Hawaii. This work is based on data products produced at TERAPIX and at the Canadian Astronomy Data Centre as part of the CFHTLS, a collaborative project of NRC and CNRS.

REFERENCES

- Arnouts, S., Moscardini, L., Vanzella, E., et al. 2002, MNRAS, 329, 355
- Avni, Y. & Bahcall, N. A. 1976, ApJ, 209, 16
- Best, P. N. 2000, MNRAS, 317, 720
- Best, P. N. 2004, MNRAS, 351, 70
- Best, P. N., Kaiser, C. R., Heckman, T. M., & Kauffmann, G. 2006, MNRAS, 368, L67
- Best, P. N., Kauffmann, G., Heckman, T. M., et al. 2005, MNRAS, 362, 25
- Best, P. N., Lehnert, M. D., Miley, G. K., & Röttgering, H. J. A. 2003, MNRAS, 343, 1
- Best, P. N., von der Linden, A., Kauffmann, G., Heckman, T. M., & Kaiser, C. R. 2007, MNRAS, 527
- Clewley, L. & Jarvis, M. J. 2004, MNRAS, 352, 909
- Croton, D. J., Farrar, G. R., Norberg, P., et al. 2005, MNRAS, 356, 1155
- Dunlop, J. S. & Peacock, J. A. 1990, MNRAS, 247, 19
- Evans, D. A., Worrall, D. M., Hardcastle, M. J., Kraft, R. P., & Birkinshaw, M. 2006, ApJ, 642, 96
- Fontana, A., Pozzetti, L., Donnarumma, I., et al. 2004, A&A, 424, 23
- Fontana, A., Salimbeni, S., Grazian, A., et al. 2006, A&A, 459, 745

- Gebhardt, K., Bender, R., Bower, G., et al. 2000, *ApJ*, 539, L13
- Gómez, P. L., Nichol, R. C., Miller, C. J., et al. 2003, *ApJ*, 584, 210
- Grazian, A., Fontana, A., de Santis, C., et al. 2006, *A&A*, 449, 951
- Hardcastle, M. J., Evans, D. A., & Croston, J. H. 2006, *MNRAS*, 370, 1893
- Hardcastle, M. J., Evans, D. A., & Croston, J. H. 2007, *MNRAS*, 376, 1849
- Hill, G. J. & Lilly, S. J. 1991, *ApJ*, 367, 1
- Hine, R. G. & Longair, M. S. 1979, *MNRAS*, 188, 111
- Jackson, N. & Rawlings, S. 1997, *MNRAS*, 286, 241
- Kauffmann, G., Heckman, T. M., Tremonti, C., et al. 2003, *MNRAS*, 346, 1055
- Kurk, J. D., Pentericci, L., Overzier, R. A., Röttgering, H. J. A., & Miley, G. K. 2004, *A&A*, 428, 817
- Laing, R. A., Jenkins, C. R., Wall, J. V., & Unger, S. W. 1994, in *Astronomical Society of the Pacific Conference Series*, Vol. 54, *The Physics of Active Galaxies*, ed. G. V. Bicknell, M. A. Dopita, & P. J. Quinn, 201–+
- Le Borgne, D. & Rocca-Volmerange, B. 2002, *A&A*, 386, 446
- Lonsdale, C. J., Smith, H. E., Rowan-Robinson, M., et al. 2003, *PASP*, 115, 897
- Mathews, W. G. & Brighenti, F. 2003, *ARA&A*, 41, 191
- Ogle, P., Whysong, D., & Antonucci, R. 2006, *ApJ*, 647, 161
- Pacaud, F., Pierre, M., Adami, C., et al. 2007, *MNRAS*(in prep.)
- Pacaud, F., Pierre, M., Refregier, A., et al. 2006, *MNRAS*, 372, 578
- Pierre, M., Pacaud, F., Duc, P.-A., et al. 2006, *MNRAS*, 372, 591
- Pierre, M., Valtchanov, I., Altieri, B., et al. 2004, *Journal of Cosmology and Astro-Particle Physics*, 9, 11
- Polletta, M. d. C., Wilkes, B. J., Siana, B., et al. 2006, *ApJ*, 642, 673
- Popesso, P., Biviano, A., Böhringer, H., Romaniello, M., & Voges, W. 2005, *A&A*, 433, 431
- Sanders, D. B. & Mirabel, I. F. 1996, *ARA&A*, 34, 749
- Sanders, D. B., Soifer, B. T., Elias, J. H., et al. 1988a, *ApJ*, 325, 74
- Sanders, D. B., Soifer, B. T., Elias, J. H., Neugebauer, G., & Matthews, K. 1988b, *ApJ*, 328, L35
- Schmidt, M. 1968, *ApJ*, 151, 393
- Schmitt, H. R. 2004, in *IAU Symposium*, Vol. 222, *The Interplay Among Black Holes, Stars and ISM in Galactic Nuclei*, ed. T. Storchi-Bergmann, L. C. Ho, & H. R. Schmitt, 395–400
- Seymour, N., McHardy, I., Gunn, K., & Moss, D. 2005, in *ESA Special Publication*, Vol. 577, *ESA Special Publication*, ed. A. Wilson, 323–324
- Seymour, N., Stern, D., De Breuck, C., et al. 2007, *ApJS*, 171, 353
- Springel, V., Di Matteo, T., & Hernquist, L. 2005a, *ApJ*, 620, L79
- Springel, V., Di Matteo, T., & Hernquist, L. 2005b, *MNRAS*, 361, 776
- Sutherland, W. & Saunders, W. 1992, *MNRAS*, 259, 413
- Tasse, C., Cohen, A. S., Röttgering, H. J. A., et al. 2006, *A&A*, 456, 791
- Tasse, C., Le Borgne, D., Röttgering, H. J. A., et al. 2007a, *A&A* (Submitted)

- Tasse, C., Röttgering, H. J. A., Best, P. N., et al. 2007b, *A&A*, 471, 1105
- Veilleux, S. 2003, in *Astronomical Society of the Pacific Conference Series*, Vol. 290, *Active Galactic Nuclei: From Central Engine to Host Galaxy*, ed. S. Collin, F. Combes, & I. Shlosman, 11–+
- Venemans, B. P. 2006, *Astronomische Nachrichten*, 327, 196
- Whysong, D. & Antonucci, R. 2004, *ApJ*, 602, 116
- Willott, C. J., Rawlings, S., Blundell, K. M., Lacy, M., & Eales, S. A. 2001, *MNRAS*, 322, 536

APPENDIX

A NUMBER DENSITY ESTIMATOR

The S1 sample presented in Tasse et al. (2007a), contains for each radio source i , an association probability $P_{id}^i(j)$ that its true counterpart is the j^{th} optical candidate. As discussed in Tasse et al. (2007a) the probabilities $P_{id}^i(j)$ have been modified in order to take into account contamination from a remaining missidentification fraction.

In order to compute a number density in the comoving space, we use the standard $1/V_{max}$ estimator first described in Schmidt (1968). Using the S1 sample we estimate the mean comoving number density in a region R of the parameter space as:

$$\langle\phi_R\rangle = C \sum_{\Omega_{i,j}(R)} [P_{id}^i(j)/V_{max}^i(j)]_R \quad (\text{A1})$$

where $\Omega_{i,j}(R)$ is the set of $\{i, j\}$ optical candidates which are located within the region R , V_{max} is the maximum comoving volume over which a given source can enter our sample and C is a constant designed to compensate for (i) the random selection of the objects in the optical catalog and (ii) the $\sim 30\%$ of the optical field that is masked. The error bar associated with $\langle\phi_R\rangle$ is:

$$\sigma(\langle\phi_R\rangle) = C \sqrt{\sum_{\Omega_{i,j}(R)} [P_{id}^i(j)/V_{max}^i(j)]_R^2} \quad (\text{A2})$$

In practice, we set $V_{max} = V(z_{max}) - V(z_{min})$ where $V(z)$ is the comoving volume enclosed out to a given z , while z_{max} and z_{min} are the maximum and minimum redshifts for which a given object is selected. V_{max} depends on the effective surveyed area at each given flux density. We have estimated that dependence by comparing our observed source counts to a field with deeper radio source counts (Seymour et al. 2005). The redshifts lower and upper bounds z_{min} and z_{max} depend upon (i) the redshift range corresponding to the cell R of the parameter space in which we estimate $\langle\phi_R\rangle$ (ii) the selection criteria of our optical data and (iii) the selection criteria of our radio surveys. For each of the selection types (i), (ii) and (iii), we consider a z_{min} and a z_{max} .

Estimating z_{min} and z_{max} for the selection type (i) is trivial and just depends on the redshift bin used to derive the comoving number density. To calculate the maximum redshifts corresponding to the selection (ii) for a given object, we consider its radio power and the estimate of the spectral index as derived by Tasse et al. (2006) and Tasse et al. (2007b). We estimate z_{max} as the redshift corresponding to that object being detected at the limiting flux density of the radio survey at either 325 or 610 MHz. Estimating z_{min} and z_{max} based on the third selection criterion uses the magnitude

selection criteria 1 and 2 of Sec. 5.2. For each optical object we consider the best fitting ZPEG SED template. The lower bound z_{min} is then the redshift corresponding to an observed i-band magnitude $i = 18$, whereas z_{max} is either the redshift for which $i = 24$ or the maximum redshift for which the selection criteria 2 is satisfied (Sec. 5.2).

For each object, the final z_{min} and z_{max} to be used is derived as $z_{min} = \max(\{z_{min}(i), z_{min}(ii), z_{min}(iii)\})$ and $z_{max} = \min(\{z_{max}(i), z_{max}(ii), z_{max}(iii)\})$ where the indices (i) and (ii) and (iii) refer the selection types (i), (ii) and (iii) defined above.

B OVERDENSITY ESTIMATOR

B1 Probability functions

The use of photometric redshifts codes is generally limited to the determination of the values associated to the best fitting template, which do not include multiple solutions for example. In order to fully use the information derived from the fitting of the magnitude points, as described in Tasse et al. (2007a), the least χ^2 has been recorded as a function of the redshifts for 200 values in $0 < z < 2$. Following Arnouts et al. (2002), for each object, we relate the $\chi^2(z)$ function to the photometric redshift probability function $p(z)$ as follows:

$$p(z) \propto \chi^{r-2}(z) \exp(-\chi^2(z)/2) \quad (\text{B3})$$

where r is the number of degrees of freedom. Assuming that all optical sources have their true redshift in $0 < z < 2$, $\int p(z)dz$ is normalized to 1 over this redshift interval.

B2 Overdensity parameter

In order to build our overdensity parameter, we calculate the mean number density around a chosen galaxy within an arbitrary chosen comoving volume, using the information contained in the probability function $p(z)$.

A radius R_{kpc} is first chosen in the comoving space. It defines a comoving scale to which the overdensity estimate refers. Overdensities over large scales may refer to galaxy clusters, whereas smaller scales may refer to small groups of galaxies or even galaxy pairs.

The redshift space is then binned so that the volume V of the cone of radius R_{kpc} and line-of-sight comoving length $D_c(\Delta z_i)$ stays constant. We choose V so that $\Delta z_i = z_{i+1} - z_i \approx 0.1$, the typical error bar on photometric redshifts (Tasse et al. 2007a). This leads to $z_i = \{0.05, 0.12, 0.19, 0.28, 0.38, 0.49, 0.62, 0.76, 0.92, 1.10, 1.29\}$. In each redshift bin i centered at $(z_i + z_{i+1})/2$, the angular diameter $R_{\text{i,deg}}$ corresponding to R_{kpc} is calculated. Then, we derive the density around the given object inside each redshift slice:

$$n_i = f_{\text{eff}} \sum_{j \in \Omega_i} \left(\int_{z_i}^{z_{i+1}} p_j(z) dz \right) \quad (\text{B4})$$

where Ω_i is the set of the objects found within $R_{\text{i,deg}}$ around the considered objects, and f_{eff} is a term designed to correct for edges effects, for example, when the circle of diameter $R_{\text{i,deg}}$ overlaps

with a masking region or the edges of the field. In that case, we make the assumption that the number density of sources within the masked area is the same as the unmasked area within $R_{i,\text{deg}}$. We then have $f_{\text{eff}} = \pi R_{i,\text{deg}}^2 / (\pi R_{i,\text{deg}}^2 - A_{\text{masked}})$, with A_{masked} being the masked area. Then, the mean density around the considered source can be written as:

$$n = \sum_i \left(n_i \int_{z_i}^{z_{i+1}} p(z) dz \right) \quad (\text{B5})$$

where $p(z)$ is the probability function of the considered object. The estimate of n greatly depends upon the given object probability function. In order to quantify the significance of the number density estimate around the given object with a given probability function, we determine the mean and standard deviation of n (eq. B5) in a similar catalog but in the absence of clustering. In practice, we extract a catalog in a $0.2^\circ \times 0.2^\circ$ square around the source in the CFHTLS-Wide catalog, and reassign them a uniformly distributed random position. We make 20 realisations of such a catalog, and in each we derive the number density n_{unif} around the considered objects using Eq. B4&B5. We compute the mean $\langle n_{\text{unif}} \rangle$ and the standard deviation $\sigma(n_{\text{unif}})$ of the number density around the considered object when there is no clustering. The overdensity is finally defined as $\rho_{sc} = (n - \langle n_{\text{unif}} \rangle) / \sigma(n_{\text{unif}})$, giving us the significance of the number density estimate.

CHAPTER 6

Internal and environmental properties of X-ray selected AGN.

C. Tasse, H. Röttgering, P. N. Best

To be submitted

There is mounting evidence to suggest that active galactic nuclei (AGN) selected through optical emission lines or radio luminosities actually comprise two distinct AGN populations. In this paper we study the properties of a sample of Type-2 AGN which were selected using their [2-10] keV X-ray flux. The X-ray luminosity function is in good agreement with previous studies. The fraction of galaxies that are X-ray AGN is a strong function of the stellar mass of the host galaxy. The shape of this relation is similar to the fraction of galaxies that are emission-line AGN, while it significantly differs from that relation observed for radio selected AGN. The AGN in our sample are preferentially located in underdense environment where galaxy mergers and interactions are likely to occur. They display a strong infrared excess at short ($\sim 3.5 \mu\text{m}$) wavelength, suggesting the presence of hot dust. The results of this paper suggest that the X-ray selection criteria probes a population of AGN with actively accreting black holes (quasar mode), which is similar to the emission-line selected AGN population.

6.1 INTRODUCTION

It is becoming increasingly clear that active galactic nuclei (AGN) play an important role in the framework of galaxy formation. The enormous amounts of energy produced by AGN during their short lifetime can dramatically influence the evolution of both their host galaxies and their surrounding environment (eg. Croton et al. 2006; Springel et al. 2005).

Although AGN have been studied for decades, many aspects of their physics remain poorly understood. In the picture of the unified scheme of AGN, energy is produced by the accretion of matter onto a super-massive black hole, which is surrounded by a dusty torus. This simple scheme can explain many properties of the different classes of AGN in different wavelength bands. However, observational evidence is mounting to suggest that this picture does not give a proper description for low-luminosity radio-loud AGN. These objects produce weaker or no emission lines (Hine & Longair 1979; Jackson & Rawlings 1997), while they lack the dusty torus infrared emission (Ogle et al. 2006) and the accretion related X-ray emission (Hardcastle et al. 2006). It has been suggested that there are indeed two very different modes of AGN activity named the “Quasar mode” and the “Radio mode” (Best et al. 2005; Hardcastle et al. 2007). A physical interpretation has been proposed in which the infall of cold gas onto the super-massive black hole gives rise to the radiatively efficient quasar mode, while the hot gas infall produces the radiatively inefficient radio mode (Hardcastle et al. 2007).

The undertaking of large surveys provides the opportunity to conduct tests on the nature of the AGN activity (see Heckman & Kauffmann 2006, for a review of the SDSS results). Based on a sample of radio selected AGN in the Canada France Hawaii Telescope Legacy Survey (CFHTLS) field (Tasse et al. 2007a) we have argued in favour of a dichotomy on stellar mass with a separation at $M_{cut} \sim 10^{10.5-10.8} M_{\odot}$ (Tasse et al. 2007b). The high stellar mass systems were preferentially found in cluster-like environments, and were not showing any signs of hot dust emission in the infrared. The properties of the lower stellar mass systems were quite different: they had a lower radio power on average, were displaying a hot dust component, and were laying in large 500 kpc scale underdensities, as well as small 75 kpc overdensities. We have argued (Tasse et al. 2007b) that these radio selected AGN are indeed very different population, with the AGN activity of the low mass population triggered by galaxy mergers and interactions, and the high mass systems with their AGN activity triggered by the gas cooling in their hot atmosphere (Best et al. 2005). Based on the hot infrared excess that is observed only in the low mass systems, we have argued that these observations are consistent with the picture discussed in Hardcastle et al. (2007), where the hot gas cooling produces radiatively inefficient accretion (radio mode), and the cold gas accretion is triggered by galaxy mergers and interactions which drives radiatively efficient accretion (quasar mode).

A good way to further test the scheme in which the type of the accretion mode is connected to the nature of the triggering mechanism, is to select AGN based on their X-ray properties. In the picture of unified scheme, the hard X-ray emission is produced in the hot corona that surrounds the black hole, by the comptonisation of soft UV photons which are emitted by the accretion disk (eg. Liu et al. 2002). In this paper we present a similar study to that of Tasse et al. (2007b), using a sample of hard X-ray selected AGN ([2-10] keV band) from the XMM-Large Scale Structure field Pierre et al. (XMM-LSS, 2004). By using the photometric redshifts, stellar masses, and overdensity estimates (Tasse et al. 2007b), we study the internal and environmental properties of the host galaxies of the X-ray selected AGN in an independent manner. Our results suggest that the

X-ray selected AGN population is dominated by AGN in their quasar mode, which are triggered by galaxy mergers and interactions (cold gas).

In Sec. 6.2 we present the infrared, optical and X-ray data available for the XMM-LSS field. In Sec. 6.3, we proceed with the optical identification, and we select a subsample of Type-2 sources for which we can derive physical parameter estimates. We present the results in Sec. 6.4, and discuss them in Sec. 6.5.

6.2 MULTIWAVELENGTH DATASET

Fig. 6.1 shows the location of the XMM-Newton pointings with respect to the SWIRE, CFHTLS-W1, and low frequency radio surveys.

6.2.1 XMM-LSS X-ray survey

The XMM-LSS field is a wide ~ 10 degree² extragalactic window situated at high galactic latitudes which was surveyed by the XMM-Newton satellite in the [0.5-10] keV energy band. Galaxy clusters are detected as extended X-ray emission, and X-ray emitting AGN are detected as point-like sources. Their surface densities reach ~ 12 and ~ 200 deg⁻², respectively (see Pierre et al. 2004, for a layout of the XMM-LSS and associated surveys).

In this paper we consider the X-ray catalog described in great detail in Pacaud et al. (2006). The catalog was built from the raw X-ray data in three steps: (i) solar proton flares are removed, (ii) the X-ray images are filtered using wavelets, and (iii) using a maximum likelihood procedure, the profiles of detected sources are fitted to determine whether they are point-like or extended. This pipeline has been characterised in great detail using extensive Monte-Carlo simulations (Pacaud et al. 2006). The final band-merged catalog contains sources detected in the [0.5-2] and [2-10] keV bands respectively, referred to as 'soft' and 'hard' band.

The absorption of X-ray photons in general produces a strong decline of the flux measurement in the soft X-ray bands (eg. Reynolds 1997), while this effect is less important at higher energies. For our purposes, we select those X-ray sources that have been classified as point-like and that have a likelihood ratio of detection LR_{DET} such that $LR_{DET} > 15$ (see Pacaud et al. 2006, for a detailed description of LR_{DET}). The flux in the two available bands was computed from the photon count rates assuming a single power law spectrum $F_\nu \propto \nu^{-0.8}$ and the average galactic column density of the XMM-LSS field: $N_H = 2.61 \times 10^{20}$ cm⁻² (Dickey & Lockman 1990).

In order to proceed with the optical identification we have selected X-ray sources overlapping with the CFHTLS-W1 field (Sec. 6.2.2). The final X-ray sample contains 1001 sources. Following Chiappetti et al. (2005), we assume that the error on the position of X-ray sources is $\sigma_{\alpha,\delta} = 3''$.

6.2.2 Optical and infrared surveys

The XMM-LSS field is partially covered by the Wide-1 component of the Canada France Hawai'i Telescope Legacy Survey (CFHTLS¹, Fig. 6.1). Observations were conducted using the five u*g'r'i'z' broad

¹<http://www.cfht.hawaii.edu/Science/CFHLS/>

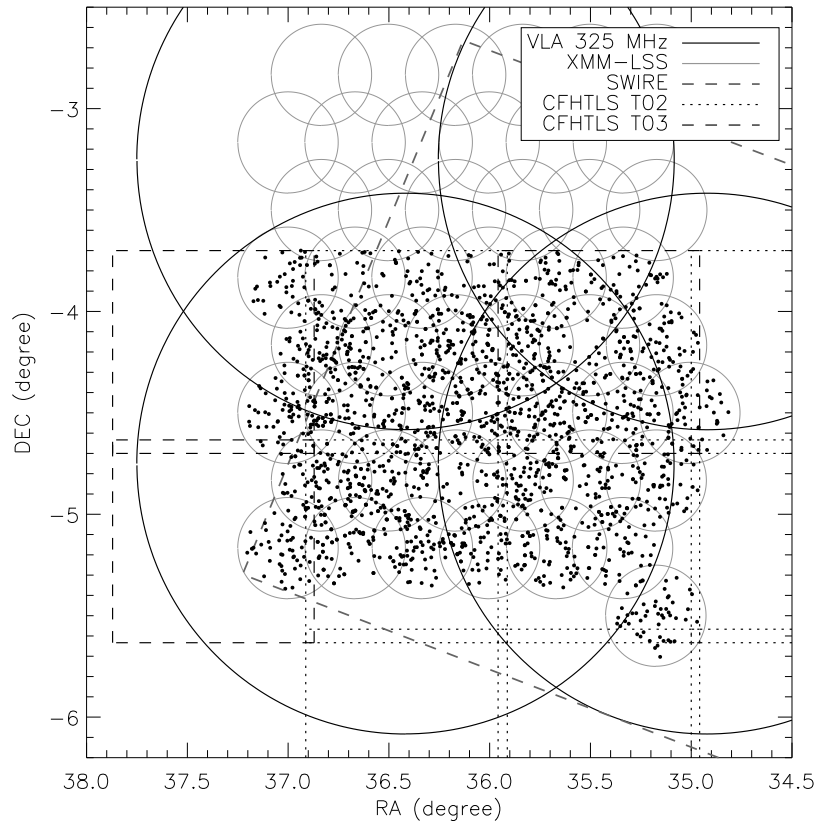


Figure 6.1: The location of the CFHTLS, SWIRE, XMM-LSS fields. The black dots show the X-ray sources selected for optical and infrared identification.

band optical filters, with typical exposures of 1 hour in each filter. The *i*-band limiting magnitude is $i \sim 24.5$ (80% completeness level), with positional uncertainties of $\sim 0.3''$. In this paper we have used the band merged catalogs Terapix T02 and T03 releases².

The Spitzer Wide-area InfraRed Extragalactic legacy survey (SWIRE, Lonsdale et al. 2003) covers the XMM-LSS field over 9.1 degree^2 , using the IRAC instrument from 3.6 to $8.0 \mu\text{m}$ and MIPS from 24 to $160 \mu\text{m}$ (See Fig. 6.1). Throughout this paper we have used the data release 2 (DR2 hereafter) band merged catalog, available online³, containing the flux density measurements at 3.6 , 4.5 , 5.8 , 8.0 and $24 \mu\text{m}$ for a total of $\sim 2.5 \cdot 10^5$ objects. This catalog contains sources detected at 5σ from the 3.6 to $8.0 \mu\text{m}$ images and at 3σ from the $24 \mu\text{m}$ images, corresponding to sensitivities of 14 , 15 , 42 , 56 , and $280 \mu\text{Jy}$, respectively, with positional accuracies better than $0.5''$ (2σ). The data reduction and quality assessment is extensively discussed in Surace et al. (2004).

²<http://terapix.iap.fr/>

³see <http://swire.ipac.caltech.edu/swire/> for more information.

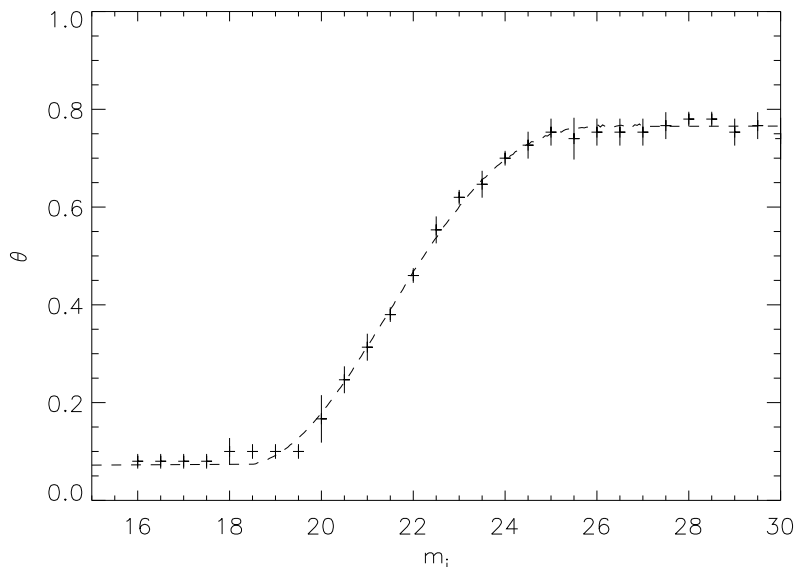


Figure 6.2: In order to identify the optical counterparts of X-ray AGN, we take into account the magnitude distribution that is different from the confusing background sources. The estimated fraction (y-axis) of X-ray AGN having an optical counterpart with i-band below magnitude m (x-axis), has been determined using a Monte-Carlo simulation. Around 80% of X-ray sources have an optical counterpart at the limiting magnitude of our survey.

6.3 A SAMPLE OF X-RAY SELECTED TYPE-2 AGN

6.3.1 Optical identification

In this section we identify optical counterparts for the point-like X-ray sources in the sample described in Sec. 6.2, and using the SWIRE infrared data, we associate infrared flux density measurements to these optical objects. We follow the method of Tasse et al. (2007a) who used a modified version of the likelihood ratio method (Sutherland & Saunders 1992). This likelihood ratio method is discussed in detail in Tasse et al. (2007a), but for completion we briefly describe the technique here.

The likelihood ratio is defined as the probability that the X-ray source has its true optical candidate detected and laying at a distance r , over the probability that the given optical candidate is a background or foreground source. As we do not possess *a priori* knowledge on the properties of the optical counterparts of X-ray sources, the likelihood ratio is first estimated only using the *a priori* probability that an X-ray counterpart has a magnitude m . This information is derived through Monte-Carlo simulations and we find that nearly 80% of the X-ray sources have an optical counterpart in the CFHTLS optical data (Fig. 6.2).

However, it appears that taking into account only the information on magnitude, drives a contamination effect by background sources (see discussion in Tasse et al. 2007a). The second step consists in correcting for this effect, by using the identified population source list to extend the *a priori* knowledge of the optical counterparts of X-ray sources to parameters other than the magni-

tude (stellar mass, redshift, and star formation rate). Monte-Carlo simulations are used to separate the properties of the background sources from the intrinsic properties of optical hosts of X-ray sources. This aspect is discussed in detail in Tasse et al. (2007a). For each X-ray source we obtain a probability of association with its 5 closest optical objects.

In order to conduct an association between infrared and the optical counterparts of X-ray sources, we follow Surace et al. (2004), and require them to be closer than $1.5''$. The source density in the SWIRE DR2 band merged catalog is $\sim 3.2 \times 10^4 \text{ deg}^{-2}$. Assuming a Poisson statistics, the chance of association with a random background source is $\sim 2\%$. Of the sources associated with an optical counterpart in the CFHTLS data, 78% are also associated with an infrared source as detected by IRAC.

6.3.2 Spectral energy distribution fitting and sample selection

In Tasse et al. (2007a) we fit the $u^*g'r'i'z'$ and IRAC flux density measurements with spectral energy distribution (SED) templates for the 2×10^6 galaxies detected in the CFHTLS optical data. We have used two complementary SED fitting methods. The first method uses ZPEG, whose SED template library was built from the stellar synthesis model of Le Borgne & Rocca-Volmerange (2002). For each of the best fitting templates, ZPEG returns estimates for the redshift, stellar masses, and specific star formation rate ($sSFR_{0.5}$ hereafter). Because the stellar synthesis model does not take into account the dust emission, we have used only the $u^*g'r'i'z'$ magnitude measurements to constrain the SED fitting. The second approach uses the SWIRE template library of Polletta et al. (2006), which was built from both observations and theoretical modelling. This library contains both normal galaxy templates and optically active AGN templates such as QSO type 1. The combination of these two methods allows us to (i) obtain a good understanding of the overall content of our sample and (ii) reject the objects for which the ZPEG output parameters are unreliable.

In order to study the properties of X-ray AGN using the photometric redshifts, stellar masses, and $sSFR_{0.5}$ as estimated by ZPEG, we first need to determine and remove various contamination effects. There are two main sources of contamination: (i) the CFHTLS $u^*g'r'i'z'$ photometry that has been used for the physical parameter estimates can be either corrupted (eg. by saturated regions of the CCD) or too noisy for a reliable physical parameter estimate and (ii) the X-ray selected population is known to be biased toward a population of optically active AGN, which means that the photometric redshift will not be reliable for a significant fraction of the sample. Our purpose is to study the physical parameter estimates of the X-ray emitting AGN population, and thus we select a subsample of type-2 X-ray sources for which the photometric redshifts and associated parameters estimates are reliable. We follow the method of Tasse et al. (2007a) who have discussed in detail the criteria used to select Type-2 radio sources' hosts: the rejected AGN are sources best fit by a type-1 AGN template (open circles in Fig. 6.5), or the sources lying in the dashed area of Fig. 6.5. The remaining sample has $18 < i < 24$ and we estimate the remaining contamination is approximately $\sim 1.8\%$.

The X-ray spectra of Type-2 AGN can show strong absorption at lower energies, due to the presence of obscuring material in the line of sight (see Sec. 6.2.1). Following Tajer et al. (2007), we define the hardness ratio as $HR = (CR_H - CR_S)/(CR_H + CR_S)$, where CR_H and CR_S are the count rates in the hard [2-10] and soft [0.5-2] keV band, respectively. Fig 6.3 shows the distribution of HR for the sources selected as contaminating or normal as described above. On average, the

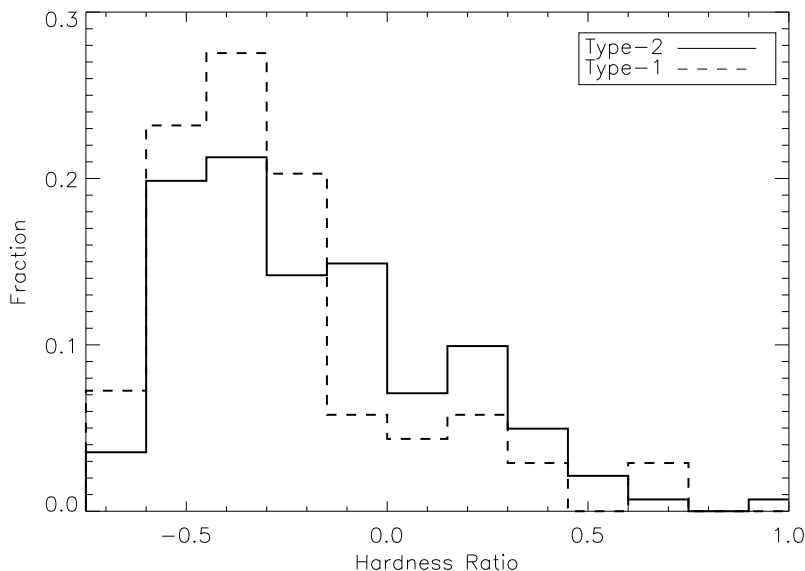


Figure 6.3: Hardness ratio distribution for the sources that have been selected (Type-2) and rejected (Type-1). As is expected the sources showing signs of absorption in the optical and infrared domains, have higher hardness ratios.

rejected AGN population has lower hardness ratios than the population of normal galaxies. As expected, these results indicate that we selected Type-2 AGN, that have a higher hardness ratio due to their higher column density (Tajer et al. 2007).

6.3.3 Extinction correction

In this section we estimate the hydrogen column density of the obscuring material in each of the individual sources, and derive their intrinsic luminosities.

Sazonov & Revnivtsev (2004) have estimated column densities from the flux ratio $F_{[8-20]}/F_{[3-8]}$, where $F_{[8-20]}$ and $F_{[3-8]}$ are the flux measurements in the [8-20] and [3-8] keV X-ray bands respectively. They have shown that these estimates are good first-order approximations of the estimate derived from fitting the X-ray spectra with an absorption model. Using the X-ray pipeline XSPEC, we follow a similar approach. We assume an X-ray AGN spectrum $F_\nu \propto \nu^{-0.8}$ at a redshift z , absorbed with an equivalent hydrogen column density of n_H (model named “zphabs*pow” in XSPEC). From this model, we compute the observed ratio $F_{[0.5-2]}/F_{[2-10]}$ in the $\{z, n_H\}$ parameter space, where $F_{[0.5-2]}$ and $F_{[2-10]}$ are the fluxes measured in the soft and hard X-ray band respectively (Sec. 6.2.1). We have further used the estimates of the hydrogen column density n_H to convert the observed luminosities to intrinsic luminosities.

Fig. 6.4 shows the estimated column density for the sample of optically selected Type-2 AGN. As is expected, the population of selected objects (Sec. ??) has higher hydrogen column density. Tajer et al. (2007) have derived the column densities for optically selected Type-1 and Type-2 sources, by fitting the X-ray spectra with a photo-absorption model. In their sample of ~ 130 X-ray AGN they find that the objects selected as obscured by optical criterion, $63 \pm 18\%$ and $36 \pm 12\%$

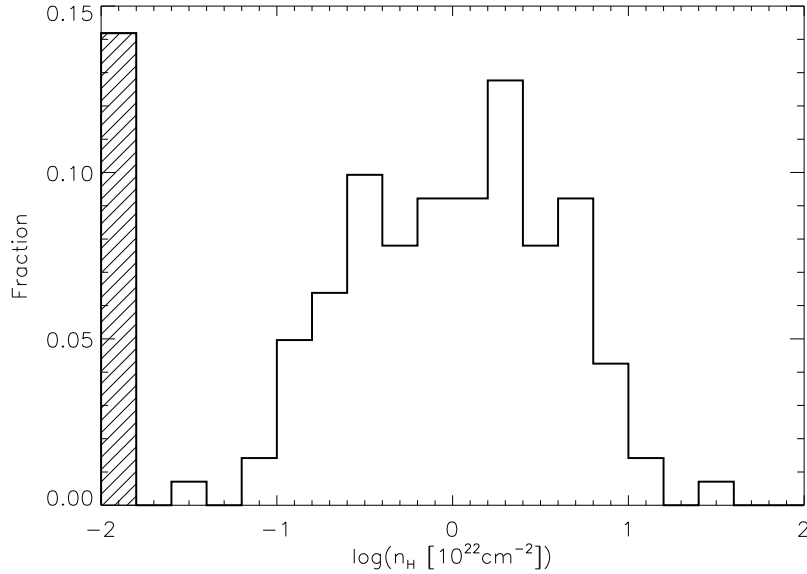


Figure 6.4: Based on the observed flux ratio $F_{[0.5-2]}/F_{[2-10]}$, assuming a underlying $F_\nu \propto \nu^{-0.8}$ X-ray spectra, we have estimated the hydrogen column density for the sample selected in Sec. 6.3.2. As expected, most of the AGN we have selected show signs of absorption in their X-ray spectra.

have $n_H > 10^{21}$ and $n_H > 10^{22} \text{ cm}^{-2}$, respectively, while only $\sim 20\%$ of the objects classified as unobscured have $n_H > 10^{21} \text{ cm}^{-2}$. In our selected sample, we find that $83 \pm 10\%$ and $45 \pm 7\%$ have $n_H > 10^{21}$ and $n_H > 10^{22} \text{ cm}^{-2}$, respectively. These estimates are in quite good agreement, even though we are using a simplistic approach to estimate n_H .

6.4 PROPERTIES OF X-RAY SELECTED AGN

6.4.1 Basic properties of X-ray selected AGN

In this section we discuss the properties of the optical and infrared counterparts of X-ray sources identified in Sec. 6.3.1, and compare them with our radio loud AGN sample (Tasse et al. 2007a).

The top panel of Fig. 6.5 shows the location of the optical counterpart of the X-ray and radio AGN (Tasse et al. 2007a) in a $g'-r'$ versus $r'-i'$ color-color diagram. The dashed area indicates the selection criteria that have been used to classify the sources as Type-1, whereas the open circles show the sources classified as contaminating, using the spectral fits as described in Tasse et al. (2007a). Clearly, X-ray selected AGN optical counterparts show greater differences with the normal galaxy population than with the optical hosts of radio loud AGN. The major fraction of the X-ray selected AGN ($\sim 51\%$) lie inside the Type-1 area, versus a $\sim 12\%$ fraction for the radio loud AGN. A significant fraction of X-ray AGN that are located outside that area are classified as contaminating ($\sim 11\%$) by the spectral fit criteria. These objects were, in general, best fit by a template having both starburst and bright AGN components.

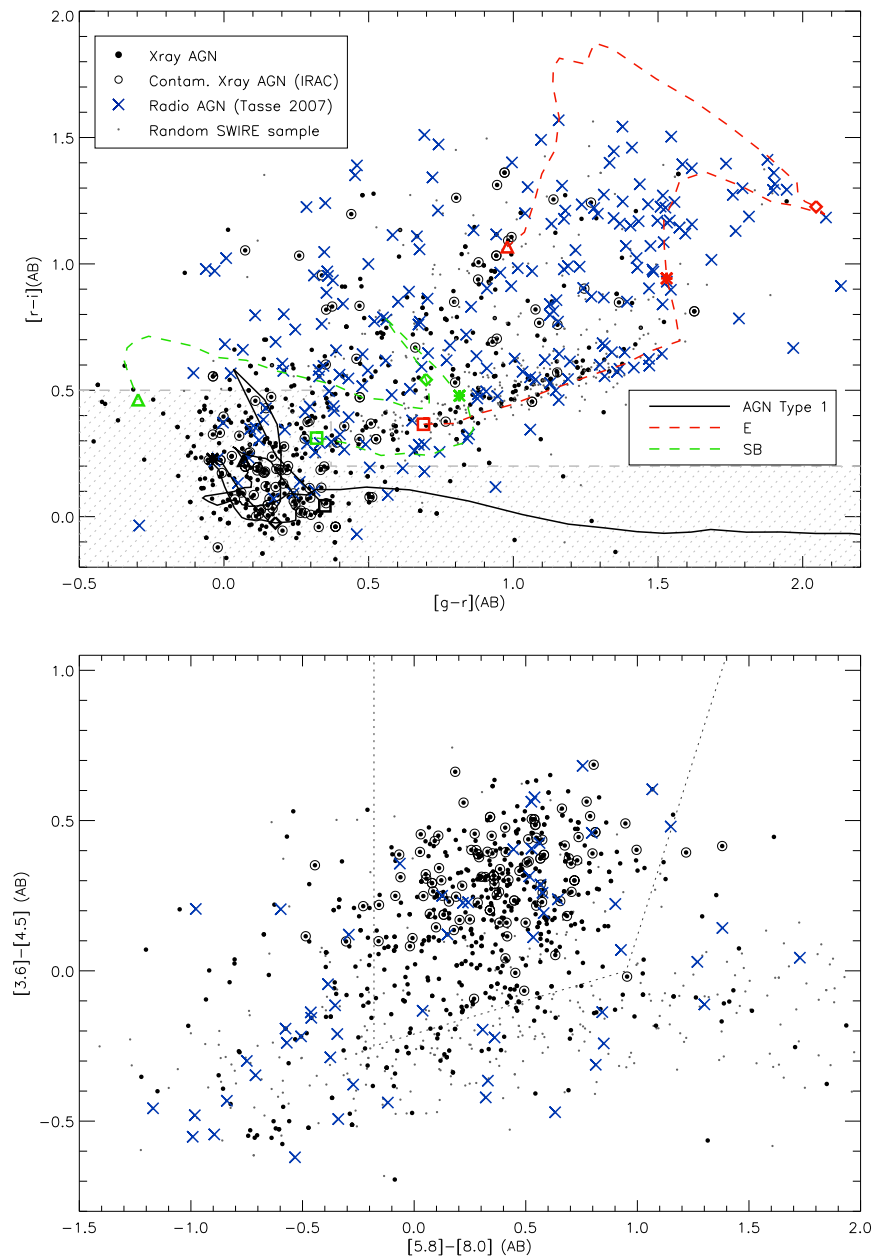


Figure 6.5: Top panel: The $g'-r'$ versus $r'-i'$ color-color diagram for the optical counterparts of X-ray sources (black dots). Open circle indicate the optical counterparts of X-ray sources that have been classified as Type-1 AGN by the spectral fit criteria using the IRAC bands. The dashed area indicates the region corresponding to the optical selection criteria used to reject the contaminating Type-1 AGN. Radio sources' hosts and X-ray optical counterparts clearly occupy different regions of this plot, with the radio loud AGN being hosted by galaxies that do not show strong signs of AGN activity in the optical. Bottom panel: The $[3.6]-[4.5]$ versus $[5.8]-[8.0]$ infrared color-color diagram. Stern et al. (2005) find $\sim 90\%$ of the broad-line AGN lying in the area delimited by the dotted line. The sources marked as open circle have been rejected from our sample.

The bottom panel of Fig. 6.5 shows the [3.6]-[4.5] versus [5.8]-[8.0] infrared color-color plot. Stern et al. (2005) argues that 90% of the broad-line AGN lie within this area, as well as $\sim 40\%$ of the narrow-line AGN, and 7% of normal galaxies. We find that $\sim 51\%$ of our sources that have flux density measurement in all the IRAC bands lie within this region, while this fraction goes to $\sim 95\%$ for the sources best fit by a Type-1 galaxy template, in agreement with the estimate of Stern et al. (2005). However $\sim 60\%$ of the sources classified as Type-2 lay in this region, in contrast with the $\sim 20\%$ found for the radio selected AGN (Tasse et al. 2007a).

6.4.2 Luminosity function

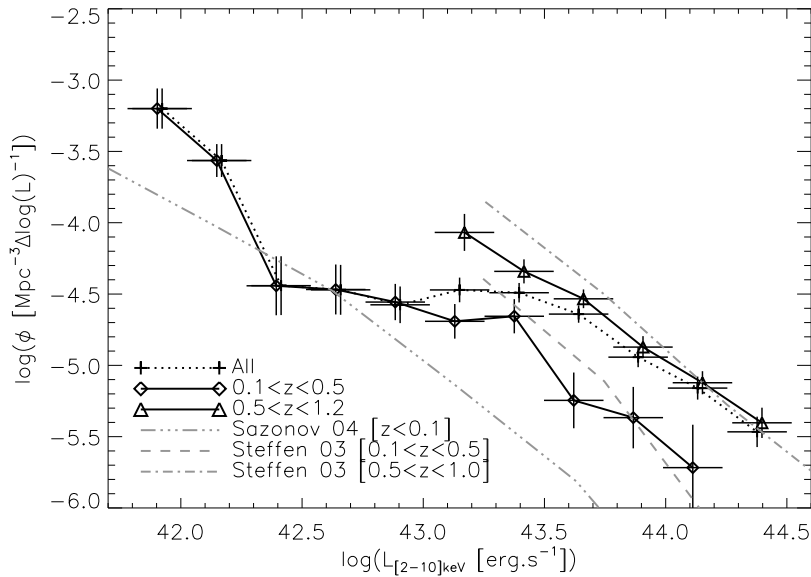


Figure 6.6: We have estimated the X-ray luminosity function in the $0.1 < z < 1.2$, $0.1 < z < 0.5$ and $0.5 < z < 1.0$. Our estimates are in good agreement with Steffen et al. (2003) and Sazonov & Revnivtsev (2004) at low redshifts.

In order to derive comoving number density estimates, we use the $1/V_{max}$ estimator (Schmidt 1968), where V_{max} is the maximum volume over which a given object is observable. We first estimate the dependence of the effective area on the X-ray flux. For this, we follow Steffen et al. (2003), and simply compare our source count at each flux to the source counts given within Cowie et al. (2002). For each given X-ray source we then use XSPEC, as well as the estimated luminosity and column density, to obtain the flux at each redshift, as well as the corresponding effective area. We obtain V_{max} by integrating between z_{min} and z_{max} the probed volume at each redshift. We have estimated z_{min} and z_{max} for the optical data according to the method described in Tasse et al. (2007b).

Fig. 6.6 shows the X-ray luminosity function computed using the $1/V_{max}$ estimator in the $0.1 < z < 1.2$, $0.1 < z < 0.5$ and $0.5 < z < 1.2$ redshift ranges. Based on a sample of ~ 150 sources having spectroscopic redshifts, Steffen et al. (2003) have computed the X-ray luminosity function for the ranges $0.1 < z < 0.5$ and $0.5 < z < 1.0$ in the [2-8] keV band. In order to compare our results with theirs, we assume X-ray spectra with $F_{\nu} \propto \nu^{-0.8}$, and derive an $L_{[2-8]}-L_{[2-10]}$ conversion

factor. Our estimates are in good agreement with Steffen et al. (2003) for both the high and the low redshift ranges. We also compare our estimate of the X-ray luminosity function with the estimate of Sazonov & Revnivtsev (2004) at $z \lesssim 1$ in the [3-20] keV energy band. In order to do this, we estimate the conversion factor as described previously. Our results are in good agreement and are further discussed in Sec. 6.5.

6.4.3 Stellar mass function

Using the number density estimator described in Sec. 6.4.2, we have computed the mass function (ϕ_X) for the host galaxies of X-ray AGN and the fraction f_X of galaxies that are X-ray AGN above a certain X-ray luminosity. This is simply computed as $f_X = \phi_X / \phi_{opt}$, where ϕ_{opt} is our estimate of the mass function for normal galaxies. Fig. 6.7 shows the estimates of f_X for the redshift ranges $0.1 < z < 0.6$ and $0.6 < z < 1.2$ and for X-ray luminosities $L_X > 10^{43}$ erg.s⁻¹.

For comparison, we have plotted the low redshift $z \lesssim 0.3$ fraction of AGN versus mass relation, with emission line luminosities $L_{O[III]} > 10^{6.5} L_\odot$ and $L_{O[III]} > 10^{7.5} L_\odot$, and with 1.4 GHz radio luminosities $P_{1.4} > 10^{24}$ W.Hz⁻¹ and $P_{1.4} > 10^{25}$ W.Hz⁻¹ (Best et al. 2005). Interestingly, the slope of the $f_X \propto M^{-1.5}$ relation is in good agreement with the AGN fraction versus the stellar mass relation for the emission line AGN, but disagrees with the relation for the radio selected AGN. In order to directly compare our X-ray luminosities with emission line luminosities, we use the $L_{[3-20]}$ versus $L_{O[III]}$ relation given by Heckman et al. (2005) in the [3-20] keV band ($\log(L_{[3-20]}/L_{O[III]}) = 2.15$), with a conversion factor between the [3-20] and [2-10] keV bands (assuming an X-ray spectra with $F_\nu \propto \nu^{-0.8}$). The $L_X > 10^{43}$ erg.s⁻¹ X-ray luminosity we consider here correspond to [OIII] line luminosities of $L_{O[III]} > 10^{7.5} L_\odot$. In the lower redshift bin the difference is as high as ~ 1.5 dex, while in the higher redshift bin the shape of the $f_X - M$ relation follows that of the emission-line AGN, with an average difference of 1 dex. Differences are to be expected: Heckman et al. (2005) have shown that X-ray selection criteria miss a significant fraction of emission-line AGN. Specifically, at $z \lesssim 0.1$ the AGN luminosity function using emission lines and X-ray criteria are different by ~ 0.5 dex (Heckman et al. 2005). In the framework of the unified scheme of AGN these differences were often suggested to be due to the existence of an AGN population heavily obscured in the X-ray regime (Levenson et al. 2002). The difference of $\sim 1 - 1.5$ dex we observe between comoving number density of the X-ray selected AGN, and that of emission line AGN is higher than that observed by Heckman et al. (2005). This is to be expected however, as we have rejected a significant fraction of X-ray AGN, classified as contaminating Type-1 ($\sim 30\%$), corresponding to 0.15 dex. Furthermore, Heckman et al. (2005) used the X-ray luminosity function as estimated from harder [8-20] keV X-rays, meaning more objects are detected because the X-rays are less absorbed at those higher energies. These results are further discussed in Sec. 6.5.

6.4.4 Infrared properties

In order to study the infrared properties of the optical hosts of X-ray AGN, leading on from Tasse et al. (2007b), we have derived an infrared excess parameter at 3.6, 4.5, 5.8, 8.0 μm . This excess is calculated in the observer frame, using the Z-PEG best fit template (which does not take into account dust infrared emission), and by computing the difference of the observed flux density to the flux density of the stellar population as deduced using the u*g'r'i'z' magnitude measurements.

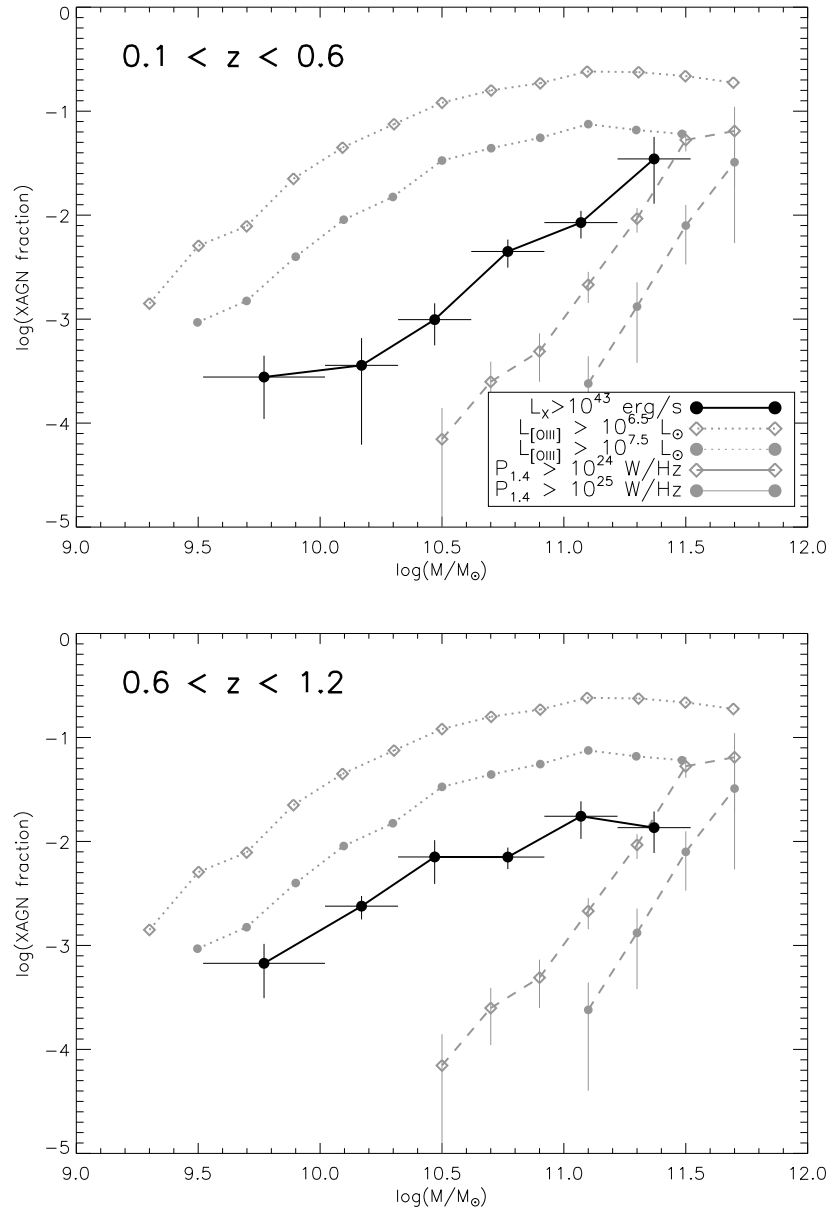


Figure 6.7: The fraction of galaxies that are X-ray AGN with $L_{[2-10]} > 10^{43}$ erg.s $^{-1}$, as a function of the stellar mass, in the $0.1 < z < 0.6$ and $0.6 < z < 1.2$ redshift ranges. The slope of the relationship shows good agreement with the fraction of galaxies that satisfy AGN based emission line criteria, while it disagrees with this relation for radio selected AGN.

In order to compare the infrared excess of the optical hosts of AGN to the infrared excess of the normal galaxy population, we compute the difference between their infrared excesses Δ_{IR} in similar stellar mass and redshift bins (see Tasse et al. 2007b, for details). Fig. 6.8 shows Δ_{IR} for the X-ray selected AGN using different stellar mass bins. As suggested by the distribution of these sources in the infrared [3.6]-[4.5] versus [5.8]-[8.0] color-color plot (Fig. 6.5), X-ray selected AGN show an infrared excess at short wavelength.

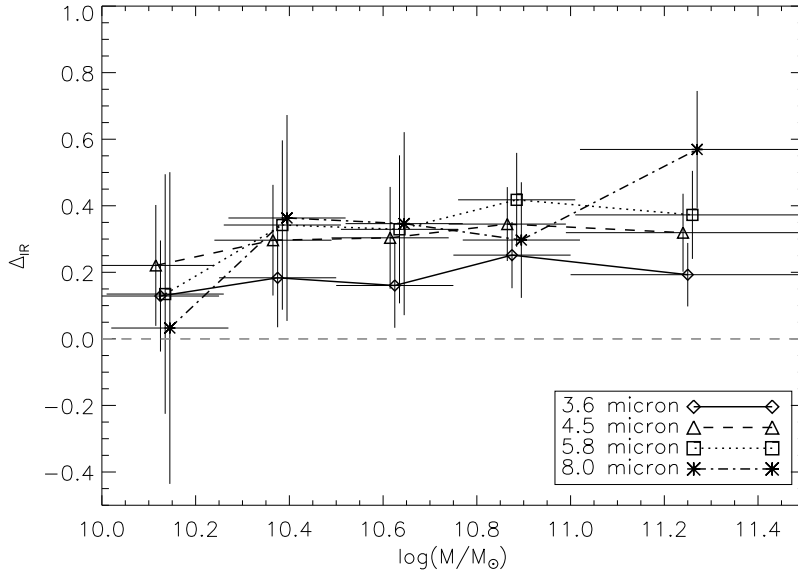


Figure 6.8: Following Tasse et al. (2007b) we have computed the infrared excess for the normal galaxies and for the host galaxies of X-ray selected AGN. This plot shows the difference in infrared excess between these two populations. The X-ray selected AGN show a hot infrared excess, at short wavelengths.

6.4.5 Environment

In Tasse et al. (2007b) we described an overdensity parameter that is based on the photometric redshifts probability functions. It gives the significance of the number density found around a given object at a given comoving scale. Following Tasse et al. (2007b), we have computed this overdensity parameter at 75, and 450 kpc for the sample of X-ray selected AGN, and compare the overdensity of the AGN population with the overdensities of the normal galaxies. As discussed in Tasse et al. (2007b), the estimated overdensity may be biased toward lower values when the redshift increases. In order to compare the environment of distinct population, for each X-ray selected AGN, we compute the quantity $\Delta\rho = \rho_i - q_{0.5}[\rho^N(dz, dM)]$, where ρ_i is the estimated overdensity of the given object and $q_{0.5}[\rho^N(dz, dM)]$ is the median overdensity of non-radio-loud galaxies that have comparable stellar mass, and redshift estimates. In practice, we take redshift bin $dz = 0.1$, and mass bin $dM = 0.2$. Fig. 6.9 shows the median value of $\Delta\rho$ for the X-ray AGN situated in given stellar mass range.

The environment of X-ray AGN is quite different from the environment of normal galaxies. The X-ray AGN are preferentially situated in large scale underdensities $\Delta\rho_{450} \sim -0.4$, while they seem quite insensitive to the small scale environment.

6.5 SUMMARY AND DISCUSSION

In this paper we have proceeded to optically identify a sample of ~ 1000 point-like X-ray sources in the XMM-LSS field, leading to a fraction of X-ray sources having an optical counterpart of $\sim 80\%$. In order to reject the Type-1 AGN for which we cannot retrieve reliable photometric

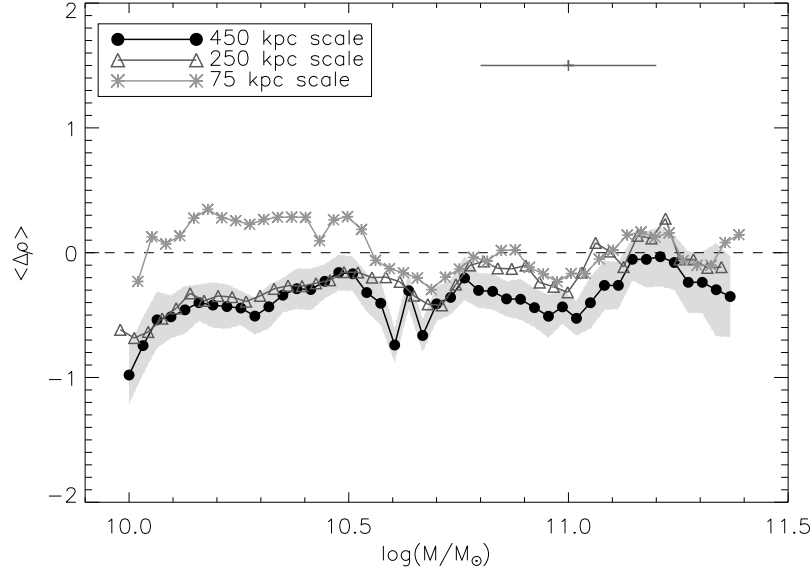


Figure 6.9: We have computed the overdensity parameter for the normal galaxies and for the X-ray selected AGN. This figure shows the differences between these two populations: the X-ray selected AGN lay in large scale (450 kpc) underdense environments.

redshifts estimates, we have followed, in detail, the method described in Tasse et al. (2007a). We estimate that the remaining contamination by Type-1 AGN is on the level of $\sim 2\%$. In order to correct for the extinction by dust in the line of sight, we have estimated the hydrogen column density. A significant fraction of our selected sample ($\gtrsim 50\%$) shows such absorption in the X-ray, with column densities $n_H > 10^{22} \text{ cm}^{-2}$ (Fig. 6.4). These estimates are in quite good agreement with results from previous surveys (Tajer et al. 2007). Based on these estimates, we have corrected for the extinction, and estimate the intrinsic X-ray luminosities. The main results from this work are as follows:

- (i) The X-ray luminosity function of the X-ray selected AGN sample in the redshift ranges $0.1 < z < 0.5$ and $0.5 < z < 1.0$ (Fig. 6.6) shows good agreement with previous measurements (Steffen et al. 2003), with a strong comoving number density evolution at $L_{[2-10]} > 10^{43} \text{ erg.s}^{-1}$.
- (ii) The fraction f_X of galaxies that are X-ray luminous with $L_X > 10^{43} \text{ erg.s}^{-1}$ have a strong stellar mass dependence with $f_X \propto M^{1.5}$, which is similar to the slope found for the emission line AGN (Best et al. 2005). By using an X-ray versus [OIII] luminosity relationship (Heckman et al. 2005), we found that the comoving number density of X-ray selected and emission line selected AGN (Best et al. 2005) differ by ~ 1 dex at low redshift.
- (iii) Compared with normal galaxies of the same mass, X-ray selected AGN show an infrared excess in the IRAC 3.6, 4.5, 5.8 and $8.0 \mu\text{m}$ bands and over the full mass range (Fig. 6.8).
- (iv) Compared with normal galaxies of the same mass, X-ray selected AGN are preferentially found in underdense large-scale (450 kpc) environments over the full stellar mass range.

Their small 75 kpc overdensities is similar to the overdensities found around normal galaxies.

Many authors have suggested that there are indeed two different modes of accretion: the Quasar mode is radiatively efficient, while on the other hand the Radio mode is radiatively inefficient (see Sec. 6.1 for a discussion). In Tasse et al. (2007b), based on a sample of radio selected AGN, we have argued that the accretion mode in the most massive galaxies has low efficiency. These sources may have their AGN activity triggered by the cooling of the hot gas that is observed in their atmosphere (Mathews & Brighenti 2003; Best et al. 2005). Conversely, the lower stellar mass systems ($M < 10^{10.5-11.0} M_{\odot}$) show signs of actively accreting black holes. We have argued that their AGN activity is triggered by major galaxy mergers and interaction in underdense environments. In the following, we argue that X-ray selected AGN may correspond to the radiatively efficient Quasar mode.

Result (ii) above shows that, as expected, the fraction of galaxies that are X-ray AGN is a strong function of stellar mass (Fig. 6.7). However, using an $L_{[OIII]} - L_X$ relationship (Heckman et al. 2005), the number densities of X-ray selected and emission line selected AGN show strong differences. We have argued in Sec. 6.4.3 that this effect is indeed expected as many Type-2 emission line AGN are not seen to produce significant X-ray flux, even in the hard [2-10] keV X-ray bands (Heckman et al. 2005). This is often interpreted as sources that are heavily absorbed and even compton thick (Levenson et al. 2002). Although we have corrected for the intrinsic absorption in each individual source, this suggests that there are many obscured X-ray sources, that we do not detect. However, the slope of the relation between stellar mass and fraction of X-ray selected AGN ($f_X \propto M^{1.5}$) is in relatively good agreement with the relation between the fraction of galaxies that are classified as AGN using emission line criteria, while it disagrees with the fraction f_{Rad} of radio loud AGN versus stellar mass relation $f_{Rad} \propto M^{2.5}$. This suggests that although we are missing a significant fraction of the X-ray luminous AGN population, we are indeed selecting the same AGN galaxy population of emission line AGN that have been recognised as AGN which have radiatively efficient accretion (“Quasar mode”, Heckman et al. 2004; Best et al. 2005). This picture is supported by the result (iii) on the infrared properties of X-ray selected AGN: these objects have a hot dust component at wavelength as short as $3.6 \mu\text{m}$ (observer frame), which are often interpreted as being due to an actively accreting black hole where UV light heats the surrounding dust at temperatures of 500 – 1000 K (Seymour et al. 2007). Result (iv) suggests that these AGN are preferentially located in large 450 kpc scale underdensities at levels of ~ -0.5 . Consistently, luminous $L_{[OIII]} > 10^7 L_{\odot}$ emission line AGN are preferentially found in underdense environment (Kauffmann et al. 2004; Best et al. 2005).

The internal and environmental properties of this X-ray selected AGN population are very similar to the characteristics of the low stellar mass radio selected AGN population. Both of these classes of AGN have a rather flat fraction mass relation ($f \propto M^{1.5}$), an infrared excess, and they lie in large scale underdense environments. These factors suggest that X-ray, optical, and low-mass radio AGN are indeed similar populations, which are dominated by quasar mode AGN. However, environmental differences are found at the smaller scale: contrary to the radio AGN, the X-ray selected AGN seem quite insensitive to their small 75 kpc scale overdensities.

It has often been proposed that luminous AGN activity is triggered by the galaxy mergers and interactions, and this process has been suggested to occur more frequently in underdense environments (eg. Gómez et al. 2003; Best 2004). Galaxy mergers and interactions, as the dominant

triggering processes for these AGN, provide a natural explanation to the underdensities found around X-ray selected, and low-mass radio-selected AGN. The differences found in the small 75 kpc scale environment might be caused by various effects. If the AGN are triggered by a major merger, there might be an observational sequence that AGN follow during their lifetime: while the radio emission is seen to be associated with small scale overdensities, it might be that during the X-ray emitting phase, the two interacting galaxies have already merged into a single system. Alternatively, Taniguchi (1999) suggests that minor mergers that are produced by the interaction between a given galaxy and a low mass satellite galaxy can play an important role in triggering AGN activity. In such cases our dataset would certainly not allow us to detect a galaxy pair as a small 75 kpc overdensity. It could be that the intergalactic medium gas state is different in these underdense regions, and actually favours such scenarios.

ACKNOWLEDGMENTS

The optical images were obtained with MegaPrime/MegaCam, a joint project of CFHT and CEA/DAPNIA, at the CFHT which is operated by the National Research Council (NRC) of Canada, the Institut National des Sciences de l'Univers of the Centre National de la Recherche Scientifique (CNRS) of France and the University of Hawaii. This work is based on data products produced at TERAPIX and at the Canadian Astronomy Data Centre as part of the CFHTLS, a collaborative project of NRC and CNRS.

REFERENCES

- Best, P. N. 2004, *MNRAS*, 351, 70
- Best, P. N., Kauffmann, G., Heckman, T. M., et al. 2005, *MNRAS*, 362, 25
- Chiappetti, L., Tajer, M., Trinchieri, G., et al. 2005, *A&A*, 439, 413
- Cowie, L. L., Garmire, G. P., Bautz, M. W., et al. 2002, *ApJ*, 566, L5
- Croton, D. J., Springel, V., White, S. D. M., et al. 2006, *MNRAS*, 365, 11
- Dickey, J. M. & Lockman, F. J. 1990, *ARA&A*, 28, 215
- Gómez, P. L., Nichol, R. C., Miller, C. J., et al. 2003, *ApJ*, 584, 210
- Hardcastle, M. J., Evans, D. A., & Croston, J. H. 2006, *MNRAS*, 370, 1893
- Hardcastle, M. J., Evans, D. A., & Croston, J. H. 2007, *MNRAS*, 376, 1849
- Heckman, T. M. & Kauffmann, G. 2006, *New Astronomy Review*, 50, 677
- Heckman, T. M., Kauffmann, G., Brinchmann, J., et al. 2004, *ApJ*, 613, 109
- Heckman, T. M., Ptak, A., Hornschemeier, A., & Kauffmann, G. 2005, *ApJ*, 634, 161
- Hine, R. G. & Longair, M. S. 1979, *MNRAS*, 188, 111
- Jackson, N. & Rawlings, S. 1997, *MNRAS*, 286, 241
- Kauffmann, G., White, S. D. M., Heckman, T. M., et al. 2004, *MNRAS*, 353, 713
- Le Borgne, D. & Rocca-Volmerange, B. 2002, *A&A*, 386, 446
- Levenson, N. A., Krolik, J. H., Życki, P. T., et al. 2002, *ApJ*, 573, L81

- Liu, B. F., Mineshige, S., Meyer, F., Meyer-Hofmeister, E., & Kawaguchi, T. 2002, *ApJ*, 575, 117
- Lonsdale, C. J., Smith, H. E., Rowan-Robinson, M., et al. 2003, *PASP*, 115, 897
- Mathews, W. G. & Brighenti, F. 2003, *ARA&A*, 41, 191
- Ogle, P., Whyson, D., & Antonucci, R. 2006, *ApJ*, 647, 161
- Pacaud, F., Pierre, M., Refregier, A., et al. 2006, *MNRAS*, 372, 578
- Pierre, M., Valtchanov, I., Altieri, B., et al. 2004, *Journal of Cosmology and Astro-Particle Physics*, 9, 11
- Polletta, M. d. C., Wilkes, B. J., Siana, B., et al. 2006, *ApJ*, 642, 673
- Reynolds, C. S. 1997, *MNRAS*, 286, 513
- Sazonov, S. Y. & Revnivtsev, M. G. 2004, *A&A*, 423, 469
- Schmidt, M. 1968, *ApJ*, 151, 393
- Seymour, N., Stern, D., De Breuck, C., et al. 2007, *ArXiv Astrophysics e-prints*
- Springel, V., Di Matteo, T., & Hernquist, L. 2005, *ApJ*, 620, L79
- Steffen, A. T., Barger, A. J., Cowie, L. L., Mushotzky, R. F., & Yang, Y. 2003, *ApJ*, 596, L23
- Stern, D., Eisenhardt, P., Gorjian, V., et al. 2005, *ApJ*, 631, 163
- Surace, J. A., Shupe, D. L., Fang, F., et al. 2004, *VizieR Online Data Catalog*, 2255, 0
- Sutherland, W. & Saunders, W. 1992, *MNRAS*, 259, 413
- Tajer, M., Polletta, M., Chiappetti, L., et al. 2007, *A&A*, 467, 73
- Taniguchi, Y. 1999, *ApJ*, 524, 65
- Tasse, C., Le Borgne, D., Röttgering, H. J. A., et al. 2007a, *A&A* (Submitted)
- Tasse, C., N. Best, P. N., Röttgering, H. J. A., & Le Borgne, D. 2007b, *A&A* (In prep.)

APPENDIX

A TABLE

Table A1: Properties of the selected X-ray sources.

Name	X-ray				Optical						IR				Phys. prop.					
	RA (J2000)	DEC (J2000)	log(F _S)	log(F _H)	RA (J2000)	DEC (J2000)	u (AB)	g (AB)	r (AB)	i (AB)	z (AB)	3.6 μ m (AB)	4.5 μ m (AB)	5.8 μ m (AB)	8.0 μ m (AB)	z	log(M) [M _⊙]	log(S) [yr ⁻¹]	n _H [cm ⁻²]	L[2-10] [erg.s ⁻¹]
X888	02 19 15.85	-04 29 49.39	-14.18	-13.50	02 19 15.83	-04 29 50.11	23.54	23.11	22.28	22.07	> 23.60	19.37	19.06	18.69	18.14	0.42	9.32	-8.92	22.3	43.3
X885	02 19 41.80	-04 28 02.55	-13.85	-13.48	02 19 41.78	-04 28 06.34	25.61	25.08	24.24	22.94	21.91	> 21.03	> 20.96	> 19.84	> 19.53	1.14	10.49	-∞	22.3	44.4
X880	02 19 52.30	-04 24 47.10	-13.29	-13.04	02 19 52.37	-04 24 48.75	22.57	21.59	20.51	19.79	19.39	18.22	18.17	17.84	17.80	0.54	10.97	-10.25	21.6	44.0
X909	02 19 59.19	-04 08 00.60	.	-13.84	02 19 59.36	-04 08 02.06	24.18	24.15	23.49	22.67	22.21	> 21.03	> 20.96	> 19.84	> 19.53	0.94	10.18	-9.31	22.1	43.8
X899	02 20 15.59	-04 03 03.99	.	-13.82	02 20 15.73	-04 03 07.64	24.72	24.97	23.34	22.46	21.84	13.78	14.29	14.70	15.33	0.87	10.75	-10.85	22.1	43.8
X898	02 20 16.18	-04 03 00.08	.	-13.80	02 20 16.16	-04 02 59.49	24.30	23.00	21.53	20.41	20.05	13.78	14.29	14.70	15.33	0.70	10.95	-∞	22.1	43.6
X826	02 20 16.74	-04 56 48.34	-13.81	-13.49	02 20 16.84	-04 56 46.16	23.63	22.70	21.44	20.77	20.44	19.64	19.67	19.34	19.50	0.48	10.57	-10.85	21.7	43.5
X914	02 20 20.06	-04 10 06.14	.	-13.77	02 20 20.10	-04 10 06.21	24.73	22.85	21.63	20.76	20.42	18.53	18.45	18.14	17.75	0.57	10.49	-∞	22.0	43.4
X789	02 20 23.28	-04 39 00.03	.	-13.64	02 20 22.97	-04 39 03.00	25.34	24.72	> 25.00	22.49	21.90	0.00	0.00	0.00	0.00	0.96	10.20	-∞	22.5	44.1
X929	02 20 26.37	-04 16 20.98	-14.70	-13.83	02 20 26.26	-04 16 23.50	21.97	20.62	19.31	18.68	18.35	18.17	18.25	18.53	18.30	0.46	11.35	-10.85	22.5	43.1
X788	02 20 27.43	-04 37 27.99	-14.19	-13.23	02 20 27.18	-04 37 25.22	24.33	23.87	23.38	22.44	22.15	0.00	0.00	0.00	0.00	0.77	10.26	-9.59	22.8	44.3
X894	02 20 27.30	-04 37 25.61	.	-13.38	02 20 27.18	-04 37 25.22	24.33	23.87	23.38	22.44	22.15	> 21.03	> 20.96	> 19.84	> 19.53	0.77	10.26	-9.59	22.7	44.1
X806	02 20 27.57	-04 49 34.80	-13.55	-13.26	02 20 27.65	-04 49 33.40	22.63	22.62	> 25.00	21.55	21.49	19.58	18.99	18.69	18.03	0.86	9.82	-8.93	21.9	44.3
X976	02 20 29.63	-05 19 39.41	.	-13.18	02 20 29.86	-05 19 39.55	22.84	21.84	20.75	20.25	19.85	19.59	19.73	> 19.84	> 19.53	0.42	10.70	-10.12	22.6	43.7
X802	02 20 32.58	-04 45 57.38	-14.35	-14.05	02 20 32.69	-04 45 58.06	22.85	22.45	21.97	21.24	20.80	19.17	19.41	19.82	> 19.53	0.93	10.85	-9.41	22.0	43.6
X990	02 20 39.44	-05 29 26.75	-14.37	-13.96	02 20 39.66	-05 29 28.42	21.21	20.40	19.54	19.06	18.76	18.19	18.15	18.34	17.72	0.28	10.74	-9.99	21.8	42.4
X940	02 20 41.36	-03 48 41.91	.	-13.74	02 20 41.27	-03 48 41.77	22.62	21.07	19.64	18.82	18.52	18.03	18.27	18.30	18.36	0.56	11.15	-∞	22.1	43.4
X1000	02 20 43.14	-05 39 33.64	-14.08	-13.12	02 20 43.33	-05 39 34.30	> 24.90	22.19	20.75	20.00	19.68	18.16	18.00	17.83	17.63	0.50	10.77	-∞	22.6	43.9
X793	02 20 48.29	-04 41 30.36	.	-13.89	02 20 48.24	-04 41 30.42	> 24.70	26.39	24.94	23.77	23.16	19.89	19.63	> 19.84	> 19.53	0.93	9.82	-∞	22.0	43.8
X934	02 20 52.13	-04 20 32.88	-14.77	-13.79	02 20 52.34	-04 20 32.93	23.45	22.53	21.47	20.60	20.20	18.73	19.01	19.07	18.75	0.59	10.85	-10.49	22.7	43.4
X825	02 20 52.81	-04 56 14.43	.	-13.84	02 20 53.00	-04 56 16.38	26.62	24.17	24.16	23.02	23.23	19.54	19.36	19.11	19.31	0.82	9.20	-8.93	22.1	43.7
X921	02 20 58.19	-04 11 50.13	-14.06	-13.74	02 20 57.96	-04 11 52.20	25.15	24.26	23.21	21.98	21.40	19.35	19.53	> 19.84	> 19.53	0.96	10.40	-∞	22.1	44.0
X857	02 20 58.23	-04 32 41.75	-14.58	-13.81	02 20 58.19	-04 32 43.34	23.96	22.72	21.80	20.73	20.23	19.22	19.65	19.76	19.86	0.73	11.15	-10.85	22.6	43.6
X943	02 21 01.78	-03 54 14.10	.	-13.78	02 21 02.12	-03 54 13.40	22.46	21.34	20.67	20.37	20.16	20.78	21.00	> 19.84	> 19.53	0.13	9.18	-10.09	21.7	41.9
X843	02 21 02.41	-04 26 00.53	-14.30	-13.71	02 21 02.27	-04 26 01.13	23.05	22.51	21.79	21.14	20.70	19.15	19.32	> 19.84	19.17	0.68	10.59	-9.51	22.4	43.6
X946	02 21 05.21	-03 56 01.69	-13.53	-13.24	02 21 05.15	-03 56 01.07	21.36	20.37	19.49	18.98	18.66	17.69	17.54	17.43	17.15	0.26	10.71	-10.23	21.5	43.1
X989	02 21 05.48	-05 29 16.17	-14.23	-13.74	02 21 05.26	-05 29 18.12	24.44	24.03	23.34	22.60	20.88	20.00	20.02	> 19.84	> 19.53	1.18	10.81	-∞	22.5	44.2
X925	02 21 16.04	-04 13 45.89	-14.75	-14.02	02 21 16.02	-04 13 44.22	22.86	22.02	21.13	20.07	19.59	18.60	18.89	18.96	18.82	0.79	11.43	-10.38	22.6	43.5
X837	02 21 15.95	-04 19 55.89	.	-13.67	02 21 16.21	-04 19 54.92	23.93	23.31	22.53	21.94	21.90	> 21.03	> 20.96	> 19.84	> 19.53	0.62	9.85	-9.17	22.3	43.6
X983	02 21 17.00	-05 25 09.44	-14.75	-13.94	02 21 17.03	-05 25 09.51	23.86	22.18	20.93	20.39	20.15	19.54	19.64	19.66	19.45	0.22	10.13	-∞	22.3	42.3
X851	02 21 17.90	-04 31 01.99	-13.77	-13.67	02 21 17.96	-04 31 01.58	21.39	21.78	20.90	20.64	20.39	19.07	19.06	18.71	18.38	0.67	10.15	-9.16	< 21.0	43.6
X923	02 21 18.98	-04 12 51.26	.	-13.80	02 21 19.06	-04 12 45.92	23.84	23.97	23.18	22.43	21.52	0.00	0.00	0.00	0.00	1.12	11.17	-10.38	22.3	44.1
X939	02 21 21.35	-03 46 13.88	.	-13.81	02 21 21.38	-03 46 13.73	24.11	22.80	> 24.90	20.38	19.91	15.75	16.24	16.64	17.25	0.54	11.10	-∞	21.9	43.3
X930	02 21 22.95	-04 16 56.34	.	-13.67	02 21 22.68	-04 16 53.12	24.18	23.97	24.07	23.25	23.45	0.00	0.00	0.00	0.00	0.87	9.12	-8.63	22.4	43.9
X841	02 21 24.23	-04 25 17.51	.	-14.01	02 21 24.49	-04 25 17.66	21.82	20.25	19.09	18.57	18.20	17.62	17.33	16.96	16.38	0.18	10.74	-∞	21.1	41.9
X913	02 21 24.64	-04 09 28.72	.	-13.62	02 21 24.81	-04 09 30.80	24.57	24.49	23.52	22.81	22.37	19.94	19.60	> 19.84	19.24	0.93	10.27	-9.67	22.5	44.1
X835	02 21 36.54	-04 18 29.93	-14.11	-13.82	02 21 36.57	-04 18 28.67	26.02	25.62	23.92	23.20	23.39	> 21.03	> 20.96	> 19.84	> 19.53	0.61	9.23	-∞	21.8	43.4
X877	02 21 36.38	-04 18 28.78	-14.07	-13.37	02 21 36.57	-04 18 28.67	26.02	25.62	23.92	23.20	23.39	> 21.03	> 20.96	> 19.84	> 19.53	0.61	9.23	-∞	22.5	43.9
X972	02 21 42.68	-05 20 37.46	-13.87	-13.57	02 21 42.63	-05 20 37.67	21.88	21.25	20.83	20.34	20.15	18.72	18.72	18.44	18.33	0.71	10.36	-8.66	21.9	43.8
X872	02 21 42.82	-04 13 43.17	-14.30	-13.68	02 21 43.04	-04 13 43.65	24.04	24.06	23.37	21.86	21.80	19.51	19.71	19.39	> 19.53	0.82	9.97	-8.90	22.5	43.9
X521	02 21 46.98	-05 00 14.52	-14.08	-13.55	02 21 47.10	-05 00 16.12	24.82	23.75	22.83	22.62	24.20	19.59	19.30	19.78	18.98	0.35	8.75	-8.91	22.0	43.1
X956	02 21 46.96	-05 00 16.43	-13.85	-13.40	02 21 47.10	-05 00 16.12	24.82	23.75	22.83	22.62	24.20	19.59	19.30	19.78	18.98	0.35	8.75	-8.91	21.9	43.2
X520	02 21 49.86	-04 59 17.67	-14.09	-13.43	02 21 49.87	-04 59 18.61	24.13	23.59	23.04	22.32	22.19	18.70	18.17	17.81	17.30	0.71	9.80	-9.01	22.5	44.0
X518	02 21 53.62	-04 55 07.10	-14.22	-13.96	02 21 53.81	-04 55 10.17	23.84	23.52	23.86	23.12	23.05	20.34	20.09	19.72	> 19.53	0.43	7.26	-8.74	21.6	42.0
X868	02 21 56.61	-04 07 55.44	.	-13.69	02 21 56.50	-04 07 57.82	21.00	20.66	20.35	19.40	20.53	18.37	17.68	16.88	16.18	0.73	10.55	-8.93	22.3	43.7
X508	02 22 02.31	-04 48 42.01	-14.36	-13.90	02 22 02.22	-04 48 41.66	22.22	20.66	19.84	19.40	19.25	19.32	19.76	> 19.84	> 19.53	0.19	9.92	-∞	21.8	42.1
X655	02 22 02.70	-05 09 42.54	-13.88	-13.43	02 22 02.75	-05 09 44.39	20.30	19.77	19.03	18.62	18.25	17.65	17.42	17.21	16.73	0.28	10.78	-9.75	21.9	43.0
X964	02 22 02.67	-05 09 44.42	-12.92	-12.55	02 22 02.75	-05 09 44.39	20.30	19.77	19.03	18.62	18.25	17.65	17.42	17.21	16.73	0.28	10.78	-9.75	21.7	43.9
X502	02 22 06.81	-04 41 36.29	.	-13.81	02 22 06.73	-04 41 38.48	22.31	20.67	19.76	19.25	18.90	> 21.03	> 20.96	> 19.84	> 19.53	0.11	9.97	-∞	21.6	41.7
X650	02 22 15.43	-05 07 12.51	-14.94	-14.22	02 22 15.59	-05 07 11.23	> 24.70	24.41	24.15	22.81	21.52	> 21.03	> 20.96	> 19.84	> 19.53	1.19	10.62	-∞	22.8	43.7
X876	02 22 18.28	-04 14 57.64	-13.97	-13.28	02 22 18.18	-04 14 57.82	24.37	23.16	22.60	22.18	22.08	> 21.03	> 20.96	> 19.84						

Name	X-ray				Optical						IR				Phys. prop.					
	RA (J2000)	DEC (J2000)	log(F _S)	log(F _H)	RA (J2000)	DEC (J2000)	u (AB)	g (AB)	r (AB)	i (AB)	z (AB)	3.6 μ m (AB)	4.5 μ m (AB)	5.8 μ m (AB)	8.0 μ m (AB)	z	log(M) [M \odot]	log(S) [yr ⁻¹]	n _H [cm ⁻²]	L[2-10] [erg.s ⁻¹]
X322	02 22 31.52	-04 26 43.44	-14.48	-13.92	02 22 31.39	-04 26 43.37	22.53	21.13	20.52	19.49	19.28	16.32	16.82	17.28	17.94	0.72	11.19	-9.67	22.4	43.5
X354	02 22 34.42	-04 37 08.52	-14.05	-13.74	02 22 34.48	-04 37 09.76	21.79	20.60	19.88	19.39	19.18	19.29	19.40	> 19.84	19.06	0.16	10.09	-10.35	21.5	42.1
X715	02 22 36.49	-03 53 43.79	-14.09	-13.59	02 22 36.60	-03 53 43.81	24.56	24.37	22.99	22.33	21.31	19.16	19.11	19.07	19.08	1.14	10.68	-∞	22.5	44.3
X637	02 22 38.20	-05 00 57.62	-14.28	-13.38	02 22 38.18	-05 00 59.34	23.48	23.12	> 25.00	21.06	20.46	18.40	18.16	17.82	17.11	0.87	11.14	-10.73	22.8	44.3
X647	02 22 40.11	-05 06 56.33	.	-14.19	02 22 39.82	-05 06 57.99	21.42	20.55	> 25.00	19.33	19.08	19.19	19.31	> 19.84	18.54	0.20	10.33	-10.09	< 21.0	41.9
X320	02 22 40.89	-04 26 15.12	-14.70	-14.13	02 22 40.84	-04 26 14.73	24.86	25.85	24.44	23.98	23.59	20.19	20.29	> 19.84	> 19.53	1.01	10.07	-9.59	22.5	43.6
X712	02 22 41.00	-03 50 37.63	-13.43	-13.27	02 22 41.01	-03 50 36.93	21.65	20.94	19.81	19.27	18.91	18.68	18.69	18.98	18.47	0.42	11.08	-10.12	21.3	43.5
X474	02 22 44.79	-04 47 55.52	.	-13.96	02 22 45.01	-04 47 51.56	22.41	21.61	20.57	19.84	19.44	18.54	18.94	19.49	19.21	0.57	10.96	-10.09	21.6	43.2
X314	02 22 50.26	-04 22 54.15	-13.91	-13.65	02 22 50.31	-04 22 53.87	23.75	22.76	21.88	20.96	20.51	18.76	18.74	18.47	18.11	0.68	10.80	-10.25	21.7	43.7
X119	02 22 50.73	-04 00 31.69	-13.97	-13.54	02 22 50.88	-04 00 32.20	23.56	22.89	22.13	21.35	20.69	18.52	18.56	18.29	18.14	1.02	10.87	-9.87	22.4	44.2
X710	02 22 51.37	-03 48 43.35	-13.94	-13.50	02 22 51.45	-03 48 44.35	24.90	24.60	23.86	23.14	22.57	19.66	19.52	19.59	> 19.53	0.97	10.23	-9.67	22.3	44.2
X152	02 22 51.63	-04 15 39.92	.	-13.88	02 22 51.57	-04 15 41.15	24.93	23.96	23.23	22.25	21.71	20.57	20.60	> 19.84	> 19.53	0.84	10.53	-10.09	22.0	43.7
X645	02 22 52.10	-05 06 21.67	-14.64	-14.15	02 22 52.14	-05 06 23.31	21.71	21.11	20.57	19.86	19.67	18.53	18.81	18.65	18.65	0.71	10.88	-9.26	22.3	43.2
X498	02 22 58.78	-04 58 51.86	-13.31	-13.29	02 22 58.88	-04 58 52.35	19.90	19.73	19.36	19.10	18.86	17.77	17.67	17.40	16.99	0.71	10.52	-8.63	< 21.0	44.1
X635	02 22 58.80	-04 58 52.26	-13.31	-13.28	02 22 58.88	-04 58 52.35	19.90	19.73	19.36	19.10	18.86	17.77	17.67	17.40	16.99	0.71	10.52	-8.63	< 21.0	44.1
X470	02 22 59.93	-04 46 25.22	.	-14.05	02 22 59.88	-04 46 26.54	22.69	21.64	20.40	19.56	19.26	18.24	18.46	18.14	17.98	0.56	11.23	-10.85	21.1	43.1
X340	02 23 01.93	-04 32 04.64	-14.42	-13.98	02 23 02.06	-04 32 05.15	22.04	21.21	20.34	19.78	19.57	18.04	17.98	17.79	17.49	0.26	10.38	-10.23	21.8	42.4
X471	02 23 02.28	-04 46 51.67	-14.40	-13.83	02 23 02.26	-04 46 52.03	24.40	23.50	22.44	21.28	20.93	19.89	20.33	> 19.84	> 19.53	0.72	10.88	-10.85	22.4	43.6
X135	02 23 05.92	-04 08 35.99	-14.71	-13.98	02 23 05.91	-04 08 35.45	25.19	24.38	23.98	22.81	22.38	19.38	19.24	19.63	> 19.53	0.83	10.08	-9.67	22.6	43.6
X144	02 23 06.82	-04 12 53.75	.	-13.89	02 23 06.84	-04 12 53.67	25.53	25.46	24.66	23.10	22.72	20.30	20.50	> 19.84	> 19.53	0.88	9.69	-8.90	22.0	43.7
X134	02 23 07.59	-04 08 18.38	-14.25	-14.12	02 23 07.60	-04 08 18.31	20.55	20.01	19.18	18.85	18.54	18.16	18.11	18.06	17.47	0.39	10.85	-9.48	21.1	42.6
X117	02 23 09.94	-04 23 04.30	-13.99	-13.77	02 23 10.02	-04 23 04.03	22.02	21.03	20.42	20.04	19.82	19.83	19.89	> 19.84	18.43	0.13	9.54	-9.90	21.3	41.9
X318	02 23 15.39	-04 25 58.45	-14.37	-13.81	02 23 15.33	-04 25 58.49	20.19	19.16	18.56	18.21	18.06	18.28	18.25	18.11	17.13	0.14	10.31	-9.81	21.9	41.9
X624	02 23 18.30	-05 12 07.51	-13.63	-13.34	02 23 18.34	-05 12 08.46	21.64	20.41	19.15	18.57	18.26	17.88	17.88	18.02	17.66	0.43	11.32	-10.85	21.7	43.5
X658	02 23 18.09	-05 12 09.09	-13.60	-13.42	02 23 18.34	-05 12 08.46	21.64	20.41	19.15	18.57	18.26	17.88	17.88	18.02	17.66	0.43	11.32	-10.85	21.4	43.4
X472	02 23 19.54	-04 47 31.49	-13.78	-13.45	02 23 19.60	-04 47 30.89	22.10	20.45	19.30	18.69	18.31	17.09	16.86	16.67	16.29	0.46	11.32	-10.49	21.8	43.5
X630	02 23 19.60	-05 14 18.33	.	-13.93	02 23 19.72	-05 14 18.86	28.34	24.87	23.68	22.74	21.83	19.70	19.80	19.75	19.69	1.11	10.51	-∞	22.0	43.9
X296	02 23 21.20	-04 33 04.79	.	-13.68	02 23 21.16	-04 33 04.19	23.18	22.76	22.54	21.72	21.44	20.41	20.74	> 19.84	> 19.53	0.85	10.25	-9.15	22.4	43.9
X494	02 23 21.90	-04 57 38.97	-14.62	-13.26	02 23 21.99	-04 57 38.42	22.29	21.66	20.79	19.65	19.27	17.57	17.13	16.75	15.95	0.73	11.47	-10.38	23.1	44.2
X668	02 23 22.17	-05 16 28.74	-14.67	-13.47	02 23 22.43	-05 16 27.09	26.66	24.90	23.36	22.60	21.51	19.70	19.98	> 19.84	> 19.53	0.79	10.88	-∞	23.0	44.1
X301	02 23 35.26	-04 36 12.29	-14.38	-13.79	02 23 35.57	-04 36 13.45	22.66	22.17	21.62	21.28	21.00	19.54	19.34	19.05	19.08	0.66	9.92	-8.66	22.4	43.5
X272	02 23 39.34	-04 20 00.11	.	-13.71	02 23 39.27	-04 20 05.08	22.79	21.66	20.42	19.80	19.45	19.08	19.24	19.52	18.98	0.45	10.89	-10.85	22.1	43.2
X280	02 23 40.33	-04 24 20.20	-14.02	-13.70	02 23 40.38	-04 24 20.02	24.96	24.66	24.65	23.40	22.29	20.73	20.53	> 19.84	> 19.53	1.17	10.11	-8.90	22.2	44.2
X297	02 23 46.97	-04 33 45.69	-14.17	-13.86	02 23 47.03	-04 33 48.00	21.25	20.56	19.76	19.23	18.93	17.96	17.95	17.81	17.37	0.56	11.17	-9.59	21.8	43.3
X598	02 23 47.30	-05 00 27.08	-14.24	-13.90	02 23 47.41	-05 00 28.72	22.73	22.28	21.38	21.01	21.22	20.26	20.33	> 19.84	> 19.53	0.60	9.81	-8.92	21.9	43.3
X306	02 23 49.33	-04 40 09.74	-14.50	-13.80	02 23 49.50	-04 40 11.00	23.58	22.56	21.64	20.69	20.29	19.01	19.16	19.09	18.64	0.68	10.90	-10.25	22.5	43.5
X626	02 23 50.18	-05 13 11.52	-13.80	-13.56	02 23 50.32	-05 13 10.91	22.43	21.97	21.41	21.00	20.69	19.84	19.47	19.45	18.54	0.67	10.14	-8.74	21.7	43.8
X274	02 23 51.18	-04 20 54.33	-14.45	-13.62	02 23 51.24	-04 20 53.33	20.87	19.97	19.50	19.22	19.21	19.24	19.33	19.58	17.55	0.14	9.65	-9.71	22.2	42.1
X283	02 23 51.83	-04 24 36.27	.	-13.90	02 23 51.79	-04 24 35.77	23.64	22.05	20.75	20.01	19.67	19.01	18.97	18.74	18.24	0.47	10.78	-∞	21.7	43.0
X728	02 23 52.83	-03 56 41.63	-13.93	-13.54	02 23 52.84	-03 56 42.44	24.01	22.77	21.66	21.10	20.57	18.13	17.66	17.27	16.81	0.46	10.38	-10.49	21.9	43.4
X305	02 23 54.36	-04 39 16.01	.	-13.92	02 23 54.21	-04 39 20.17	23.87	23.03	22.21	21.33	20.89	0.00	0.00	0.00	0.00	0.81	10.75	-9.89	21.8	43.6
X273	02 23 55.86	-04 20 17.90	-14.37	-13.70	02 23 55.95	-04 20 18.41	27.68	25.25	24.31	23.56	23.24	20.22	20.10	> 19.84	> 19.53	0.56	9.44	-10.09	22.4	43.4
X292	02 23 56.62	-04 31 16.73	-14.03	-13.90	02 23 56.67	-04 31 18.00	23.69	23.27	22.63	22.13	22.09	> 21.03	> 20.96	> 19.84	> 19.53	0.64	9.67	-8.83	21.2	43.4
X730	02 23 59.72	-03 57 48.69	-14.18	-13.73	02 23 59.68	-03 57 47.28	26.80	25.17	23.90	22.81	22.24	19.98	20.15	> 19.84	> 19.53	0.94	10.11	-∞	22.3	44.0
X277	02 24 03.84	-04 21 58.29	-15.01	-13.83	02 24 03.72	-04 21 56.97	24.80	24.64	23.64	22.66	21.86	20.10	20.58	> 19.84	> 19.53	1.05	10.25	-8.90	23.2	44.1
X481	02 24 03.97	-04 51 20.43	-13.86	-13.61	02 24 04.05	-04 51 18.51	22.59	22.25	21.44	21.14	20.70	18.62	18.43	18.26	18.02	0.32	9.84	-9.60	21.5	42.9
X729	02 24 03.91	-03 57 26.07	-14.37	-13.48	02 24 04.09	-03 57 28.13	23.64	23.31	22.70	21.57	20.61	18.34	18.34	18.34	18.01	1.11	10.82	-8.90	23.0	44.4
X282	02 24 05.34	-04 24 23.83	-14.73	-14.10	02 24 05.49	-04 24 23.73	23.17	22.19	21.25	20.47	20.05	18.14	18.22	18.12	17.68	0.58	10.79	-10.25	22.4	43.1
X597	02 24 08.54	-04 58 55.62	-14.70	-13.63	02 24 08.48	-04 58 56.65	22.69	21.97	21.27	20.53	20.30	19.36	19.53	19.28	19.31	0.66	10.83	-9.59	22.8	43.7
X106	02 24 15.56	-04 14 17.40	-13.86	-13.70	02 24 15.76	-04 14 16.66	22.46	22.13	21.76	21.23	21.20	19.47	18.98	18.36	17.96	0.71	9.92	-8.62	21.4	43.7
X622	02 24 18.23	-05 10 34.24	-13.76	-13.58	02 24 18.39	-05 10 34.83	21.11	20.69	20.11	19.78	19.44	18.73	18.54	18.48	17.93	0.67	10.54	-8.66	21.5	43.

Name	X-ray				Optical							IR				Phys. prop.				
	RA (J2000)	DEC (J2000)	log(F ₅)	log(F _H)	RA (J2000)	DEC (J2000)	u (AB)	g (AB)	r (AB)	i (AB)	z (AB)	3.6 μ m (AB)	4.5 μ m (AB)	5.8 μ m (AB)	8.0 μ m (AB)	z	log(M) [M _☉]	log(S) [yr ⁻¹]	n _H [cm ⁻²]	L[2-10] [erg.s ⁻¹]
X618	02 24 30.51	-05 08 39.59	-13.86	-13.69	02 24 30.56	-05 08 41.69	21.66	20.48	19.37	18.86	18.50	18.54	18.70	19.02	18.59	0.45	11.07	-10.09	21.3	43.2
X573	02 24 32.72	-05 09 28.09	.	-13.58	02 24 32.81	-05 09 33.40	24.66	23.93	23.00	22.03	21.34	0.00	0.00	0.00	0.00	1.02	10.43	-8.90	22.6	44.2
X574	02 24 32.81	-05 09 34.04	-14.14	-13.50	02 24 32.81	-05 09 33.40	24.66	23.93	23.00	22.03	21.34	19.46	19.36	19.24	18.89	1.02	10.43	-8.90	22.6	44.3
X620	02 24 32.75	-05 09 33.82	-14.12	-13.31	02 24 32.81	-05 09 33.40	24.66	23.93	23.00	22.03	21.34	19.46	19.36	19.24	18.89	1.02	10.43	-8.90	22.8	44.5
X87	02 24 33.54	-04 07 52.92	.	-14.18	02 24 33.23	-04 07 54.83	22.83	22.00	21.48	21.24	21.23	> 21.03	> 20.96	> 19.84	> 19.53	0.20	9.09	-9.56	< 21.0	41.9
X235	02 24 39.72	-04 23 59.07	-13.59	-13.30	02 24 39.72	-04 24 01.47	21.11	20.49	19.87	19.38	19.11	17.96	17.90	17.71	17.38	0.65	11.00	-9.26	21.8	44.0
X279	02 24 39.58	-04 24 02.12	-13.80	-13.63	02 24 39.72	-04 24 01.47	21.11	20.49	19.87	19.38	19.11	17.96	17.90	17.71	17.38	0.65	11.00	-9.26	21.4	43.6
X70	02 24 40.10	-03 59 43.62	.	-13.86	02 24 39.97	-03 59 42.13	24.97	24.98	24.15	23.65	23.21	21.00	20.96	> 19.84	> 19.53	0.97	10.09	-9.51	22.1	43.8
X563	02 24 48.66	-05 06 10.59	.	-14.00	02 24 48.74	-05 06 14.91	25.93	23.83	22.47	21.35	21.12	19.54	20.03	> 19.84	19.77	0.71	10.33	-∞	21.5	43.4
X110	02 24 49.21	-04 18 01.27	-13.74	-13.66	02 24 49.23	-04 18 02.01	22.00	21.56	21.05	20.50	20.24	19.34	19.33	18.91	19.15	0.70	10.44	-8.83	< 21.0	43.7
X74	02 24 52.07	-04 02 59.43	.	-13.57	02 24 51.97	-04 02 59.88	21.66	20.32	19.51	19.01	18.71	18.04	18.15	18.14	16.78	0.11	10.00	-∞	22.0	41.9
X101	02 24 52.06	-04 12 09.96	-13.96	-13.78	02 24 52.36	-04 12 11.97	23.54	23.20	22.82	22.04	21.72	20.86	21.04	> 19.84	> 19.53	0.82	10.20	-9.26	21.6	43.7
X111	02 24 53.12	-04 18 09.78	-14.15	-13.89	02 24 53.30	-04 18 07.92	22.94	22.52	21.94	21.41	21.12	> 21.03	> 20.96	> 19.84	> 19.53	0.68	10.11	-9.15	21.8	43.4
X569	02 24 54.91	-05 08 26.38	-14.36	-14.13	02 24 54.96	-05 08 25.75	22.43	21.81	21.27	20.64	20.26	19.03	19.24	19.12	18.98	0.72	10.61	-9.26	21.7	43.3
X751	02 25 00.45	-04 00 39.17	-14.38	-13.51	02 25 00.32	-04 00 37.98	23.39	22.74	21.60	21.28	21.19	19.18	18.68	18.18	17.76	0.44	9.84	-9.44	22.5	43.4
X71	02 25 00.50	-04 00 40.70	-14.40	-13.77	02 25 00.61	-04 00 38.18	22.53	21.60	21.06	20.70	20.56	20.63	20.70	> 19.84	> 19.53	0.13	9.18	-9.75	22.0	41.9
X575	02 25 11.24	-05 09 41.26	.	-13.89	02 25 11.31	-05 09 40.87	26.33	24.98	23.56	22.32	21.68	19.66	19.78	> 19.84	> 19.53	0.83	10.68	-∞	21.9	43.7
X245	02 25 17.93	-04 27 52.29	.	-14.06	02 25 18.25	-04 27 50.31	23.84	22.84	21.74	20.71	20.34	18.72	18.95	18.95	18.40	0.67	11.02	-10.85	21.2	43.2
X403	02 25 20.32	-04 42 43.03	-14.93	-13.76	02 25 20.43	-04 42 38.86	22.40	21.74	20.90	20.55	20.46	20.32	20.81	> 19.84	> 19.53	0.26	9.88	-9.73	22.6	42.6
X244	02 25 22.89	-04 26 49.04	-14.45	-13.56	02 25 22.86	-04 26 47.78	24.03	23.05	22.06	21.02	20.42	18.28	18.24	18.09	17.73	0.83	11.24	-10.85	22.8	44.0
X231	02 25 24.21	-04 19 50.73	.	-13.90	02 25 24.55	-04 19 50.76	22.80	22.34	21.80	21.47	21.35	21.22	21.23	> 19.84	> 19.53	0.62	9.78	-8.66	21.8	43.3
X576	02 25 26.86	-05 09 43.69	-14.33	-13.81	02 25 26.84	-05 09 45.20	23.48	22.86	22.28	21.90	21.66	18.91	18.78	18.82	> 19.53	0.66	9.75	-8.74	22.3	43.5
X580	02 25 30.83	-05 10 49.01	-13.91	-13.74	02 25 30.85	-05 10 50.19	23.22	22.21	21.51	20.71	20.46	18.48	18.55	18.18	18.07	0.66	10.88	-9.70	21.5	43.6
X404	02 25 31.92	-04 43 42.45	.	-13.78	02 25 32.01	-04 43 46.54	23.02	21.44	20.15	19.57	19.17	18.70	18.74	19.12	18.73	0.45	10.98	-10.85	21.9	43.1
X595	02 25 35.05	-05 19 59.73	-14.55	-13.64	02 25 35.02	-05 19 57.49	22.28	21.12	20.16	19.72	19.39	18.59	18.47	18.40	17.65	0.14	9.96	-∞	22.3	42.1
X557	02 25 36.10	-05 03 15.23	-14.09	-13.69	02 25 36.12	-05 03 14.12	25.40	22.79	21.36	20.15	19.74	18.21	18.24	18.02	17.68	0.64	11.18	-∞	22.0	43.6
X585	02 25 44.77	-05 12 33.97	-14.46	-14.06	02 25 44.79	-05 12 34.52	23.96	23.41	22.78	21.73	21.06	19.22	19.43	19.60	> 19.53	1.03	10.47	-8.90	22.3	43.7
X401	02 25 50.99	-04 41 39.34	-14.37	-13.83	02 25 50.90	-04 41 40.96	24.56	23.66	22.87	21.67	21.06	18.91	18.92	18.71	18.40	0.99	10.50	-8.90	22.5	43.9
X438	02 25 53.26	-05 00 18.73	.	-13.87	02 25 53.14	-05 00 18.55	24.02	24.28	23.73	22.95	21.79	19.60	19.68	> 19.84	19.86	1.16	10.24	-8.91	22.2	44.0
X424	02 25 54.23	-04 49 19.44	-14.49	-14.03	02 25 54.18	-04 49 21.05	24.00	23.60	22.79	22.00	21.76	19.69	19.62	19.49	19.37	0.66	10.33	-9.73	22.2	43.3
X53	02 26 14.36	-03 59 35.54	-14.47	-13.61	02 26 14.53	-03 59 38.34	24.72	22.42	20.92	19.84	19.46	18.39	18.74	18.71	19.39	0.64	11.25	-∞	22.7	43.7
X430	02 26 15.11	-04 53 55.05	-14.12	-13.64	02 26 15.10	-04 53 55.82	23.67	22.89	22.22	21.44	20.83	19.40	19.64	19.01	19.51	0.73	10.81	-9.87	22.3	43.8
X211	02 26 15.14	-04 22 31.54	-14.45	-13.81	02 26 15.43	-04 22 32.45	23.71	22.80	21.86	20.75	20.23	18.76	18.43	18.02	17.25	0.79	11.26	-10.85	22.5	43.7
X51	02 26 17.28	-03 58 31.36	.	-13.61	02 26 16.86	-03 58 30.38	20.22	19.13	18.51	18.15	18.04	0.00	0.00	0.00	0.00	0.15	10.39	-9.81	22.0	42.2
X704	02 26 18.58	-05 17 23.52	-14.10	-13.63	02 26 18.70	-05 17 25.47	23.20	22.58	21.58	20.86	20.54	19.19	19.48	> 19.84	> 19.53	0.56	10.73	-9.99	22.1	43.5
X215	02 26 26.55	-04 27 36.69	.	-13.86	02 26 26.41	-04 27 36.83	23.12	23.02	22.69	21.99	21.82	19.98	20.04	> 19.84	> 19.53	0.90	9.92	-8.61	22.1	43.8
X64	02 26 26.45	-04 12 13.07	.	-13.46	02 26 26.59	-04 12 12.75	23.73	22.77	21.71	20.67	20.28	18.21	18.17	17.72	17.06	0.68	11.06	-10.85	22.6	43.9
X431	02 26 27.34	-04 57 10.36	-13.64	-13.37	02 26 27.41	-04 57 10.81	> 25.00	21.96	22.00	21.43	21.48	16.64	17.12	17.36	17.25	0.91	9.80	-8.71	21.9	44.3
X683	02 26 27.49	-04 57 10.21	-14.04	-11.96	02 26 27.41	-04 57 10.81	> 25.00	21.96	22.00	21.43	21.48	16.64	17.12	17.36	17.25	0.91	9.80	-8.71	23.5	45.9
X428	02 26 28.11	-04 53 12.69	-14.02	-13.74	02 26 28.09	-04 53 12.93	> 25.00	21.63	21.45	20.79	20.64	19.19	19.22	19.23	> 19.53	0.85	10.30	-9.10	21.9	43.8
X372	02 26 33.34	-04 46 34.60	-13.91	-13.44	02 26 33.29	-04 46 37.08	26.69	24.56	22.99	21.64	20.95	19.25	19.49	19.93	19.32	0.82	11.07	-∞	22.3	44.1
X415	02 26 33.35	-04 46 37.78	-14.00	-13.55	02 26 33.29	-04 46 37.08	26.69	24.56	22.99	21.64	20.95	19.25	19.49	19.93	19.32	0.82	11.07	-∞	22.3	44.0
X752	02 26 37.86	-03 45 37.52	-13.74	-13.42	02 26 37.86	-03 45 40.18	25.37	25.07	23.85	22.88	22.05	NC	NC	NC	NC	1.05	10.25	-∞	22.1	44.4
X219	02 26 38.82	-04 29 32.90	.	-14.13	02 26 38.83	-04 29 33.30	24.78	24.15	23.28	22.03	21.45	19.20	19.31	18.94	18.55	0.96	10.38	-∞	< 21.0	43.6
X755	02 26 42.09	-03 50 10.19	.	-13.76	02 26 42.24	-03 50 10.50	21.43	20.10	19.08	18.60	18.34	NC	NC	NC	NC	0.18	10.60	-∞	21.7	42.2
X676	02 26 43.45	-05 03 58.34	.	-13.62	02 26 43.14	-05 03 57.50	23.78	23.39	22.69	21.92	21.66	20.28	20.72	> 19.84	> 19.53	0.70	10.29	-9.51	22.4	43.8
X44	02 26 43.84	-04 16 24.95	-13.84	-13.26	02 26 43.93	-04 16 27.07	21.82	20.11	19.06	18.52	18.28	17.38	17.35	17.39	17.01	0.20	10.78	-∞	22.0	42.8
X67	02 26 43.93	-04 16 25.84	.	-13.24	02 26 43.93	-04 16 27.07	21.82	20.11	19.06	18.52	18.28	17.38	17.35	17.39	17.01	0.20	10.78	-∞	22.4	42.9
X218	02 26 49.31	-04 29 21.11	-14.48	-13.89	02 26 49.35	-04 29 22.04	23.88	22.52	21.35	20.43	20.04	18.70	18.99	18.81	19.15	0.59	10.96	-10.85	22.3	43.3
X33	02 26 49.83	-04 12 39.02	-13.91	-13.65	02 26 49.82	-04 12 40.58	22.11	20.99	19.77	19.18	18.86	18.38	18.49	18.51	18.42	0.45	11.10	-10.49	21.6	43.2
X10	02 26 53.46	-04 05 35.58	-14.26	-13.99	02 26 53.52	-04 05 37.49	24.41	23.58	22.85	22.37	22.04	19.75	19.71	> 19.84	> 19.53	0.20	9.11	-10.09	21.5	42.1
X18	02 26 56.14	-04 08 20.98	-14.93	-13.96</																

Name	X-ray				Optical							IR				Phys. prop.				
	RA (J2000)	DEC (J2000)	log(F _S)	log(F _H)	RA (J2000)	DEC (J2000)	u (AB)	g (AB)	r (AB)	i (AB)	z (AB)	3.6 μ m (AB)	4.5 μ m (AB)	5.8 μ m (AB)	8.0 μ m (AB)	z	log(M) [M _⊙]	log(S) [yr ⁻¹]	n _H [cm ⁻²]	L[2-10] [erg.s ⁻¹]
X45	02 27 10.12	-04 16 49.94	-13.93	-13.69	02 27 10.11	-04 16 48.42	22.10	21.20	20.39	20.04	19.84	19.44	19.45	> 19.84	18.62	0.24	10.10	-9.80	21.4	42.6
X19	02 27 13.18	-04 09 12.33	-13.98	-13.68	02 27 13.21	-04 09 12.45	25.20	24.14	23.37	22.46	22.24	NC	NC	NC	NC	0.64	9.96	-9.89	21.8	43.6
X530	02 27 13.49	-05 06 51.21	-14.54	-13.55	02 27 13.44	-05 06 51.76	> 25.00	24.00	23.52	22.25	21.84	18.89	18.71	18.93	18.66	0.94	10.02	-8.91	23.0	44.2
X693	02 27 13.49	-05 06 52.82	-14.32	-13.78	02 27 13.44	-05 06 51.76	> 25.00	24.00	23.52	22.25	21.84	18.89	18.71	18.93	18.66	0.94	10.02	-8.91	22.5	43.9
X196	02 27 26.27	-04 33 27.02	-14.27	-13.74	02 27 26.31	-04 33 28.00	22.18	20.60	19.70	19.23	19.01	18.76	18.86	18.86	18.75	0.14	10.12	-∞	21.9	42.0
X395	02 27 36.23	-04 58 07.16	-14.34	-14.07	02 27 36.06	-04 58 07.50	NC	23.90	22.75	22.19	NC	19.53	19.14	18.81	18.50	0.58	9.63	-9.58	21.7	43.1
X777	02 27 36.18	-03 56 49.75	-14.52	-13.49	02 27 36.24	-03 56 52.31	NC	22.42	21.13	20.46	NC	NC	NC	NC	NC	0.62	10.31	-8.90	22.8	43.8
X4	02 27 37.04	-04 01 01.17	.	-13.86	02 27 36.86	-04 01 02.60	NC	23.21	22.46	22.08	NC	NC	NC	NC	NC	0.11	8.69	-10.46	21.5	41.6
X204	02 27 38.03	-04 38 06.02	.	-14.03	02 27 38.24	-04 38 04.90	NC	21.80	20.26	19.43	NC	18.18	18.43	18.47	18.56	0.47	11.17	-∞	21.2	42.9
X761	02 27 39.96	-03 42 26.07	-13.91	-13.57	02 27 39.80	-03 42 27.18	NC	22.39	22.00	21.31	NC	NC	NC	NC	NC	0.76	9.99	-8.61	22.0	43.9
X166	02 27 40.66	-04 18 57.90	-14.21	-13.60	02 27 40.58	-04 18 58.24	NC	24.31	24.50	23.52	NC	NC	NC	NC	NC	0.89	9.19	-9.04	22.5	44.0
X41	02 27 49.24	-04 14 48.19	-14.28	-13.94	02 27 49.34	-04 14 45.45	NC	24.41	23.54	22.66	NC	NC	NC	NC	NC	1.19	10.62	-∞	22.3	44.0
X543	02 27 53.18	-05 12 29.06	-14.66	-13.76	02 27 53.26	-05 12 29.71	NC	22.68	21.76	20.78	NC	18.43	18.41	18.20	17.90	0.91	11.40	-10.38	22.9	43.9
X544	02 27 54.03	-05 12 43.25	-14.76	-13.69	02 27 53.98	-05 12 43.48	NC	21.73	20.48	19.90	NC	18.67	18.70	18.57	18.58	0.44	10.77	-10.49	22.7	43.2
X531	02 27 54.44	-05 06 58.27	-14.05	-13.77	02 27 54.47	-05 06 58.93	NC	20.96	20.30	19.80	NC	18.81	18.81	18.69	18.51	0.64	10.65	-9.41	21.8	43.5
X776	02 27 54.59	-03 55 40.84	-14.60	-13.70	02 27 54.52	-03 55 39.19	NC	23.42	22.82	21.93	NC	NC	NC	NC	NC	1.00	10.45	-9.38	22.9	44.1
X784	02 27 56.20	-04 00 17.63	-14.08	-13.76	02 27 56.27	-04 00 18.03	NC	24.26	23.13	21.92	NC	NC	NC	NC	NC	0.92	10.34	-∞	22.0	43.9
X532	02 27 56.90	-05 07 34.97	-14.22	-13.64	02 27 56.89	-05 07 34.86	NC	20.82	19.90	19.43	NC	18.17	18.30	18.31	17.86	0.53	10.90	-9.43	22.3	43.4
X773	02 28 02.15	-03 52 50.21	-14.26	-13.85	02 28 02.15	-03 52 47.45	NC	20.86	20.58	20.06	NC	NC	NC	NC	NC	0.78	10.38	-8.62	22.2	43.6
X17	02 28 02.05	-04 08 09.86	-14.07	-13.88	02 28 02.43	-04 08 09.38	NC	22.46	22.28	21.57	NC	NC	NC	NC	NC	0.87	10.10	-9.14	21.6	43.7
X174	02 28 02.31	-04 25 49.23	-14.65	-13.68	02 28 02.46	-04 25 47.00	NC	22.77	21.55	20.95	NC	NC	NC	NC	NC	0.48	10.28	-10.35	22.6	43.3
X37	02 28 04.22	-04 12 39.50	.	-13.94	02 28 04.31	-04 12 39.36	NC	20.26	19.24	18.75	NC	NC	NC	NC	NC	0.63	10.81	-8.92	21.7	43.3
X165	02 28 04.77	-04 18 18.18	.	-13.39	02 28 04.67	-04 18 15.02	NC	24.14	23.20	22.97	NC	NC	NC	NC	NC	0.46	9.09	-9.01	22.5	43.6
X169	02 28 08.22	-04 20 47.61	.	-13.79	02 28 08.20	-04 20 42.70	NC	22.02	21.14	20.66	NC	NC	NC	NC	NC	0.56	10.39	-9.35	22.0	43.3
X781	02 28 08.88	-03 58 43.74	-14.14	-13.94	02 28 08.89	-03 58 45.14	NC	22.19	21.80	21.44	NC	NC	NC	NC	NC	0.69	9.66	-8.90	21.6	43.4
X552	02 28 12.70	-05 19 04.51	.	-13.82	02 28 12.75	-05 19 01.98	NC	24.19	23.82	22.90	NC	> 21.03	> 20.96	> 19.84	> 19.53	0.83	9.32	-8.93	22.1	43.7
X771	02 28 12.99	-03 51 15.87	-14.44	-13.93	02 28 12.76	-03 51 18.12	NC	19.65	18.90	18.46	NC	NC	NC	NC	NC	0.59	11.10	-9.32	22.2	43.3
X527	02 28 27.75	-05 02 36.42	-13.96	-13.72	02 28 27.88	-05 02 40.41	NC	22.93	22.45	21.88	NC	> 21.03	> 20.96	> 19.84	> 19.53	1.10	11.08	-9.59	21.9	44.1
X539	02 28 43.35	-05 10 11.61	-14.18	-13.48	02 28 43.29	-05 10 11.51	NC	19.93	18.91	18.48	NC	NC	NC	NC	NC	0.12	10.35	-∞	22.1	42.1
X179	02 28 46.93	-04 28 00.53	.	-13.73	02 28 47.02	-04 28 00.04	NC	24.42	23.22	22.17	NC	NC	NC	NC	NC	0.71	9.84	-∞	22.2	43.7

Description of columns:

1. X-ray source Name.
2. X-ray source right ascension.
3. X-ray source declination.
4. X-ray source flux in the soft [0.5-2] keV band in erg.s⁻¹.cm⁻².
5. X-ray source flux in the hard [2-10] keV band in erg.s⁻¹.cm⁻².
6. Optical counterpart right Ascension (J2000).
7. Optical counterpart declination (J2000).
8. u-band magnitude. Note 'NC' means the field has not been observed in that band.
9. g-band magnitude. Note 'NC' means the field has not been observed in that band.
10. r-band magnitude.
11. i-band magnitude.
12. z-band magnitude. Note 'NC' means the field has not been observed in that band.
13. 3.6 μ m magnitude (AB). Tag 'NC' (standing for 'Not Covered') has been used when the location of the object is not overlapping with the SWIRE field. Tag 'NI' stands for 'Not investigated', and is used when the object has no optical counterpart, so we did not investigate either if the radio source has an IRAC counterpart. We have used the same notation for the following columns.
14. 4.5 μ m magnitude (AB).
15. 5.8 μ m magnitude (AB).
16. 8.0 μ m magnitude (AB).
17. Photometric redshift as estimated by ZPEG.
18. Stellar mass as estimated by ZPEG in logarithm base-10 scale.
19. Specific SFR as estimated by ZPEG in logarithm base-10 scale.
20. Estimated hydrogen column density in cm⁻².
21. Estimated rest-frame intrinsic X-ray luminosity in the [2-10] keV band.

CHAPTER 7

Summary and discussion

As discussed in the introduction of this thesis, unified schemes are very successful in explaining properties of many classes of AGN. However, many authors have argued that it does not properly describe the low-power radio-loud AGN. These AGN often lack the observed features of the unified scheme: they do not show evidence for luminous emission lines (Jackson & Rawlings 1997), infrared emission from dusty torus (Whysong & Antonucci 2004; Ogle et al. 2006) and accretion related X-ray emission (Hardcastle et al. 2006; Evans et al. 2006). It has been proposed that the super-massive black hole in these systems may be accreting with a radiatively inefficient accretion (“Radio mode”), as opposed to the emission line selected AGN, which are recognised as being associated with radiatively efficient accretion (“Quasar mode”, Heckman et al. 2004; Best et al. 2005). Interestingly, Best et al. (2005) have shown that AGN as selected using criteria on emission line luminosity or on radio power are statistically independent, suggesting these classes of AGN are triggered by different mechanisms. These two accretion modes might be driven by the temperature of the gas reaching the super massive black hole (see Hardcastle et al. 2007, for a discussion). In this framework, the accretion of cold gas produces a radiatively efficient accretion disk, while hot gas accretion drive an advective accretion, having low radiative efficiency. It has also been proposed that the type of triggering process determines the temperature of the gas reaching the black hole: “wet” galaxy mergers bring the cold gas to the central super massive black hole, thereby triggering quasar mode AGN, while the intergalactic medium (IGM) hot gas cooling triggers a low efficiency hot gas accretion (radio mode).

7.1 SUMMARY

In order to test this scheme, we have studied in this thesis the properties of AGN populations in the XMM-LSS field. Specifically, we have selected two samples of AGN based on (i) radio luminosity and (ii) X-ray luminosity. To do this, we have carried out a deep low-frequency radio survey with the Very Large Array at 74 and 325 MHz, covering 132 and 15.3 degree², leading to the detection of 1500 radio sources. To increase our sample size, we have also observed the XMM-LSS field with the Giant Meterwave Radio Telescope at 240 and 610 MHz. From our radio sources catalog and from the X-ray catalogs of Pacaud et al. (2006), we have identified the radio and point-like X-ray sources with their optical and infrared counterparts in the CFHTLS-W1

and SWIRE surveys. Using the ZPEG stellar synthesis code, we have estimated stellar masses, star formation rates, and redshifts for the normal galaxies, and for the AGN. In order to obtain samples of AGN having reliable photometric redshifts we have developed a method for rejecting the broad line Type-1 AGN. In addition, we have constructed an overdensity parameter based on the photometric redshifts probability function, that gives the significance of the density around a galaxy.

We have classified the radio and X-ray selected AGN in three classes based on their generic properties. The results are as follows:

- (I) **Radio selected** AGN with $M \gtrsim 10^{10.5-10.8} M_{\odot}$: The fraction, f_R , of radio-loud AGN is a strong function of the galaxies stellar mass following the $f_R \propto M^{2.5}$ relationship as found at $z \lesssim 0.3$ (Best et al. 2005). These AGN do not show signs of infrared excess. They are preferentially found in poor cluster environment, while no signs of small 75 kpc scale overdensity is detected around them.
- (II) **Radio selected** AGN with $M \lesssim 10^{10.5-10.8} M_{\odot}$: The fraction of radio-loud AGN has a flatter $f_R - M$ relation as compared to the $M \gtrsim 10^{10.5-10.8} M_{\odot}$ galaxies. These galaxies show a hot infrared excess at wavelength as short as $3.6 \mu\text{m}$ (observer frame). Their environment is very different from the environment of the higher stellar masses objects, in that they lie in large scale underdensities, while their small 75 kpc scale overdensity is higher.
- (III) **X-ray selected** AGN: The fraction of X-ray selected AGN with $L_{[2-10]\text{keV}} > 10^{43} \text{ erg.s}^{-1}$ is a strong function of the stellar mass. The slope of that function is in good agreement with the same relation for the emission line selected AGN, while it disagrees with the fraction-mass relation for the radio selected AGN. Over all the probed stellar mass range X-ray selected AGN show an infrared excess in the near infrared. These AGN are preferentially found in environment underdense on large scales.

7.2 DISCUSSION

We argue in this section that the properties of AGN in the XMM-LSS field support the picture in which there are indeed two very distinct populations of AGN (“Quasar mode” versus “Radio mode”, Best et al. 2005; Hardcastle et al. 2007). We further discuss the relations that might link the triggering processes to these accretion modes.

Our radio selected AGN (I) with $M \gtrsim 10^{10.5-11} M_{\odot}$ seem to be radio mode AGN, as no hot infrared emission is observed for these objects. Best et al. (2005) has argued that the fraction f_R of radio-loud galaxies versus their stellar mass relation ($f_R \propto M^{2.5}$) is generated by the dependency of the IGM gas cooling rate on the stellar mass (Mathews & Brighenti 2003). The mass fraction relation found for the radio selected AGN (I) in our sample agrees with $f_R \propto M^{2.5}$ found at $z \lesssim 0.3$ in the SDSS (Best et al. 2005). These AGN that are in their radio mode, are not sensitive to their local (75 kpc) density, but their large (450 kpc) scale environments are denser than the average. In other words, in such stellar mass range, increasing the density of the surrounding environment on large scales increases the probability that a galaxy is a radio-loud AGN. Altogether, this supports the picture in which their AGN activity is triggered by the IGM hot gas cooling in their atmosphere.

Interestingly, populations (II) and (III) have similar internal and environmental properties, while they are both very different from population (I). The slope of their AGN fraction versus mass relation is similar to the one for emission line selected AGN that are recognised as being AGN in their highly accreting quasar mode (Heckman et al. 2004; Best et al. 2005; Heckman & Kauffmann 2006). In addition, both the (II) and (III) population show infrared emission from hot dust at $3.6 \mu\text{m}$, indicating that black holes are accreting in a radiatively efficient quasar mode. Furthermore, their environments are similar: in a given stellar mass bin, they are found to be preferentially located in large 450 kpc scale underdense environment, with their small 75 kpc scale overdensity being higher on average, which suggests that these populations are indeed the same. Gas-rich galaxy mergers and interaction have often been proposed as mechanisms for triggering the black hole activity (Springel et al. 2005), while this process has been suggested to occur more frequently in underdense environment (Gómez et al. 2003; Best 2004). It may therefore be that the activity of those AGN is triggered by the galaxy mergers and interactions that feed the black hole with cold gas. Alternatively the AGN may be fuelled by cold gas that is infalling from the IGM and also forming stars in the host galaxy. In order to have such cold gas infall, the gas cooling time must be lower than the dynamical infall time, and that is more likely in underdense regions: in the context of large scale structure formation, overdensity correspond the shock-heated, high temperature IGM, while the temperature of the IGM gas in underdense regions is lower.

Altogether, our results are consistent with the picture in which there are two types of accretion, with the first being radiatively efficient “Quasar mode” and the second being radiatively inefficient “Radio mode” (Best et al. 2005; Heckman & Kauffmann 2006; Hardcastle et al. 2007). Our most important result is that those two classes of AGN seem to lie in very different ~ 450 kpc scale environments, suggesting that the nature of the triggering mechanisms might be connected to the rise of these two accretion modes. Hardcastle et al. (2007) discussed a physical picture in which the accretion mode is determined by the temperature of the gas reaching the black hole, with that temperature being connected with both the nature of the triggering process and the environment. In such scenario, for the radio mode accretion, the IGM hot gas cools and reaches the black hole at too high temperature to form a radiatively efficient accretion disk, so it rather accretes spherically. In contrast, the gas-rich galaxy mergers or the cold IGM gas in underdense regions might preferentially bring cold gas to the central black hole, giving rise to a disk-like radiatively efficient accretion (quasar mode).

In this picture these competing triggering processes depend on the large scale environment. It might be that there is quite a direct link between the large scale structure formation and the observed evolution of the AGN luminosity functions.

REFERENCES

- Best, P. N. 2004, MNRAS, 351, 70
Best, P. N., Kauffmann, G., Heckman, T. M., et al. 2005, MNRAS, 362, 25
Evans, D. A., Worrall, D. M., Hardcastle, M. J., Kraft, R. P., & Birkinshaw, M. 2006, ApJ, 642, 96
Gómez, P. L., Nichol, R. C., Miller, C. J., et al. 2003, ApJ, 584, 210
Hardcastle, M. J., Evans, D. A., & Croston, J. H. 2006, MNRAS, 370, 1893
Hardcastle, M. J., Evans, D. A., & Croston, J. H. 2007, MNRAS, 376, 1849

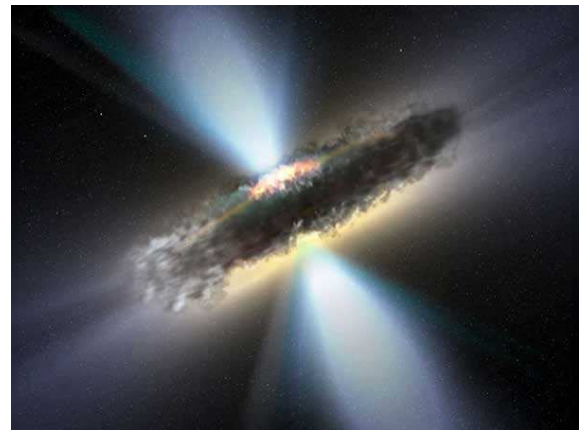
- Heckman, T. M. & Kauffmann, G. 2006, *New Astronomy Review*, 50, 677
- Heckman, T. M., Kauffmann, G., Brinchmann, J., et al. 2004, *ApJ*, 613, 109
- Jackson, N. & Rawlings, S. 1997, *MNRAS*, 286, 241
- Mathews, W. G. & Brighenti, F. 2003, *ARA&A*, 41, 191
- Ogle, P., Whyson, D., & Antonucci, R. 2006, *ApJ*, 647, 161
- Pacaud, F., Pierre, M., Refregier, A., et al. 2006, *MNRAS*, 372, 578
- Springel, V., Di Matteo, T., & Hernquist, L. 2005, *ApJ*, 620, L79
- Whyson, D. & Antonucci, R. 2004, *ApJ*, 602, 116

Nederlandse samenvatting

De kernen van actieve sterrenstelsels (AGN) vormen ongetwijfeld één van de interessantste onderzoeksgebieden binnen de sterrenkunde (zie Figuur 8.1). In de gangbare AGN theorie wordt hier energie op de meest efficiënte manier opgewekt, via materie die zich op een super zwaar zwart gat (van zo'n 10^{6-9} zonsmassa's) stort. Ofschoon we nog niet de details van dit proces kennen, weten we wel dat hierbij veel licht van korte golflengten wordt geproduceerd, en ook bundels van relativistische deeltjes. Rondom de schijf van waaruit massa op het punt staat naar het zwarte gat te vallen (de zogenaamde accretieschijf) zit nog een dikke ring van stof die dit centrale deel van de AGN verhult. Al deze onderdelen samen vormen wat bekend staat als de "overkoepelende theorie" van actieve sterrenstelsels (zie Figuur 8.2).

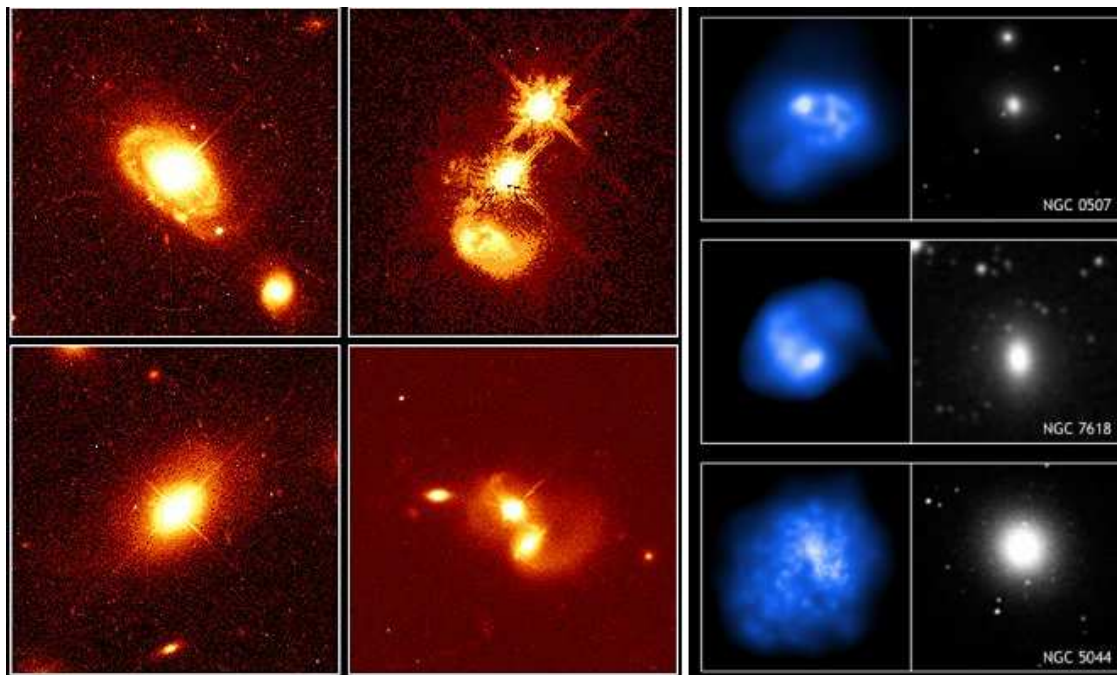


Figuur 8.1: Het sterrenstelsel NGC 7742, dat geclassificeerd is als een Seyfert 1-type sterrenstelsel, vertoont tekenen van activiteit in zijn centrale deel. Men denkt dat hier energie wordt opgewekt doordat massa op een super zwaar zwart gat valt.



Figuur 8.2: Een afbeelding van hoe de kern van zo'n sterrenstelsel er van dichtbij uit zou kunnen zien volgens de overkoepelende theorie van AGN. Rondom het zwarte gat in het centrum van het sterrenstelsel bevindt zich een dikke stofring die dit centrale deel verhult. Ioniserende straling en relativistische deeltjes bewegen zich loodrecht op deze ring weg van de kern.

De overkoepelende theorie van AGN kan echter niet verklaren waarom het vermogen op radio golflengten van sommige radio-luide AGN niet al te groot is. Ook ontbreken heldere emissielijnen in het spectrum van deze sterrenstelsels, terwijl de overkoepelende theorie die juist wel voorspelt. Bij deze sterrenstelsels wordt meestal ook geen warmtestraling waargenomen die afkomstig is van de stofring rond het centrum van de AGN, en ook niet de Röntgenstraling die afkomstig is van de accretieschijf. Sommige wetenschappers hebben daarom voorgesteld dat er twee klassen van AGN zijn: één waarbij straling op een efficiënte manier door de accretieschijf wordt uitgezonden (de zogenaamde "quasar groep"), en één waarbij straling niet efficiënt kan worden uitgezonden (de "radio groep"). Die laatste groep past nog niet binnen het kader van de overkoepelende AGN



Figuur 8.3: Linker 2×2 plaatjes: Vaak zijn heldere AGN in het nabije deel van het heelal geassocieerd met botsende sterrenstelsels. Door zo'n botsing komt koud gas in het centrum van een sterrenstelsel terecht, waar het kan worden opgeslokt door het super zware zwarte gat in het centrum van dat stelsel. Hierdoor zal de AGN gaan stralen. In het rechter paneel laat de linker kolom van 3 plaatjes heet gas zien dat in de buurt van 3 sterrenstelsels koelt en Röntgenstraling uitzendt, terwijl de rechter kolom de sterrenstelsels zelf laat zien in het zichtbare deel van het spectrum. Volgens veel onderzoekers is het koelen van heet gas in de buitenste delen van een sterrenstelsel een alternatieve manier om een AGN aan de praat te krijgen.

theorie. Volgens deze wetenschappers ligt de oorzaak voor deze tweedeling bij de temperatuur van de materie die richting het zwarte gat beweegt. Hun idee is dat als de materie koud genoeg is, deze materie een accretieschijf kan vormen rond het zwarte gat, van waaruit straling makkelijk kan worden weggetransporteerd (de quasar groep). Heet gas kan geen accretieschijf vormen, en daardoor zal straling niet op een efficiënte manier uitgezonden kunnen worden (de radio groep).

De temperatuur van het gas zou inderdaad bepaald kunnen worden door de manier waarop gas in centrale deel van het sterrenstelsel, waar het super zware zwarte gat zich bevindt, terecht komt. Voor heldere AGN is er behoorlijk duidelijk bewijs dat botsingen en interacties van sterrenstelsels een rol spelen. Quasars die zijn geselecteerd op grond van hun eigenschappen in het zichtbare of infrarode deel van het spectrum worden bijvoorbeeld vaker aangetroffen in vervormde sterrenstelsels (Zie Figuur 8.3). Het idee hierbij is dat door een botsing van sterrenstelsels koud gas in de buurt van het zwarte gat komt, en daarbij kan gemakkelijk energie worden uitgestraald. Heet gas dat van nature voorkomt tussen sterrenstelsels (het IGM) koelt af in de buitendelen van zware elliptische sterrenstelsels (Zie Figuur 8.3), en dit is volgens sommigen een andere manier om een normaal sterrenstelsel te veranderen in een actief sterrenstelsel. Recent onderzoek toont aan dat AGN met een laag radio vermogen, en dan vooral van de “radio groep”, door dit mechanisme ontstaan. Het koelen van heet gas produceert dan heet gas dat maar heel lastig straling kan uitzenden als het naar het zwarte gat beweegt.



Figuur 8.4: Een aantal telescopen die voor het onderzoek in dit proefschrift zijn gebruikt. Van links naar rechts, en van boven naar beneden: de Very Large Array en Giant Meterwave Radio Telescope radio interferometers, die zich respectievelijk in New Mexico (VS) en Pune (India) bevinden, de Spitzer infrarood satelliet, de Canada France Hawaii Telescope, en de XMM-Newton Röntgensatelliet.

Dit proefschrift

Doel van dit proefschrift is om te onderzoeken of de theorie klopt die hierboven staat beschreven, waarin het actief worden van een sterrenstelsel afhangt van de eigenschappen van het gas dat naar het zwarte gat valt, en dat op die manier de waarneembare eigenschappen van de AGN bepaalt. Dit zijn daarbij de belangrijkste vragen. Waar bevinden de verschillende typen AGN zich ten opzichte van de grote-schaal verdeling van andere sterrenstelsels? Waardoor wordt de kern van een sterrenstelsel een AGN? Bestaat er een verband tussen de manier waarop een AGN actief wordt en de toestand waarin gas het zwarte gat bereikt (dus “quasar groep” tegenover “radio groep”)? Hoe veranderen deze eigenschappen gedurende de geschiedenis van het heelal?

Een goede manier om deze vragen te beantwoorden is door de statistische eigenschappen van een groot aantal AGN te bestuderen. In dit proefschrift selecteren we 2 groepen AGN in de XMM-Large Scale Structure survey op grond van (i) hun helderheid op radio golflengten (hoofdstuk 2 t/m 5) en (ii) hun helderheid op Röntgen golflengten (hoofdstuk 6). Ons idee daarbij is dat de eerste groep AGN gedomineerd wordt door AGN uit de “radio groep”, en de tweede door AGN uit de “quasar groep”. Van elke AGN in deze dataset bepalen we de interne en omgevings eigenschappen, zoals totale massa aan sterren, roodverschuiving, hoeveelheid sterren die worden gevormd in het sterrenstelsel, teveel aan infrarode emissie, en aantal naburige sterrenstelsels. Door de interne en omgevings eigenschappen te bestuderen van de stelsels die we hebben geselecteerd op grond van hun eigenschappen op radio en Röntgen golflengtes kunnen we de vragen die hierboven

zijn gesteld proberen te beantwoorden. Hierna geef ik een gedetailleerdere beschrijving van de verschillende hoofdstukken.

In **hoofdstuk 2** beschrijven we een lage-frequentie radio survey van het XMM-LSS veld die we hebben uitgevoerd met de Very Large Array (VLA, figuur 8.4) op frequenties van 74 en 325 MHz. Deze data beslaan 132 en 15.3 vierkante graden aan de hemel respectievelijk. Vanwege de storende invloeden van de ionosfeer en vanwege het grote oppervlak aan de hemel dat we waarnemen, hebben we extra aandacht besteed aan de calibratie van onze data.

Om het aantal radiobronnen dat we kunnen gebruiken te vergroten, en om ook de radio spectra van deze bronnen te kunnen bepalen, gebruiken we in **hoofdstuk 3** het grote antenne-oppervlak van de Giant Meterwave Radio Telescope (GMRT, figuur 8.4) om het XMM-LSS veld op 240 en 610 MHz waar te nemen.

We identificeren de radiobronnen die we op frequenties van 74, 240, 325 en 610 MHz hebben waargenomen met sterrenstelsels in het zichtbare deel van het spectrum in **hoofdstuk 4**. Hierbij maken we gebruik van een catalogus van bronnen in het optische deel van het spectrum, en van afbeeldingen van de hemel. We schatten dat $\sim 75\%$ van de radio bronnen een optische tegenhanger hebben, en we bepalen fotometrische roodverschuivingen voor de 3 miljoen sterrenstelsels in het onderzochte gebied aan de hemel, inclusief de gaststelsels waarin zich radiobronnen bevinden. We ontwikkelen een methode om sterrenstelsels met een verkeerde fotometrische roodverschuiving te verwijderen uit onze bronnenlijst. Deze methode maakt gebruik van 2 verschillende manieren om de fotometrische roodverschuiving te berekenen, in combinatie met een optisch kleur-kleur criterium.

In **hoofdstuk 5** bestuderen we met de catalogus van sterke radiobronnen die we in hoofdstuk 4 hebben samengesteld de interne eigenschappen van deze radiosterrenstelsels, en ook hoe hun omgeving eruit ziet. Om de omgeving van zo'n radiostelsel te karakteriseren definiëren we een maat voor de dichtheid van naburige sterrenstelsels, waarbij we rekening houden met de onzekerheden in de fotometrische roodverschuiving. We beargumenteren dat de resultaten van de analyse uit dit hoofdstuk consistent zijn met het beeld dat bij botsingen van sterrenstelsels een accretieschijf ontstaat die efficiënt energie uitstraalt, en dat de AGN uit de "radio groep" vooral ontstaan doordat gas koelt in de buitendelen van een zwaar elliptisch sterrenstelsel.

In **hoofdstuk 6** presenteren we een catalogus van AGN die we hebben geselecteerd in de harde Röntgenband (2-10 keV), en we analyseren deze data op een vergelijkbare manier als die we in hoofdstuk 4 en 5 hebben beschreven. We laten in dit hoofdstuk zien dat AGN die op basis van hun Röntgenstraling zijn geselecteerd, van hetzelfde type zijn als de AGN die we hebben geselecteerd op grond van hun emissielijnen. Hieruit concluderen we dat het in beide gevallen gaat om AGN uit de "quasar groep".

Tenslotte presenteren we in **hoofdstuk 7** de belangrijkste conclusies van dit proefschrift, en we bespreken mogelijke implicaties. Onze resultaten bevestigen dat er twee verschillende typen AGN zijn ("quasar groep" en "radio groep"), en dat deze AGN worden gevonden in sterk verschillende omgevingen. betekenen dat de manier waarop een AGN actief wordt te maken heeft met de manier waarop materie naar een zwart gat in de kern van het sterrenstelsel valt. Volgens dit beeld stroomt bij een botsing van sterrenstelsels koud gas naar het zwarte gat. Dit gas vormt dan een accretieschijf, en kan op die manier heel efficiënt straling uitzenden. Gas dat koelt in de atmosfeer van een zwaar elliptisch sterrenstelsel is te heet om een accretieschijf te vormen, en het zal daarom veel minder efficiënt straling kunnen uitzenden. Het aantal botsingen tussen sterrenstelsels en de

hoeveelheid gas die zich in de buurt van een sterrenstelsel bevindt hangt af van het aantal sterrenstelsels dat zich in een bepaald volume van het heelal bevindt. Daarom kan er een heel direct verband bestaan tussen de vorming van sterrenstelsels en groepen van sterrenstelsels enerzijds, en de waargenomen verandering in de helderheidsverdeling van AGN anderzijds.

Résumé en français

Les noyaux actifs de galaxies (NAG) sont des objets fascinants (cf. la figure 9.1). La principale théorie les décrivant, le *Modèle Unifié*, établit que les propriétés que l'on observe au sein des NAG sont la conséquence de la chute de matière dans un trou noir dont la masse peut atteindre plusieurs milliards de masses solaires. En tombant dans le trou noir, la matière forme un disque, et libère de gigantesques quantité d'énergie suivant un processus que l'on nomme *accrétion* (on parle alors du *disque d'accrétion*). Ce processus de transformation d'énergie est le plus efficace que l'on connaisse : il correspond à la transformation d'énergie gravitationnelle en énergie thermique, avec une efficacité de l'ordre d'une dizaine de pour cent (contre $\sim 1\%$ pour la fusion thermonucléaire). Dans cette théorie, le trou noir est entouré d'un *tore de poussière* et de nuages de gaz orbitants autour et à l'intérieur du système tore/trou noir. Le disque d'accrétion dégage un rayonnement intense dans les domaines ultraviolet et X. Ce rayonnement provoque notamment le chauffage du tore de poussière (cf. la figure 9.2). Dans certains NAG (les NAG radio), on observe des jets de particules qui se propagent orthogonalement au plan du tore de poussière, en émettant des ondes radio.



FIG. 9.1: La galaxie NGC 7742 est de type Seyfert 1. Elle montre des signes d'activité dans ses régions centrales. Dans l'image communément acceptée, cette immense quantité d'énergie est produite par la chute de matière dans un trou noir supermassif situé en son centre.

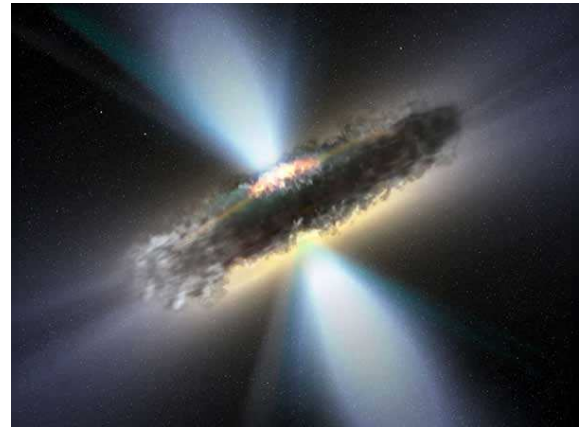


FIG. 9.2: Vue d'artiste d'un NAG tel que décrit par le Modèle Unifié (elle correspond aux régions centrales de la galaxie de la figure 9.1). Le trou noir super massif est entouré d'un tore de poussière. Le rayonnement ionisant, ainsi que les éventuels jets radio, se propagent dans la direction orthogonale au plan du tore.

Bien que le trou noir ait une masse négligeable à côté de celle de sa galaxie hôte, son rôle quant à la formation des structures dans l'Univers, pourrait-être déterminant. En effet, l'immense quantité d'énergie dégagée lors d'une courte période d'activité d'un de ces monstrueux trous noirs peut

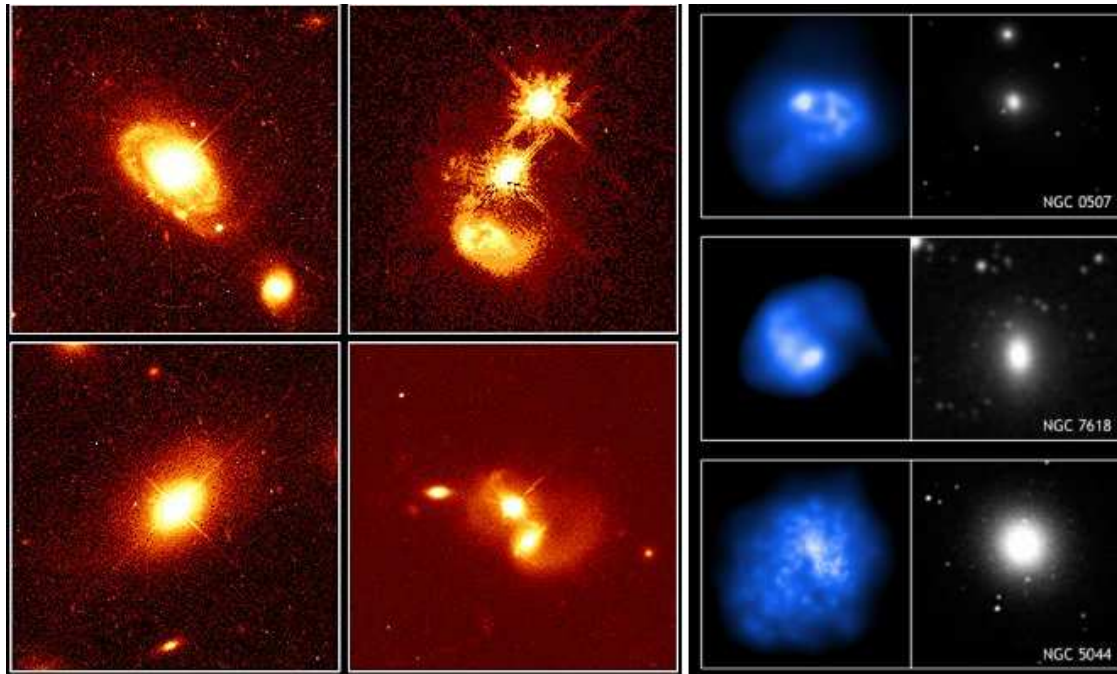


FIG. 9.3: (A gauche) Dans l’univers local, les NAG sont associés à des collisions de galaxies. On pense que l’interaction entre galaxies peut causer la chute de gaz froid vers les régions centrales de la galaxie – où réside le trou noir – et déclencher l’activité du NAG dans son mode Quasar (voir texte). (A droite) De grandes quantités de gaz chaud du milieu inter-galactique sont observées dans l’atmosphère des galaxies elliptiques massives (le gaz à gauche, les étoiles à droite). Certains auteurs proposent que ce gaz chaud, en refroidissant, est à même d’atteindre les régions centrales de la galaxie. Ce mécanisme peut constituer un moyen alternatif afin de déclencher l’activité des NAG dans leur mode Radio.

égaler l’énergie de liaison d’un amas de galaxie, qui contient plusieurs milliers de galaxies, chacune contenant plusieurs centaines de milliards d’étoiles. Ainsi, il est de plus en plus couramment accepté que pour conter la grande histoire de l’univers et décrire son état actuel, il est nécessaire de parler de l’existence des NAG, et de leur rôle.

Bien que le Modèle Unifié (Fig. 9.2) décrive fidèlement nombre de propriétés observationnelles des NAG, certaines classes y échappent. C’est notamment le cas des radio-galaxies de faible puissance qui ne présentent ni raies d’émission, ni excès en infrarouge, ni émissions en X liés à l’existence d’un disque d’accrétion, alors que ces propriétés sont prédites par le Modèle Unifié. Il a été démontré récemment que l’activité du trou noir dans ces NAG radio de faible puissance résulteraient d’un phénomène différent et indépendant. Certains auteurs ont alors proposé qu’il existe deux classes distinctes de NAG, dont l’émergence est liée à la température du gaz atteignant le trou noir central. Dans ce schéma, l’accrétion de gaz froid produit une accrétion en disque, qui transforme efficacement l’énergie gravitationnelle en énergie thermique (on dit alors qu’il est *radiativement efficace*). Les propriétés perdues par le Modèle Unifié sont alors observées. En revanche, l’accrétion d’un gaz chaud produirait une accrétion advective ou sphérique, radiativement inefficace, où la majeure partie de l’énergie gravitationnelle serait transformée en énergie cinétique dans les jets radio. Dans la suite, le mode d’accrétion en disque, radiativement efficace et caractérisant le Modèle Unifié, est nommé “mode Quasar”, tandis que le mode d’accrétion sphérique, radiative-

ment inefficace, est nommé “mode Radio”.

Comme nous l’avons exposé précédemment, les ingrédients nécessaires pour créer un NAG sont : un trou noir super massif, un réservoir de gaz pour l’alimenter, et un mécanisme permettant de faire chuter le gaz dans le trou noir. Si la température du gaz accrété détermine les propriétés des NAG, on peut se demander ce qui détermine la température du gaz. Pour les NAG de forte luminosité, il semble que cette chute se produise lors des collisions et interactions entre galaxies (cf. Fig. 9.3). La collision de galaxie est alors le *mécanisme déclencheur* de l’activité du NAG. Un schéma alternatif a été proposé, dans lequel ce n’est pas le gaz du milieu inter-stellaire (intra-galactique) qui alimente le trou noir et déclenche son activité, mais le gaz chaud du milieu inter-galactique. On observe de très grandes quantités de ce gaz chaud se refroidissant dans l’atmosphère de galaxies elliptiques massives (cf. Fig. 9.3). En refroidissant, ce gaz chute vers le fond du puits de potentiel gravitationnel généré par la galaxie et alimente éventuellement le trou noir central, ce qui déclenche son activité.

Il a ainsi été proposé que le type de mécanisme déclencheur pouvait être lié au mode d’accrétion (mode Quasar/Radio). Dans ce schéma, la collision/interaction entre galaxies chargées de gaz froid déclencherait l’accrétion en disque du gaz froid (processus radiativement efficace). Quant au gaz chaud du milieu inter-galactique, il alimenterait le trou noir central lors de son refroidissement, déclenchant l’accrétion sphérique radiativement inefficace qui caractérise le mode radio.

Cette thèse

Le but de cette thèse est de tester le schéma décrit plus haut, dont les différents mécanismes déclencheur de l’activité radio sont liés au type d’accrétion, donc aux propriétés des NAG et à leur influence sur leur environnement. Les principales questions abordées lors de cette étude sont les suivantes : comment sont distribuées les différentes classes de NAG, dans la structure à grande échelle de l’univers ? Quels sont les mécanismes déclencheurs de l’activité des NAG ? Quels sont les connexions entre mécanisme déclencheur et mode d’accrétion (mode Quasar/Radio) ? Comment ces relations ont évolué dans l’histoire de l’univers ?

Une manière moderne d’aborder ces questions consiste à étudier les propriétés statistiques d’un grand échantillon de NAG. Dans cette thèse, nous sélectionnons deux échantillons de NAG dans le champ XMM-LSS (XMM est le nom du satellite et LSS est l’acronyme pour “*Large Scale Structure*” ou “*structure à grande échelle*” en français), basés sur (i) la luminosité radio et (ii) la luminosité X. L’idée sous-jacente est de sélectionner deux échantillons de NAG en mode d’accrétion Radio et en mode d’accrétion Quasar respectivement. En utilisant des modèles physiques, une série d’estimateurs a été attachée à chaque objet dans ces échantillons : masse stellaire, distance, taux de formation stellaire, excès en infrarouge et paramètre environnemental de surdensité. En étudiant les propriétés statistiques de ces estimateurs sur ces ensembles d’objets, il est possible de contraindre la nature de ces populations. Par exemple, les observations infrarouges nous informent sur la présence de poussières chaudes, et donc sur la nature du mode d’accrétion. Voici le descriptif détaillé du contenu de cette thèse :

Dans le **Chapitre 2** un sondage à basse fréquence (domaine radio) du champ XMM-LSS à 74 et 325 MHz est présenté. Ces observations ont été conduites en utilisant l’interféromètre radio *Very Large Array* (Fig. 9.4).

Pour augmenter la taille des échantillons de NAG, dans le **Chapitre 3**, le champs XMM-LSS



Fig. 9.4: Les données utilisées dans le cadre de cette thèse proviennent principalement des instruments suivants (*de gauche à droite, de haut en bas*) : interféromètre radio *Very Large Array* (Nouveau Mexique, USA), interféromètre radio *Giant Meterwave Radio Telescope* (Pune, Inde), télescope spatial infrarouge *Spitzer*, télescope optique *Canada France Hawaii Telescope*, télescope spatial *XMM-Newton*.

est observé à 240 et 610 MHz avec l'interféromètre *Giant Meterwave Radio Telescope* (Fig. 9.4).

Dans le **Chapitre 4**, en utilisant les observations du satellite *Spitzer* et du télescope Canada-France Hawaï Telescope (CFHT), on identifie les contreparties optiques et infrarouges des NAG détectées dans le domaine radio. En utilisant un modèle de synthèse de population stellaire nous estimons les masses, distance, et taux de formation stellaire de ~ 3 million de galaxies normales, et de quelques centaines de NAG. Nous construisons une méthode de rejection des NAG pour lesquels ces estimations ne sont pas fiables.

Dans le **Chapitre 5**, nous étudions les propriétés de l'échantillon de NAG défini dans le Chapitre 4. Afin de quantifier l'environnement de ces sources, nous construisons un estimateur statistique de surdensité. Cette étude révèle une dichotomie à la fois interne et environnementale. Les NAG localisés dans des galaxies massives ne présentent pas d'excès en infrarouge, alors qu'ils sont situés dans des environnements denses. Les NAG de plus petite masses montrent un excès infrarouge, et sont situés dans des environnements sous-denses. Nos données sont consistantes avec l'idée que le mode quasar est déclenché par les interactions de galaxies, alors que le mode radio est déclenché par le refroidissement du gaz inter-galactique chaud.

Dans le **Chapitre 6**, un échantillon de NAG sélectionné en bande X durs en suivant la démarche décrite dans les chapitres 4&5. Contrairement aux NAG sélectionnés en utilisant un critère dans le domaine radio, cette population est très homogène : elle présente des excès importants en infrarouge à travers toute la gamme de masse stellaire, et réside dans des environnements sous-denses. De la présence d'excès infrarouge, nous déduisons que cette population de NAG accrete dans son

mode Quasar, et de sa préférence des milieux sous-denses, nous déduisons que les collisions de galaxies jouent un rôle dans le déclenchement de l'activité de ces NAG.

Dans le **Chapitre 7**, les résultats importants de cette étude sont présentés, et nous discutons leurs implications possibles. Nos résultats indiquent l'existence de deux types de NAG, résidants dans des environnements différents. La relation entre environnement et type de NAG suggère un lien entre mécanisme de déclenchement et mode d'accrétion. Les caractéristiques des échantillons de NAG présentés dans cette these sont consistant avec le schéma suggéré par plusieurs auteurs, dans lequel la collision de galaxies apporte du gaz froid au trou noir central et déclenche une accrétion en disque, radiativement efficace, alors que l'accrétion du gaz chaud du milieu inter-galactique produit une accrétion sphérique radiativement inefficace. Ces résultats mettent en lumière la nature possible de la relation entre formation de la structure à grande échelle, et évolution des NAG.

Curriculum vitae

I was born in Saint-Brieuc (Cotes d'Armor, Breizh, France) on the 18th of August 1979 from Michel Tasse and Beatrice Tasse (born Guillou). I grew up in Landerneau (Finistère), where I spent most of my childhood observing our cloudy sky with a 115/900 Newton telescope, and building home made explosives and rockets. In 1995 I moved to Rennes the capital of Brittany, where I graduated from high school in 1997. During the same year I entered the *Institut National des Sciences Appliquées* (INSA) engineering school. I had my first professional contact with astronomy in 2001 at the Observatory of Sofia (Bulgaria) under the supervision of Valeri Golev, where I worked on the calibration of the CCDs of the Rosen observatory. For my final research project in 2002, I worked on the Weakly Interacting Massive Particle (WIMP) dark matter detection experiment (EDELWEISS) at the Commissariat à l'Énergie Atomique (CEA) in Saclay. During that period, I modeled and experimentally characterised superconducting thin layers (with critical temperatures of ~ 10 mK), in the goal of building a μ K sensitive thermometer. In 2002 I both graduated from the *Génie Physique* department at the INSA, and from the *Physique, matière et rayonnement* master degree of the Rennes university. During the same year I entered an astrophysics oriented master degree of the Observatoire de Meudon (*Astrophysique et méthodes associées*). I did my final research project at the European Southern Observatory (ESO) in Santiago (Chile), trying unsuccessfully to detect Ly α emitters at $z \sim 6.5$.

I arrived in Leiden in september 2003, where I started my PhD research on the relationship between active galactic nuclei and large scale structure, under the supervision of Huub Röttgering and George Miley. During my PhD I had a few working periods abroad with Aaron Cohen at the Naval Research Laboratory in Washington, Philip Best at the Royal Observatory of Edinburgh, and Damien Leborgne and Marguerite Pierre at the CEA. I went observing twice at the Giant Meterwave Radio Telescope (NCRA, Puna, India), and at the William Herschel Telescope in La Palma (Canary Islands). I participated in the Very Large Array summer school in Socorro (New-Mexico, USA), in the high redshift radio galaxies conference at Granada (Spain), and in various XMM-LSS consortium meeting. I have been a teaching-assistant for the active galactic nuclei lectures at Leiden Observatory.

Acknowledgement

During these four years, there have been many good moments, and more rarely, difficult ones. During all that time, my family and friends have been there. This thesis is dedicated to them: Papa, Maman, Gilles, Marie, Mami Monique, Papi Jacques, Mami Emilienne, Papi Robert, Herve & Marie and their children, Marie-Paul & Guillaume and their children, Maryse et Jean and their children. This thesis is equally dedicated to the people who were a great source of inspiration for me (in order of appearance): Ty & Aude & Elliott, Mik, Ben, Pedro & Miss & Edouard-Hamidou, Doudouze & Cathel, Neven & Clémence, Jeff, Jean-Marie, Nivanh & Bea, Julien & Barbara, Guillaume & Mayil, Jacques-Edern & Hélène, Cedric & Christelle, Fab', Jean-No, Elen & Unar, Gil, Caro, Biloute, Olive, Jule-Millien & Dim' & Pinpin & Cat' & Alain, Evelyne, Sylvouille, Paty, Jose-Luís, La Vero, Calbuco, Bea & Alberto & Nagual, Andy, Carlos, Erik-Jan, Mirek & Lucia, Tomash & Tia, Sophie, Pierre-Guillaume, Marta, Alma, Marie & Patricia, Cedrouze, Mario & Daisy, Eline, Bruno & Veronica, Maud, Toto & Eloïse & Chloé, Estelle, Olivera & Martin, Niruj, Claudio, Annette la Paquerette, Simone, David-Charles, Eric, Brent, Raymond, Thibaud & Emilie, Hayden & Laura, Malcom, Robert, Luc, Matthieu & Lara, and the Multipleks crew.

I thank Valeri Golev, Xavier-François Navick, Daniel Rouan, Didier Pelat, Jacqueline Plancy, and Jean-Gabriel Cuby for helping me cross the important steps towards starting a PhD in Astrophysics. I thank my collaborators Aaron Cohen, Damien Le Borgne for always supporting me when I needed it. I address my endless gratitude to Philip Best, without whom this thesis would not be as it is. I thank the computer group, the secretaries, as well as all the administrative staff from the observatory that have always been very nice and helpful to me. I thank the man that succeeded in translating the abstract of the thesis to dutch: Dominic Schnitzeler! A special thank to the people who have been reading this thesis, to correct the many spelling mistakes: Tracy, Brent, George, Niruj, and Nina. Thanks to Reinout who translated the stellingen to dutch. Finally, I thank my brother Gilles for designing the cover of this thesis.

Cyril Tasse
Leiden, January 18, 2008

